

# Modeling, Design, and Optimization of Radio-Frequency Microelectromechanical Structures

## Dissertation

zur Erlangung des akademischen Grades

**Doktoringenieur  
(Dr.-Ing.)**

von **M.Sc. Ehab Khalaf Ibrahim Hamad**  
geb. am 8. November 1970 in Assuit, Ägypten

genehmigt durch die Fakultät für Elektrotechnik und Informationstechnik  
der Otto-von-Guericke-Universität Magdeburg

## Gutachter:

Prof. Dr.-Ing. Abbas S. Omar  
Prof. Dr.-Ing. Edmund P. Burte  
Doc. Ing. DrSc. Jan Macháč

Promotionskolloquium am: 03. November 2006

This work is dedicated to my family for all their love and sacrifice on my behalf.

*Ehab*

# Acknowledgement

First of all, I would like to thank God, who gives us every thing and without him nothing can be done.

I would like to thank all of the people who have helped me through the difficult task of creating this dissertation. First and foremost, I would like to thank my advisor, Professor A. S. Omar, for allowing me to continue with this thesis topic, even after six months of nearly no progress. His encouragement and insight were extremely valuable throughout my graduate career. I would also like to thank my committee members for their time and support: Professor J. Macháć from Czech Technical University, Prague and Professor E. P. Burte.

I owe many thanks to Dr. Amr Safwat from Ain Shams University, Cairo, Egypt for his guidance through the early years of chaos and confusion. Professor Elsherbeni from the University of Mississippi, USA expressed his interest in my work and supplied me with the preprints of some of his recent joint work in finite difference technique, which gave me a better perspective on my own results and friendly encouragement.

Additionally, I would like to thank all members in the Chair of Semiconductor Technology for their continuous trying to get the MEMS technology established in our faculty, specially Anatoliy, Mr. Vierhaus, and Mr. Kuhlemann in addition to the head of the Chair, Prof. Burte. A big thanks goes out to Mr. Rodiek, this very high technical man in our workshop.

I would like to thank all my colleagues in the Institute for Electronics, Signal Processing, and Communications, specially Ali Ramadan, Ahmed Boutejdar, Alex Teggatz, and Ayan Bandyopadhyay for continuous discussion and useful comments on my thesis in the revising process.

At Last and not least, I would like to thank my family; parents, brothers, and sisters provided much needed support. I declare my deepest dept of gratitude to my wife, *Lobna*, who has preserved countless nights and weekends alone and with our children while I studied, who provided understanding and loving support when I needed it most even though they could not be right here with me.

Magdeburg, 25.09.2006

*Ehab K. I. Hamad*

# Zusammenfassung

Im Rahmen der Dissertation mit dem Titel "Modellierung, Entwurf und Optimierung von hochfrequenten mikroelektromechanischen Strukturen" werden zwei und dreidimensionale verbundene elektromechanische Modelle für sogenannte HF-MEMS Schalter entwickelt. Die elektrostatische Lösung wird berechnet, indem man entweder die Gleichung von Laplace in den homogenen Regionen und das Gesetz von Gauss an den Schnittpunkten anwendet oder indem man das Gesetz von Gauss in der kompletten Region anwendet. Im Falle der Anwendung der Gleichung von Laplace wird ein System von Gleichungen mit der Bandmatrixmethode erzeugt und gelöst, während bei der Anwendung des Gesetzes von Gauss in der kompletten Region eine Aktualisierungsgleichung für das Potential erzeugt wird, die mit Hilfe einer leistungsfähigen iterativen Methode berechnet wird. Das mechanische Modell basiert auf der Lösung der mechanischen Gleichungen, welche die Bewegung der Membrane entweder analytisch oder numerisch beschreiben. Die Interaktion zwischen dem elektrostatischen und dem mechanischen Modellen wird iterativ betrachtet. Die Form der Brücke, als Funktion der angewandten Spannung und die Spannung des Zuges nach unten werden berechnet, wobei eine allgemeine Übereinstimmung mit existierenden Messdaten für ähnliche Schaltungsgeometrien festgestellt werden kann. Die Modelle werden mit Hilfe eines numerischen Simulationsprogramms implementiert (*MATLAB<sup>TM</sup>*).

Diese Dissertation umfasst auch die Entwurfs- und Optimierungsaspekte von HF-MEMS Schaltern mit Hilfe von elektromagnetischen (EM) 3-D Simulatoren. Zwei Entwürfe sind vorgeschlagen worden. Der erste Entwurf ist der eines MEMS Schalters in  $\pi$ -Konfiguration für Breitbandanwendungen mit guten Isolationseigenschaften. Der zweite Entwurf ist der eines Einsauf-Drei-Umschalter (SP3T). Beide Schalter sind auf einem hochresistiven Silikonsubstrat entworfen und basieren auf einer doppelgestützten Membranarchitektur. Ein Ersatzschaltbild für die Beschreibung des Schalters wird vorgeschlagen.

Zusätzlich wird eine zweidimensionale periodische Schlitz auf der Rückseite der Struktur (DGS) mit einem L-förmigen DGS in koplanarer Wellenleitertechnologie (CPW) vorgeschlagen. Die Abhängigkeit der Ersatzschaltungselemente von den Entwurfsparametern der DGS wird demonstriert. Die vorgeschlagenen DGS Strukturen

sind sehr gut geeignet um leistungsfähige Bandstop-Filter zu entwerfen. Alle theoretischen Ergebnisse werden experimentell überprüft.

Als Anwendung für DGS und MEMS Schalter wird ein rekonfigurierbarer HF-MEMS DGS Resonator entworfen, der unter Verwendung einer 2-D periodischen DGS und von HF-MEMS Schaltern die Resonanzfrequenz steuert. Ein neues Ersatzschaltungsmodell für den Resonator wird vorgeschlagen und eine Methode um die Werte der Schaltkreiselemente zu extrahieren wird abgeleitet. Die vorgeschlagene Struktur kann unter anderem in Automobil- und Transceiverbauteilen verwendet werden.

# Abstract

This dissertation develops two and three-dimensional coupled electrostatic-mechanical models for RF MEMS switches. The electrostatic solution is obtained either by applying Laplace's equation in the homogenous regions and Gauss's law at the interface nodes or by applying Gauss's law in the whole regions. In case of applying Laplace's equation, a system of equations is generated and solved using the band matrix method, while in case of applying Gauss's law in the whole region an updating equation for the potential is generated then an efficient iterative technique is employed to compute it. The mechanical model is based on solving the mechanical equation that describes the movement of the switch's bridge either analytically or numerically. The interaction between the electrostatic and mechanical models is considered iteratively. The shape of the bridge, as a function of applied voltage, and the pull down voltage have been calculated and are found to be in close agreement with published measurement data for similar switches geometries. The models are implemented with a numerical simulation program (*MATLAB<sup>TM</sup>*).

This thesis covers also the design and optimization aspects of RF MEMS switches using full-wave 3-D EM simulators. Two designs have been proposed. One is a  $\pi$ -configuration MEMS switch for wideband and high-isolation applications. Second is a single-pole, three-throw switch. Both switches are designed on a high resistivity *Si* substrate and are based on fixed-fixed membrane architecture. An equivalent circuit model for each switch is proposed to describe the switch RF-performance very well.

Additionally, a two-dimensional periodic and an L-shaped defected ground structures (DGS) in the coplanar waveguide technology are proposed. A criterion that determines the dependence of the equivalent circuit elements on the design parameters of the defect is demonstrated. The proposed DGS structures are efficient to design high-performance bandstop filters. All theoretical results are verified experimentally and results agree very well.

Last, as an application for the DGS and MEMS switches, an RF MEMS reconfigurable DGS resonator is designed using a 2-D periodic DGS and RF MEMS switches to control the resonant frequency. A new equivalent circuit model for the resonator is proposed and the method to extract the circuit element values is derived as well. The proposed structure can be used in automotive and transceiver applications.

# Table of Contents

<b>Dedications</b>	<b>i</b>
<b>Acknowledgement</b>	<b>ii</b>
<b>Zusammenfassung</b>	<b>iii</b>
<b>Abstract</b>	<b>v</b>
<b>Table of Contents</b>	<b>vi</b>
<b>List of Symbols</b>	<b>ix</b>
<b>1 Introduction</b>	<b>1</b>
1.1 RF MEMS Switches . . . . .	3
1.1.1 State-of-the-art . . . . .	5
1.1.2 RF MEMS Switch Modeling . . . . .	7
1.2 Defected Ground Structures . . . . .	9
1.3 MEMS Resonator . . . . .	11
1.4 Contribution . . . . .	11
1.5 Thesis Organization . . . . .	13
<b>2 Two-Dimensional Coupled Electromechanical MEMS Analysis</b>	<b>14</b>
2.1 RF MEMS Switches Operation . . . . .	15
2.2 Electromechanical Coupled Analysis Algorithm . . . . .	15
2.3 2-D Electrostatic Analysis . . . . .	17
2.3.1 Potential Computation . . . . .	17
2.3.2 Electrostatic Field Calculation . . . . .	25
2.3.3 Capacitance Determination . . . . .	25
2.3.4 Electrostatic Charge and Force Induced on the Membrane . . . . .	27
2.4 2-D Mechanical Analysis . . . . .	29
2.4.1 1st Algorithm: Analytical Solution . . . . .	30
2.4.2 2nd Algorithm: Numerical Solution . . . . .	32
2.5 Coupling the Electrostatic and Mechanical Models . . . . .	33
2.6 Results and Discussions . . . . .	35
2.7 Conclusion . . . . .	37

<b>3</b>	<b>Three-Dimensional Coupled Electromechanical MEMS Analysis</b>	<b>38</b>
3.1	The Simulation Program Algorithm . . . . .	39
3.1.1	The 3-D Electrostatic Analysis . . . . .	40
3.1.2	The Mechanical Model . . . . .	46
3.1.3	The Electrostatic-Mechanical Coupling Process . . . . .	48
3.2	Results and Discussions . . . . .	50
3.3	Conclusion . . . . .	52
<b>4</b>	<b>Design and Optimization of RF MEMS Switches</b>	<b>53</b>
4.1	$\pi$ -Configuration RF MEMS Switch . . . . .	53
4.1.1	Design and Description . . . . .	55
4.1.2	Numerical Experimentations . . . . .	57
4.1.3	Circuit Modeling . . . . .	59
4.1.4	Switch Layout . . . . .	61
4.2	SP3T Wideband RF MEMS Switch . . . . .	63
4.2.1	Design and Description . . . . .	63
4.2.2	EM Simulation and Circuit Modeling . . . . .	66
4.2.3	Switch Layout . . . . .	66
4.3	Conclusion . . . . .	66
<b>5</b>	<b>DGS: Design and Applications</b>	<b>69</b>
5.1	Introduction . . . . .	69
5.2	2-D Periodic DGS for CPW Line . . . . .	69
5.2.1	Structure Design Methodology . . . . .	70
5.2.2	EM Simulation and Circuit Modeling . . . . .	71
5.2.3	Experimental Verifications . . . . .	73
5.2.4	Cascaded 2-D Periodic DGS for CPW Line . . . . .	74
5.3	L-Shaped DGS for CPW Line . . . . .	76
5.3.1	Theory and Basic Idea . . . . .	78
5.3.2	Structure Design and Discription . . . . .	80
5.3.3	EM Simulation and Circuit Modeling . . . . .	80
5.3.4	Parametric Analysis . . . . .	81
5.3.5	Measurements and Applications . . . . .	85
5.4	Conclusion . . . . .	86
<b>6</b>	<b>RF MEMS Reconfigurable DGS Resonator</b>	<b>89</b>
6.1	2-D PDGS for CPW on Si-Substrate . . . . .	90
6.2	RF MEMS Series-Resistive Switch . . . . .	92
6.3	RF MEMS Reconfigurable DGS Resonator . . . . .	94
6.3.1	Circuit Model and Parameters Extraction . . . . .	97
6.4	Conclusion . . . . .	99

<b>7</b>	<b>Conclusions</b>	<b>101</b>
7.1	Contributions . . . . .	101
7.2	Suggestions for Future Work . . . . .	103
	<b>Appendices:</b>	<b>104</b>
<b>A</b>	<b>Matlab 2-D Coupled Electrostatic-Mechanical Model Scripts</b>	<b>105</b>
A.1	Matlab Code of the 2-D Coupled Model . . . . .	105
<b>B</b>	<b>Matlab 3-D Coupled Electrostatic-Mechanical Model Scripts</b>	<b>117</b>
B.1	Matlab Code of the 3-D Coupled Model . . . . .	117
	<b>Bibliography</b>	<b>130</b>
	<b>Curriculum Vitae</b>	<b>136</b>
	<b>Related Publications</b>	<b>137</b>

# List of Symbols

Symbol	Description	Unit
$b$	Beam width	m
$D$	Plate stiffness	N/m
$E$	Young's modulus	N/m <sup>2</sup>
$E$	Electrostatic field	V/m
$f$	Electrostatic force density	N/m
$f_o$	Resonant frequency	Hz
$g_o$	Nominal gap height	m
$I$	Moment of inertia	m <sup>4</sup>
$k$	Spring constant	N/m
$L$	Beam length	m
$p$	Pressure induced on the beam	N/m <sup>2</sup>
$t$	Beam thickness	m
$T_a$	Axial stress	N/m <sup>2</sup>
$T_r$	Residual stress	N/m <sup>2</sup>
$U$	Storage energy	Joule
$V$	Applied voltage	Volts
$V_{pi}$	Pull down voltage	Volts
$w$	Transverse beam displacement	m
$W$	Lower electrode width	m
$\rho$	Electrostatic charge density	Q/m <sup>2</sup>
$\nu$	Poisson's ration	—
$\sigma$	Biaxial residual stress	N/m <sup>2</sup>
$\varepsilon_o$	Free space permittivity	F/m

# Chapter 1

## Introduction

Micro-Electro-Mechanical Systems (MEMS) are miniature devices or systems combining electrical and mechanical components, fabricated using integrated circuit (IC) compatible batch processing techniques with characteristic sizes ranging from micrometers to millimeters. MEMS devices have many applications in different broadband/RF/wireless systems [1,2,3,4,5,6,7]. These include RF switches, phase shifters, routing switches, time delay networks, reconfigurable antenna, tuning filters and other passive components at microwaves and millimeterwaves. The broadband systems or subsystems using these devices include phased-array antenna for beam scanning, beam steers in quasi-optical transceiver, high-speed front-end switching, monolithic microwave/millimeterwave integrated-circuits (MMICs) and high-speed data processing. MEMS devices provide many advantages over conventional devices because of their unique actuation, miniature, and integration features. The miniature feature of MEMS devices reduces the sizes and weights of the integrated components, which also reduces driving-power consumption. Furthermore, lots of different components can be integrated on a single chip to achieve more functionality without extra connector losses or impedance mismatch losses. In addition, potential low cost manufacturing into a variety of substrates

This field of technology is known by a wide variety of names in different parts of the world: in United States is known as Micro Electro Mechanical Systems (MEMS), in Europe it is called Micro System Technology (MST), while in Japan it is named Micromechanics, and is called also Nano Technology by others (Nano technology usually refers to devices ranging in size from a nanometer to a micron). In general, MEMS combine many disciplines, including physics, bioinformatics, biochemistry, electrical engineering, optics and electronics.

There are different fabrication technologies used in the realization of three-dimensional MEMS [9]:

- Bulk silicon micromachining techniques use either etches that stop on the crystallographic planes of a silicon wafer or etches that act isotropically to generate mechanical

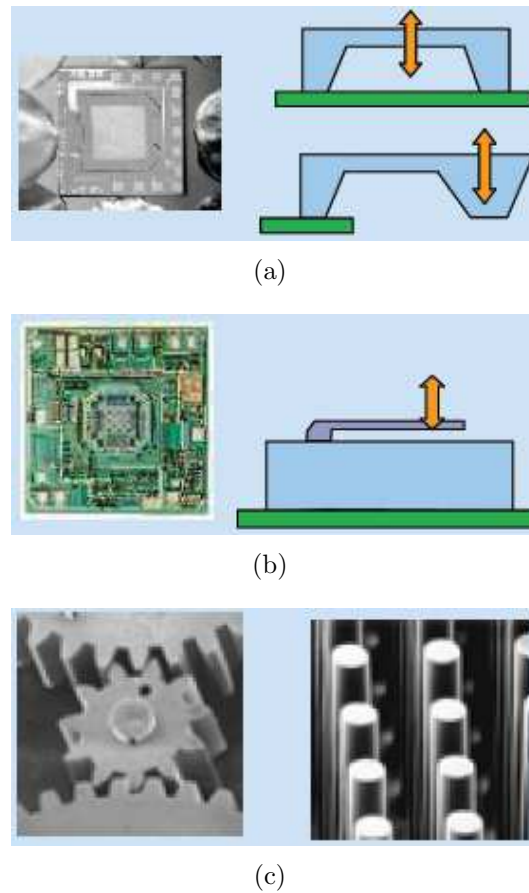


Figure 1.1: MEMS fabrication technologies (a) Bulk micromachining, (b) Surface micromachining , (c) LIGA, [8].

parts, i.e. form the microstructures by etching away the bulk of the silicon wafer to achieve the desired result, Fig. 1.1(a).

- Surface micromachining techniques build up the structure in layers of thin films on the surface of the silicon wafer (or any other suitable substrate), Fig. 1.1(b).

- The LIGA (Lithographie, Galvanoformung und Abformung, a German acronym for Lithography, Electrodeposition, and Molding) is a technology, which creates small, but relatively high aspect ratio devices using x-ray lithography, Fig. 1.1(c).

The MEMS technology has existed since 1970 in the form of sensors, however radio frequency devices have been rare. The most common RF device is the MEMS switch (which sacrifices the speed of a PIN diode for greatly enhanced isolation). MEMS microwave switch technology was first developed in 1980 by Dr. Larry Larson at Hughes Research Labs (Malibu, CA).

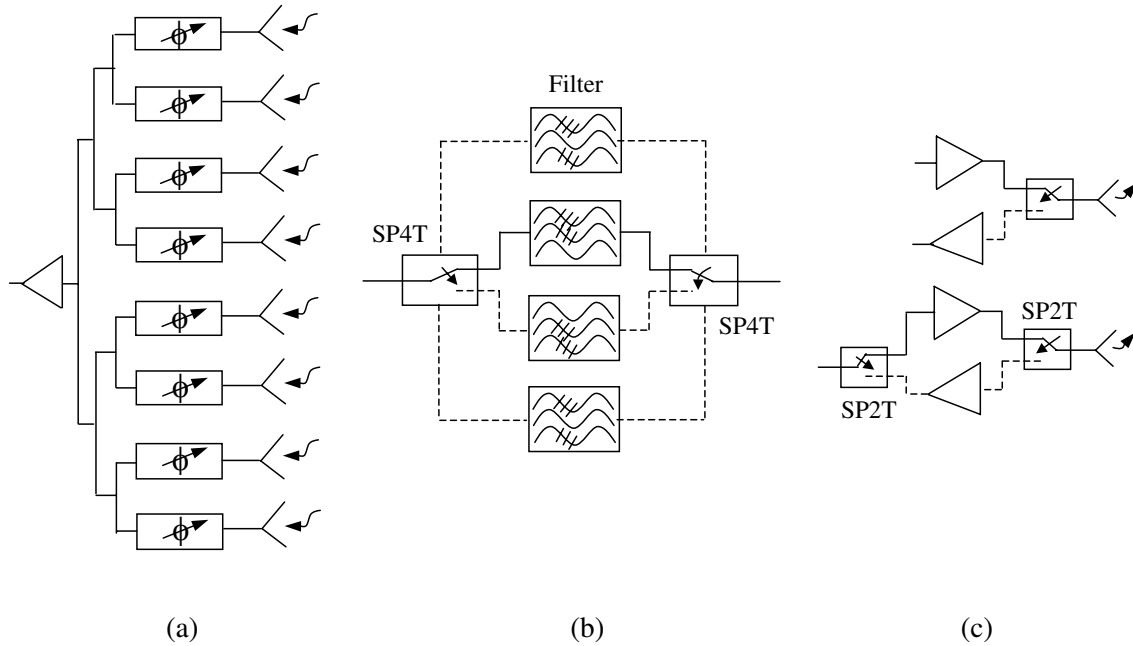


Figure 1.2: Some application areas of RF MEMS switches: (a) Phased-array antenna, (b) Switched filter banks for wireless applications, and (c) Single-pole double-throw (SP2T) transceiver switches.

## 1.1 RF MEMS Switches

RF MEMS switches are devices that use mechanical movement to achieve a short circuit or an open circuit in RF transmission line. These MEMS devices are primarily designed for low-loss applications that do not require fast switching rates such as in airborne and satellite communication. The advantages of RF MEMS switches over their solid-state counterparts such as FETs or PIN diodes are:

1. *Low Power Consumption:* The electrostatic actuation requires a DC voltage but does not consume any current, leading to a very low power dissipation.
2. *Very Low Insertion Loss* in the ON state.
3. *Very High Isolation* in the OFF state.
4. *High Intermodulation Products:* RF MEMS switches are very linear devices since they do not contain a p-n junction, they exhibit negligible intermodulation distortion.
5. *Very Low Fabrication Cost:* RF MEMS switches are fabricated using surface micromachining techniques and can be built on quartz, pyrex, high-resistivity silicon, or GaAs substrates.

However, RF MEMS switches have also their share of problems, such as:

1. *Relatively Low Speed:* The switching speed of most MEMS switches is around 2-40  $\mu$ s. Certain communication and radar systems require much faster switches. However, access holes in the plates on top of the ground planes allows faster operation by reducing the air-damping effect underneath the plate.
2. *Low Power Handling:* Most MEMS switches cannot handle more than 20-50 mW.
3. *High-Voltage Drive:* Electrostatic MEMS switches require 20-80 Volts for reliable operation. However, a lot of work has been done to reduce the driving voltage by incorporating mender-shaped supports [10, 11].
4. *Low Reliability:* The reliability of mature MEMS switches is 0.1-10 billion cycles. However, many systems require switches with 20-200 billion cycles.
5. *Difficulty of Packaging:* Packaging costs are currently high, and the packaging technique itself may adversely effect the reliability of the MEMS switch.
6. *High Total Cost:* While MEMS switches have the potential of very low manufacturing cost, one must add the cost of packaging and the high-voltage drive chip.

Generally, the RF MEMS switches can be classified as follows:

1. Actuation mechanism:

- The mechanical movement in the MEMS devices can be obtained using electrostatic, magnetostatic, piezoelectric, or thermal design. The majority of RF-MEMS switches rely on electrostatic actuation, which is based on the attractive Coulomb force existing between charges of opposite polarity. Some advantages of using electrostatic actuation are the relatively simple fabrication technology, much simpler compared to, for instance, electromagnetic excitation, the high degree of compatibility with a standard IC process line, and the ease of integration with planar and micro-strip transmission lines. A drawback is the high actuation voltage, which is in the range of 12-60 Volts. In case the available supply voltage is limited, e.g., to 3-5 Volts as in handheld phones, on-chip high-voltage generators such as the "Dickson-type dc voltage multiplier circuit" may be incorporated. This is either done monolithically or in a hybrid fashion as has recently been demonstrated by Motorola.

2. Construction:

- The movable part in the MEMS structures can be cantilever or double-supported beam. Clearly, the cantilever offers the important advantage of factor

of eight reduction in the actuation voltage, when compared to that required by the suspension bridge [2]. However, the fixed-fixed beam architecture is not very sensitive to the residual stress in the supporting beam. It is also usually easy to be fabricated and does not require special processing compared to the dielectric beams or the thick low-stress electroplated cantilever [12].

### 3. Contacting mechanism:

- There are two different contact mechanisms in RF MEMS switches, a capacitive contact and metal-to-metal (ohmic) contact. The capacitive contact is characterized by the capacitance ratio between the up-state (open circuit) and down-state (short circuit) positions, and this is typically 80-160 depending on the design. The down-state capacitance is typically 2-3 pF, and is suitable for 8-100 GHz applications. In general, it is hard to obtain a large down-state capacitance using nitride or oxide layers, and this limits the low-frequency operation of the device. On the other hand, DC-contact switches with small up-state capacitances (open circuit) can operate from 0.01 to 40 GHz, and in some cases, to 60 GHz (for example, the Rockwell Scientific [13] switch has an up-state capacitance of only 1.75 fF and an isolation of 23 dB at 60 GHz). In the down-state position (short-circuit), the DC-contact switch becomes a series resistor with a resistance of 0.5-2  $\Omega$ , depending on the contact metal used. The direct contact series switch has a disadvantage of short contact lifetime compared to the capacitive coupled one [14].

### 4. Circuit and Substrate Configurations:

As is the case with all two-terminal devices, the switches can be placed in series or in shunt across a transmission line. Typically, capacitive switches have been used in a shunt configuration [15], while DC-contact switches are placed in series [16]. The reason is that it is easier to get a good isolation with a limited impedance ratio (such as the capacitive switch) in a shunt-circuit than in a series circuit. Also, MEMS switches are compatible with both microstrip and CPW lines on glass, silicon and GaAs substrates, and have been used in these configurations all the way up to 100 GHz. For low loss applications at microwave frequencies, it is important to use high-resistivity substrates.

#### 1.1.1 State-of-the-art

RF-MEMS switching devices and circuits have originated at several industrial research labs and universities and many others different research organizations overall the world and have experienced an exponential growth in the last few years. In Europe more than 120 research centers, laboratories, or university institutes are involved in microsystems technologies, producing a large variety of innovative processes

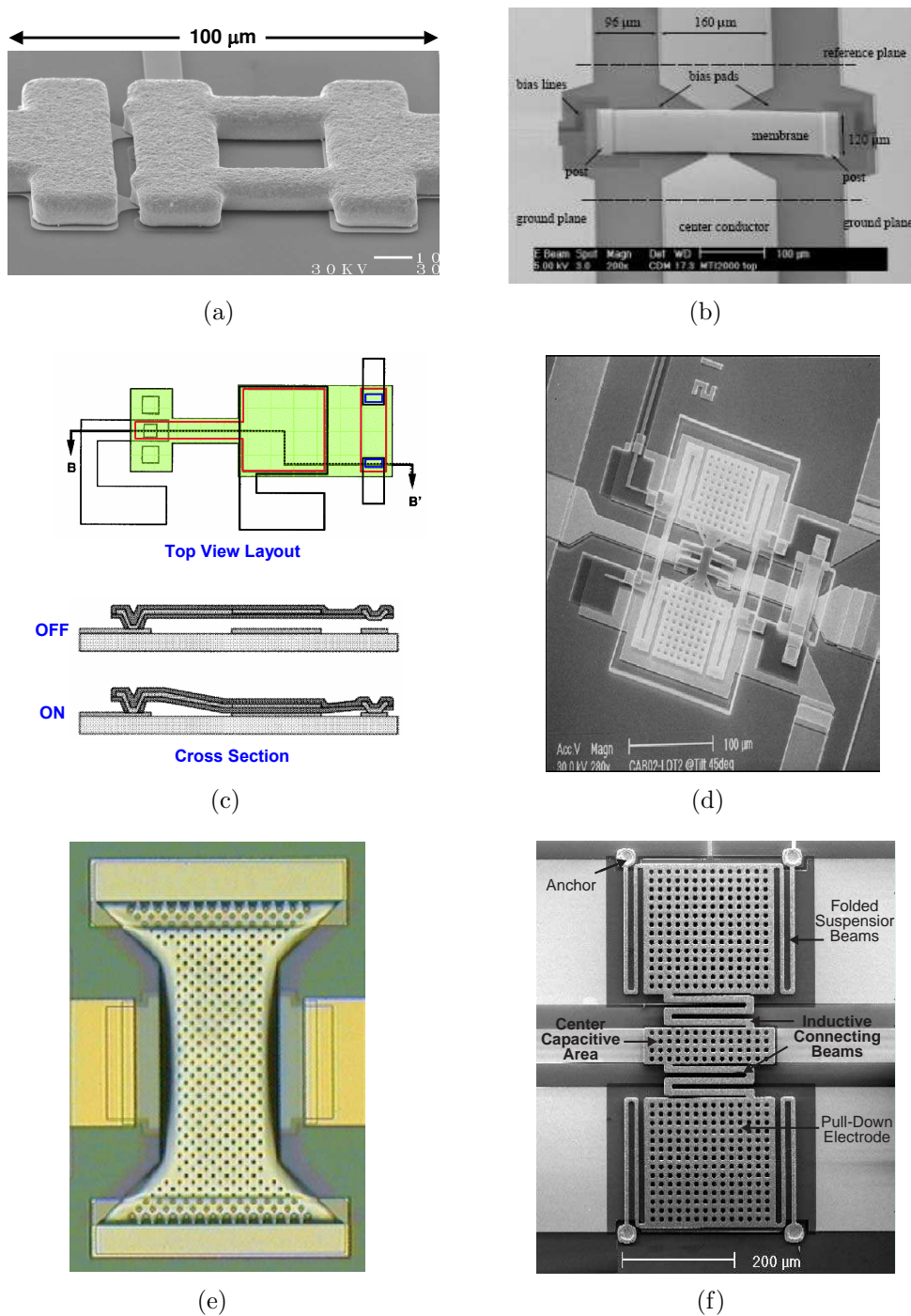


Figure 1.3: Photomicrograph of (a) the Radant MEMS series switch [17], (b) the University of Michigan metal membrane series switch [18], (c) the HRL's cantilever switch [19], (d) the Rockwell Scientific MEMS series switch [13], (e) the Raytheon MEMS capacitive shunt switch [20,15], and (f) the University of Michigan low-voltage MEMS shunt capacitive switch [21].

and device concepts and yielding considerable expertise. Many RF-MEMS switching devices have been developed, tested, and intensively published because of their attractive performances. The selection of the switch type depends upon the required performance, application and manufacturing facilities. Examples of these switches are shown in Fig. 1.3.

### 1.1.2 RF MEMS Switch Modeling

RF MEMS switches are constructed using thin metal membrane, which can be electrostatically actuated using dc-biasing voltage. The design of a MEMS device is a complex task that involves both electrical and mechanical optimization steps. The geometry of such a device, in fact, must satisfy technological constraints while achieving good reliability and very high electrical performances [22]. The challenges in the simulation of electrostatic-mechanical transducers can be summarized as: one has to deal with at least two different physical fields, usually the electrostatic and mechanical fields. Since they are designed on scales on which an electrostatic force is capable to move or deform the membrane, three-dimensional (3-D) or at least two-dimensional (2-D) coupled electrostatic-mechanical model is needed for accurate prediction of the switch behavior. So that an effort to realize efficient models has to be made.

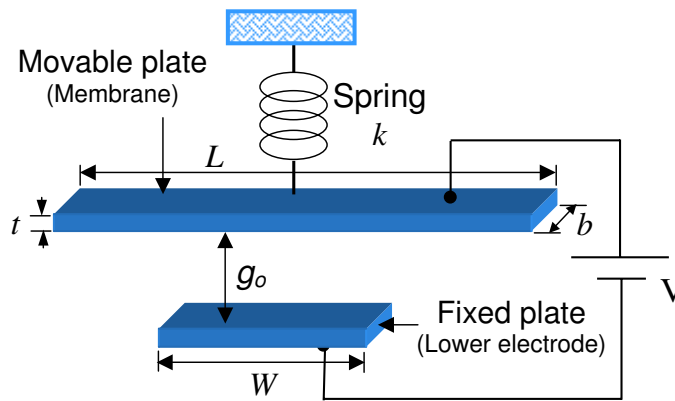


Figure 1.4: Simple lumped capacitor-spring model for RF MEMS switch.

Reduced order models consisting of one, two or several coupled Ordinary Differential Equations (ODEs) are often used to understand the behavior of electrostatically actuated devices when three-dimensional or even detailed two-dimensional models are too computationally intensive. In the literatures, a simple 1-D lumped model, shown in Fig. 1.4 used a single parallel-plate approximation for capacitance and neglected all fringing fields has been introduced in [23]. When a DC voltage is applied between the fixed plate (lower electrode) and the movable plate (membrane), an electrostatic force will induced to pull the membrane downward to the fixed plate with a pull-down

voltage given by:

$$V_{pi} = \sqrt{\frac{8k}{27\epsilon_o W b} g_o^3} \quad (1.1)$$

where  $k$  is the effective spring constant of the membrane,  $W$  is the lower electrode width,  $b$  is the membrane width,  $\epsilon_o$  is the free space permittivity, and  $g_o$  is the nominal gap height. The effective spring constant  $k$  of the membrane can be approximated by [24]

$$k = \frac{32\mathbf{E}t^3b}{L^3} + \frac{8\sigma(1-\nu)tb}{L} \quad (1.2)$$

where  $\mathbf{E}$  is the Young's modulus of the membrane material,  $t$  is the membrane thickness,  $L$  is the membrane length,  $\sigma$  is the residual tensile stress in the membrane, and  $\nu$  is Poisson's ratio for the membrane material. This single-degree-of-freedom model is the simplest and most intuitive analytically, but is the least accurate. Its purpose is for first-cut analysis to gain physical insight, explore design options and understand overall behavior.

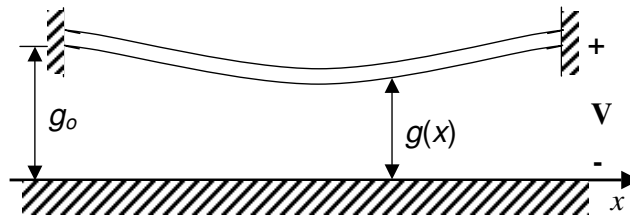


Figure 1.5: Simplified schematic of 2-D distributed model for fixed-fixed beam based MEMS switch showing realistic position-dependent gap.

A two-dimensional model used a distributed parallel-plate approximation for capacitance and incorporated a fringing field correction but ignored the effect of conductor curvature on electric fields has been investigated in [25]. It accounts for the fact that actual structures have non-rigid, position-dependent gaps as shown in Fig. 1.5. Adding the first-order fringing field correction term to the electrostatic force improves the accuracy of the 2-D model but still has some limitations.

Other investigations related to the 2-D electrostatic-mechanical coupled analysis can be found in [26, 27, 28, 29, 30, 31]. To the author's knowledge, the electrostatic force calculated in the literature is not very accurate; in some works the fringing field is neglected or an approximate expression is used or the electrostatic force is assumed to be uniformly distributed along the membrane. Through this study, the electrostatic force is calculated very accurately using a non-uniform mesh distribution along the membrane. 1-D, 2-D, and 3-D nonlinear analytical models to analyze the

electrostatic pull-in of a fixed-fixed beam at small structural deflection are proposed in [32]. However, most RF MEMS switch structures work at large deflection range. Several commercial software tools, specifically designed for RF MEMS development, are appearing in the market. Generally, these tools perform a full device analysis concerning the mechanical and thermal aspects but are lacking the accurate electrical modeling. 3-D numerical simulations of the membrane deflections using shell elements and multi-body contact algorithm has been reported in [33]. A 3-D quasi-static electro-mechanical model as application of CoSolve-EM software by combining the electromagnetic and mechanical simulators to determine the beam deformation has been studied in [34]. 3-D coupled electro-mechanical simulation tools for RF MEMS structures are available in commercial packages such as CoventorWare [35] and Abaqus [36], or multi-physics simulation tools such as IntelliCAD [37] and Ansys [38]. Most of these solvers are to find a self-consistent solution to the coupled electro-mechanical problem using the boundary-based coupling between a mechanical finite element solver and an electrostatic boundary element solver. Although accurate results using some of those tools can be obtained, however those coupled analyses software packages are more sophisticated and also computationally intensive.

## 1.2 Defected Ground Structures

Defected ground structures (DGS) have shown increasing potential for implementation in different applications: MIC, MMIC, and RFIC [39,45,44,43,46]. They provide sharp, distinct electromagnetic band-gap and high slow wave factor, which lead to smaller size circuits. They have been used numerously in the recent years, however most of the applications are in microstrip structures [47]. In these structures, well-defined shapes are etched at the back metal. This requires a precise double-sided processing and adequate packaging to keep an air-gap between the ground and the package. On the other hand, coplanar waveguide (CPW) have both signal and ground on the same surface. Though they occupy larger area than microstrip lines, they can be considered as a good compromise for DGS structures. Moreover, CPW are used for circuit design since they can be easily integrated into existing RF ICs without the need for incorporating via-holes. They are less sensitive to the substrate thickness and substrate dielectric constant than the microstrip structures [48].

Consequently this opens the door to a wide range of applications [49,50]. Different shapes of defects have been studied, among them are: dumbbell [47], periodic [51], fractal [52], circular [44], spiral [41], T-shaped [40], and different geometrical shapes like circular, squared, and arrow-heads in microstrip circuit are presented in [42]. To our knowledge, few applications for DGS on CPW circuits have been reported, among them are: The dumbbell shaped DGS is presented in [39], a vertically periodic DGS is proposed in [43] for microstrip and CPW line in which the periodicity takes place in the vertical direction only, a one-dimensional DGS structure where the periodicity is

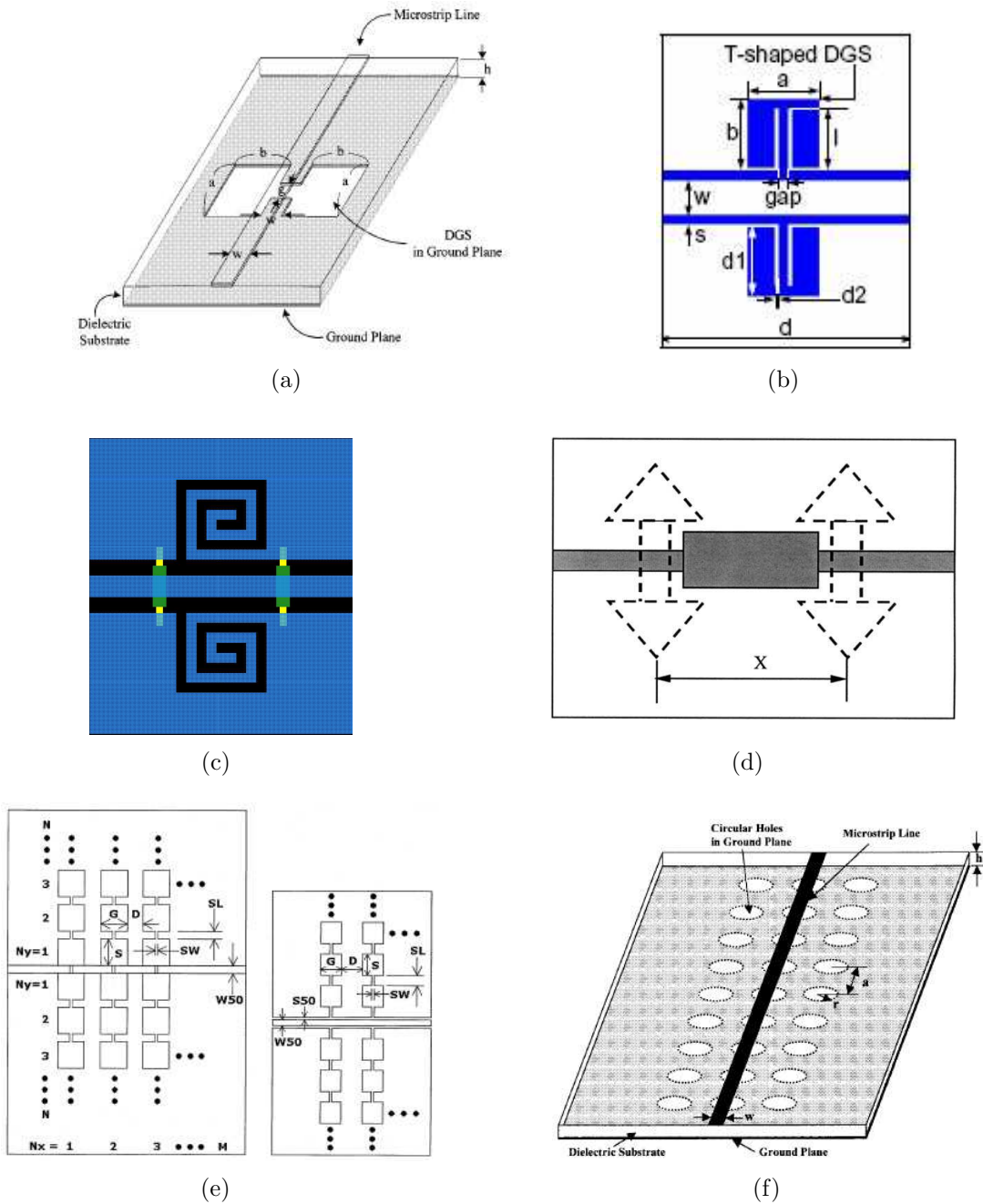


Figure 1.6: Examples of the defected ground structures (a) Schematic view of the lattice shape DGS, which is etched in the ground plane of a microstrip line [39], (b) the T-shaped DGS [40], (c) The layout of the CPW based spiral-shaped DGS [41], (d) Hi-Lo LPF with two arrowhead DGS slots,  $X = 1.12$  cm [42], (e) transmission lines with vertical periodic DGS [43], and (f) Schematic of a 2-D PBG structure for microstrip, the square lattice circles are etched in the ground plane of a microstrip line [44].

in the horizontal direction is presented in [53]. Some examples of these DGS structures are shown in Fig. 1.6. In general, these techniques also best utilizes the area to get very low stop band frequencies.

### 1.3 MEMS Resonator

As an application of the DGS structures in the MEMS technology, an RF MEMS reconfigurable DGS resonator is designed and optimized for automotive and transceiver applications. For these reasons a short review on RF resonators is presented below.

Resonators find widespread use in transceiver architectures, e.g., frequency controlling elements in reference oscillators, tunable resonator for VCOs and building elements for filters and duplexers [54]. Based upon their principle of operation, resonators can be classified into two types: Firstly, electromagnetic wave resonators, e.g., lumped element LC-type resonators, transmission line resonators, cavity resonators and dielectric resonators. Secondly, electromechanical or acoustic wave resonators, e.g., mechanical resonators, bulk acoustic wave resonators and surface acoustic wave resonators. MEMS technology has emerged in each of the above and they have shown promising characteristics in achieving important filter parameters, such as narrow bandwidth, low loss, and good stability [5]. In the literature, silicon micromachined RF MEMS resonators, open-end patch resonator and short circuit via resonator were investigated in [55]. A MEMS-based photonic bandgap (PBG) band-stop filter designed using etched lattice shape of CPW PBG unit cell and fabricated using MEMS surface micromachining process on a high-resistivity silicon substrate was presented in [56].

For many applications, the resonant frequency of the resonator must have a small degree of tunability to cover certain frequency band. Tuning can be obtained electrically or mechanically. Micromachined tunable dielectric resonator was implemented in [57]. In this case, tunability was achieved by coupling the membrane to the dielectric resonator. In [58], the fabrication of a micromechanical tunable resonator using the commercial  $0.35\ \mu\text{m}$  complementary metal oxide semiconductor (CMOS) process and the post-process of only one maskless wet etching has been investigated.

### 1.4 Contribution

With the recent rapid growth of RF MEMS switches, it has developed an emergent requirement for more accurate theoretical models to predict their electromechanical behaviors. In this dissertation, 2-D and 3-D coupled electrostatic-mechanical models for the RF MEMS switches are developed, considering simultaneously the axial stress, residual stress, and the actual field distribution on bridge structure. The developed

simulation programs combine the electrostatic and mechanical analyses together to accurately describe the switch deformation and predict the pull down voltage in a quite short CPU time, which proves its potential for implementation in the computer-aided design tools for RF MEMS structures. The models are implemented in a numerical simulation program (MATLAB version 7.0). Verification of the models and simulations has been done by considering a lot of standard RF MEMS switches from the literatures.

A  $\pi$ -configuration RF MEMS switch is designed and optimized based on numerical experimentations using full-wave 3-D electromagnetic (EM) simulators. The proposed switch exhibits a very high isolation ( $> 50$  dB) in the OFF-state over a very wide frequency band (2-50 GHz). The insertion loss in the ON-state ranges from 0.2 to 2 dB over the whole range while the return loss is kept a minimum of 25 dB. Based on the same technique, a single-pole, three-throw (SP3T) RF MEMS switch is also designed and optimized to be used in the switching networks for satellite communications and both portable unites and base stations for wireless applications. Circuit models that describe the switches' RF-performance well are also introduced and they can be easily applied to circuit design.

Different new defected ground structures (DGS) effective to miniaturize the circuit area of CPW filters are introduced. The first one is a 2-D periodic DGS (PDGS) based on the repetition of the lattice-shape unit-cell in both vertical and horizontal directions to control the resonant frequency. The proposed structure has the advantage of having an almost constant capacitance while the inductance varies linearly as the number of cell increases, which simplifies the design process. The second one is an L-shaped DGS for CPW technology. The L-section is again repeated at one side or at both sides to prolong the current path and hence to increase the effective inductance and capacitance of the structure, which makes it easy to control the cutoff frequency characteristics. A criterion that determines the dependance of the equivalent circuit elements on the design parameters of the defect is presented as well. High performance bandstop filters using cascaded DGS are designed and experimentally verified.

A MEMS reconfigurable DGS resonator using the 2-D PDGS and RF-MEMS series-resistive switches is also proposed. The proposed resonator has approximately a fixed bandwidth over a wideband regime (K-band), which is interesting for automotive and transceiver applications. We also introduce a new cascaded two parallel-resonance circuit model, which describe the resonator's performance very well. In addition, the equivalent circuit parameters extraction methods are derived.

## 1.5 Thesis Organization

This theoretical modeling of MEMS structures objectives were to carry out theoretical studies to gain a fundamental understanding of electromechanical phenomenon of microfabricated MEMS devices and to produce models which can predict the electromechanical performance of these devices. A thorough understanding of these electromechanical properties as well as predictive theoretical models is necessary for successful design and fabrication of electromechanical systems. This thesis consists of seven chapters where Chapter 1 gives an introduction for the microelectromechanical systems. It discusses the state-of-the-art of RF MEMS switches and the defected ground structures. It presents the contributions of the thesis in the MEMS topic.

Chapters 2 and 3 deal with the 2-D and 3-D coupled electrostatic-mechanical models for suspension bridge RF MEMS switches, respectively. The electrostatic model solves the electrostatic problem for the potential distribution in the computational domain. The electrostatic field and hence the electrostatic force density distribution induced on the membrane are determined. The mechanical model calculates the bridge deformation arising from the induced electrostatic force. This is done by solving the mechanical equation covering the beam/plate motion using the finite difference method (FDM).

Chapter 4 focuses on new RF MEMS switch designs based on numerical experimentations technique using full-wave 3-D EM simulators. The equivalent circuit models describe the switches performance are discussed as well.

In Chapter 5, two different designs of defected ground structures in CPW technology are investigated. To evaluate the RF performance of the proposed DGS structures, sample structures are implemented and measured. Comparing with the data obtained from simulation, good agreement is observed.

In Chapter 6, one of the DGS structures investigated in Chapter 5 is combined with series-resistive RF MEMS switches to construct a novel MEMS reconfigurable DGS resonator. Methods to extract the equivalent circuit model parameters are derived in this chapter.

Conclusions and possible future works are presented in Chapter 7. The developed programs are presented in Matlab version 7. Samples from these programmes are given in Appendices A and B at the end of the thesis.

## Chapter 2

# Two-Dimensional Coupled Electromechanical MEMS Analysis

This chapter deals with the two-dimensional (2-D) coupled electrostatic-mechanical model for RF MEMS switches. Two different algorithms for the solution of the electrostatic problem for the potential computation are presented. The first algorithm is based on solving the Laplace's equation in the different homogenous regions while Gauss's law is applied at the interface nodes in the 2-D computational domain. Applying Laplace's equation in conjunction with Gauss's law in 2-D Cartesian coordinate system to all free nodes using the finite difference method (FDM) results in a system of equations, where the quadratic interpolation approximation is used to approximate the derivatives appearing in the FDM analyses. The generated system of equations is solved using the band matrix method to compute the potential distribution in the computational domain. The second algorithm is based on applying Gauss's law to all free nodes in the computational domain using the FDM with the central difference approximation for the derivatives appearing in the analyses. Gauss's law is applied to the inhomogeneous region with a non-uniform discretization for accurate numerical simulation. This results in a one updating equation for the potential. An efficient iterative procedure is employed to this updating equation to get the steady state solution for the potential distribution. Another two different algorithms for the solution of the mechanical problem for the beam deformation determination are also presented. The first one is based on solving the beam equation analytically using the method of variation of parameters to determine the beam deformation, while the second algorithm calculates the beam deformation based on solving the beam equation numerically using the FDM. The strong interaction between the electrostatic and mechanical domains is considered iteratively.

Through this study, the effects of residual stress due to the fabrication process and the axial force resulting from the beam stretching are taken into account. The electrostatic force is calculated very accurately and as a non-uniform force distributed along the beam. Most of the publications, either neglect the effect of the residual stress

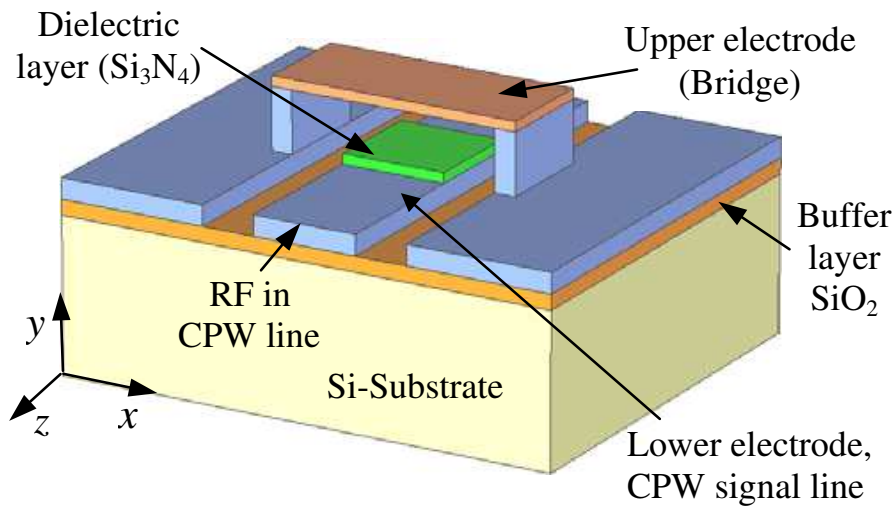
or the axial force or both of them [31]. To the authors' knowledge, the electrostatic force calculated in the literature is not very accurate; some time the fringing field is neglected or used an approximate expression or the electrostatic force assumes uniformly distributed along the membrane [28,59]. The analyses and simulations here are dedicated to the fixed-fixed beam bridge RF MEMS shunt-capacitive switches, although they are also applicable to other types of electrostatic MEMS structures. This type of the switch structure is chosen because it is used quite often in RF MEMS applications.

## 2.1 RF MEMS Switches Operation

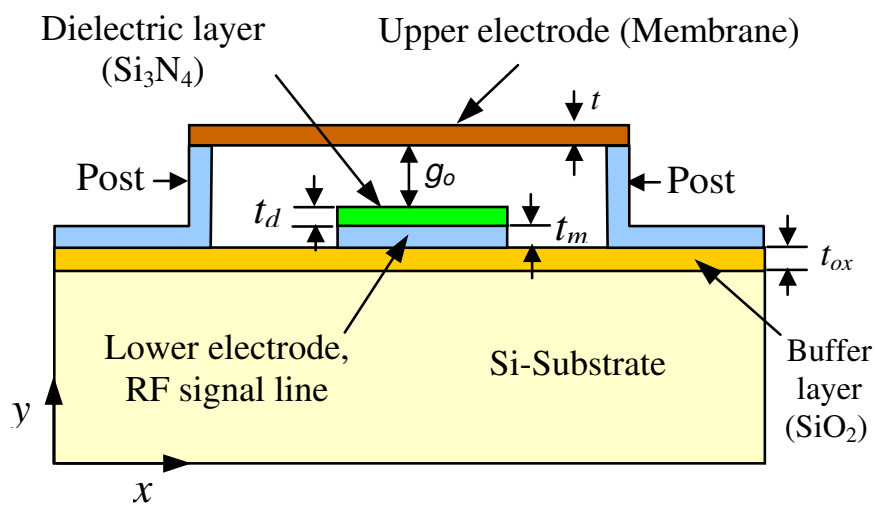
A typical RF MEMS shunt-capacitive switch, shown in Fig. 2.1, consists of a fixed-fixed thin metallic membrane which is suspended over a bottom electrode insulated by a dielectric film. This dielectric film serves to prevent the electric short between two conductors (the membrane and lower electrode) and provide a low impedance path for the RF signal. The membrane is made of good mechanical properties metal like *Au* or *Cu* prepared by electroplating process. When the switch is not actuated, the membrane is in the up-position, there is low capacitance between the membrane and the bottom electrode, and the device is in the ON state. When a dc voltage is applied between the movable structure and the fixed bottom electrode, electrostatic charges are induced on both the movable structure and the bottom electrode. The electrostatic charges cause a distributed electrostatic force, which deforms the movable structure. In turn, such deformation leads to storage of elastic energy, which tries to restore the structure to its original shape. The structure deformation also results in the reorganization of all surface charges on the device. This reorganization of charges causes further structural deformation; hence, the device exhibits a highly nonlinear, coupled electromechanical behavior. Until a certain voltage is applied, the so-called pull-in voltage or actuation voltage, an equilibrium position exists through a balance between the elastic restoring force and electrostatic force. After pull-in, the device is in the OFF state and its capacitance is much larger than that in the ON state. The switch actuation is therefore a coupled-field problem of electrostatics and structural response. In order to accurately describe the switch deformation and predict the pull-in voltage, numerical iterations between electrostatic and mechanical domains have to be made.

## 2.2 Electromechanical Coupled Analysis Algorithm

The developed coupled electrostatic-mechanical model starts by solving the electrostatic problem in the two-dimensional domain of the switch structure for the potential distribution. Having computed the potential, the electric field distribution and hence the electrostatic force induced on the membrane can be determined. Consequently,



(a)



(b)

Figure 2.1: Fixed-fixed beam bridge RF MEMS shunt-capacitive switch, (a) 3-D structure, (b) 2-D structure.

the mechanical model can be initiated using the determined electrostatic forces to calculate the beam deformation, which in turn alters the electrostatic force distribution. This cycle between the electrostatic and mechanical models is considered as one-iteration. In this cycle the electrostatic problem has to be solved for the new switch structure with the deformed bridge of a displacement, which is calculated from the last iteration. The program goes back and forth between the electrostatic and mechanical models until the difference between the maximum-displacement in the membrane in two successive iterations is less than a specified error, which is considered as the program convergence criterion defined by the user.

The results reported in the current chapter are given for a fixed-fixed beam RF MEMS shunt-capacitive switch geometrically similar to that reported in [23]. This switch has the following dimensions, the membrane length  $L$ , width  $b$ , and thickness  $t$  are 300, 80, and 2  $\mu\text{m}$ , respectively. It is made of aluminum with residual stress  $\sigma$  of 20 MPa and Young's modulus  $\mathbf{E}$  of 70 MPa. The MEMS switch is built on a coplanar waveguide (CPW) line with dimensions of  $G/W/G = 60/100/60 \mu\text{m}$  and a 50  $\Omega$  characteristic impedance on a high-resistivity silicon substrate with 11.9 dielectric constant and 400  $\mu\text{m}$  height. This is coated by a 0.4  $\mu\text{m}$  silicon dioxide buffer layer ( $t_{ox}$ ). A 0.15  $\mu\text{m}$  silicon nitride dielectric layer ( $t_d$ ) coats the lower electrode, which has a thickness ( $t_m$ ) of 0.8  $\mu\text{m}$ . The initial gap height ( $g_o$ ) is 1.5  $\mu\text{m}$ . The computational domain is assumed as a rectangular box as shown in Fig. 2.2, which has dimensions of 300 and 35  $\mu\text{m}$  in the  $x$  and  $y$  directions, respectively. Because the electrostatic field is mostly confined in the gap regions, the entire substrate has not been considered in the calculations. Instead, only seven times of the sum ( $t_{ox} + t_m + t_d + g_o$ ) was considered, which assures a negligible field.

## 2.3 2-D Electrostatic Analysis

### 2.3.1 Potential Computation

*First Algorithm:* Matrix Inversion

The electrostatic model starts by generating the meshes with non-uniform finite difference steps in both directions to get the minimum execution time with the highest possible accuracy as shown in Fig 2.2. Next, the 2-D Laplace's equation is applied to all free nodes in the different homogenous regions as following:

$$\frac{\partial^2 V(x, y)}{\partial x^2} + \frac{\partial^2 V(x, y)}{\partial y^2} = 0 \quad (2.1)$$

For accurate solution, this second order partial differential equation is approximated using the quadratic interpolation approximation with non-uniformly spaced finite difference mesh. For any general function  $V(x)$ , shown in Fig. 2.3, can be approximated at three adjacent nodes using a polynomial  $P(x)$  of second order degree

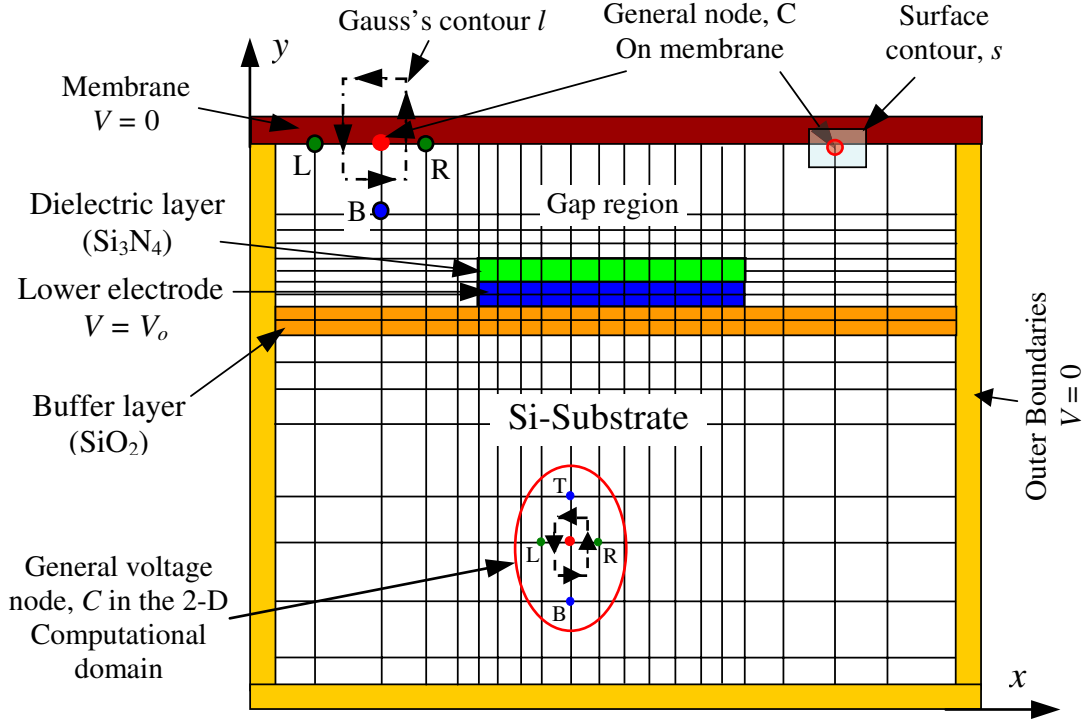


Figure 2.2: 2-D computation domain with a non-uniformly spaced finite difference mesh distribution.

as follow:

$$P(x) = c_0 + c_1(x - x_0) + c_2(x - x_0)(x - x_1) \quad (2.2)$$

Imposing  $P(x_i) = V(x_i)$ ,  $(1 \leq i \leq 3)$ , one can determine  $c_0$ ,  $c_1$ , and  $c_2$  from the following matrix equation:

$$\begin{bmatrix} 1 & 0 & 0 \\ 1 & (x_1 - x_0) & 0 \\ 1 & (x_2 - x_0) & (x_2 - x_0)(x_2 - x_1) \end{bmatrix} \begin{bmatrix} c_0 \\ c_1 \\ c_2 \end{bmatrix} = \begin{bmatrix} V(x_0) \\ V(x_1) \\ V(x_2) \end{bmatrix}$$

Substituting this back in (2.2) using  $c$ 's coefficients, which is determined from the last matrix equation with some rearrangements, the following expression for the approximated function  $P(x)$  can be written in the form:

$$P(x) = \frac{(x - x_1)(x - x_2)}{(x_0 - x_1)(x_0 - x_2)}V(x_0) + \frac{(x - x_0)(x - x_2)}{(x_1 - x_0)(x_1 - x_2)}V(x_1) + \frac{(x - x_0)(x - x_1)}{(x_2 - x_0)(x_2 - x_1)}V(x_2)$$

$P(x)$  is a second order degree polynomial which coincides with the exact function  $V(x)$  at three nodes  $x_0$ ,  $x_1$ , and  $x_2$ . Let  $x_0 = x_L$ ,  $x_1 = x_C$ , and  $x_2 = x_R$  and  $V(x_0) = V_L$ ,

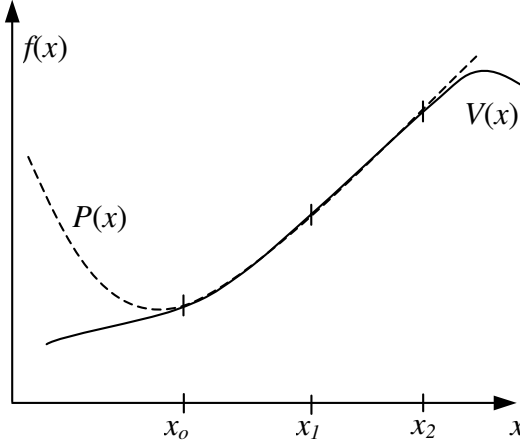


Figure 2.3: Quadratic interpolation.

$$V(x_1) = V_C, \quad V(x_2) = V_R.$$

Thus,

$$P(x) = \frac{(x - x_C)(x - x_R)}{(x_L - x_C)(x_L - x_R)} V_L + \frac{(x - x_L)(x - x_R)}{(x_C - x_L)(x_C - x_R)} V_C + \frac{(x - x_L)(x - x_C)}{(x_R - x_L)(x_R - x_C)} V_R \quad (2.3)$$

Equation (2.3) can be differentiated to obtain the approximations for the first and second order derivatives as:

$$\frac{dP(x)}{dx} = \frac{2x - x_C - x_R}{(x_L - x_C)(x_L - x_R)} V_L + \frac{2x - x_L - x_R}{(x_C - x_L)(x_C - x_R)} V_C + \frac{2x - x_L - x_C}{(x_R - x_L)(x_R - x_C)} V_R \quad (2.4a)$$

$$\frac{d^2P(x)}{dx^2} = \frac{2V_L}{(x_L - x_C)(x_L - x_R)} + \frac{2V_C}{(x_C - x_L)(x_C - x_R)} + \frac{2V_R}{(x_R - x_L)(x_R - x_C)} \quad (2.4b)$$

Similar expressions can be obtained in the  $y$  direction:

$$\frac{dP(y)}{dy} = \frac{2y - y_C - y_T}{(y_B - y_C)(y_B - y_T)} V_B + \frac{2y - y_B - y_T}{(y_C - y_B)(y_C - y_T)} V_C + \frac{2y - y_B - y_C}{(y_T - y_B)(y_T - y_C)} V_T \quad (2.5a)$$

$$\frac{d^2P(y)}{dy^2} = \frac{2V_B}{(y_B - y_C)(y_B - y_T)} + \frac{2V_C}{(y_C - y_B)(y_C - y_T)} + \frac{2V_T}{(y_T - y_B)(y_T - y_C)} \quad (2.5b)$$

Using equations (2.4b) and (2.5b) the Laplace's equation (2.1) can be approximated at any general node  $C$  shown in Fig. 2.4(a) as follow:

$$\begin{aligned} & \frac{2V_L}{(x_L - x_C)(x_L - x_R)} + \frac{2V_C}{(x_C - x_L)(x_C - x_R)} + \frac{2V_R}{(x_R - x_L)(x_R - x_C)} \\ & + \frac{2V_B}{(y_B - y_C)(y_B - y_T)} + \frac{2V_C}{(y_C - y_B)(y_C - y_T)} + \frac{2V_T}{(y_T - y_B)(y_T - y_C)} = 0 \end{aligned}$$

Thus, the general system of equation for any free node in a homogenous medium is in the form:

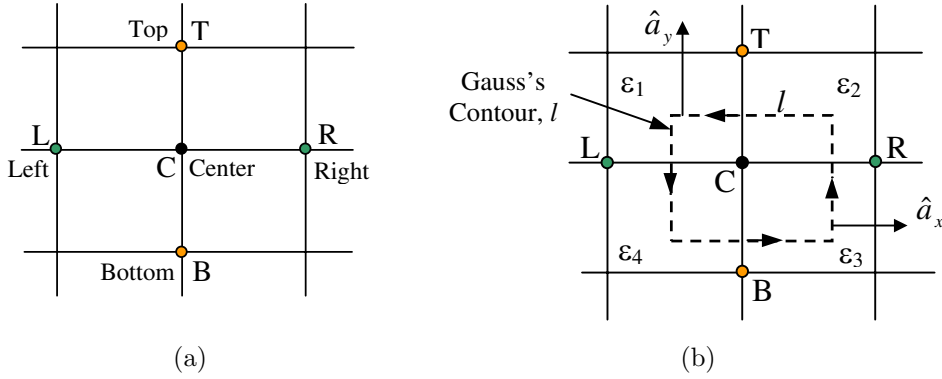


Figure 2.4: General voltage node  $C$  in the computational domain is surrounded by four voltage-nodes  $L, R, B,$  and  $T$ , (a) In the homogenous region, (b) Interface node between different media.

$$\begin{aligned}
 & \left[ \frac{1}{(y_C - y_B)(y_T - y_B)} \right] V_B + \left[ \frac{1}{(x_C - x_L)(x_R - x_L)} \right] V_L \\
 & + \left[ \frac{-1}{(x_C - x_L)(x_R - x_C)} + \frac{-1}{(y_C - y_B)(y_T - y_B)} \right] V_C \\
 & + \left[ \frac{1}{(x_R - x_L)(x_R - x_C)} \right] V_R + \left[ \frac{1}{(y_T - y_B)(y_T - y_C)} \right] V_T = 0
 \end{aligned} \tag{2.6}$$

At the same time Gauss's law is applied at the dielectric interface nodes between the different media as following:

$$- \oint_l \varepsilon \left( \frac{\partial V}{\partial x} \hat{a}_x + \frac{\partial V}{\partial y} \hat{a}_y \right) \cdot \hat{a}_n dl = 0 \tag{2.7}$$

where  $\varepsilon$  is the medium permittivity and  $\hat{a}$  is the normal unit vector to the Gauss's contour  $l$ . Dividing the Gauss's contour  $l$  into four segments as shown in Fig. 2.4(b) takes each segment parallel to the main axes gives the next equation:

$$- \int_{right} \varepsilon(y) \frac{\partial V}{\partial x} dy - \int_{top} \varepsilon(x) \frac{\partial V}{\partial y} dx + \int_{left} \varepsilon(y) \frac{\partial V}{\partial x} dy + \int_{bottom} \varepsilon(x) \frac{\partial V}{\partial y} dx = 0 \tag{2.8}$$

Applying the finite difference technique to the last equation gives the following expression:

$$\begin{aligned}
 & - \frac{V_R - V_C}{x_R - x_C} \left[ \frac{\varepsilon_2(y_T - y_C) + \varepsilon_3(y_C - y_B)}{2} \right] - \frac{V_T - V_C}{y_T - y_C} \left[ \frac{\varepsilon_1(x_C - x_L) + \varepsilon_2(x_R - x_C)}{2} \right] \\
 & + \frac{V_C - V_L}{x_C - x_L} \left[ \frac{\varepsilon_1(y_T - y_C) + \varepsilon_4(y_C - y_B)}{2} \right] + \frac{V_C - V_B}{y_C - y_B} \left[ \frac{\varepsilon_4(x_C - x_L) + \varepsilon_3(x_R - x_C)}{2} \right] = 0
 \end{aligned} \tag{2.9}$$

where the subscripts  $L, R, T$ , and  $B$  denote left, right, top, and bottom, respectively and  $\varepsilon_i, i = 1, 2, 3, 4$  are the different medium permittivities.

Thus, the general system of equation for any interface node can be expressed as follow:

$$\begin{aligned} & \left[ \frac{\varepsilon_4(x_C - x_L) + \varepsilon_3(x_R - x_C)}{y_C - y_B} \right] V_B + \left[ \frac{\varepsilon_1(y_T - y_C) + \varepsilon_4(y_C - y_B)}{x_C - x_L} \right] V_L \\ & + \left[ \frac{\varepsilon_2(y_T - y_C) + \varepsilon_3(y_C - y_B)}{x_R - x_C} \right] V_R + \left[ \frac{\varepsilon_1(x_C - x_L) + \varepsilon_2(x_R - x_C)}{y_T - y_C} \right] V_T \\ & - \left[ \frac{\varepsilon_4(x_C - x_L) + \varepsilon_3(x_R - x_C)}{x_R - x_C} + \frac{\varepsilon_1(y_T - y_C) + \varepsilon_4(y_C - y_B)}{y_C - y_B} + \frac{\varepsilon_2(y_T - y_C) + \varepsilon_3(y_C - y_B)}{x_R - x_C} + \frac{\varepsilon_1(x_C - x_L) + \varepsilon_2(x_R - x_C)}{y_T - y_C} \right] V_C = 0 \end{aligned} \quad (2.10)$$

Equations (2.6) and (2.10) are the general system of equations for any node in the 2-D computational domain in a homogenous medium and at interface nodes, respectively. Those equations are derived assuming that mesh is rectangular i.e. the grid lines are parallel to the main axes. Upon applying an actuation voltage, the membrane is deformed and it loses its parallelness to the mesh lines as illustrated in Fig. 2.5. For these reasons, Eq. (2.6) has to be correspondingly modified.

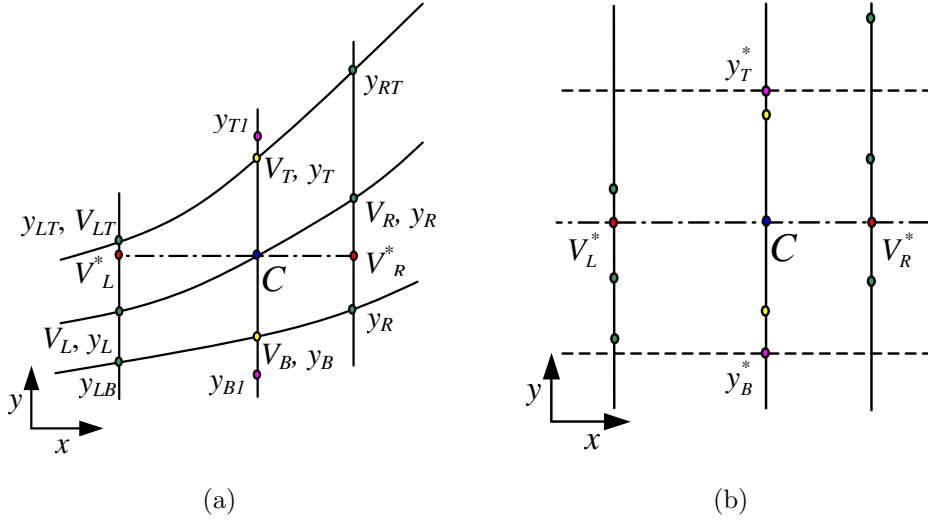


Figure 2.5: A General voltage node in the 2-D computational domain when the switch gets distorted due to the actuation, (a) Actual grid, (b) Interpolated grid.

Using a linear interpolation, one can obtain two voltage nodes at the left  $V_L^*$  and at the right  $V_R^*$  of the general node  $C$  on the horizontal axis in the  $x$ - $y$  plane as shown in Fig. 2.5. Both have the same  $y$ -coordinates  $y_c$  as  $C$ :

$$V_L^* = V_L + \frac{y_C - y_L}{y_{LT} - y_L} (V_{LT} - V_L) \quad (2.11a)$$

$$V_R^* = V_{RB} + \frac{y_C - y_{RB}}{y_R - y_{RB}} (V_R - V_{RB}) \quad (2.11b)$$

To restore a rectangular grid, one can take the average value of the  $y$ -components and re-calculate the new coordinates  $y_T^*$  and  $y_B^*$  as follows:

$$y_T^* = \left( \frac{y_{RT} + y_T}{2} + \frac{y_{LT} + y_T}{2} \right) / 2 \quad (2.12a)$$

$$y_B^* = \left( \frac{y_{RB} + y_B}{2} + \frac{y_{LB} + y_B}{2} \right) / 2 \quad (2.12b)$$

Consequently, if a membrane deformation takes place, the system of equations formed by (2.6) has to be modified using the interpolated values  $V_L^*(x_L, y_C)$  and  $V_R^*(x_R, y_C)$  instead of using  $V_L(x_L, y_B)$  and  $V_R(x_R, y_T)$ , as follow:

$$\begin{aligned} & \left[ \frac{1}{(y_B - y_C)(y_B - y_T)} \right] V_B + \left[ \frac{1}{(y_T - y_B)(y_T - y_C)} \right] V_T \\ & + \left[ \frac{1}{(x_L - x_C)(x_L - x_R)} \right] \cdot \left[ \frac{y_C - y_L}{y_{LT} - y_L} V_{LT} + \frac{y_{LT} - y_C}{y_{LT} - y_L} V_L \right] \\ & + \left[ \frac{1}{(x_R - x_L)(x_R - x_C)} \right] \cdot \left[ \frac{y_R - y_C}{y_R - y_{RB}} V_{RB} + \frac{y_C - y_{RB}}{y_R - y_{RB}} V_R \right] \\ & + \left[ \frac{1}{(x_C - x_L)(x_C - x_R)} + \frac{1}{(y_C - y_B)(y_C - y_T)} \right] V_C = 0 \end{aligned} \quad (2.13)$$

Using the boundary conditions of  $V = 0$  at the outer boundary nodes and at the nodes on the bridge, while  $V = V_o$  on the lower electrode,  $V_o$  is the applied voltage. The application of (2.6) in conjunction with (2.10) and (2.13) to all free nodes in the 2-D computational domain results in a set of simultaneous equations of the form:

$$[A] [X] = [B]$$

where  $[A]$  is a sparse matrix has the coefficients of the system of equations,  $[X]$  is a column matrix consisting of the unknown values of the potential at the free nodes, and  $[B]$  is a column matrix containing the known values of the potential at the fixed nodes.

$$[X] = [A]^{-1} [B] \quad (2.14)$$

After getting  $[X]$ , the potential of all nodes in the computational domain is known.

#### *Second Algorithm: Iterative Technique*

In this algorithm the potential distribution in the computation domain is computed based on an iterative technique for an updating equation for the potential distribution in the 2-D computational domain. This updating equation is obtained by applying Gauss's law in two-dimensions to all free nodes in the computational domain using the finite difference method to approximate the derivatives. The boundary conditions are  $V = V_o$  on the lower electrode (CPW signal line) and  $V = 0$  on the upper electrode (MEMS bridge) and the outer boundaries. On the dielectric interface and at any

node in the computational domain other than those on the electrodes, Gauss's law is applied (2.7). The finite difference approximations translate this integral equation at a general node  $C$  on the grid inside the computational domain enclosed by a closed contour  $l$  as illustrated in Fig. 2.4(b) gives:

$$V_C = \frac{\left[ \frac{V_L}{x_C - x_L} [(y_T - y_C)\varepsilon_1 + (y_C - y_B)\varepsilon_4] + \frac{V_R}{x_R - x_C} [(y_T - y_C)\varepsilon_2 + (y_C - y_B)\varepsilon_3] + \frac{V_B}{(y_C - y_B)} [(x_R - x_C)\varepsilon_3 + (x_C - x_L)\varepsilon_4] + \frac{V_T}{y_T - y_C} [(x_R - x_C)\varepsilon_2 + (x_C - x_L)\varepsilon_1] \right]}{\left[ \left( \frac{y_C - y_B}{x_R - x_C} + \frac{x_R - x_C}{y_C - y_B} \right) \varepsilon_3 + \left( \frac{y_T - y_C}{x_R - x_C} + \frac{x_R - x_C}{y_T - y_C} \right) \varepsilon_2 + \left( \frac{y_C - y_B}{x_C - x_L} + \frac{x_C - x_L}{y_C - y_B} \right) \varepsilon_4 + \left( \frac{y_T - y_C}{x_C - x_L} + \frac{x_C - x_L}{y_T - y_C} \right) \varepsilon_1 \right]} \quad (2.15)$$

This equation can be rearranged in the following general form [60]:

$$V_C = C_R V_R + C_L V_L + C_T V_T + C_B V_B \quad (2.16)$$

where

$$C_R = C_o \frac{(y_T - y_C)\varepsilon_2 + (y_C - y_B)\varepsilon_3}{x_R - x_C}, \quad C_L = C_o \frac{(y_T - y_C)\varepsilon_1 + (y_C - y_B)\varepsilon_4}{x_C - x_L},$$

$$C_T = C_o \frac{(x_R - x_C)\varepsilon_2 + (x_C - x_L)\varepsilon_1}{y_T - y_C}, \quad C_B = C_o \frac{(x_R - x_C)\varepsilon_3 + (x_C - x_L)\varepsilon_4}{y_C - y_B},$$

and

$$C_o = \left[ \left( \frac{y_C - y_B}{x_R - x_C} + \frac{x_R - x_C}{y_C - y_B} \right) \varepsilon_3 + \left( \frac{y_T - y_C}{x_R - x_C} + \frac{x_R - x_C}{y_T - y_C} \right) \varepsilon_2 + \left( \frac{y_C - y_B}{x_C - x_L} + \frac{x_C - x_L}{y_C - y_B} \right) \varepsilon_4 + \left( \frac{y_T - y_C}{x_C - x_L} + \frac{x_C - x_L}{y_T - y_C} \right) \varepsilon_1 \right]^{-1}$$

In the same way, equation (2.15) is derived assuming the grid is rectangular and the grid lines are parallel to each other and parallel to the main axes. But this is not correct in the gap region more than ever as the beam gets deformed when a dc voltage is applied between the membrane and the lower electrode. Thus, the same trick of the interpolation discussed earlier can be used to estimate the potential for two nodes on a horizontal line passing through the center node  $C$ , as given by equations (2.11). Therefore, equation (2.15) for any node in the gap region in case distorted switch can be expressed as follows:

$$V_C = \frac{\left[ \frac{V_R^*}{x_R - x_C} [y_T^* - y_B^*] + \frac{V_T}{y_T - y_C} [x_R - x_L] + \frac{V_L}{x_C - x_L} [(y_T^* - y_B^*)] + \frac{V_B}{(y_C - y_B)} [x_R - x_L] \right]}{\left[ \frac{y_T^* - y_B^*}{x_R - x_C} + \frac{x_R - x_L}{y_T - y_C} + \frac{y_T^* - y_B^*}{x_C - x_L} + \frac{x_R - x_L}{y_C - y_B} \right]} \quad (2.17)$$

where  $y_T^*$  and  $y_B^*$  as given by (2.12).

Or in the general form:

$$V_C = C_L^* V_L^* + C_R^* V_R^* + C_B^* V_B + C_T^* V_T$$

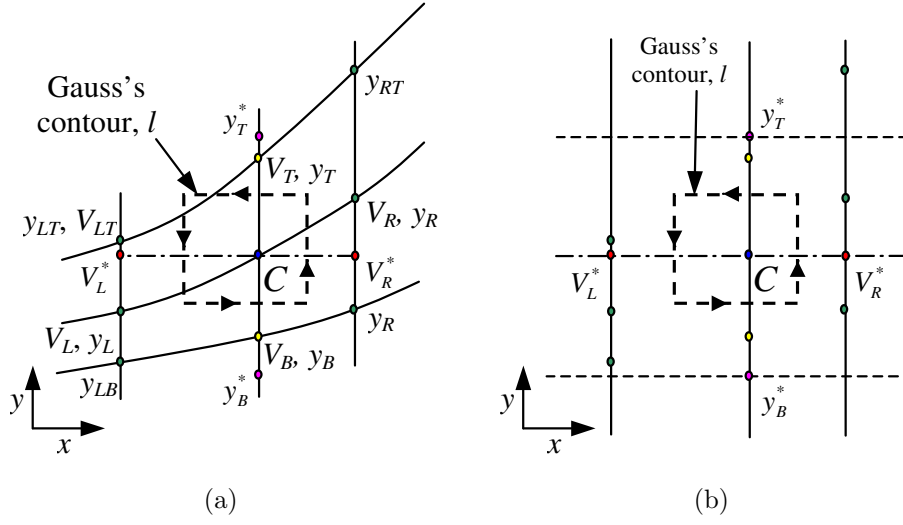


Figure 2.6: A General voltage node in the computational domain when the switch gets deformed.

where

$$C_L^* = C_o^* \frac{y_{i+1,j}^* - y_{i-1,j}^*}{x_{i,j} - x_{i,j-1}}, \quad C_R^* = C_o^* \frac{y_{i+1,j}^* - y_{i-1,j}^*}{x_{i,j+1} - x_{i,j}},$$

$$C_B^* = C_o^* \frac{x_{i,j+1} - x_{i,j-1}}{(y_{i,j} - y_{i-1,j})}, \quad C_T^* = C_o^* \frac{x_{i,j+1} - x_{i,j-1}}{y_{i+1,j} - y_{i,j}},$$

and

$$C_o^* = \left[ \frac{y_{i+1,j}^* - y_{i-1,j}^*}{x_{i,j+1} - x_{i,j}} + \frac{x_{i,j+1} - x_{i,j-1}}{y_{i+1,j} - y_{i,j}} + \frac{y_{i+1,j}^* - y_{i-1,j}^*}{x_{i,j} - x_{i-1,j}} + \frac{x_{i,j+1} - x_{i,j-1}}{y_{i,j} - y_{i-1,j}} \right]^{-1}$$

To obtain the potential distribution in the 2-D computational domain, first all free nodes are initiated with zero potential and then an iterative procedure is employed to (2.16) to update itself until the potential for all free nodes get saturated. The accuracy of the results depends on the number of iterations, which updates the potential. This number of iterations is calculated by the program for a given percentage accuracy for the calculated potential in terms of the applied voltage. The error is measured as the largest difference between two successive values in the potential for any node in the computational domain. Fig. 2.7 illustrates the potential residual error versus the number of iterations for different required accuracies. From Fig. 2.7(a) we can see that for an error of 0.5 %, the required number of iterations is 81. While 267 iterations is needed for 0.1 % error as illustrated in Fig. 2.7(b).

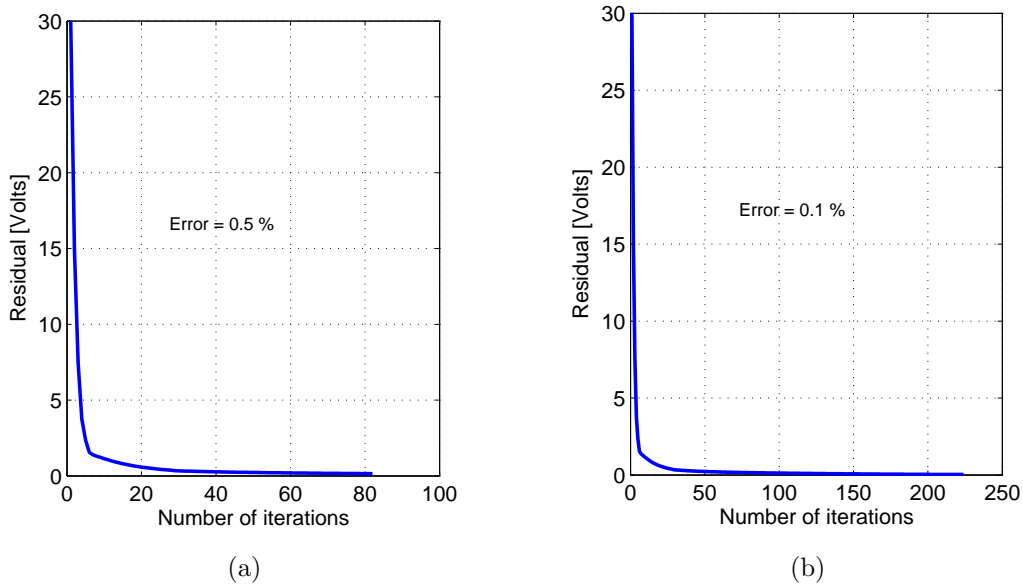


Figure 2.7: Convergence of error in the potential computational (a) 0.5 % error and (b) 0.1 % error.

### 2.3.2 Electrostatic Field Calculation

Having computed the potential distribution, the electric field vectors can be calculated from the relation  $\vec{E} = -\nabla V$  at any node. Since we are using a non-uniform grid, the quadratic interpolation for approximating the first derivative (which is needed to determine the electric field components) is a better approximation as compared to the linear one as given by equations (2.4a) and (2.5a). The  $x$ -component, as an example, of the electric field at any arbitrary node is then given by:

$$E_x(x) = -\frac{2x - x_C - x_R}{(x_L - x_C)(x_L - x_R)}V_L - \frac{2x - x_L - x_R}{(x_C - x_L)(x_C - x_R)}V_C - \frac{2x - x_L - x_C}{(x_R - x_L)(x_R - x_C)}V_R \quad (2.18)$$

In the same way, the  $y$ -components at all nodes can be computed.

### 2.3.3 Capacitance Determination

In order to calculate the switch capacitance one needs to compute the total charge on the lower electrode then divide it by the applied voltage. Gauss's law is applied around the lower electrode as shown in Fig. 2.10. This leads to the following expression for the total enclosed charge after using the FDM.

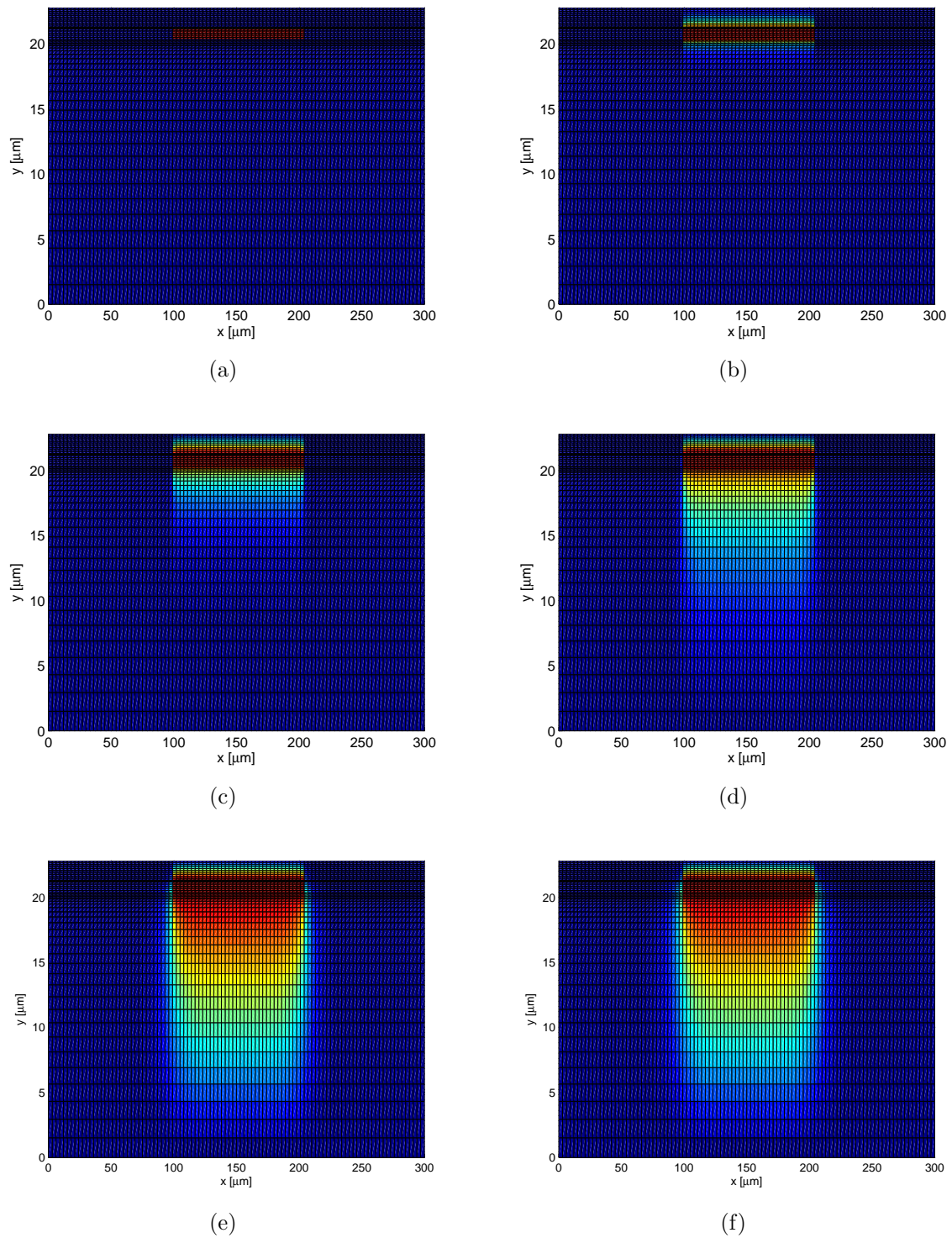


Figure 2.8: 2-D potential distribution with different values of the number of iterations for the potential computation iterative procedure (a) one iteration (b) 20 iterations, (c) 50 iterations, (d) 100 iterations, (e) 500 iterations, and (f) 1000 iterations.

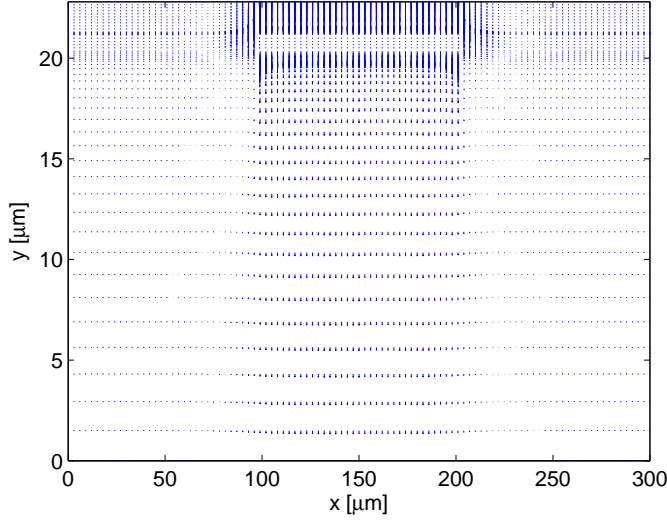


Figure 2.9: Electrostatic field distribution in the 2-D computational domain.

$$\begin{aligned}
 \rho^{enc} = & - \sum_{right} \frac{V_R - V_C}{x_R - x_C} \left[ \frac{\varepsilon_2(y_T - y_C) + \varepsilon_3(y_C - y_B)}{2} \right] \\
 & - \sum_{top} \frac{V_T - V_C}{y_T - y_C} \left[ \frac{\varepsilon_1(x_C - x_L) + \varepsilon_2(x_R - x_C)}{2} \right] \\
 & + \sum_{left} \frac{V_C - V_L}{x_C - x_L} \left[ \frac{\varepsilon_1(y_T - y_C) + \varepsilon_4(y_C - y_B)}{2} \right] \\
 & + \sum_{bottom} \frac{V_C - V_B}{y_C - y_B} \left[ \frac{\varepsilon_4(x_C - x_L) + \varepsilon_3(x_R - x_C)}{2} \right]
 \end{aligned} \tag{2.19}$$

The capacitance  $C$  per unit length is given next by  $C = \rho^{enc}/V_o$ , where  $V_o$  is the applied voltage between the lower and upper electrodes.

### 2.3.4 Electrostatic Charge and Force Induced on the Membrane

The electrostatic model calculates the electrostatic force induced on the movable beam when a dc-actuation voltage is applied between the upper and lower electrodes. When the DC voltage is applied between the electrodes, charges are induced on the membrane and opposite charges accumulate on the lower electrode. The charge density per unit length  $\rho$  induced on the membrane are calculated using Gauss's law in two dimensions as follow:

$$\rho = - \oint_l \varepsilon \frac{\partial V}{\partial n} \hat{n} \cdot \hat{a}_n dl \tag{2.20}$$

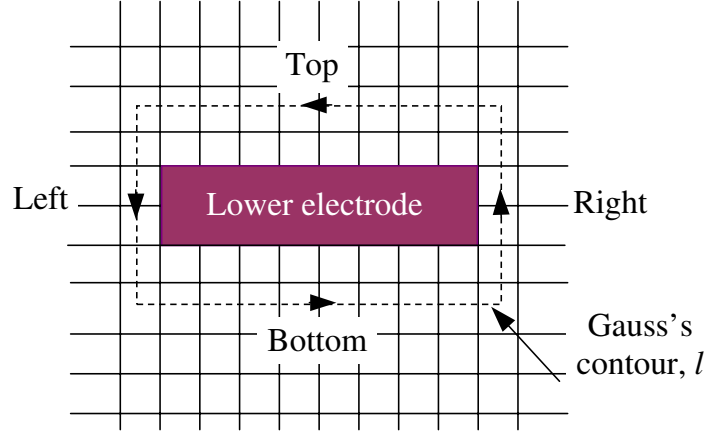


Figure 2.10: Computation of the total charge accumulated on the lower electrode to be used for structure-capacitance determination.

where  $l$  is a closed contour surrounds a subsection of the membrane as shown in Fig. 2.2. Here  $\hat{a}_n$  is a normal unit vector to the contour segments. By dividing the Gauss's contour into four segments, one can obtain:

$$\rho = - \int_{right} \varepsilon(y) \frac{\partial V}{\partial x} dy - \int_{top} \varepsilon(x) \frac{\partial V}{\partial y} dx + \int_{left} \varepsilon(y) \frac{\partial V}{\partial x} dy + \int_{bottom} \varepsilon(x) \frac{\partial V}{\partial y} dx$$

Assuming the field outside the metallic boundaries and the voltage applied to the membrane to be zero, and the adjacent medium to the bridge surface is air with  $\varepsilon_r = 1$ . Thus, the accumulated charge per unit length distributed in the  $z$ -direction for any segment on the membrane centered at  $(x_c, y_c)$  can be calculated as:

$$\rho(x_C) = \varepsilon_o \frac{V_B}{y_C - y_B} \left[ \frac{x_R - x_L}{2} \right]$$

This equation is divided by the segment length  $(x_R - x_L)/2$  to find the charge density and multiplying it by  $b$ , the beam width in the  $z$ -direction, one can obtain the distributed charge per unit length on the bridge along the  $x$ -axis for any segment centered at  $x_c$  as:

$$\rho(x_C) = \varepsilon_o \frac{V_B}{y_C - y_B} b \quad (2.21)$$

Having obtained the electric field components, the electrostatic force induced on the bridge can be determined. The normal electrostatic force per unit length can be determined in terms of the storage energy  $U$  per unit length as:  $f(x) = -dU(x, y)/dy$ , where  $U$  is defined as  $U = (1/2) \int \varepsilon E^2 dx dy$ , and  $s$  is the surface contour shown in Fig. 2.2. Thus,  $f(x) = (1/2) \int_l \varepsilon E^2 dx$  in Newton per unit length along the  $z$ -direction.

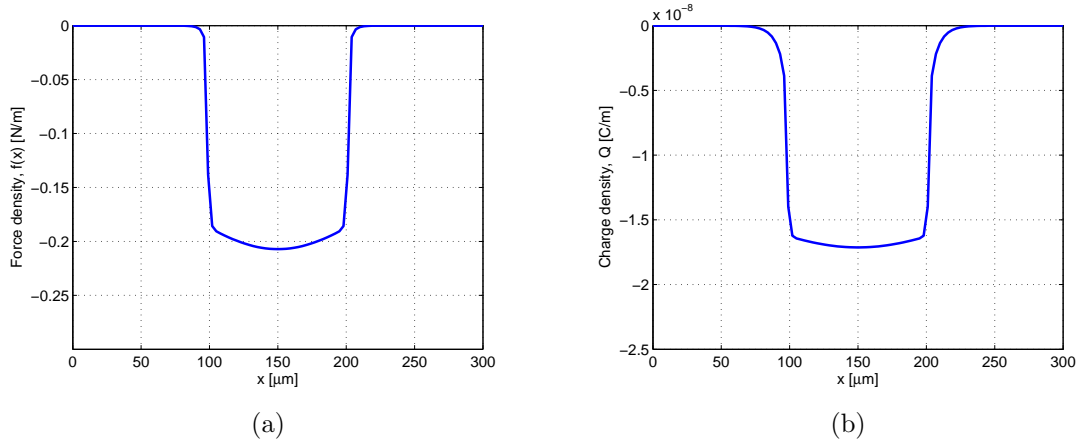


Figure 2.11: Electrostatic (a) force and (b) charge densities distributions induced on the membrane with actuation voltage of 30 Volts.

Therefore, the amount of the electrostatic force induced on a certain segment of length  $\Delta x$  on the membrane is calculated by:

$$\Delta f(x) = (1/2)\varepsilon_o E^2(x, y)\Delta x$$

This equation is divided by  $\Delta x$  to find the force density and multiplying it by the beam width  $b$  in the  $z$ -direction gives the distributed force per unit length in the  $x$ -direction induced on the bridge. Thus, at any arbitrary node  $x$  the distributed force per unit length is given as:

$$f(x) = \frac{b}{2}\varepsilon_o (E_x^2 + E_y^2) \quad (2.22)$$

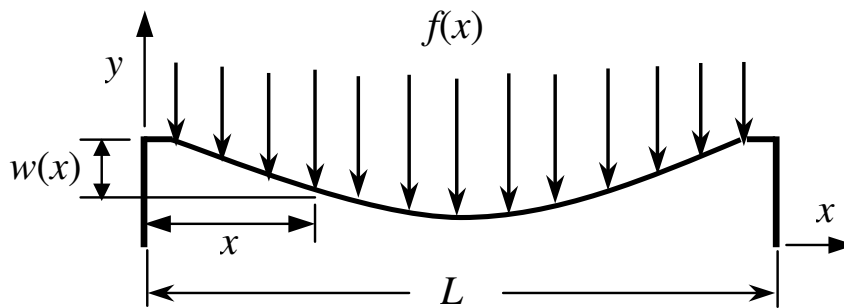


Figure 2.12: Schematic diagram of a deformed electrostatic loaded double-supported beam.

## 2.4 2-D Mechanical Analysis

The mechanical model is based on solving the beam equation that describes the beam movement, which is electrostatically loaded when applying a dc voltage between

the lower electrode and the upper movable one (membrane) to determine the beam deformation. Figs. 2.1 and 2.12 show the fixed-fixed beam diagram and the load configuration, respectively. The step-up support in this beam has been approximated as a "fixed" boundary condition [24]. The transverse deflection of the movable beam  $w(x)$  is governed by Euler-Bernoulli beam equation given in [61] as:

$$\widehat{E} \tilde{I} \frac{d^4 w}{dx^4} - (T_r + T_a) \frac{d^2 w}{dx^2} = f(x) \quad (2.23)$$

where  $f(x)$  is the distributed force density per unit length (the beam here is electrostatically actuated and the electrostatic force  $f(x)$ , which is calculated from the electrostatic model, couples the mechanical model and the electrostatic model).  $w(x)$  is the transverse beam displacement,  $\widehat{E} = \mathbf{E} / (1 - \nu^2)$  is the beam modulus where  $\mathbf{E}$  is Young's modulus,  $\nu$  is Poisson's ratio,  $\tilde{I} = bt^3/12$  is the beam moment of inertia,  $t$  and  $b$  are the beam thickness and width, respectively.  $T_r$  is the residual force and is formulated by  $T_r = \hat{\sigma}bt$  where  $\hat{\sigma}$  is the residual stress which equals  $\sigma_o(1 - \nu)$  for the doubly supported beam, where  $\sigma_o$  is the biaxial residual stress.  $T_a$  is the axial force and is formulated by

$$T_a = \frac{\widehat{E} bt}{2L} \int_0^L \left( \frac{dw}{dx} \right)^2 dx.$$

Equation (2.23) is a non-linear, non-homogenous 4<sup>th</sup> order differential equation. To solve (2.23) to find the beam deformation, two algorithms are employed and discussed in details in the next sections.

### 2.4.1 1st Algorithm: Analytical Solution

To find the general solution of equation (2.23), it is more convenient to rewrite it in the form:

$$\frac{d^4 w}{dx^4} - k^2 \frac{d^2 w}{dx^2} = F(x) \quad (2.24)$$

where

$$k^2 = \frac{T_r + T_a}{\widehat{E} \tilde{I}} = \frac{\hat{\sigma}bt}{\widehat{E} \tilde{I}} + \frac{6b}{Lt^2} \int_0^L \left( \frac{dw}{dx} \right)^2 dx,$$

and

$$F(x) = \frac{f(x)}{\widehat{E} \tilde{I}}$$

Equation (2.24) is a fourth order nonlinear, inhomogeneous differential equation. If the axial force term  $\frac{6b}{Lt^2} \int_0^L \left( \frac{dw}{dx} \right)^2 dx$  is neglected  $k$  becomes constant (equals to  $\sqrt{\frac{\hat{\sigma}bt}{\widehat{E} \tilde{I}}}$ ). Thus the 4<sup>th</sup> order differential equation becomes linear. The general solution of a higher order inhomogeneous linear differential equation can be found easily using the

method of variation of parameters [62]. The general solution of this equation while, initially, assuming  $k$  is constant can be found by assuming the general solution of the homogenous equation of (2.24) to be in the form:

$$w_c(x) = a_o + a_1x + a_2e^{kx} + a_3e^{-kx} \quad (2.25)$$

Furthermore, by setting  $w_o(x) = 1, w_1(x) = x, w_2(x) = e^{kx}$ , and  $w_3(x) = e^{-kx}$  in the last equation, one can use the method of variation of parameters for determining a particular solution  $w_p(x)$  of Eq. (2.24) in terms of four functions  $u_o, u_1, u_2$  and  $u_3$  such that:

$$w_p(x) = u_o(x)w_o(x) + u_1(x)w_1(x) + u_2(x)w_2(x) + u_3(x)w_3(x) \quad (2.26)$$

For these functions to be determined, four conditions must be specified. The Wronskian  $W$  of functions  $w_o, w_1, w_2$ , and  $w_3$  is the determinant:

$$W(w_o, w_1, w_2, w_3) = \begin{bmatrix} w_o(x) & w_1(x) & w_2(x) & w_3(x) \\ w'_o(x) & w'_1(x) & w'_2(x) & w'_3(x) \\ w''_o(x) & w''_1(x) & w''_2(x) & w''_3(x) \\ w'''_o(x) & w'''_1(x) & w'''_2(x) & w'''_3(x) \end{bmatrix} \quad (2.27)$$

while  $u'_k = \frac{W_k}{W}$ , where  $W_k$  is the determinant obtained by replacing the  $k^{th}$  column of the Wronskian by the column consisting of the elements  $(0, 0, 0, F(x))$ . Simple integration can be used to obtain  $u_o(x), u_1(x), u_2(x)$ , and  $u_3(x)$ , while substitution in Eq. (2.26) yields the particular solution

$$\begin{aligned} u_o(x) &= \frac{1}{a_o k^2} \int xF(x)dx, & u_1(x) &= -\frac{1}{a_1 k^2} \int F(x)dx, \\ u_2(x) &= \frac{1}{2a_2 k^3} \int e^{-kx} F(x)dx, & u_3(x) &= -\frac{1}{2a_3 k^3} \int e^{kx} F(x)dx \end{aligned}$$

with,

$$w_p(x) = \frac{1}{k^2} \int xF(x)dx - \frac{x}{k^2} \int F(x)dx + \frac{e^{kx}}{2k^3} \int e^{-kx} F(x)dx - \frac{e^{-kx}}{2k^3} \int e^{kx} F(x)dx$$

Thus, the general solution of  $w(x)$  equals  $w_c(x) + w_p(x)$ , which can be found as:

$$\begin{aligned} w(x) &= a_o + a_1x + a_2e^{kx} + a_3e^{-kx} + \frac{1}{k^2} \int_0^x \lambda F(\lambda)d\lambda - \frac{x}{k^2} \int_0^x F(\lambda)d\lambda \\ &\quad + \frac{e^{kx}}{2k^3} \int_0^x e^{-k\lambda} F(\lambda)d\lambda - \frac{e^{-kx}}{2k^3} \int_0^x e^{k\lambda} F(\lambda)d\lambda \end{aligned} \quad (2.28)$$

where  $a_o, a_1, a_2$ , and  $a_3$  are constants to be determined by applying the boundary conditions  $w(0) = 0 = w'(0)$  and  $w(L) = 0 = w'(L)$ , with assumed clamped-clamped

beam. The coefficients  $a_0, a_1, a_2$ , and  $a_3$  can be determined from the following matrix equation:

$$\begin{bmatrix} a_0 \\ a_1 \\ a_2 \\ a_3 \end{bmatrix} = \begin{bmatrix} 1 & 0 & 1 & 1 \\ 0 & 1 & k & -k \\ 0 & L & e^{kL} & e^{-kL} \\ 0 & 1 & ke^{kL} & -ke^{-kL} \end{bmatrix}^{-1} \begin{bmatrix} 0 \\ 0 \\ b_1 \\ b_2 \end{bmatrix} \quad (2.29)$$

where

$$b_1 = -\frac{1}{k^2} \int_0^L \lambda F(\lambda) d\lambda + \frac{L}{k^2} \int_0^L F(\lambda) d\lambda - \frac{e^{kL}}{2k^3} \int_0^L e^{-k\lambda} F(\lambda) d\lambda + \frac{e^{-kL}}{2k^3} \int_0^L e^{k\lambda} F(\lambda) d\lambda$$

and

$$b_2 = \frac{1}{k^2} \int_0^L F(\lambda) d\lambda - \frac{e^{kL}}{2k^2} \int_0^L e^{-k\lambda} F(\lambda) d\lambda - \frac{e^{-kL}}{2k^2} \int_0^L e^{k\lambda} F(\lambda) d\lambda$$

The integrals for the coefficients  $b_1$  and  $b_2$  are all finite and are computed numerically.

Now to include the axial force in this analysis, we use the resulting  $w(x)$  to determine the axial force term  $\frac{6b}{Lt^2} \int_0^L \left(\frac{dw}{dx}\right)^2 dx$  and then calculate the new value of  $k$  and substitute back in Eq. (2.28). Using the new values of the coefficients  $a_0, a_1, a_2$ , and  $a_3$  calculated from Eq. (2.29) to determine the new  $w(x)$ . Repeating this process until the difference between two successive iterations for  $k$  is within a pre-determined value. In our procedure the error was set to be lower than  $10^3 \mu\text{m}^{-1}$ .

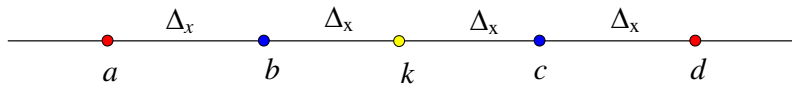


Figure 2.13: Application of FDM to find the beam deformation,  $k$  is a general node on the beam

## 2.4.2 2nd Algorithm: Numerical Solution

The beam equation, (2.23) is solved here numerically using FDM. To find the general solution of (2.23), it is more convenient to rewrite it in the form:

$$\frac{d^4 w}{dx^4} - T \frac{d^2 w}{dx^2} = F(x) \quad (2.30)$$

where

$$T = \frac{T_r + T_a}{\widehat{E} \tilde{I}} = \frac{\sigma_o(1 - \nu)bt}{\widehat{E} \tilde{I}} + \frac{6b}{Lt^2} \int_0^L \left( \frac{dw}{dx} \right)^2 dx,$$

and

$$F(x) = \frac{f(x)}{\widehat{E} \tilde{I}}$$

Equation (2.30) is a fourth order nonlinear, inhomogeneous differential equation. If the axial force term is neglected  $T$  becomes constant and the 4th order differential equation becomes linear. As was done in the electrostatic model, the quadratic interpolation is used to approximate the derivatives in (2.30) too. Using FDM, the second and fourth derivatives at general node  $k$  illustrated in Fig. 2.13 can be defined as:

$$\left( \frac{d^2w}{dx^2} \right)_k = \frac{w_c - 2w_k + w_b}{(\Delta_x)^2}$$

and

$$\left( \frac{d^4w}{dx^4} \right)_k = \frac{w_d - 4w_c + 6w_k - 4w_b + w_a}{(\Delta_x)^4}$$

So that, the system of equation for the beam equation at any general node  $k$  can be written in the following form:

$$\begin{aligned} w_a \left[ \frac{1}{(\Delta_x)^4} \right] + w_b \left[ \frac{-4}{(\Delta_x)^4} + \frac{-T}{(\Delta_x)^2} \right] + w_k \left[ \frac{6}{(\Delta_x)^4} + \frac{2T}{(\Delta_x)^2} \right] \\ + w_c \left[ \frac{-4}{(\Delta_x)^4} + \frac{-T}{(\Delta_x)^2} \right] + w_d \left[ \frac{1}{(\Delta_x)^4} \right] = F_k \end{aligned} \quad (2.31)$$

The boundary conditions of (2.30) are vanishing the displacements and slopes at both ends for the clamped-edges beam. The band matrix method is then employed to solve the generated system of equations which results in the bending function  $w(x)$  of the beam.

To include the axial force in this analysis, we use the resulting  $w(x)$  to determine the axial force term  $T_a$ . The new value of  $T$  is then substituted back in (2.31) to determine the new  $w(x)$ . This process is repeated until the difference between two successive iterations for  $T$  is less a tolerance value.

## 2.5 Coupling the Electrostatic and Mechanical Models

It is easily seen that the electrostatic model treats the beam deflection  $w(x)$  as an input parameter and produces the electrostatic force density  $f(x)$  as an output parameter. On the other hand, the input and output parameters of the mechanical

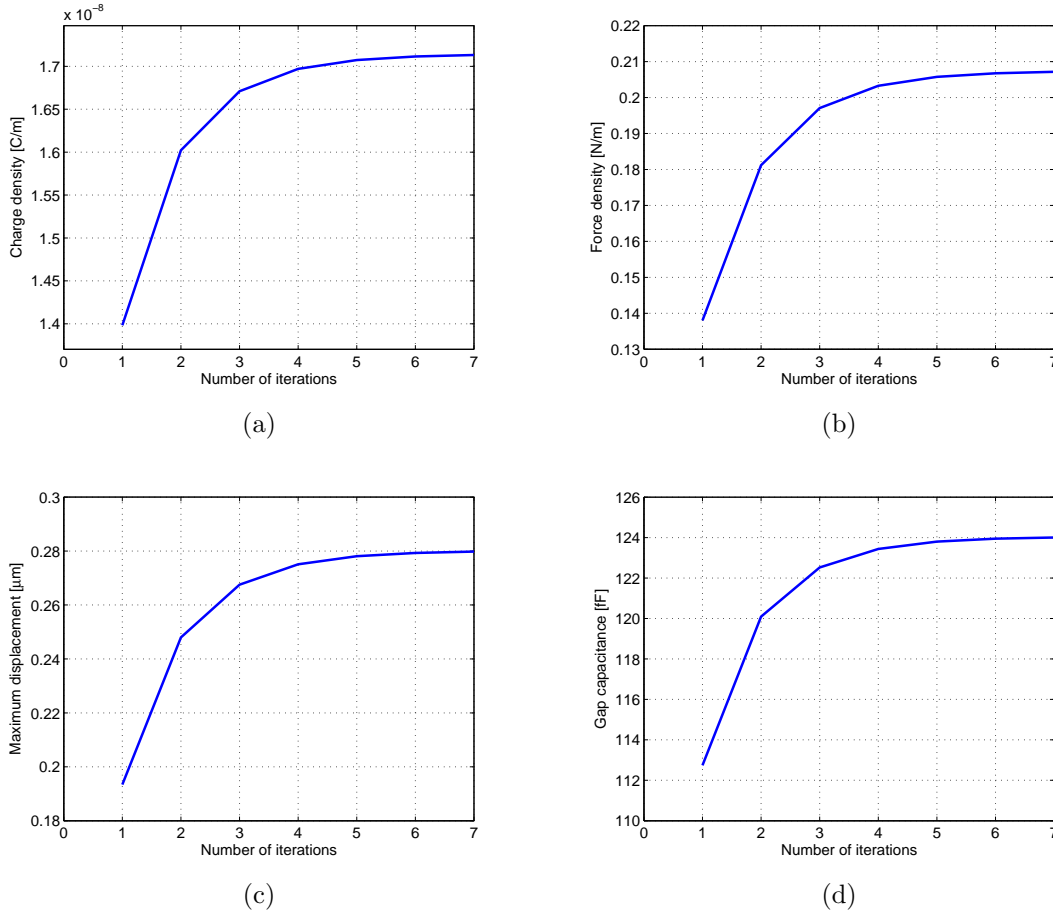


Figure 2.14: (a) Electrostatic charge, (b) Force densities induced on the medial node on the beam, (c) Corresponding node displacement, and (d) Gap capacitance, all versus the number of iterations between the electrostatic and mechanical models when the switch is actuated with a dc voltage of 30 Volts.

model are  $f(x)$  and  $w(x)$ , respectively, as may be seen from (2.23). This means that, the two models can be represented by a closed loop with the output of one model being the input to the other. The most suitable algorithm for the solution of such a closed-loop system is iterative algorithms. For a given actuation voltage  $V_o$  a deflection distribution  $w^{(0)}(x) = 0$  is initially assumed. The resulted force density distribution  $f^{(1)}(x)$  is next calculated using the electrostatic model, which is then used by the mechanical model to determine the new deflection distribution  $w^{(1)}(x)$  and this terminates the first iteration. The iterations should continue until the difference between two successive deflection distributions  $w^{(i)}(x)$  and  $w^{(i+1)}(x)$  (or equivalently two successive force density distributions  $f^{(i)}(x)$  and  $f^{(i+1)}(x)$ ) becomes less than a given tolerance.

For MEMS analyses, it is usually assumed that the pull down occurs when the microstructure deflects down to  $(2/3)g_o$ , where  $g_o$  is the initial gap height. This is considered the unstable mechanical position of the bridge. Hence the back and forth switching between the electrostatic and mechanical models converges as long as the

switch works in the mechanical stability region otherwise it may diverge. Therefore, the iterations is stopped when the maximum deflection is greater than or equal  $(1/3)g_o$ , which corresponds to the pull down voltage for the MEMS switch.

## 2.6 Results and Discussions

To validate the obtained numerical results and verify the proposed model, three standard capacitive RF MEMS switches that have been presented in [15, 23, 63] are modeled. The computed pull down voltage amounts to 33.4, 47.2, and 52.5 Volts while the experimental values for the similar configuration are 50, 30, and 39 (simulated value) Volts, respectively. There are small mismatches between the modeled and reported values, these may be due to the residual stress value, which is assumed to be constant of 20 MPa for aluminum fixed-fixed beam bridge in our calculations. As the pull down voltage is directly related to the residual stress, a considerable change in the value of the later leads to a corresponding change in the pull down voltage.

The computed electrostatic charges and forces induced on the membrane and the corresponding displacement of the beam center and the gap capacitance as functions of the number of iterations between the electrostatic and mechanical models are illustrated in Figs. 2.14(a), 2.14(b), 2.14(c) and 2.14(d), respectively. The steady-state condition with actuation voltage of 30 Volts reached after nine iterations for a tolerance in  $w(x)$  of  $10^{-3}\mu\text{m}$ . The number of iterations, which is needed to reach the steady-state beam position is completely dependent not only on the required tolerance but also on the actuation voltage. If the actuation voltage is much smaller than the pull down voltage the steady-state condition reached fast, while it needs more iterations when the actuation voltage is closer the pull down voltage. In the present example, the pull down voltage is about 34 Volts. As a consequence, 3 iterations was needed for an actuation voltage of 20 Volts, while for an actuation voltage of 33 Volts 13 iterations were needed to reach the steady-state conditions.

The iterations stopped when the error in the maximum deflection curve falls below a tolerance value (here given as  $10^{-3}\mu\text{m}$ ) or the maximum displacement increases than  $(1/3)g_o$ , which means the applied voltage is greater than or equals the pull down voltage. The shape of the deformed membrane terms of applied voltage is depicted in Fig. 2.15(a). Fig. 2.15(b) illustrates the gap height versus the applied voltage. The maximum force density induced on the membrane center node in terms of applied voltage is illustrated in Fig. 2.15(c). While Fig. 2.15(d) shows the gap capacitance versus the applied voltage. The computed pull down voltage amounts to 35 Volts while the experimental value for similar configuration is usually reported to be in the range of 30 Volts. The computed up-position capacitance of the MEMS switch is 85 fF while the experimental value is 70 fF. The theoretical results are very close to the experimental values reported in the literatures.

Those results correspond to switch geometry and dimensions similar to that reported in [23]. The number of meshes that have been used in the calculation were  $n_x = 60$  and  $n_y = 40$  in  $x$  and  $y$  directions, respectively. The mesh size was non-uniform in both  $x$  and  $y$  directions for more accurate solution. Smaller mesh size

is considered where fine geometrical details are present. The minimum and maximum values in the  $x$ -direction are  $\Delta x_{min} = 2.8 \mu\text{m}$  (over the lower electrode region, where most of the field is confined) and  $\Delta x_{max} = 7.5 \mu\text{m}$  (at the end of the membrane, where approximately no field), respectively. The corresponding values in the  $y$ -direction are  $\Delta y_{min} = 0.0375 \mu\text{m}$  (within the dielectric layer with the smallest thickness), and  $\Delta y_{max} = 2.945 \mu\text{m}$  (at the bottom of the substrate, where the field is decayed). The elapsed CPU time on a PC with Pentium IV, 1.4 GHz processor, and 2.0 GB RAM was 51.34 second to reach the steady-state bridge position, which has been achieved after nine iterations between the mechanical and electrostatic domains with a tolerance of  $10^{-3} \mu\text{m}$  in the maximum displacement at actuation voltage of 30 Volts.

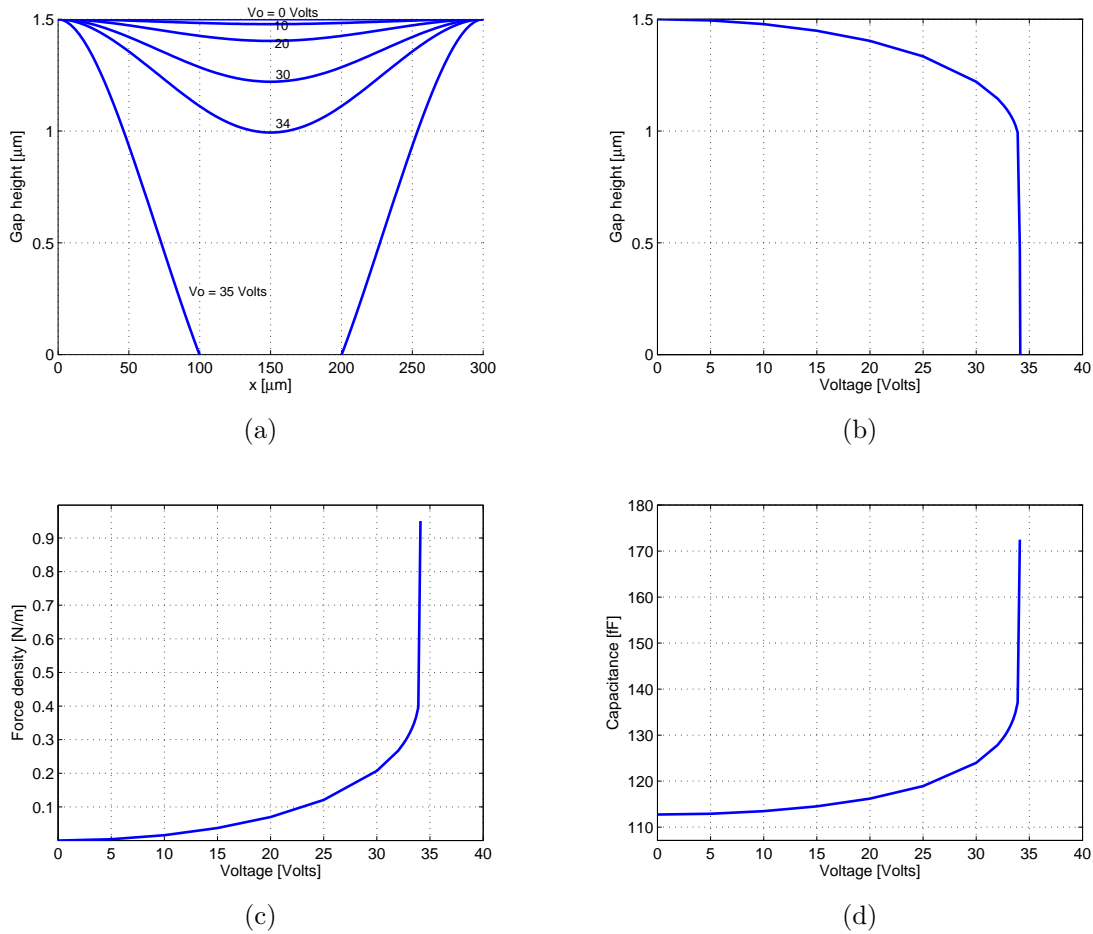


Figure 2.15: (a) The shape of the deformed membrane, (b) Beam center node displacement, (c) Electrostatic force density induced at the beam center node, and (d) Gap capacitance, all versus the applied voltage.

## 2.7 Conclusion

In this chapter, a two-dimensional coupled electrostatic-mechanical model for double-supported beam bridge RF MEMS shunt-capacitive switches has been presented, where the axial and residual stresses in the mechanical equation are taken into account. A simulation program has been developed to determine the deformation of the membrane in the MEMS switches as a function of the applied voltage.

Two algorithms for the electrostatic model have been investigated; one is based on solving Laplace's equation in the different homogenous regions using the FDM, while Gauss's law is employed at the interface nodes between different media. As a consequence, the band matrix method is employed to solve the generated system of equations to find out the potential distribution in the 2-D computational domain. The second one is based on solving Gauss's law in the 2-D Cartesian coordinates system using the central difference approximation for the derivatives. Then, an efficient iterative procedure is implemented for the solution of the potential distribution. The mechanical model is to determine the beam deformation arising from the induced electrostatic force that calculated by the electrostatic model. To do this, two algorithms for the mechanical model have been developed. The first one is solving the beam equation analytically using the method of variation of parameters to determine the beam deformation. While the second one is based on solving the beam equation numerically using the FDM, where the quadratic interpolation is used to approximate the derivatives.

The model results in an accurate determination of the switch capacitance, and the beam deformation in terms of the actuation voltage. The pull down voltage is also calculated for different structures and agrees well with the published data. The presented model combines the electrostatic and mechanical analyses and gives accurate results in a quite short CPU time. The developed algorithm and the program presented are capable to determine the bridge deformation, pull-in voltage and to investigate the effect of source fluctuations on the switch performance efficiently. Due to its numerical efficiency and small CPU time requirement, the developed algorithm and the related computer code can be easily integrated in the computer-aided design tools of RF MEMS switches saving a great deal of time allowing the designer to gain valuable physical insight.

## Chapter 3

# Three-Dimensional Coupled Electromechanical MEMS Analysis

In the last chapter, a 2-D coupled electrostatic-mechanical model for RF MEMS shunt-capacitive switches has been developed. However, the results are still little bit mismatched with the measured values. Successful MEMS devices rely not only on well-developed fabrication technologies but also on the knowledge of device behaviors, based on which a favorable structure of the device can be forged. One of the critical design issues for electro-statically actuated devices is the necessity of avoiding or intentionally initiating the occurrence of the pull-in phenomenon during operation. Some applications such as microphones or pressure sensors must only be operated within the safe range without pull-in occurring, while others such as optical switches need to tune the bias voltage across the pull-in back and forth to alternate switch-on and off. In all the aforementioned applications, the information of the critical bias voltage as the pull-in occurs and the associated deflection of the deformed plates must be precisely computed and then provided to the designers to meet the required device specifications.

This chapter deals with a three-dimensional (3-D) coupled electrostatic-mechanical model, which is a high efficient and quite accurate to characterize the capacitive RF MEMS switches. The solution of the electrostatic problem is based on applying Gauss's law to all free nodes in the 3-D computational domain. This results in a one updating equation for the potential. An efficient iterative procedure is then employed to this updating equation to get the steady state solution for the potential distribution. Having computed the potential distribution, the electrostatic field and hence the electrostatic force density induced on the membrane are determined. The mechanical problem is the determination of the bridge deformation arising from the electrostatic loading. This is done by solving the plate equation numerically using the finite difference method (FDM). The interaction between the mechanical and electrostatic domains here is considered iteratively. The analyses and simulations in

the present chapter are dedicated to the fixed-fixed beam bridge RF MEMS shunt-capacitive switches, although they are also applicable to other types of electrostatic MEMS structures. The choice of this type of switch structure is because it is used quite often in RF MEMS applications.

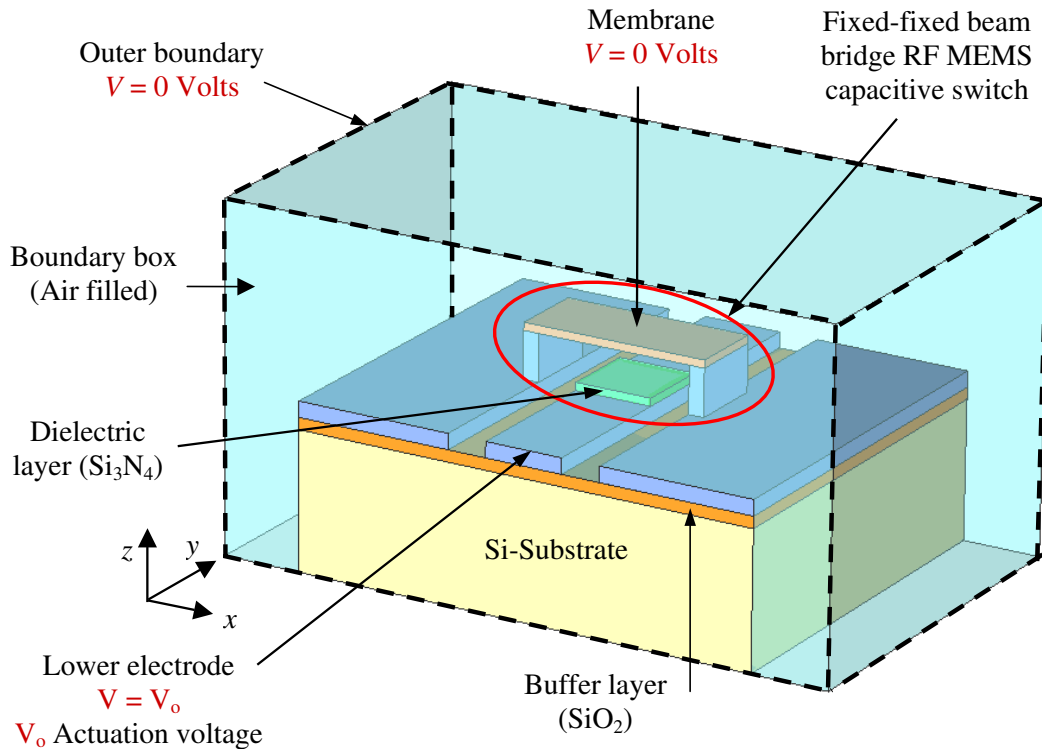


Figure 3.1: A fixed-fixed beam bridge RF MEMS shunt-capacitive switch impeded in a boundary air-filled box, 3-D computational domain.

### 3.1 The Simulation Program Algorithm

A shunt-capacitive RF MEMS switch, shown in Fig. 3.1, consists of a fixed-fixed thin metallic film suspended over a dielectric film deposited on top of the bottom electrode. This dielectric film serves to prevent the electric short between two conductors and provide a low impedance path for the RF signal. When the switch is un-actuated, there is a very small capacitance between the membrane and the bottom electrode, and the device is in the ON-state. When an electrostatic voltage is applied between the two conductors, an electrostatic force is created to pull the membrane down. At a certain voltage, the membrane collapses and comes in contact with the thin dielectric layer, which covers the bottom electrode, so a large capacitive coupling is there and the device is in the OFF-state. When a dc voltage is applied between the

movable membrane and the fixed bottom electrode, electrostatic charges are induced on both the membrane and the bottom electrode. The electrostatic charges cause an electrostatic force, which deforms the membrane. In consequence, such deformation results in an elastic force, which tries to restore the membrane to its original shape. In general, the deformation will also result in the reorganization of all surface charges on the device. This reorganization of charges is adequate to cause further membrane deformation. Thus, the device exhibits a coupled electro-mechanical behavior. For a certain applied voltage, an equilibrium position is defined by balancing the elastic and electrostatic forces. In order to model and simulate this coupled behavior, numerical iterations between the electrostatic and mechanical solutions are coupled. In the presented analyses, the balance condition takes place when the difference between two successive iterations for the transverse deflection of the membrane is less than a pre-determined value. The schematic diagram of the MEMS switch under investigation embedded in an air-filled box, where the electrostatic problem is to be solved is shown in Fig. 3.1, while Fig. 3.2 shows a general voltage node at which the electrostatic potential to be computed based on the surrounding nodes potentials and media characteristics.

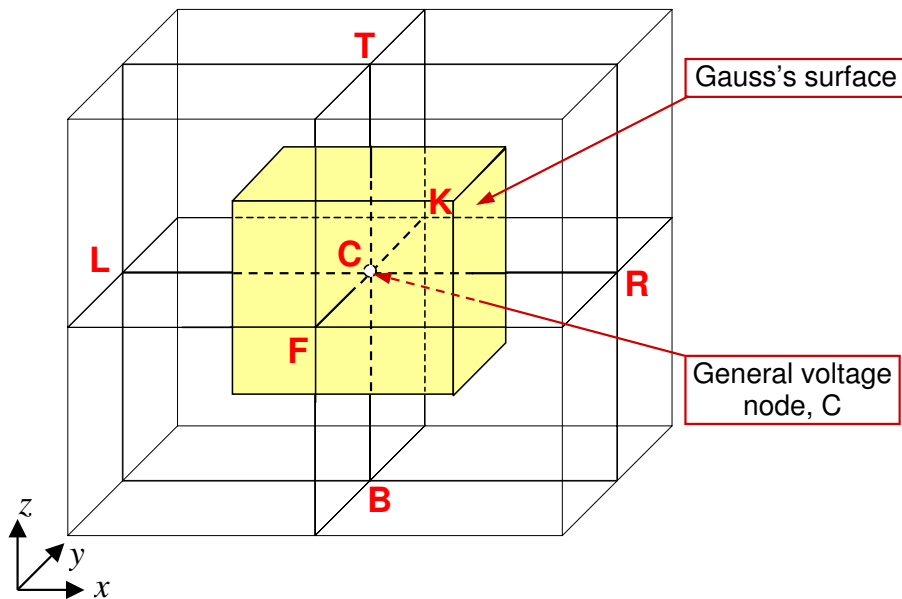


Figure 3.2: A general voltage node  $C$  in the 3-D computational domain, surrounded by six nodes  $L, R, B, T, F,$  and  $K$  with eight different media and the assumed closed Gauss's surfaces.

### 3.1.1 The 3-D Electrostatic Analysis

The developed electrostatic model is based on the solution for the potential distribution of the 3-D structure. It starts by meshing the computational domain in three

dimensions with non-uniform finite difference steps for more accurate results. The 3-D integral form of Gauss's law (3.1) is applied to all free nodes in the computational domain, i.e.

$$-\oint_s \varepsilon(x, y, z) \left( \frac{\partial V}{\partial x} \hat{a}_x + \frac{\partial V}{\partial y} \hat{a}_y + \frac{\partial V}{\partial z} \hat{a}_z \right) \cdot \hat{a}_n ds = 0 \quad (3.1)$$

where  $\varepsilon$  is the medium permittivity,  $ds$  is an element of the Gauss's surface as shown in Fig. 3.2, and  $\hat{a}_n$  is the unit vector normal to Gauss's surface. The boundary conditions are  $V = V_o$  on the lower electrode,  $V_o$  is the actuation voltage, and  $V = 0$  on the outer boundaries including all nodes on the membrane (upper electrode). In additions, Gauss's law is applied to all interface nodes except those lay on the metallic electrodes.

Applying the FDM to (3.1) on the closed surface contours after dividing it into six surfaces left, right, top, bottom, front, and back as described in Fig. 3.2 leads to an updating equation for the potential as follow:

$$\begin{aligned} & \frac{V_C - V_F}{y_C - y_F} \left[ \begin{array}{l} \varepsilon_2(x_R - x_C)(z_T - z_C) + \varepsilon_3(x_C - x_L)(z_T - z_C) \\ +\varepsilon_6(x_R - x_C)(z_C - z_B) + \varepsilon_7(x_C - x_L)(z_C - z_B) \end{array} \right] \\ & - \frac{V_K - V_C}{y_K - y_C} \left[ \begin{array}{l} \varepsilon_1(x_R - x_C)(z_T - z_C) + \varepsilon_4(x_C - x_L)(z_T - z_C) \\ +\varepsilon_5(x_R - x_C)(z_C - z_B) + \varepsilon_8(x_C - x_L)(z_C - z_B) \end{array} \right] \\ & + \frac{V_C - V_L}{x_C - x_L} \left[ \begin{array}{l} \varepsilon_3(y_C - y_F)(z_T - z_C) + \varepsilon_4(y_K - y_C)(z_T - z_C) \\ +\varepsilon_7(y_C - y_F)(z_C - z_B) + \varepsilon_8(y_K - y_C)(z_C - z_B) \end{array} \right] \\ & - \frac{V_R - V_C}{x_R - x_C} \left[ \begin{array}{l} \varepsilon_1(y_K - y_C)(z_T - z_C) + \varepsilon_2(y_C - y_F)(z_T - z_C) \\ +\varepsilon_5(y_K - y_C)(z_C - z_B) + \varepsilon_6(y_C - y_F)(z_C - z_B) \end{array} \right] \\ & + \frac{V_C - V_B}{z_C - z_B} \left[ \begin{array}{l} \varepsilon_5(x_R - x_C)(y_K - y_C) + \varepsilon_6(x_R - x_C)(y_C - y_F) \\ +\varepsilon_7(x_C - x_L)(y_C - y_F) + \varepsilon_8(x_C - x_L)(y_K - y_C) \end{array} \right] \\ & - \frac{V_T - V_C}{z_T - z_C} \left[ \begin{array}{l} \varepsilon_1(x_R - x_C)(y_K - y_C) + \varepsilon_2(x_R - x_C)(y_C - y_F) \\ +\varepsilon_3(x_C - x_L)(y_C - y_F) + \varepsilon_4(x_C - x_L)(y_K - y_C) \end{array} \right] = 0 \end{aligned} \quad (3.2)$$

where  $L, R, B, T, F$ , and  $K$  denote left, right, bottom, top, front, and back, respectively.

Equation (3.2) is derived assuming that the mesh is rectangular i.e. the grid lines are parallel together and parallel to the main axes. When the electrostatic domain is distorted due to the deformation of the switch, which arises by applying a dc voltage between the membrane and the lower electrode, the meshes are rearranged. Thus, the meshes in the gap region are not rectangular so far and furthermore the grid lines are neither parallel to each other nor parallel to the main axes as illustrated in Fig. 3.3. For these reasons, equation (3.2) must be modified to model the problem.

Using linear interpolation one can obtain two voltage nodes at the left  $V_L^*$  and at the right  $V_R^*$  with respect to the general node  $C$  on the horizontal axis in the  $x$ - $z$  plane, i.e. they have the same  $z$ -coordinates  $z_c$  as the general node  $C$  as following:

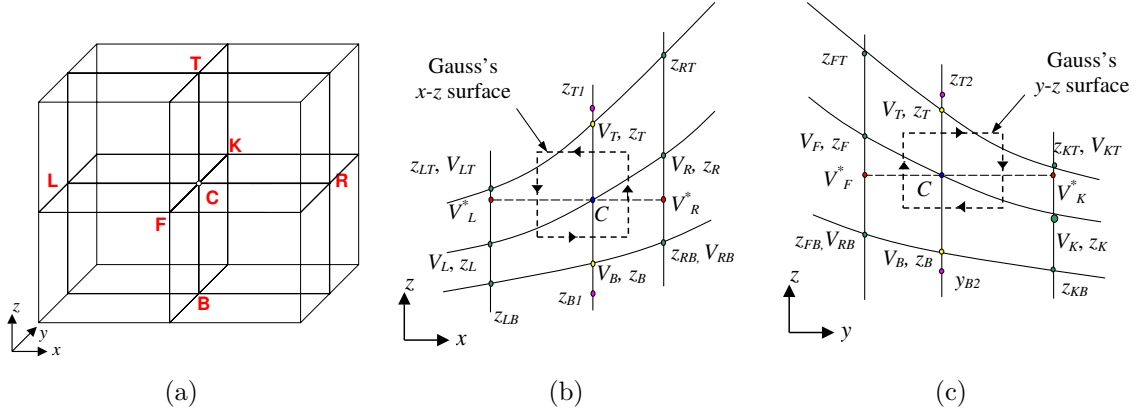


Figure 3.3: 3-D grid before and after the switch getting distorted due to the deformation of the actuated switch (a) before distortion, (b) The distorted grid in the  $x$ - $z$  plane, and (c) In the  $y$ - $z$  plane.

$$V_L^* = V_L + \frac{z_C - z_L}{z_{LT} - z_L} (V_{LT} - V_L) \quad \text{and} \quad V_R^* = V_R + \frac{z_C - z_{RB}}{z_R - z_{RB}} (V_R - V_{RB}) \quad (3.3a)$$

In the same way in the  $y$ - $z$  plane

$$V_K^* = V_K + \frac{z_C - z_K}{z_{KT} - z_K} (V_{KT} - V_K) \quad \text{and} \quad V_F^* = V_F + \frac{z_C - z_{FB}}{z_F - z_{FB}} (V_F - V_{FB}) \quad (3.3b)$$

In order to set the Gauss's top and bottom surfaces horizontal and parallel to the  $x$ - $y$  plane, we can average the  $z$ 's coordinates and re-calculate the new coordinates  $z_T^*$  and  $z_B^*$  as follow:

$$z_T^* = (z_{T1} + z_{T2})/2 \quad \text{and} \quad z_B^* = (z_{B1} + z_{B2})/2 \quad (3.3c)$$

where

$$z_{T1} = \left( \frac{z_{RT} + z_T}{2} + \frac{z_{LT} + z_T}{2} \right) / 2, \quad z_{B1} = \left( \frac{z_{RB} + z_B}{2} + \frac{z_{LB} + z_B}{2} \right) / 2,$$

$$z_{T2} = \left( \frac{z_{KT} + z_T}{2} + \frac{z_{FT} + z_T}{2} \right) / 2, \quad \text{and} \quad z_{B2} = \left( \frac{z_{KB} + z_B}{2} + \frac{z_{FB} + z_B}{2} \right) / 2.$$

The new updating potential equation, which is used in the disturbed regions, is equation (3.2) after substituting with the interpolated values  $V_L^*$ ,  $V_R^*$ ,  $V_K^*$ ,  $V_F^*$ ,  $z_B^*$ , and  $z_T^*$  as calculated above instead of using  $V_L$ ,  $V_R$ ,  $V_K$ ,  $V_F$ ,  $z_B$ , and  $z_T$ . In all cases, the updating potential equation (3.2) can be rearranged in the following general form:

$$V_C = C_F V_F + C_K V_K + C_L V_L + C_R V_R + C_B V_B + C_T V_T \quad (3.4)$$

where  $V_C, V_F, V_K, V_L, V_R, V_B$ , and  $V_T$  are the potentials at the center, front, back, left, right, bottom, and top nodes depicted in Fig. 3.3. The coefficients  $C_F, C_K, C_L, C_R, C_B$ , and  $C_T$  are easily computed from (3.2).

To obtain the potential distribution in the computational domain, first all free nodes are initialized with zero voltage and then an iterative procedure is employed to (3.4) until the potential at all free nodes converges. The coefficients  $C$ 's in (3.4) are calculated once outside the iterative loop, which helps a lot to have a quite short running time to reach the steady state solution for the potential.

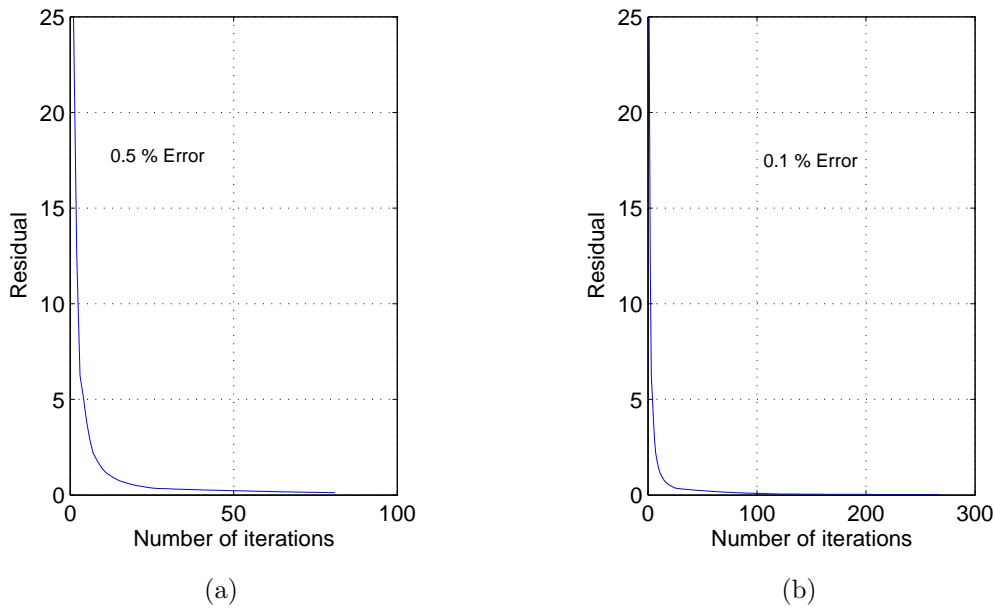


Figure 3.4: Computation of the potential with a specified accuracy (a) 0.5 % error and (b) 0.1 % error.

The accuracy of the results is completely dependent on the number of iterations for the iterative procedure, which compute the potential. Therefore, the program estimates the number of iterations automatically for a given percentage-accuracy. In this analysis, the accuracy is measured in terms of the applied voltage as the largest difference between two successive values of the potential for any node in the computational domain. Fig. 3.4 illustrates the residual potential error as a function of the number of iterations for different required accuracies. From Fig. 3.4(a) one can see that for an error of 0.5 %, the required number of iterations is 81. While 267 iterations is needed for a 0.1 % error as investigated in Fig. 3.4(b). The switch geometry that is investigated here is similar to that one reported in [23]. The switch membrane length, width, and thickness are 300, 80, and 2  $\mu\text{m}$ , respectively. It is made of aluminum with residual stress  $\sigma$  of 20 MPa and Young's modulus  $\mathbf{E}$  of 70 MPa. The coplanar waveguide (CPW) structure has a 100  $\mu\text{m}$  strip width and 60  $\mu\text{m}$  gap width, while the ground planes have 190  $\mu\text{m}$  width and 0.8  $\mu\text{m}$  thickness. The switch structure is built on a high-resistivity silicon substrate with 11.9 dielectric

constant. This is coated by a 1  $\mu\text{m}$  silicon dioxide buffer layer. A 0.15  $\mu\text{m}$  silicon nitride dielectric layer coats the lower electrode. The initial gap height is 1.5  $\mu\text{m}$ . The boundary box has a 600, 400, and 80  $\mu\text{m}$  length, width and height in the  $x$ ,  $y$  and  $z$  directions, respectively, with about 25  $\mu\text{m}$  air layer above the membrane and 50  $\mu\text{m}$  depth in the substrate, which assure a negligible field.

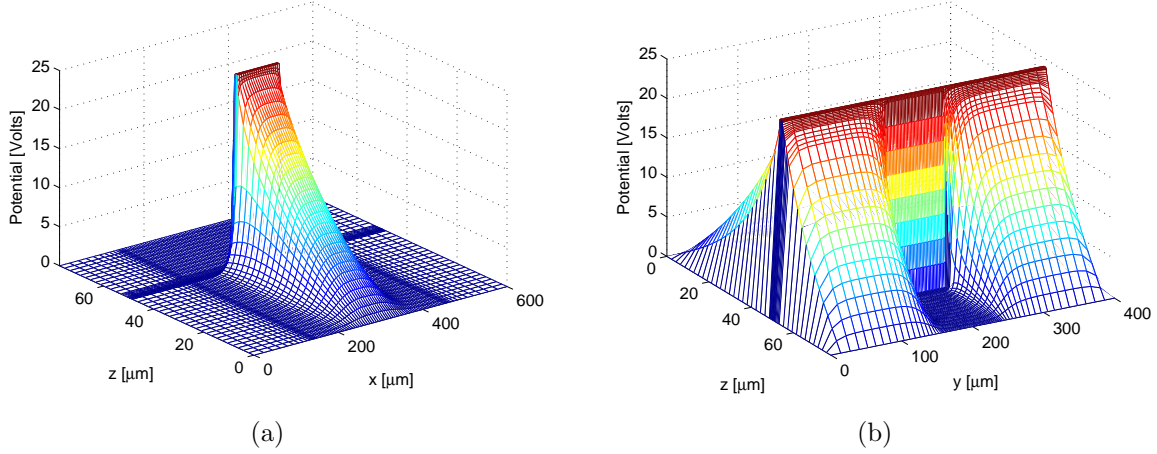


Figure 3.5: 3-D potential distribution in the computational domain (a) x-z plane at the y-symmetrical plane and (b) y-z plane at the x-symmetrical plane.

Having obtained the potential distribution, shown in Fig. 3.5, the electrostatic field distribution can be computed from the field-voltage relation;

$$\vec{E} = \partial V / \partial x \cdot \hat{a}_x + \partial V / \partial y \cdot \hat{a}_y + \partial V / \partial z \cdot \hat{a}_z$$

Using a quadratic interpolation technique, one can obtain expressions for the derivatives for a non-uniformly spaced finite difference mesh. For example, the  $x$ -component of the electric field can be written as:

$$E_x(x) = -\frac{2x - x_C - x_R}{(x_L - x_C)(x_L - x_R)}V_L - \frac{2x - x_L - x_R}{(x_C - x_L)(x_C - x_R)}V_C - \frac{2x - x_L - x_C}{(x_R - x_L)(x_R - x_C)}V_R \quad (3.5)$$

In the same way, the  $y$  and  $z$ -components for the electrostatic field can be calculated. We should mention here also that in the gap region, when the switch gets deformed, the same interpolation technique is employed in order to apply (3.5) with the interpolated values of the potential and the  $z$ -coordinates.

The main parameter that is calculated by the electrostatic model is the distributed force density induced on the membrane. The transverse components of the electrostatic force density can be determined in terms of the storage energy as  $p(x, y) = -dU/dz$ , where  $U$  is defined as  $U = (1/2) \int \varepsilon E^2 dx dy dz$ , and  $v$  is the volume enclosed by the Gauss's surfaces as depicted in Fig. 3.2. For any arbitrarily node on the membrane, the following relation can express the electrostatic force density induced on the membrane in the  $z$ -direction:

$$p(x, y) = \frac{1}{2}\varepsilon_o(E_x^2 + E_y^2 + E_z^2) \quad N/m^2 \quad (3.6)$$

where  $\varepsilon$  is the air permittivity and  $E_x, E_y$ , and  $E_z$ , are the magnitudes of field components at the corresponding node. The electrostatic force density induced on the membrane with actuation voltage of 25 Volts for the switch dimensions similar to those reported in [23] is depicted in Fig. 3.6(a).

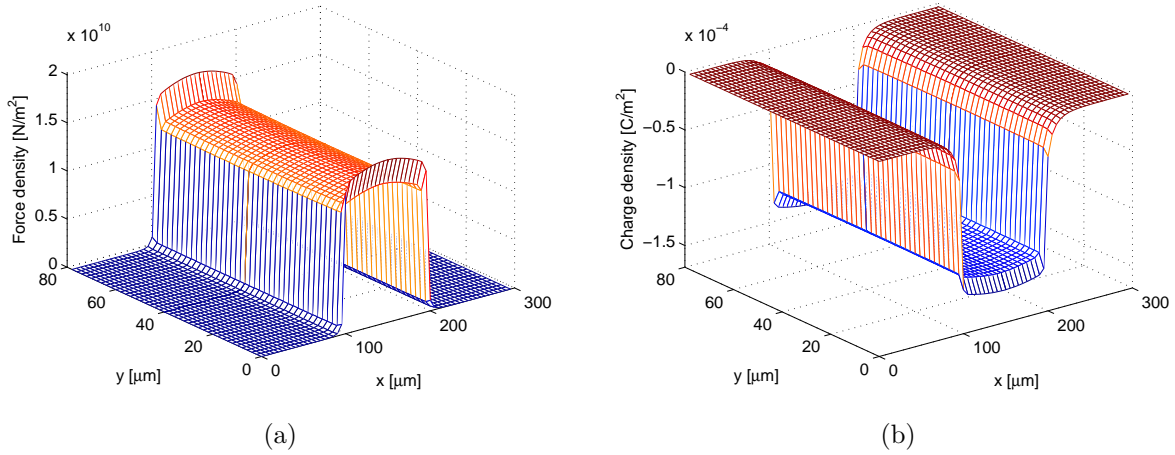


Figure 3.6: (a) Electrostatic force and (b) Charge density distributions induced on the membrane with a dc actuation voltage of 25 Volts for the switch geometries given above.

The electrostatic charge density  $\rho$  induced on the membrane, when a dc voltage is applied between the membrane and lower electrode, can be determined by applying Gauss's law for all nodes on the bridge as follow:

$$\rho = - \oint_s \varepsilon \frac{\partial V}{\partial n} \hat{n} \cdot \hat{a}_n ds \quad (3.7)$$

where  $\hat{n}$  is the unit vector normal to the membrane and  $ds$  is the Gauss's surface in the  $\hat{a}_n$  direction. Equation (3.7) is applied to all nodes on the lower-face of the membrane to calculate the accumulated charges per unit area. Assuming the membrane is biased with zero voltage and the surrounding medium is air, after applying the FDM equation (3.7) can be re-expressed in the following form:

$$\rho(x_C, y_C)|_{z_{\text{on bridge}}} = \varepsilon_o \frac{(z_T - z_B)(y_B - y_F)E_x + (z_T - z_B)(x_R - x_L)E_y + (x_R - x_L)(y_B - y_F)E_z}{(x_R - x_L)(y_B - y_F)} \quad (3.8)$$

where  $E_x, E_y$ , and  $E_z$  are the electric field  $x, y$ , and  $z$  components at the  $C$  node. The charge density distribution induced on the membrane with actuation voltage of 25 Volts is shown in Fig. 3.6(b) for the same switch dimensions.

One more important parameter for the RF MEMS switch that would be calculated by the electrostatic model is the gap capacitance. To compute this capacitance one

needs to calculate the total charges accumulated on the lower electrode then divide it by the applied voltage. Applying Gauss's law around the lower electrode leads to the following expression for the total enclosed charge using the FDM, such that

$$\begin{aligned}
\rho^{enclosed} = & - \sum_{right} \frac{V_R - V_C}{4(x_R - x_C)} \left[ \begin{array}{l} \varepsilon_2(y_T - y_C)(z_C - z_F) + \varepsilon_3(y_C - y_B)(z_C - z_F) \\ + \varepsilon_6(y_T - y_C)(z_K - z_C) + \varepsilon_7(y_C - y_B)(z_K - z_C) \end{array} \right] \\
& + \sum_{left} \frac{V_C - V_L}{4(x_C - x_L)} \left[ \begin{array}{l} \varepsilon_1(y_T - y_C)(z_C - z_F) + \varepsilon_4(y_C - y_B)(z_C - z_F) \\ + \varepsilon_5(y_T - y_C)(z_K - z_C) + \varepsilon_8(y_C - y_B)(z_K - z_C) \end{array} \right] \\
& - \sum_{top} \frac{V_T - V_C}{4(y_T - y_C)} \left[ \begin{array}{l} \varepsilon_1(x_C - x_L)(z_C - z_F) + \varepsilon_2(x_R - x_C)(z_C - z_F) \\ + \varepsilon_5(x_C - x_L)(z_K - z_C) + \varepsilon_6(x_R - x_C)(z_K - z_C) \end{array} \right] \\
& + \sum_{bottom} \frac{V_C - V_B}{4(y_C - y_B)} \left[ \begin{array}{l} \varepsilon_3(x_R - x_C)(z_C - z_F) + \varepsilon_4(x_C - x_L)(z_C - z_F) \\ + \varepsilon_7(x_R - x_C)(z_K - z_C) + \varepsilon_8(x_C - x_L)(z_K - z_C) \end{array} \right] \\
& - \sum_{back} \frac{V_K - V_C}{4(z_K - z_C)} \left[ \begin{array}{l} \varepsilon_5(x_C - x_L)(y_T - y_C) + \varepsilon_6(x_R - x_C)(y_T - y_C) \\ + \varepsilon_7(x_R - x_C)(y_C - y_B) + \varepsilon_8(x_C - x_L)(y_C - y_B) \end{array} \right] \\
& + \sum_{front} \frac{V_C - V_F}{4(z_C - z_F)} \left[ \begin{array}{l} \varepsilon_1(x_C - x_L)(y_T - y_C) + \varepsilon_2(x_R - x_C)(y_T - y_C) \\ + \varepsilon_3(x_R - x_C)(y_C - y_B) + \varepsilon_4(x_C - x_L)(y_C - y_B) \end{array} \right]
\end{aligned} \tag{3.9}$$

Then the structure capacitance  $C$  is given by  $C = \rho^{enclosed}/V_o$ , where  $V_o$  is the actuation dc voltage.

### 3.1.2 The Mechanical Model

The mechanical model is based on solving the plate (biharmonic) equation, which models the deflection arising in a 2-D rectangular isotropic symmetric laminated plates as reported in [64]. This equation is given by:

$$\frac{\partial^4 w}{\partial x^4} + 2 \frac{\partial^4 w}{\partial x^2 \partial y^2} + \frac{\partial^4 w}{\partial y^4} = \frac{p(x, y)}{D} \tag{3.10}$$

where  $w$  is the transverse displacement in the  $z$ -direction,  $p(x, y)$  is the pressure (force per area in  $N/m^2$ ), acting on the membrane, which is calculated by solving the 3-D electrostatic problem using the electrostatic model, and  $D = \mathbf{E}t^3/12(1 - \nu^2)$  is the plate stiffness.  $\mathbf{E}$  is the Young's modulus,  $t$  is the bridge thickness, and  $\nu$  is the Poisson's ratio. The fundamental assumptions of linear, elastic, and small-deflection theory of bending for thin plates are assumed [65]. Boundary conditions are applied for rectangular plate, assuming that the  $x$  and  $y$  axes are taken parallel to the edges of the plate, with two opposite clamped edges and the other two are free as shown in Fig. 3.7. For clamped edge, the deflection along this edge is zero, and the tangent plane to the deflected middle surface along this edge coincides with the initial position of the middle plane of the plate. Assuming the clamped edge to be given by  $x = 0$  and  $x = L$  where  $L$  is the bridge length, the boundary conditions are:

$$\omega(x, y)|_{x=0} = 0 = \omega(x, y)|_{x=L} \tag{3.11a}$$

$$\omega'(x, y)|_{x=0} = 0 = \omega'(x, y)|_{x=L} \tag{3.11b}$$

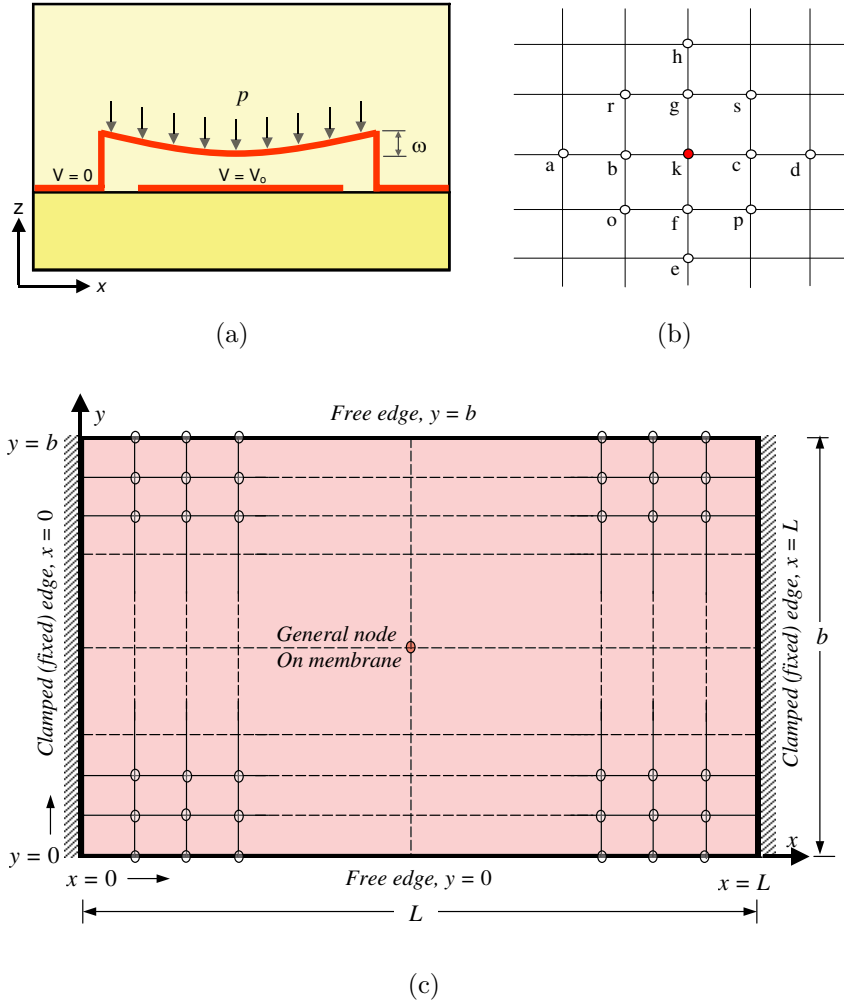


Figure 3.7: (a) Schematic diagram of the deformed electrostatic loaded fixed-fixed beam, (b) A general node on the membrane surrounded by 12 nodes ( $a, b, c, d, e, f, g, h, o, p, r,$  and  $s$ ) to be used by the FDM to approximate the 4<sup>th</sup> order derivatives in the plate equation, (c) The rectangular plate (membrane).

The free edges to be given by  $y = 0$  and  $y = b$  where  $b$  is the bridge width. Along these free edges there is no bending and twisting moments and also no vertical shearing forces. These conditions give the following boundary conditions:

$$\left[ \frac{\partial^2 \omega}{\partial y^2} + \nu \frac{\partial^2 \omega}{\partial x^2} \right]_{y=0} = 0 = \left[ \frac{\partial^2 \omega}{\partial y^2} + \nu \frac{\partial^2 \omega}{\partial x^2} \right]_{y=b} \quad (3.12a)$$

$$\left[ \frac{\partial^3 \omega}{\partial y^3} + (2 - \nu^2) \frac{\partial^3 \omega}{\partial y \partial x^2} \right]_{y=0} = 0 = \left[ \frac{\partial^3 \omega}{\partial y^3} + (2 - \nu^2) \frac{\partial^3 \omega}{\partial y \partial x^2} \right]_{y=b} \quad (3.12b)$$

Applying the FDM to (3.10) for a general node  $k$  on the membrane surrounded

by twelve nodes  $a, b, c, d, e, f, g, h, o, p, r,$  and  $s$ , shown in Fig. 3.7, the fourth order derivatives are approximated, which can be translated as follow:

$$\begin{aligned} \frac{w_e}{\Delta_y^4} + \frac{2w_o}{\Delta_x^2\Delta_y^2} + \left(\frac{-4}{\Delta_y^4} - \frac{4}{\Delta_x^2\Delta_y^2}\right)w_f + \frac{2w_p}{\Delta_x^2\Delta_y^2} + \frac{w_a}{\Delta_x^4} + \left(\frac{-4}{\Delta_x^4} - \frac{4}{\Delta_x^2\Delta_y^2}\right)w_b \\ + \left(\frac{6}{\Delta_x^4} + \frac{8}{\Delta_x^2\Delta_y^2} + \frac{6}{\Delta_y^4}\right)w_k + \left(\frac{-4}{\Delta_x^4} - \frac{4}{\Delta_x^2\Delta_y^2}\right)w_c \\ + \frac{w_d}{\Delta_x^4} + \frac{2w_r}{\Delta_x^2\Delta_y^2} + \left(\frac{-4}{\Delta_y^4} - \frac{4}{\Delta_x^2\Delta_y^2}\right)w_g + \frac{2w_s}{\Delta_x^2\Delta_y^2} + \frac{w_h}{\Delta_y^4} = \frac{P_k}{D} \end{aligned} \quad (3.13)$$

where  $\Delta x$  and  $\Delta y$  are the mesh sizes in the  $x$  and  $y$  directions, respectively. Applying (3.13) to all nodes on the bridge using the stated boundary conditions in equations (3.11a) and (3.12b), a system of equations can be generated. Solving the generated system of equations, the transverse displacement for all nodes on the bridge can be determined and hence the bridge deformation is realized.

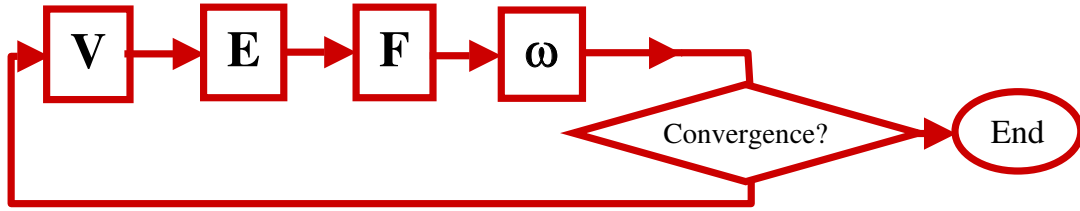


Figure 3.8: A simplified flowchart for the coupling process between the mechanical and electrostatic analysis.

### 3.1.3 The Electrostatic-Mechanical Coupling Process

The coupled models start by solving the electrostatic problem for the potential distribution in the 3-D computational domain. After having calculated the potential distribution, the electrostatic field and then the electrostatic force can be determined. Having determined the electrostatic force distribution induced on the membrane, the mechanical model can be initiated to determine the deformation in the membrane, which in turn alters the force distribution. This cycle between the electrostatic and mechanical models is considered as one iteration. The program goes back and forth between the electrostatic and mechanical models until the bridge's deformation reaches steady state. Fig. 3.9(a), 3.9(b), 3.9(c) and 3.9(d) illustrate the electrostatic charge and force densities induced on the membrane center node and the corresponding displacement at the same node and the gap capacitance as a function of the number of iterations between the electrostatic and mechanical models, respectively. The steady state conditions reached after six iterations with a tolerance of  $0.001 \mu\text{m}$

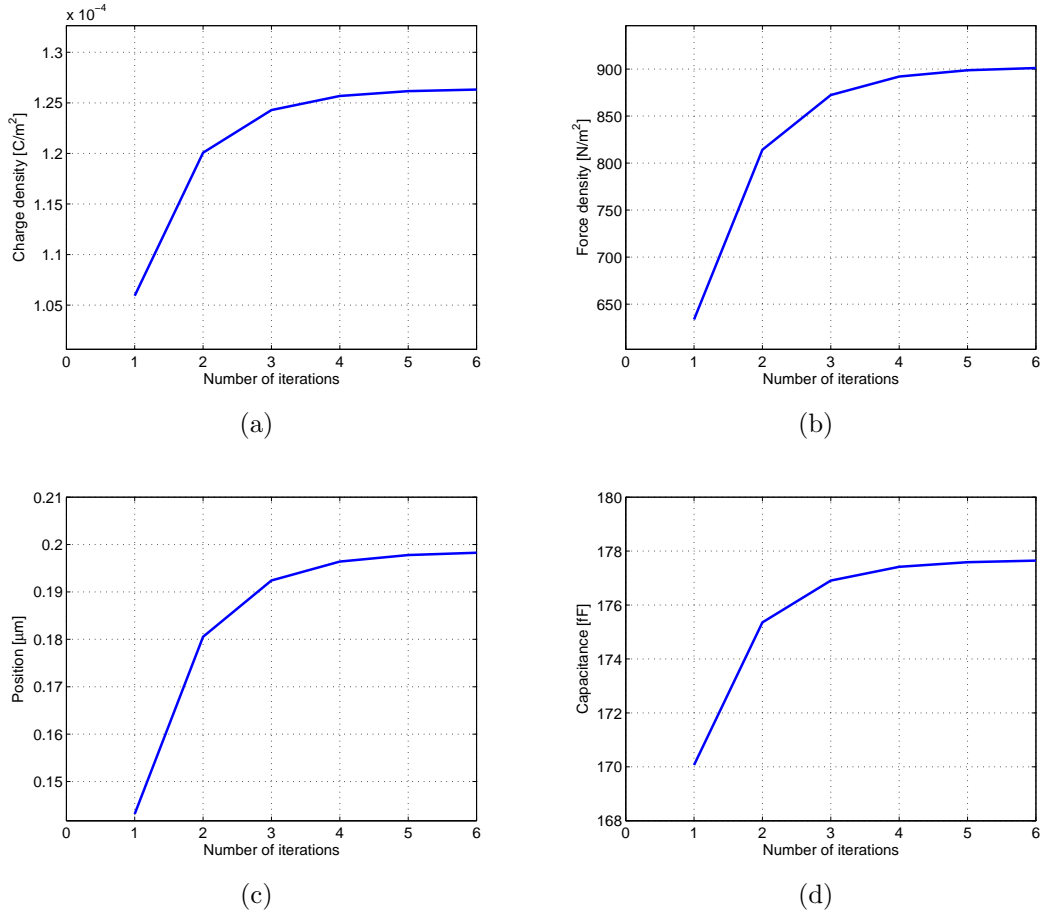
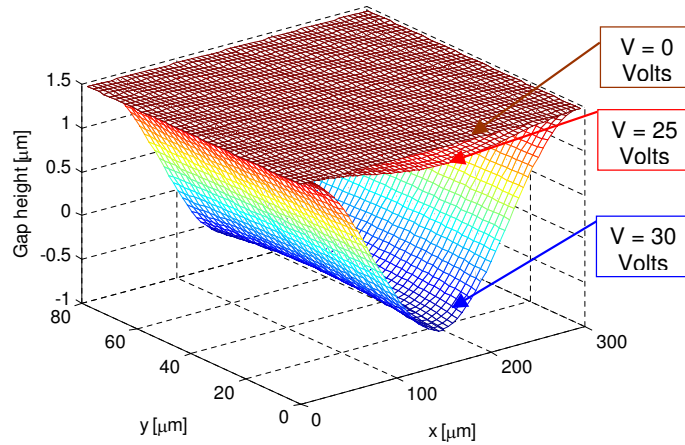


Figure 3.9: Coupling between the electrostatic and mechanical models procedure, (a) Electrostatic charge, (b) Electrostatic force densities induced on the membrane center node, (c) Membrane center node displacement, and (d) Gap capacitance, all versus the number of iterations between the electrostatic and mechanical models, all with actuation voltage of 25 Volts for the considered example.

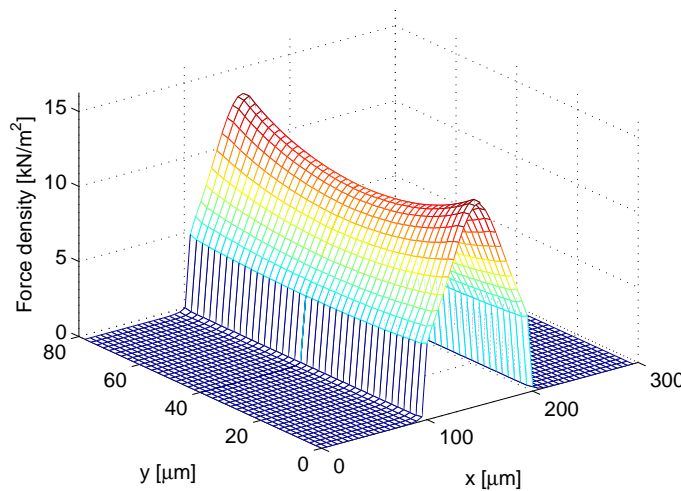
between two successive values in the displacement of the membrane center node. The input accuracy for the potential calculations is 0.1 %.

For MEMS analysis, it is usually assumed that the pull down occurs when the microstructure travels down to  $(2/3)g_o$ , where  $g_o$  is the initial gap height. This is considered the unstable mechanical position of the membrane. Hence the back and forth switching between the electric and mechanical models converges as long as the switch works in the mechanical stability region otherwise it may diverge. Therefore, the iteration is stopped when the maximum deflection is greater than or equal  $(1/3)g_o$ , which corresponds to the pull down voltage for the MEMS switch as illustrated in Fig. 3.11(c). The collapsing of the membrane to the lower electrode after being traveled more than  $(1/3)g_o$  can be explained in terms of the dramatic increase in the electrostatic force at certain biasing voltage, so-called pull down voltage (Fig. 3.11(a)), that compared to the elastic force (mechanical restored force) induced on the bridge. This elastic force is a self-induced mechanical force that tries to restore

the bridge to its original position. The stable position of the membrane reaches when the electrostatic force balances with mechanical restored force.



(a)



(b)

Figure 3.10: (a) The deformed membrane at different values of applied voltage, (b) Electrostatic force density distribution with applied voltage equals to the pull down value.

## 3.2 Results and Discussions

In the verification process, some standard fixed-fixed beam bridge RF MEMS shunt-capacitive switches are simulated and compared with the published data [23, 63, 15]. The pull down voltage calculated by the present algorithm is compared with the measured values reported in those citations and with those calculated using the 1-D

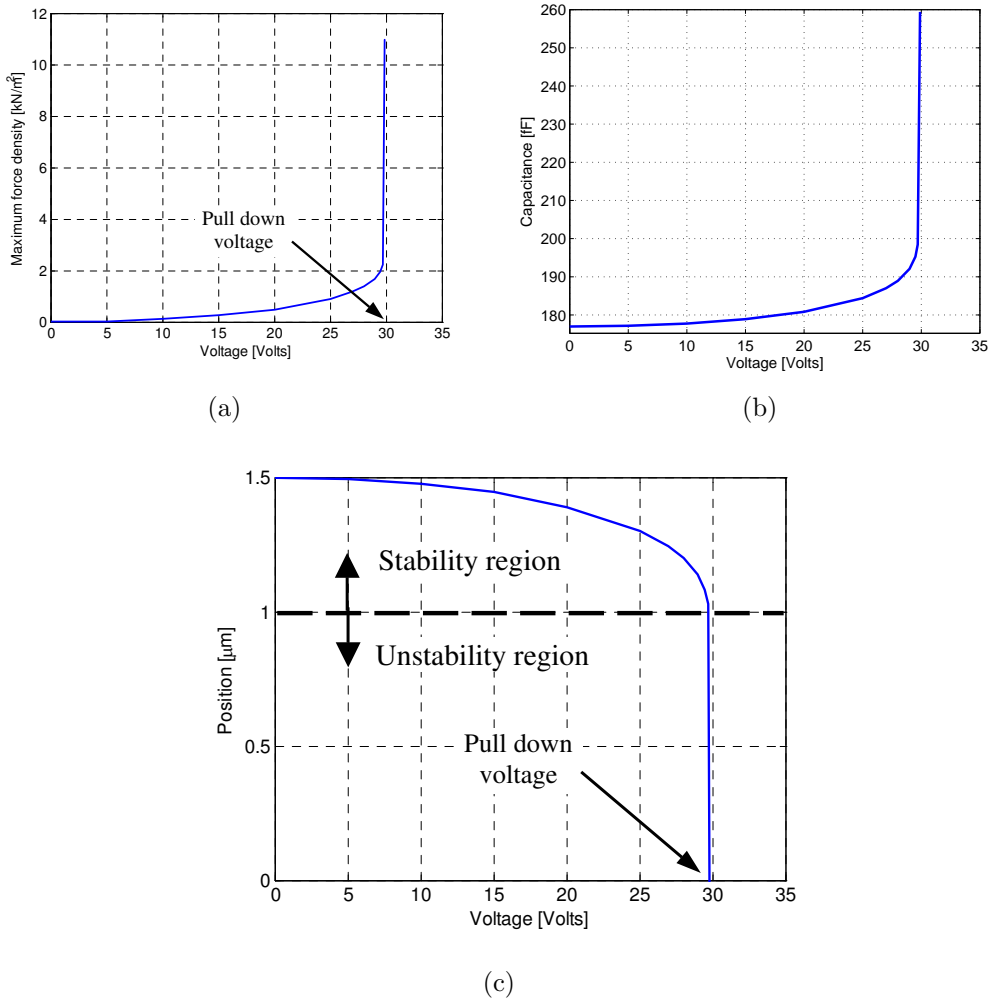


Figure 3.11: (a) Electrostatic force density induced on the bridge center node versus the applied voltage, (b) Gap capacitance versus the applied voltage, and (c) Position of the bridge center node in terms of the applied voltage, all for the switch dimensions of that reported in [23].

and 2-D models were introduced in [23] and in the last chapter, respectively. The comparison results are summarized in Table 3.2. As an example here, the shunt-capacitive RF MEMS switch reported in [23] is modeled using our approach and the computed pull down voltage was found to be very closed to the measured value, ( $V_{pi} = 29.9$  and 30 Volts modeled and measured, respectively). The Young's modulus  $\mathbf{E}$  of the membrane in our calculations was 70 GPa and the residual stress was 20 MPa. The number of cells in the mesh in the  $x$ ,  $y$ , and  $z$  directions were 45, 40, and 58, respectively have been used. To achieve a 0.05 % error in the potential computation, a maximum number of iterations of 500 in the potential computation procedure are used.

Figure 3.10(a) shows the shape of the deformed membrane at different values of applied voltage for a shunt-capacitive RF MEMS switch, geometrically was similar

to that given in [23]. The electrostatic force density distributed on the membrane at applied voltage equals to the pull down value is illustrated in Fig. 3.10(b). The maximum force density induced at the bridge center node in terms of the applied voltage is illustrated in Fig. 3.11(a), which explains how the switch gets pull down. The gap capacitance and the position of bridge center node in terms of the applied voltage are illustrated in Figs. 3.11(b) and 3.11(c), respectively. The CPU time, which is required to get a stable membrane shape when the switch is actuated with certain voltage on a PC with AMD opteron processor 250 with 3.39 GHz and 2.0 GB RAM is 3.824 minutes. The input required accuracy for the potential computation is 0.1 %.

Table 3.1: Comparison of the pull down voltage (Volts) between the 1-D, 2-D, and 3-D models ( $\sigma = 20$  MPa).

Switch's geometry	1-D Model [23]	2-D Model [66]	3-D Model [Present]	Reported values
Goldsmith [15]	48.7	47.9	36.2	30-50 [15]
Muldavin [23]	39.4	34.4	29.9	20-30 [23]
Rebeiz [63]	51.7	47.5	39.2	35-39 [63]

### 3.3 Conclusion

In the present chapter, a three-dimensional electrostatic-mechanical coupled model for the fixed-fixed beam bridge RF MEMS shunt-capacitive switches has been introduced. A simulation program is developed to determine the deformation of the bridge as a function of the actuation voltage. The electrostatic model is based on solving the integral form of Gauss's law in a 3-D Cartesian coordinates system using the central difference approximation for the derivatives. An efficient iterative procedure is employed for the solution of the potential distribution. The algorithm is very efficient to determine the pull down voltage of the RF MEMS shunt-capacitive switches. However, it can be used for other types of RF MEMS structures. The developed algorithm and the presented program are capable to determine the bridge deformation, pull-in voltage and to investigate the effect of source fluctuations on the switch performance efficiently. The developed algorithm and the presented program proved that they can be easily integrated in the computer-aided design tools for RF MEMS switches saving a great deal of CPU time allowing the designer free to gain valuable physical insight while conveniently and quickly exploring a wide design space.

# Chapter 4

## Design and Optimization of RF MEMS Switches

In the previous chapters we concerned ourselves with a purely theoretical modeling of the RF MEMS switches. In the current chapter we deal in detail with design and circuit aspects of the RF MEMS switches. Two different RF MEMS switch designs are investigated and optimized based on numerical experimentations technique using 3-D electromagnetic (EM) and circuit simulators. The first one is a  $\pi$ -configuration RF MEMS switch for high isolation and wideband applications. It is constructed using the standard fixed-fixed beam bridge shunt-capacitive and series-resistive RF MEMS switches connected in a  $\pi$ -configuration. The second one is a single-pole three-throw (SP3T) RF MEMS switch for phased arrays and switching networks for satellite communication applications. For both switches, the electrical circuit model is studied for more understanding and for the optimization purpose.

### 4.1 $\pi$ -Configuration RF MEMS Switch

The conventional RF metrics characterizing MEMS switches are: 1) The insertion loss in the ON-state; 2) The isolation (i.e.  $1/|S_{21}|$ ) in the OFF-state; and 3) The return loss (i.e.  $1/|S_{11}|$ ) in both states. During the course of this study, efforts are done to improve these metrics. In other words, achieving high isolation in the OFF-state and low insertion and return losses in the ON-state. The complexity of the proposed structure here is much less than that of different researchers, who tried to improve the isolation in the OFF-state by using multi-switch architectures [21, 18, 67]. The proposed switch is in the fabrication process, so that the demonstrated results are based on numerical experimentations using 2.5D EM simulator (Sonnet software [68]). In many applications, a wider band and a higher isolation than that offered by single switches are required. In [21] a network of four parallel switches has been designed. While in [18, 67], three alternative structures to achieve such a goal are proposed, namely, two MEMS bridges, cross and series-shunt switches. In this contribution,

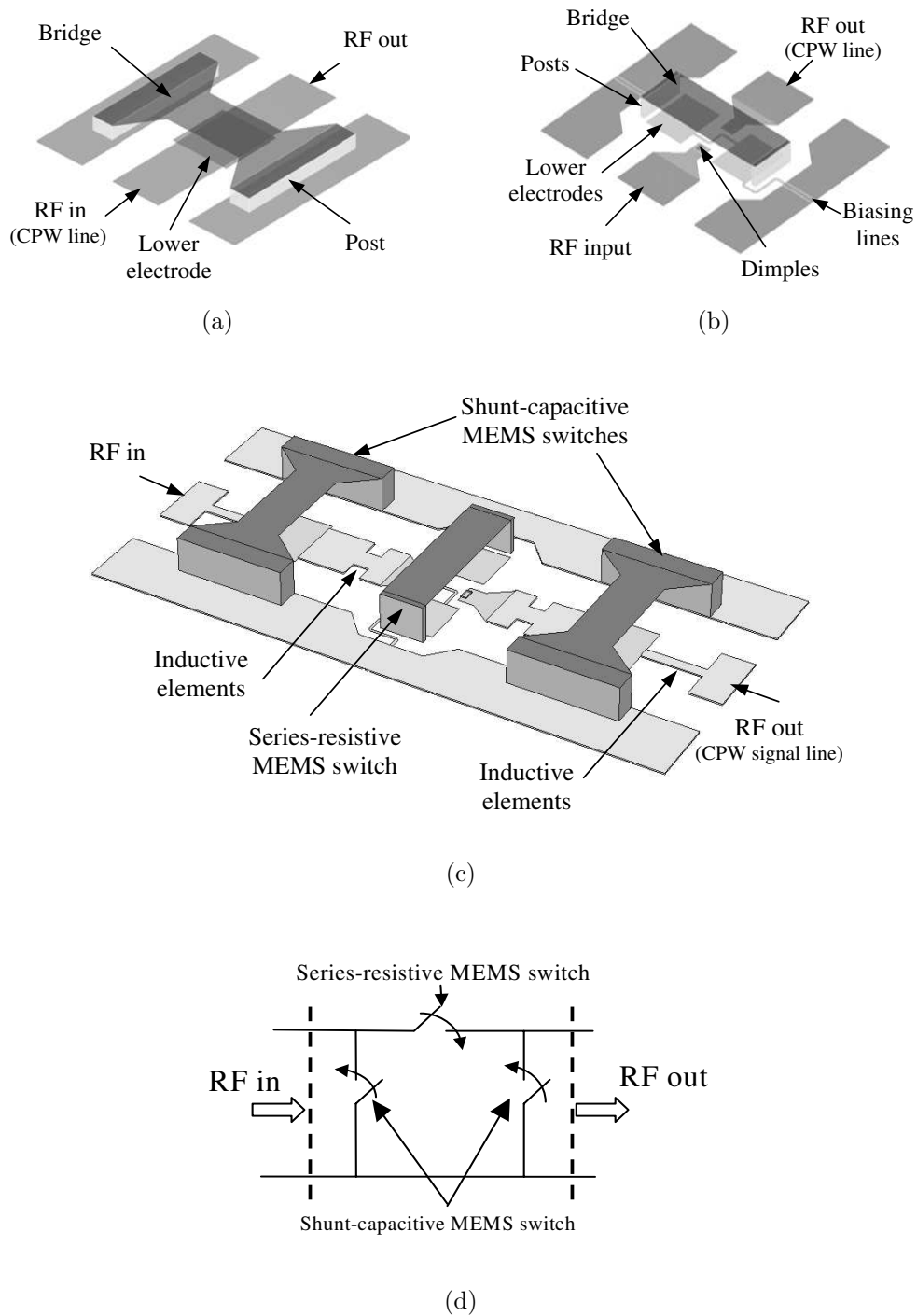
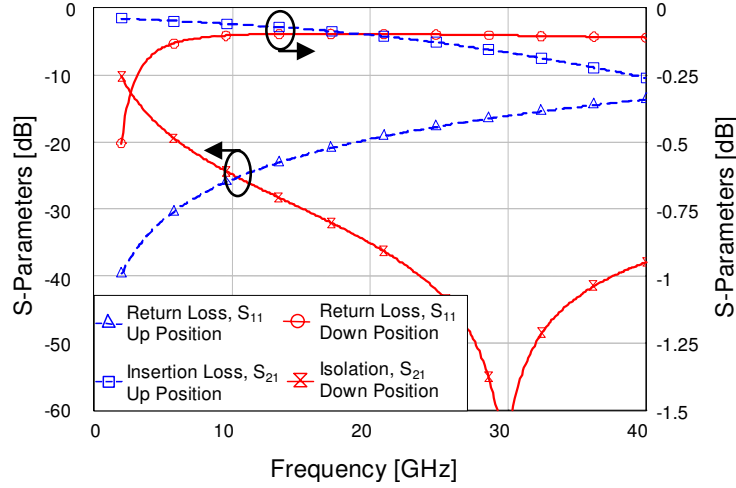
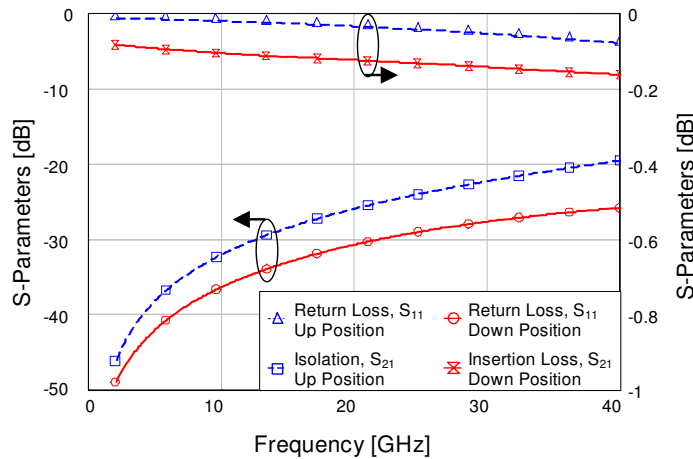


Figure 4.1: Schematic diagram of (a) shunt-capacitive MEMS switch, (b) series-resistive MEMS switch, (c)  $\pi$ -configuration RF MEMS switch, and (d) Equivalent circuit topology for the  $\pi$ -switch.

depending on the filter theory, a series-shunt combinations as a  $\pi$  configuration as shown in Fig. 4.1 are arrange to achieve that request.



(a)

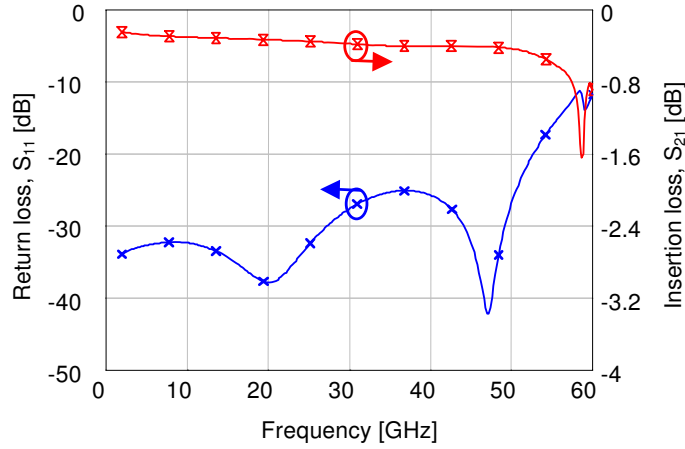


(b)

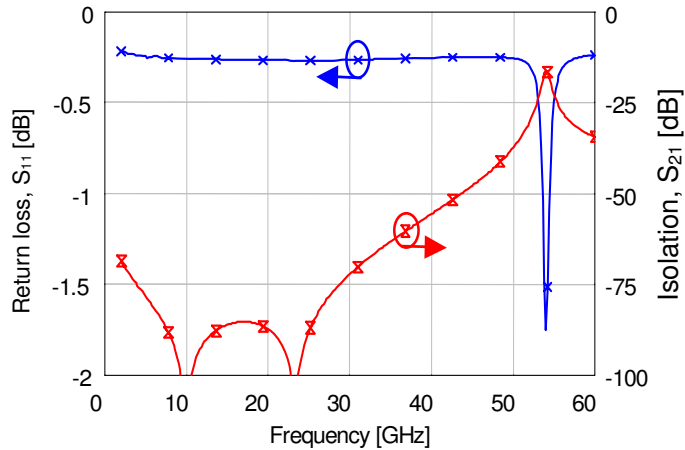
Figure 4.2: EM simulations for the single RF MEMS (a) Shunt-capacitive and (b) Series-resistive switches at Up and Down states.

#### 4.1.1 Design and Description

A  $\pi$ -type RF MEMS switch is constructed as a shunt-capacitive, series-resistive and shunt-capacitive switches connected in a cascaded configuration as illustrated in Fig. 4.1. High isolation at the high frequency portion of the band is provided by the shunt arm while at the low frequency portion this is achieved by the series arm. The shunt arms are constructed using the standard shunt-capacitive RF MEMS switch, shown in Fig. 4.1(a). While, the series arm is constructed using the series-resistive RF



(a)



(b)

Figure 4.3: EM simulations for the  $\pi$ -structure RF MEMS switch at (a) ON and (b) OFF states.

MEMS switch, shown in Fig. 4.1(b). Both series and shunt switches are constructed as fixed-fixed beam architecture. Therefore, they are not very sensitive to the residual stress in the supporting beam. The fixed-fixed beam is usually easy to fabricate and does not require special processing compared to the dielectric beams or the thick low-stress electroplated cantilever [67]. Both shunt and series arms are fabricated simultaneously using the same steps, as the fabrication processes of both switches are compatible. These switches first are designed and optimized using a 3-D EM simulator. The EM simulations of the single separate shunt and series RF MEMS switches are depicted in Figs. 4.2(a) and 4.2(b), respectively. The EM simulations of the optimized  $\pi$ -type MEMS switch at ON and OFF states are shown in Fig. 4.3. The optimized ON-state return loss ( $S_{11}$ ) is a minimum of 25 dB from dc to 50 GHz, and a minimum of 12 dB up to 60 GHz. The insertion loss ( $S_{21}$ ) is less than 0.4 dB up

to 50 GHz. The OFF-state isolation ( $S_{21}$ ) is greater than 40 dB up to 50 GHz. The isolation is only degraded above this frequency due to the existence of a resonance at 54 GHz. The  $\pi$ -switch is built on high resistivity silicon substrates ( $> 5 \text{ k}\Omega\cdot\text{cm}$ ) of  $630 \text{ }\mu\text{m}$  thickness and 11.9 relative permittivity, with a  $1 \text{ }\mu\text{m}$ -thick of silicon dioxide buffer layer ( $\epsilon_r = 3.9$ ). The switch circuit is constructed on the top of the buffer layer using a  $3 \text{ }\mu\text{m}$ -thick aluminum coplanar waveguide line with dimensions of G/W/G =  $80/120/80 \text{ }\mu\text{m}$  corresponding to a characteristic impedance of  $50\text{-}\Omega$ . The bottom electrode of the switch is built using  $0.3 \text{ }\mu\text{m}$  of refractory metal. This film provides a high value of the conductivity, which leads to the low loss performance. In addition, it achieves a good contact between the membrane and the lower electrode due to its smooth surface finish. Therefore, it minimizes any air gap between them, which results in a maximum down-state capacitance for the shunt branch. A thin film of silicon nitride of a  $0.1 \text{ }\mu\text{m}$  thickness is placed on the top of the lower electrodes to prevent the dc control signal from shorting the supply during the switch actuation. However, it allows the RF signal to capacitively couple the upper membrane with the lower electrode. The metallic switch membrane has length, width, and thickness of  $280, 80, \text{ and } 0.6 \text{ }\mu\text{m}$ , respectively, made of gold. It suspenses above the lower-electrode with initial height of  $g_o = 2.5 \text{ }\mu\text{m}$ . This membrane is made of a high conductivity metal, which produces low RF resistance and good mechanical properties. The pull-down electrodes are connected using high resistivity bias lines up to the edge of the ground plane of the CPW line. The silicon nitride layer is also used to isolate the bias lines from the ground plane. The isolation in the series switch is achieved by an air gap of  $60 \text{ }\mu\text{m}$  width in the signal line underneath the membrane. Dimples with  $10 \times 20 \text{ }\mu\text{m}^2$  area are deposited on the RF signal line underneath the membrane to achieve a good metallic contact when the series switch is actuated.

### 4.1.2 Numerical Experimentations

The radio frequency responses shown in Fig. 4.3 of the proposed  $\pi$ -type RF MEMS switch are achieved by an iterative optimization technique. Some of these trials are depicted in Fig. 4.4. A transmission line of  $230 \text{ }\mu\text{m}$  length is used to connect the shunt and the series arms. This structure produces good isolation over a wide bandwidth. The very high isolation ( $> 80 \text{ dB}$ ) is hard to obtain in practices due to the noise floor effect. Our target is to improve the return loss while preserve a high isolation over a wide band. This is achieved by incorporating a matching network between the series and the shunt arms. Fig. 4.4(a) shows the inserting of inductive elements between the series and shunt arms with a length of  $\lambda/8$  at 20 and 40 GHz and changing their widths,  $w_1$  and  $w_2$ , respectively. The S-parameters of inserting those elements in terms of changing their widths are illustrated in Fig. 4.4(b) and 4.4(c), respectively. Another inductive element is inserted at the input and output ports with an electrical length of  $\lambda/8$  at 40 GHz as depicted in Fig. 4.4(d). This figure also shows controlling

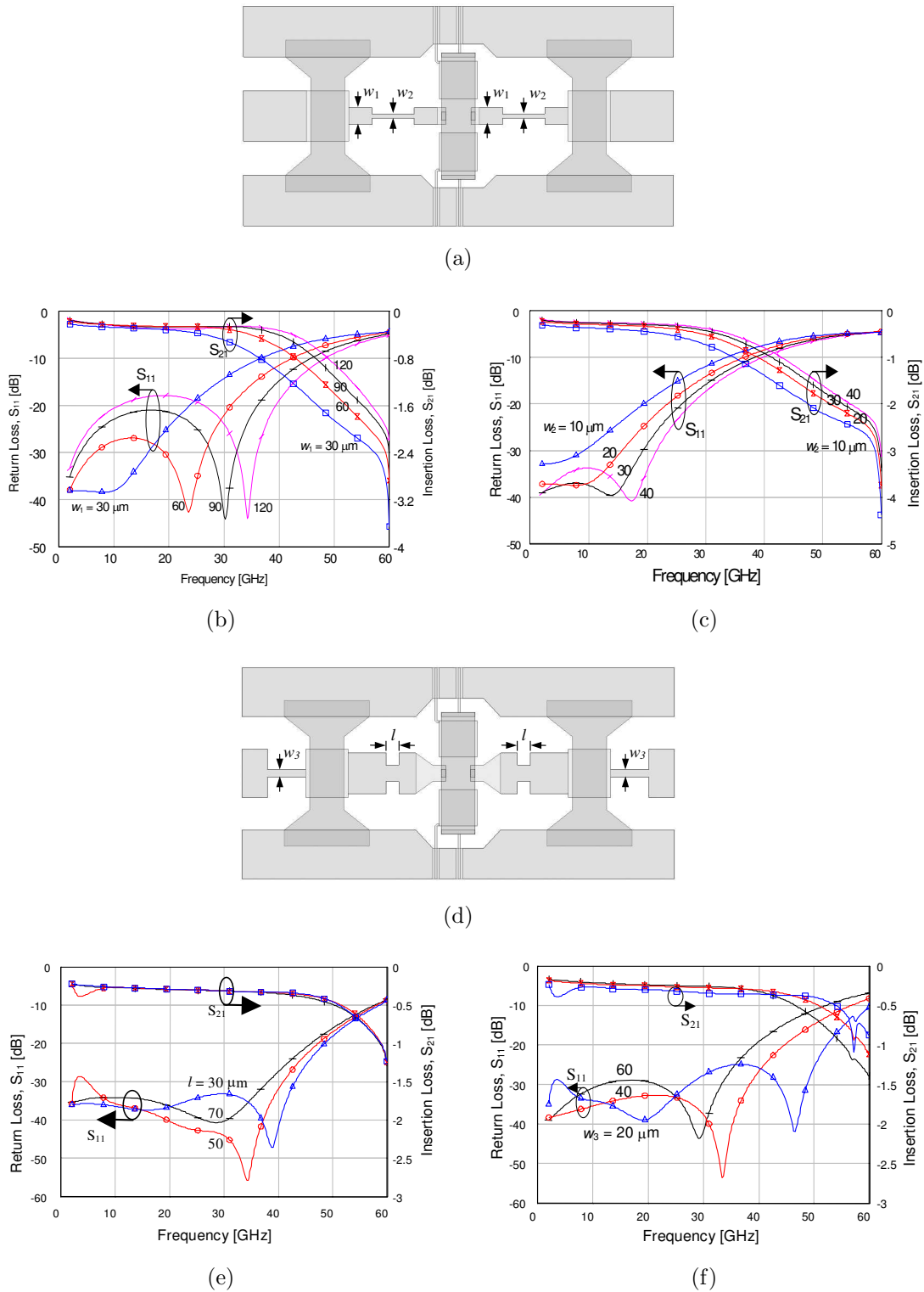


Figure 4.4:  $\pi$ -switch optimization based on numerical experimentations (a) Inserting inductive elements between the shunt and series arms, S-parameters for changing (b)  $w_1$ , (c)  $w_2$ , (d) Inserting inductive elements at the input and output ports and controlling the length of the inner inductive elements, S-parameters for changing (e)  $l$ , and (f)  $w_3$ .

length,  $l$  of the inner inductive element. The insertion and return losses versus the outer inductive element's width and the inner element's length while maintaining its width at  $40 \mu\text{m}$  are illustrated in Figs. 4.4(e) and 4.4(f), respectively. In all cases, the isolation at the OFF-state is not affected by inserting those inductive elements. This is because the isolation is controlled by the gap width in the series resistive switch at low frequencies and by the down-state capacitance of the shunt switch at high frequencies. It is sufficient to control the width of the inductive elements to obtain a very low return loss for a selected frequency range within the band of frequencies without disturbing the isolation. The power handling capability of the switch could be affected by reducing the width of the inductive elements, which puts a limitation on how much narrow width we can reach?

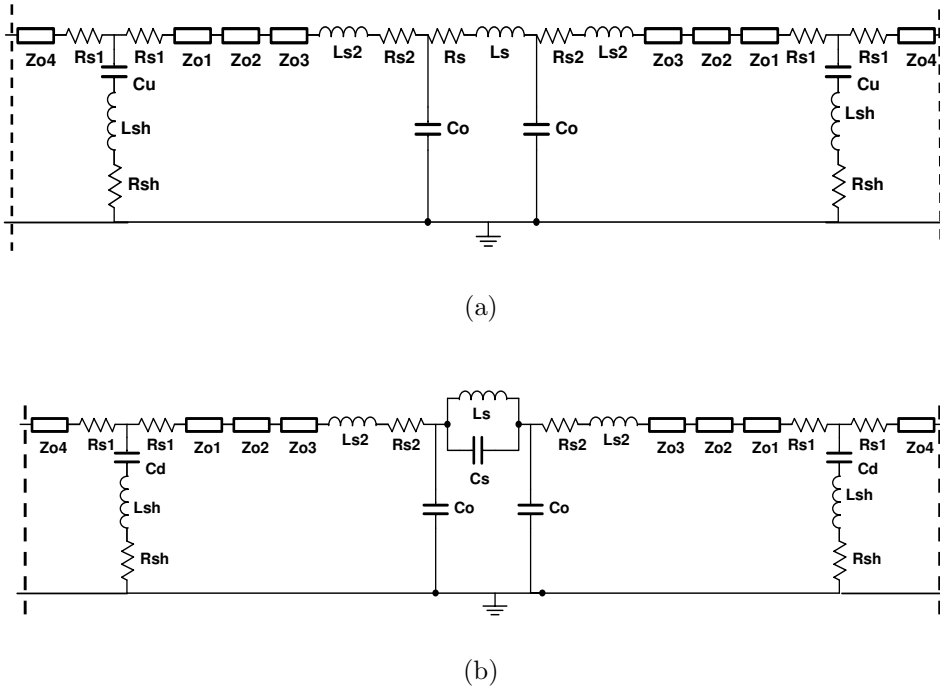
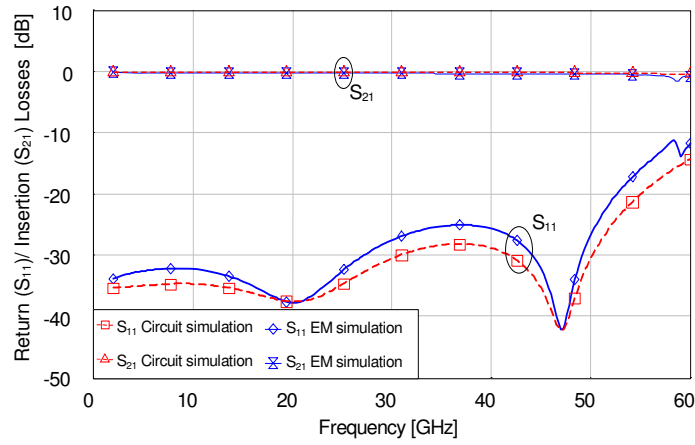


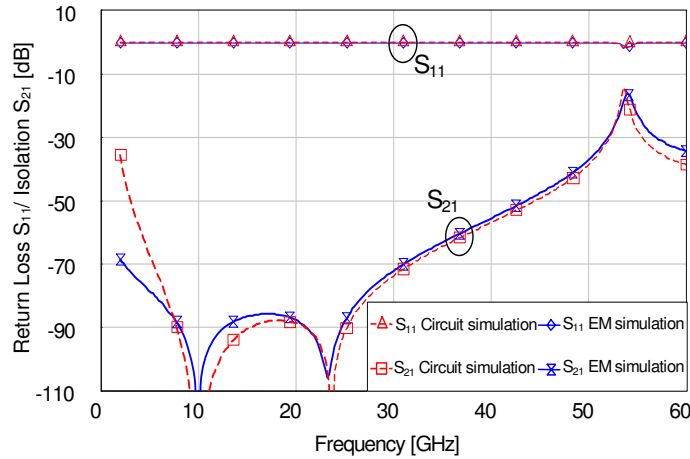
Figure 4.5: Equivalent circuit model for the  $\pi$ -structure RF MEMS switch at (a) ON state and (b) OFF state.

### 4.1.3 Circuit Modeling

The  $\pi$ -switch is first characterized using the 3D EM simulator to extract its S-parameters at both ON and OFF-states. In addition, the EM circuit simulator (Microwave Office software [69]) is used to find out an appropriate equivalent circuit for the  $\pi$ -switch. The shunt arm is modeled by one lumped CLR branch, which represents the bridge with the capacitance changing its values from up-state to down-state. The series arm is modeled by a series capacitance at the up position (OFF-state) and



(a)



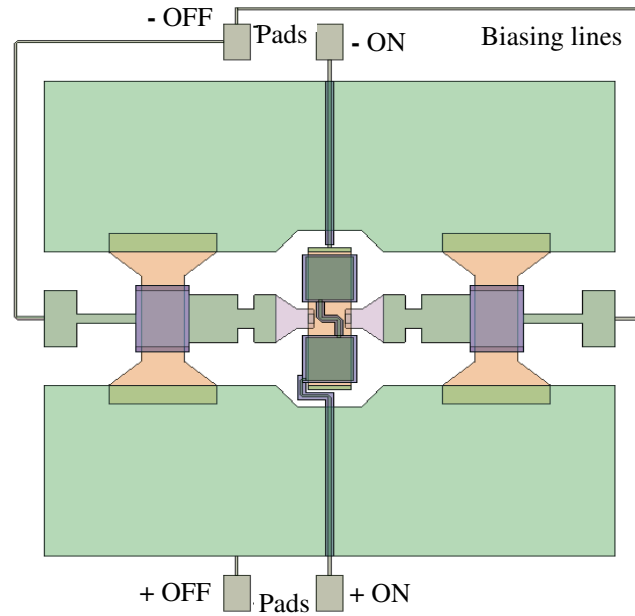
(b)

Figure 4.6: Equivalent circuit and EM simulations of the  $\pi$ -type RF MEMS switch at (a) ON state and (b) OFF state.

by a series inductance and resistance branch at the down-position (ON-state). A combination of series resistance and inductance models the taper in the series arm. The distances between the series and the shunt arms are modeled by transmission lines of different characteristic impedances. The electrical circuit models for the proposed  $\pi$ -type RF MEMS switch at ON and OFF states are shown in Figs. 4.5(a) and 4.5(b), respectively. Those circuit models are used to fit, as close as possible, the S-parameters of the switch, which are obtained using the EM simulator. The modeled and simulated results for both ON and OFF states are shown in Figs. 4.6. Good matching between the circuit and EM simulations assure that the proposed equivalent circuit model could describe the  $\pi$ -type RF MEMS switch with sufficient accuracy.

#### 4.1.4 Switch Layout

For the fabrication process a set of mask sequences for the switch is designed and these masks are shown in Fig. 4.7. Mask no. 1, deposits the lower electrodes of the shunt capacitive switches. Mask no. 2, forms the bias lines, pads, and the lower electrodes of the series switch. Mask no. 3, deposits the dielectric layer ( $Si_3N_4$ ) to isolate the bias lines and lower electrodes of both switches when the bridges are actuated. Mask no. 4 is to grow up the coplanar line and the posts for all bridges. Mask no. 5 defines the membranes for the RF MEMS switch. The proposed  $\pi$ -configuration RF MEMS switch needs five masks in total. All fabrication processes are compatible with the MMICs technology.



(a) Layout of the  $\pi$ -reconfigurable RF MEMS switch

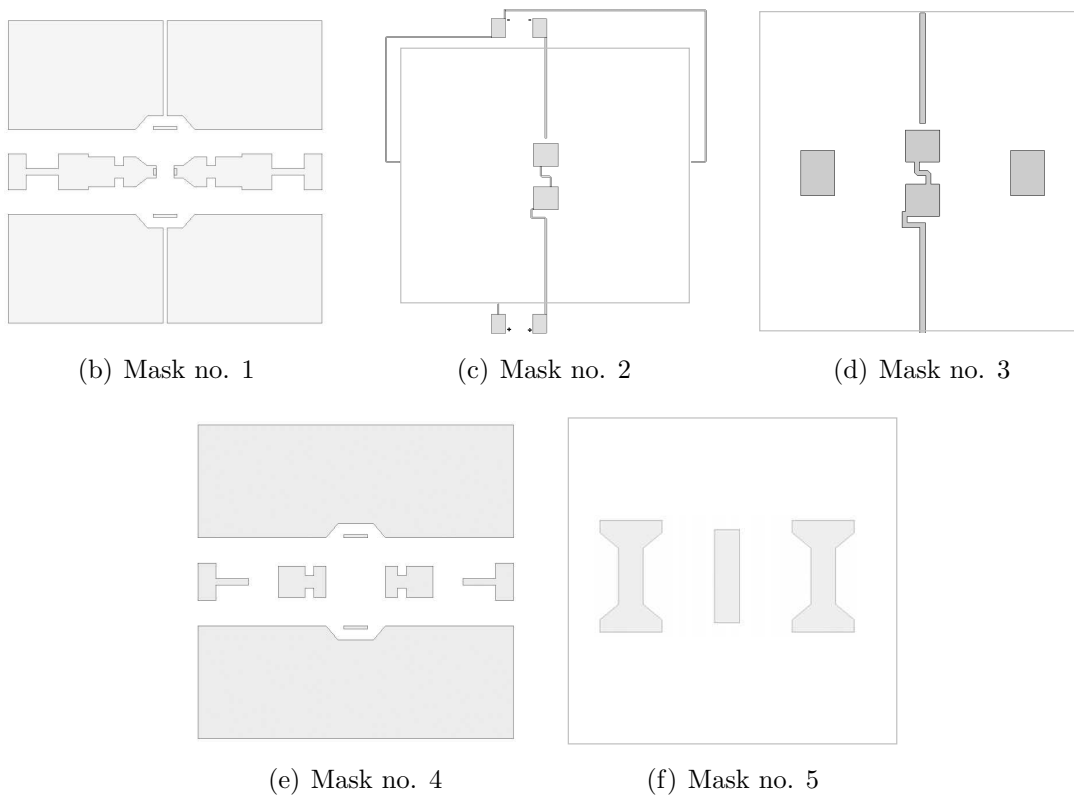


Figure 4.7: Set of the mask sequences for the  $\pi$ -configuration RF MEMS switch.

## 4.2 SP3T Wideband RF MEMS Switch

The development of RF MEMS switches has attracted a great deal of interest [63] during the last decade. However, most of the research has been directed to develop single-pole, single-throw (SPST) switches. To the best of the author's knowledge, there is a limited reported work for the multi-port RF MEMS switch. In [70] a single-pole, double-throw (SPDT) switch has been designed for X- and K-band frequency ranges, based on a shunt-capacitive switch. That switch exhibits a typical of 40 dB isolation at both 7 and 20 GHz, and an insertion loss of 0.95 dB at 7 GHz and of 0.69 dB at 20 GHz. In [71] a SP3T switch has been implemented in hybrid-form where the beams (cantilever beams) are micromachined separately and then integrated on an alumina substrate using flip-chip technology. It exhibits a typical of 0.5 dB insertion loss at 16 GHz and of 20 dB isolation at 18 GHz.

Some application areas of MEMS switches including single-pole, N-throw (SPNT) switches are in phased arrays, switching networks for satellite communications and portable unites and base stations for wireless applications. Using MEMS switches to replace solid-state switches in SP3T arrangement has many advantages as stated above. In addition, it can be implemented in a more compact area and does not require a matching network when integrated in MMICs circuits. Through this work, an SP3T RF MEMS switch is presented. Electromagnetic simulations in addition to circuit modeling are used to design and optimize the switch. Three series-configured, resistive-contact RF MEMS switches based on fixed-fixed beam architecture are used to construct the complete SP3T switch. The SP3T switch exhibits an insertion loss of about 0.45 dB, a minimum of 22 dB return loss, and a minimum isolation of 20 dB between the different ports in the frequency range from dc to 25 GHz. The proposed switch is currently in the fabrication process. So that, the demonstrated results are based on numerical experimentations only.

### 4.2.1 Design and Description

Figure 4.8(a) illustrates a single-pole, three-throw (SP3T) RF MEMS switch structure. The SP3T switch is a four-port device designed in coplanar waveguide environments to be easily integrated with IC's circuits. The input port is connected to a 50- $\Omega$  characteristic impedance CPW line with dimensions  $G/W/G$  of 80/120/80  $\mu\text{m}$ . The CPW lines are made of aluminum with thickness of 3  $\mu\text{m}$ . The series-resistive RF MEMS switches are built on the CPW lines with an initial gap height of 3  $\mu\text{m}$ . The isolation of the switch is achieved by an air gap in the RF signal lines of width 80  $\mu\text{m}$  underneath the membrane. A good contact between the membrane and the RF signal line at down-position can be achieved with help of dimples with an area of  $10 \times 20 \mu\text{m}^2$  that are employed on the RF signal line underneath the membrane. The bias lines and the lower electrodes are made of high resistivity metal (NiCr) with a sheet resistance of 1400  $\text{k}\Omega/\text{square}$ . The membranes are made of gold with thickness



of  $0.6 \mu\text{m}$  and  $300 \times 100 \mu\text{m}^2$  area. The tapers in the RF signal lines under the membranes helps a lot to reduce the parasitic capacitance of the series switch while it is in the up position and leave more space to increase the lower electrodes, which in consequence reduce the required actuation voltage. An inductive element with length of  $120 \mu\text{m}$  is used to connect it to the junction. This junction is branched into the three output ports using inductive elements of  $480 \mu\text{m}$  length for each. A series-resistive switch is constructed on the CPW line of each of the output ports. This switch is used to open or short the center conductor of the CPW line to the output port. These series switches are constructed with fixed-fixed beam architectures. When the series switch is actuated the RF input signal passes to its port. On the other hand, the RF signal is reflected away from the arm containing the non-actuated switch.

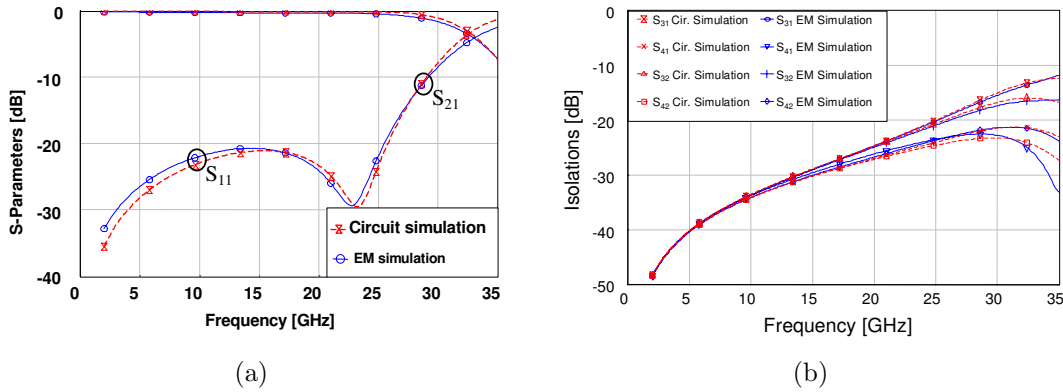


Figure 4.9: EM and equivalent circuit simulations for the SP3T RF MEMS switch in case of port 2 is ON while ports 3 and 4 are OFF, (a) Return and insertion losses, (b) Different ports isolations.

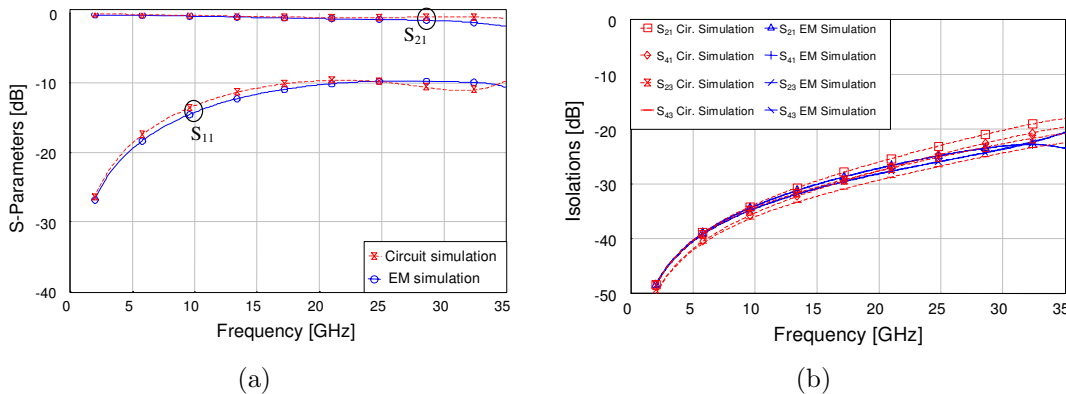


Figure 4.10: EM and equivalent circuit simulations for the SP3T RF MEMS switch in case of port 3 is ON while ports 2 and 4 are OFF, (a) Return and insertion losses, (b) Different ports isolations.

### 4.2.2 EM Simulation and Circuit Modeling

A numerical experimentation is applied to optimize the switch structure shown in Fig. 4.8(a). The radio frequency performance of the SP3T switch is characterized over a wide frequency range from dc to 40 GHz using a 2.5D electromagnetic simulator (Sonnet Suite). In addition, the corresponding circuit model is studied as well in order to get more understanding about its RF performance. The circuit model is shown in Fig. 4.8(b). Fig. 4.9 illustrates a comparison between the equivalent circuit model and the EM simulation results obtained from the EM simulator in the case where port 2 (or 4) is in the ON-state and both ports 3 and 4 (or 3 and 2) are in the OFF-state, keeping in mind the symmetry of the SP3T switch. Fig. 4.10 demonstrate the S-parameters when port 3 is in the ON-state and both ports 2 and 4 are in the OFF-state.

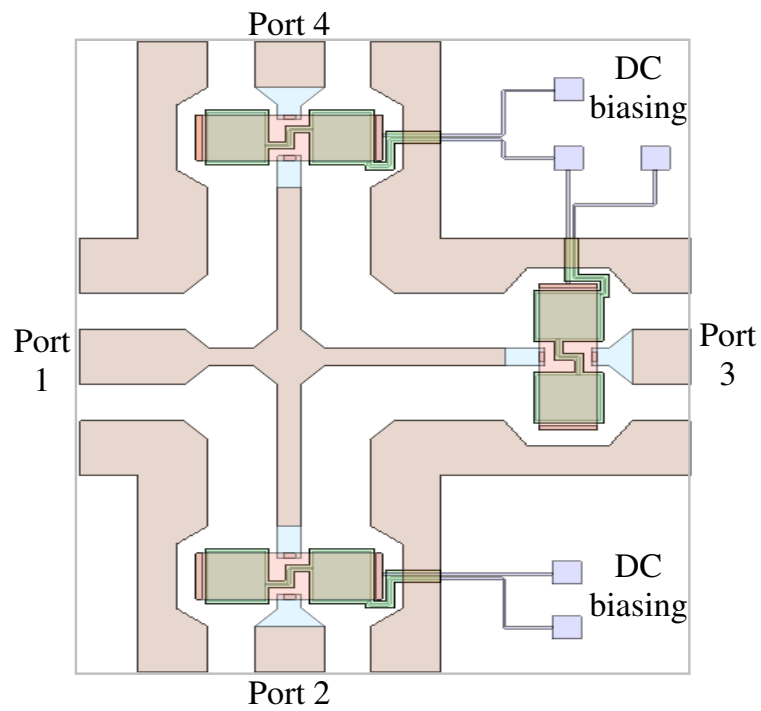
### 4.2.3 Switch Layout

For the purpose of fabrication processes, the set of mask sequences are designed as shown in Fig. 4.11. Mask no. 1 defines the CPW line and the slots for the bias lines and the dimples. Mask no. 2, is for deposition of the bias lines, pads, and the lower electrodes of the series switches. Mask no. 3 deposits the dielectric layer ( $Si_3N_4$ ) to isolate the bias lines and the lower electrodes of the series switches. Mask no. 4, is for deposition of the metal for the CPW lines and the posts for the bridges of the series switch. Mask no. 5 defines the bridges of the series switches. The switch fabrication process is compatible with conventional CMOS processes.

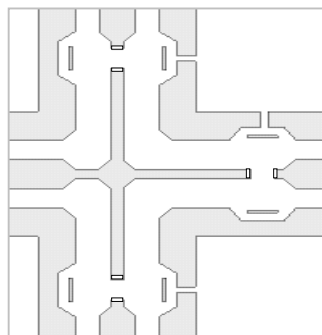
## 4.3 Conclusion

Based on numerical experimentation technique using 3-D EM and circuit simulators, two type of RF MEMS switches have been designed and optimized. The first one is a  $\pi$ -configuration RF MEMS switch for high isolation and wideband applications. It results in a minimum return loss of 25 dB in the range from dc to 50 GHz, and of 12 dB up to 60 GHz along with a minimum insertion loss of 0.4 dB up to 50 GHz in the ON-state. At the OFF-state the isolation is greater than 40 dB up to 50 GHz. To the best of our knowledge, this is the highest isolation reported so far for RF switches over such a wide frequency band. This switch is suitable for applications where a high isolation, low loss and good matching are required.

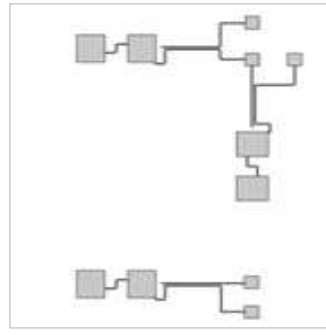
The second one is a single-pole, three-throw RF MEMS switch configuration for phased arrays, switching networks for satellite communications and portable unites applications. It consists of three series-configured, metal-to-metal contact, RF MEMS switches based on fixed-fixed beam architecture in a coplanar environment. The SP3T switch shows good results: an insertion loss of about 0.45 dB, a minimum return loss of



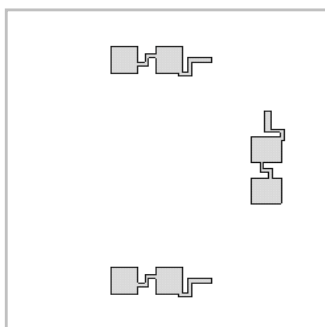
(a) Layout of the SP3T RF MEMS switch



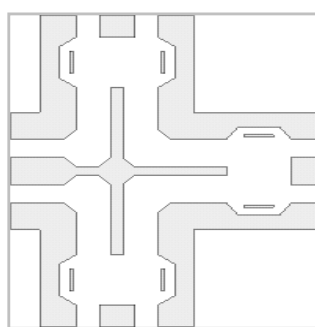
(b) Mask no. 1



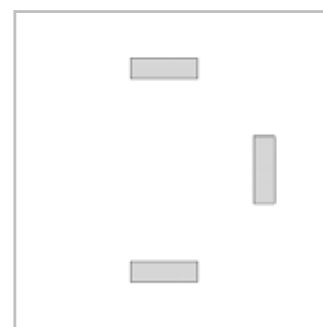
(c) Mask no. 2



(d) Mask no. 3



(e) Mask no. 4



(f) Mask no. 5

Figure 4.11: Set of the mask sequences for the SP3T RF MEMS switch.

---

22 dB, and a minimum isolation of 20 dB between the different ports in the frequency range from dc to 25 GHz have been achieved.

The expected actuation voltage for those switches lies in the range of 20 to 30 Volts depending on the fabrication conditions. The equivalent circuit models for both switches have been also studied for more understanding and optimization purpose. The equivalent circuit and EM simulations agree very well to each other, which validates the proposed equivalent circuit models. The  $\pi$  and SP3T switches have been built on a CPW environment. This makes it easy to integrate them into MICs or MMICs circuits. Both switches need five masks where the fabrication processes are compatible with the MIC's technology.

# Chapter 5

## DGS: Design and Applications

### 5.1 Introduction

Defected ground structures (DGS) add an extra degree of freedom in microwave circuit design. The defect in the ground of planar transmission line (e.g. microstrip, coplanar and conductor backed coplanar waveguides) adds parallel-connected inductor, capacitor, and resistor to the equivalent circuit model of the transmission line [39,72], which leads to a rejection of the signal at a certain frequency determined by the shape and size of the defect. The equivalent circuit can be physically interpreted as follows: The defect increases the path of the current, which induces an inductor. It is also comparable to the wavelength, thus a potential drop occurs across it, which leads to an equivalent capacitance. The resistance  $R$  corresponds to the losses in the defect.

In this chapter two different designs of defected ground structures are introduced. Those two types are simple and can be easily designed to cover a wide range of frequency band. The first one is a 2-D periodic DGS based on the repetition of a unit-cell (standard dumbbell structure) in a simplified and systematic way. The second one is an L-shaped DGS. The L-shaped section can be repeated in series at one or at both sides to prolong the current's path and thus to increase the effective inductance and capacitance of the structure. The proposed structures are designed in CPW environment. However, it can be applied for microstrip technology too. High performance bandstop filters are designed using the proposed DGS structures. The equivalent circuit models for the proposed DGS are studied and the parameters affecting the inductance, capacitance and resistance are separately determined. Several DGS structures are designed, fabricated, and measured for the validation purpose.

### 5.2 2-D Periodic DGS for CPW Line

A two-dimensional periodic dumbbell structure is proposed; the dumbbell structure is added as a unit-cell in a systematic way in both horizontal and vertical directions to

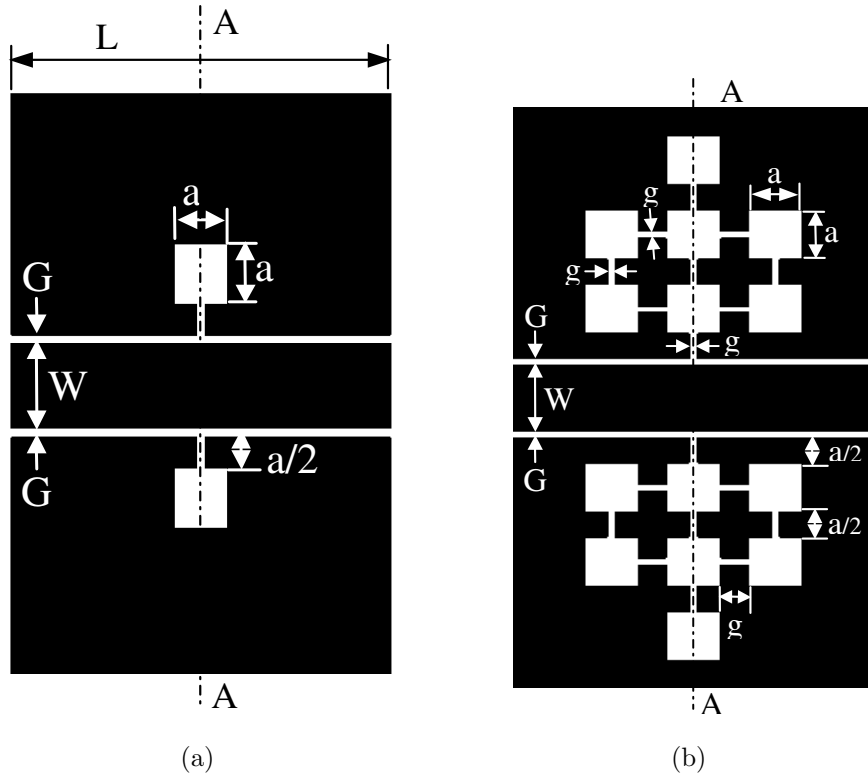


Figure 5.1: Schematic diagram of (a) Standard dumbbell structure, (b) Seven-cells 2-D periodic DGS structure, A-A is the symmetrical axis of the structures.

construct the 2-D periodic DGS. This technique best utilizes the area to get very low stop band frequencies. Design methodology, electromagnetic simulation and equivalent circuit model are presented in the next sections. These are followed by the experimental verification.

### 5.2.1 Structure Design Methodology

The 2-D periodic DGS for CPW structure is based on the standard dumbbell structure, shown in Fig. 5.1(a). The cells are added such that the symmetry along the axes (A-A) of the dumbbell is kept unchanged. Thus, for the two-cells structure, a cell is added above the first cell. For three-cells, two-cells are placed to the left and to the right of the first cell. The same process is applied for larger number of cells. The schematic diagram of seven cells is shown in Fig. 5.1(b). The schematic diagrams of two, three, four, and five-cells are shown in Fig. 5.2, respectively. For the case of seven and eight-cells, we preferred to put them in the third row instead of the first row.

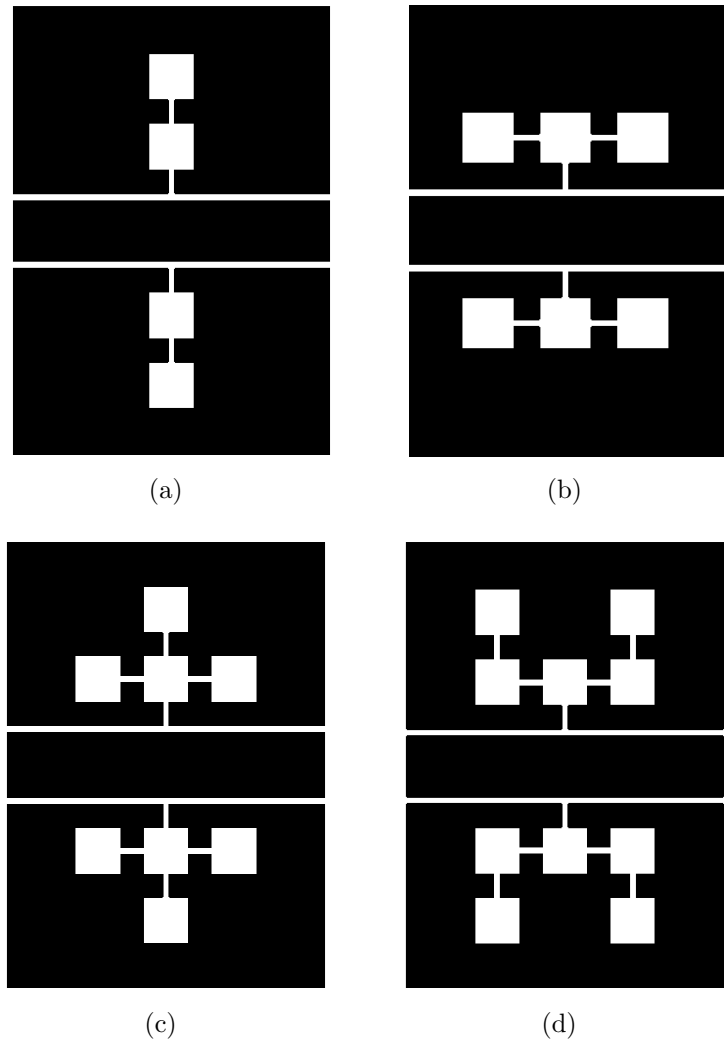


Figure 5.2: The proposed two-dimensional periodic DGS for CPW line (a) two-Cells, (b) three-Cells, (c) four-Cells, and (d) five-Cells.

### 5.2.2 EM Simulation and Circuit Modeling

The unit dumbbell structure was designed for coplanar waveguide line with  $50 \Omega$  characteristic impedance for good RF impedance matching. The CPW has dimensions of  $G/W/G$  equal to  $0.2/2.8/0.2$  mm, where  $W$  is the width of the center conductor and  $G$  is the slot width as shown in Fig. 5.1. The dielectric constant of the substrate is 3.38, its height is 0.813 mm, and the metal thickness is  $35 \mu\text{m}$ . The first step in the design is to optimize the parameters of the unit-cell to get a stop band response centered at a certain frequency, e.g. 12 GHz, with the constraint that the unit-cell has dimensions of  $a \times a$  and it is etched in both ground planes symmetrically at distance  $a/2$  far from the slots of the CPW line. This was achieved using the 3-D EM simulator, "Microwave Studio version 5.0". The optimized dimensions for the unit-cell are:  $a \times a = 2 \times 2$  mm, and a gap of width  $t = 0.2$  mm.

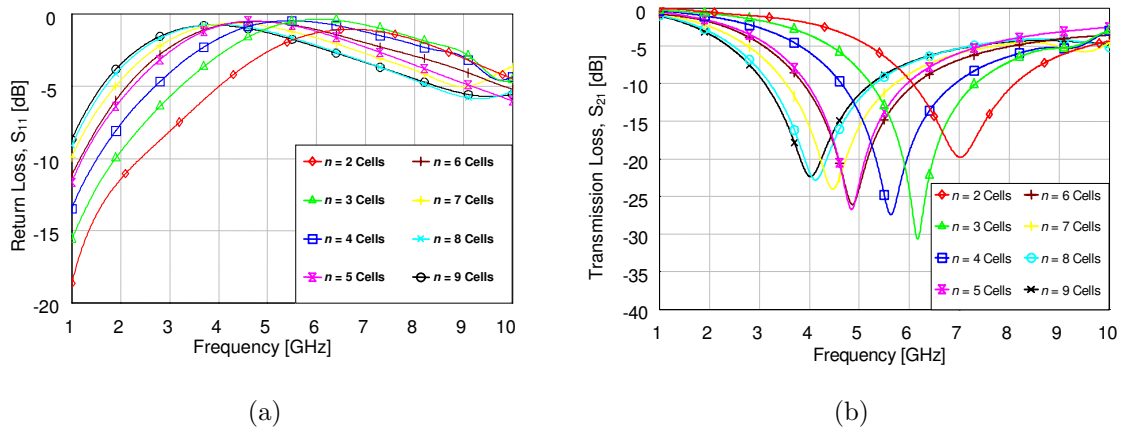


Figure 5.3: RF frequency response for the 2-D periodic DGS with different number of repeated cells (a) Return loss  $S_{11}$ , and (b) Transmission loss  $S_{21}$ .

Two, three, and up to nine-cells are arranged as explained in the previous section, shown in Fig. 5.2. Their performances are investigated using the Microwave Studio EM simulator. The S-parameters of the eight structures are illustrated in Fig. 5.3. The transmission parameter  $S_{21}$  depicts a minimum at a frequency determined by the structure geometry. Its value decreases as the number of cells increase. For  $n = 2$  ( $n$  is the number of cells) this frequency is 7 GHz, while for  $n = 9$ , the frequency is 4 GHz. In all structures, the magnitude of  $S_{21}$  at the resonant frequency is below -20 dB except  $n = 2$ .

The performance of the periodic defected ground structures is modeled using circuit lumped elements. Fig. 5.4(a). illustrates the equivalent circuit model. It consists of a parallel RLC resonance to model the defected region [73] and two sections of transmission lines connected in series at both sides of the resonant circuit. The length of the transmission line is equal to the distance from the center of the basic unit-cell to the reference plane,  $L/2 = 14$  mm, the characteristic impedance is  $50.6 \Omega$  and the effective dielectric constant is 1.885 as determined by the EM simulator. The validation of the equivalent circuit model is depicted in Fig. 5.4(b), where the EM and circuit simulations for a single unit cell are compared. This equivalent circuit model is the same for any number of repeated cells, only the values of the equivalent circuit parameters are varied. Fig. 5.4(c) shows the variation of the equivalent capacitance, inductance, and resistance as a function of the number of cells. The equivalent capacitance is approximately constant independent of the number of cells, while the equivalent inductance increases linearly as the number of cells increases and there are minor changes in the resistance. These results can be interpreted to the structure geometry as follows: As the number of cells increases, the path of the current increases, which increases the value of the inductance linearly since all cells have constant perimeter. The capacitance is mainly determined by the capacitance

of the gap of the first cell, which is kept constant in all iterations. The resistance corresponds to the radiation, conductor, and dielectric losses in the defect.

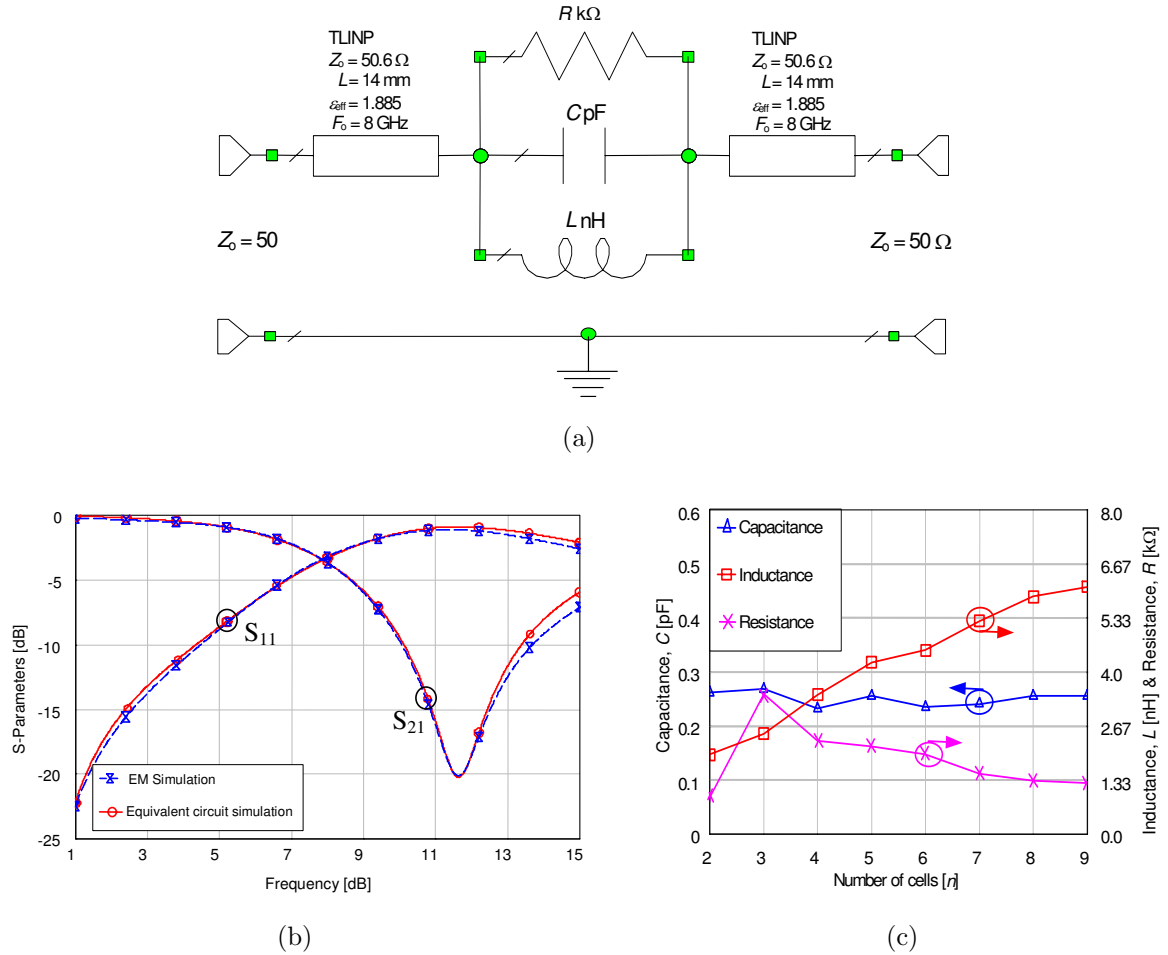


Figure 5.4: The dumbbell-shape DGS structure, (a) Equivalent circuit model,  $L$ ,  $C$ , and  $R$  correspond to the defected region (b) EM and equivalent circuit simulations, (c) Equivalent capacitance, inductance, and resistance versus the number of repeated cells for the 2-D periodic DGS structure.

### 5.2.3 Experimental Verifications

Two, three, and four-cells 2-D periodic DGS structures for CPW line are fabricated on Ro4003c substrate with all design parameters similar to that described in the simulations. The picture of the fabricated structures is shown in Fig. 5.5(a). The structures are measured using 8722D vector network analyzer from 1-10 GHz. Figs. 5.5(b), 5.5(c) and 5.5(d) show the measured S-parameters for the two, three, and four-cells 2-D periodic DGS structures, respectively. Results of the EM and circuit simulations are also shown on the same graph. Excellent agreement is achieved.

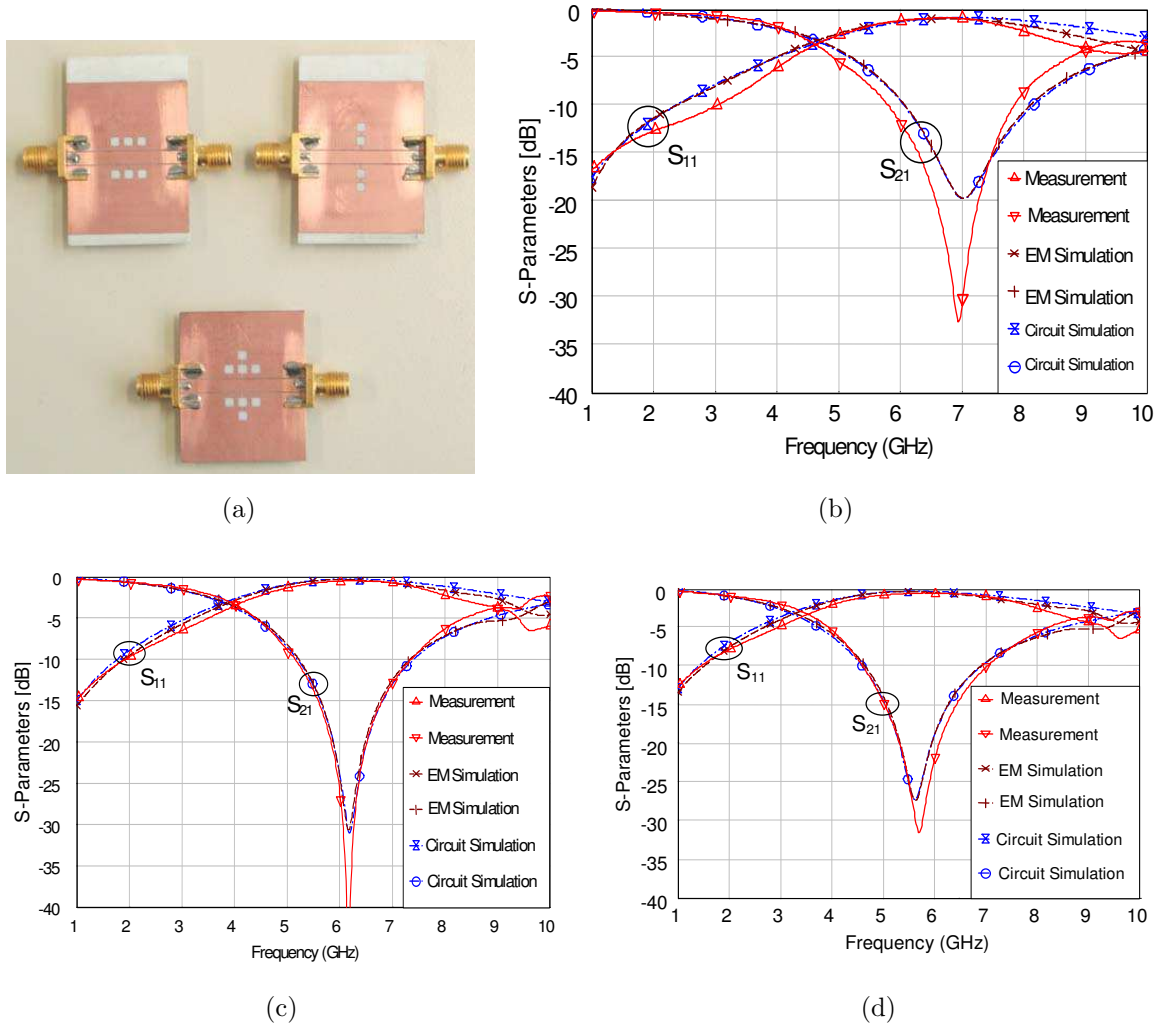
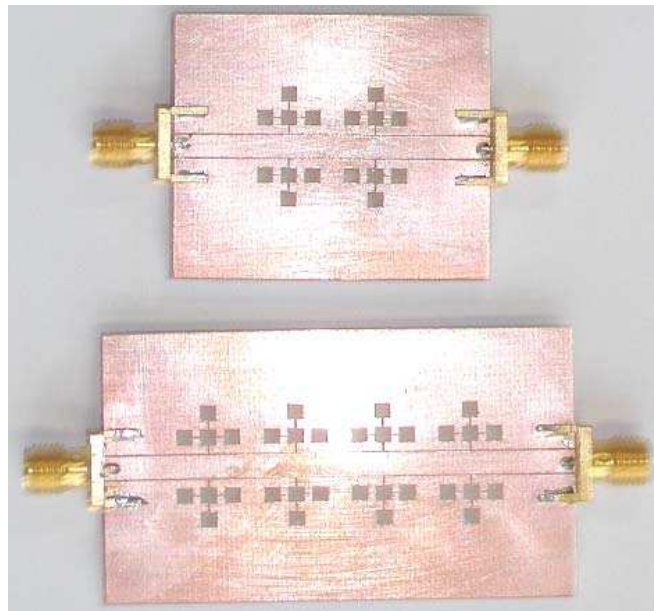


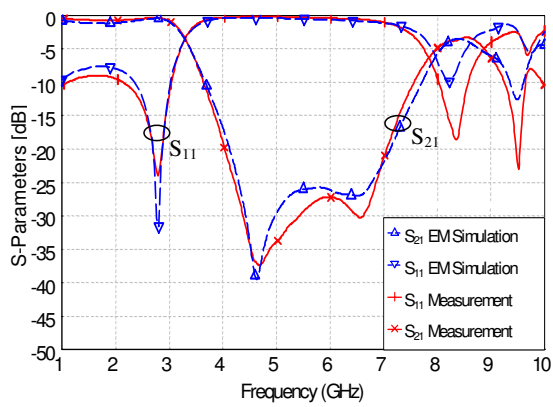
Figure 5.5: (a) Pictures of the fabricated 2-D periodic DGS structures (two, three, and four repeated cells). Measurements, EM and equivalent circuit simulations for the fabricated structures (b) two-Cells, (c) three-Cells, and (d) four-Cells.

### 5.2.4 Cascaded 2-D Periodic DGS for CPW Line

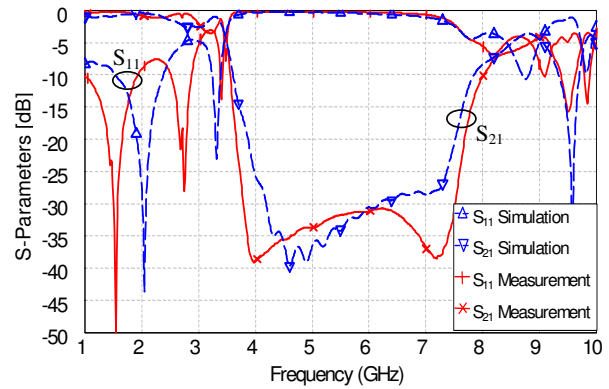
The 2-D periodic DGS is cascaded to get a wide stop band with very sharp edges bandstop filters. The number of cells in the cascaded periodic DGS sections controls the center frequency of the stop band. The number of the cascaded sections and the separation between them control the sharpness and the width of the band. Two, and four sections separated by 3 mm using four-cells 2-D periodic DGS structures are fabricated and measured with 2.5, 3.8 GHz bandwidth and more than 27, 33 dB rejection, respectively. Pictures for the fabricated structures are shown in Fig. 5.6(a). The measured and simulated RF performances are shown in Fig. 5.6(b) and 5.6(c). Good agreement is achieved.



(a)



(b)



(c)

Figure 5.6: (a) Picture of two and four-cascaded sections of four-repeated cells 2-D periodic DGS structures, (b) RF performance for the fabricated two-cascaded sections, and (c) four-cascaded sections.

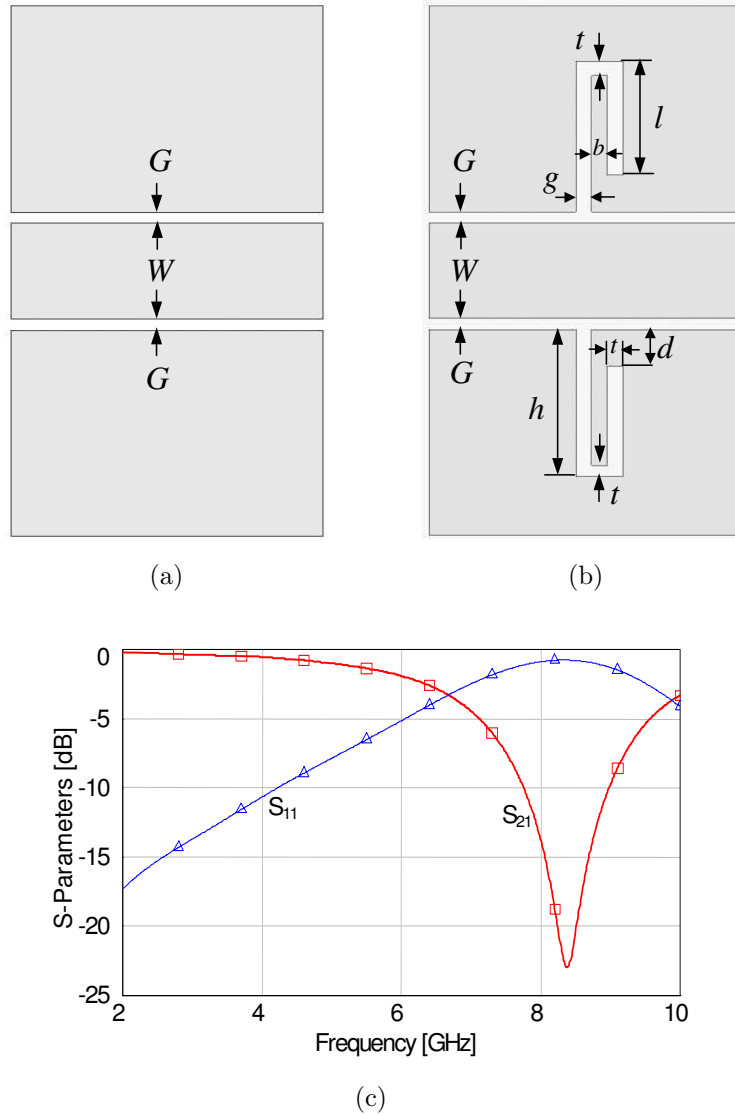


Figure 5.7: (a) Conventional coplanar waveguide transmission line, (b) L-shaped defected ground structure and (c) RF frequency response of a single-sided one-section (SS1S) L-shaped DGS.

### 5.3 L-Shaped DGS for CPW Line

An L-shaped defected ground structure for coplanar waveguide is proposed as shown in Fig. 5.7(b), which is a modification from the conventional coplanar waveguide shown in Fig. 5.7(a). The L-element is then added in series at one side, Fig. 5.8(a), or at both sides, Fig. 5.8(b). This technique increases the path of the current and thus increases the inductance of the defect. Increasing the number of the L-sections will increase the capacitance simultaneously since the area of the capacitance effectively increases. However, as it can be seen in Fig. 5.9, the surface current distribution

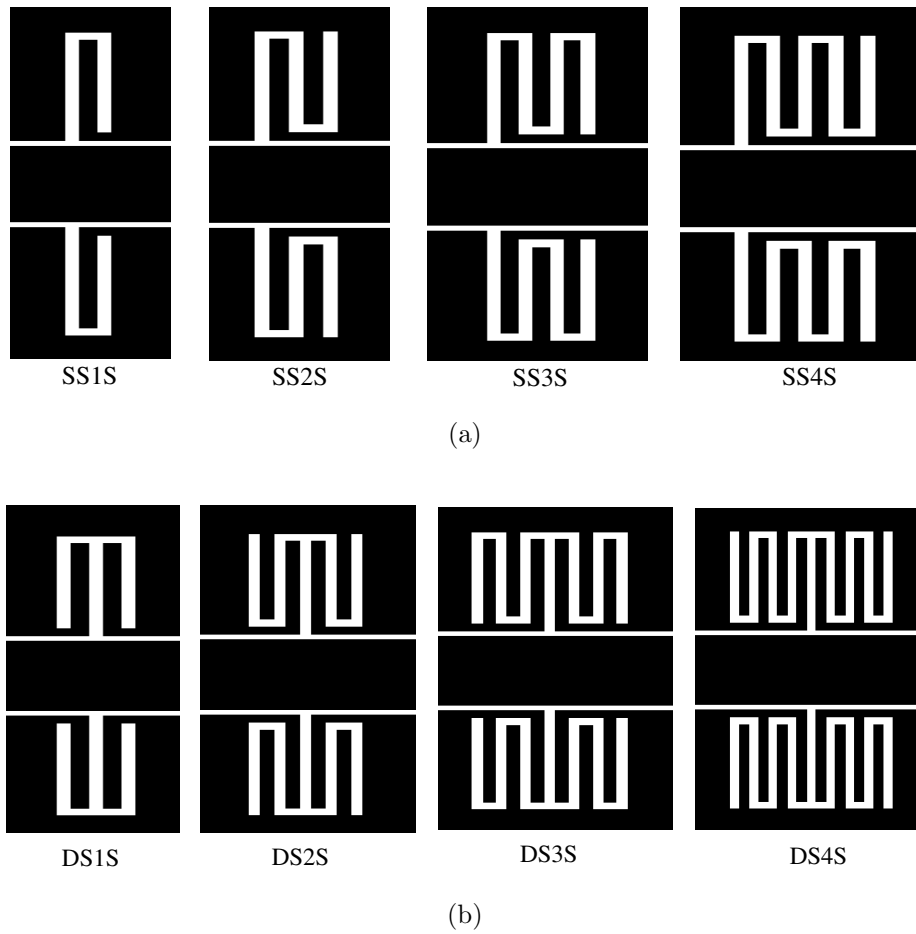


Figure 5.8: One, two, three, and four L-shaped DGS repeated in (a) Single-sided and (b) Double-sided.

calculated at 4 GHz using the 2.5D planar EM simulator Sonnet version 9.52 suggests that the magnitude varies in the direction of the propagation and thus both inductance and capacitance are not simply connected in series or in shunt, respectively.

The objective of this study is to present a criterion that determines the dependence of the equivalent circuit elements (i.e. capacitance, inductance, and resistance) on the design parameters of the defect and to incorporate these defects into filters to improve their performance compared to conventional design. However, to the author's knowledge, the physical dependence of the equivalent circuit of the defect and its design parameters on the field distribution has not yet been investigated. As consequence, the L-shaped DGS structure is studied and the electric and magnetic fields within the defect are investigated using an EM simulator. From this study, parameters affecting  $L$ ,  $R$ , and  $C$  separately are determined. Numerical experimentation of the effect of different design parameters are carried out, which leads to a very wide variation of the band-stop frequency (2.8-10.5 GHz). Based on parameter sweeping,

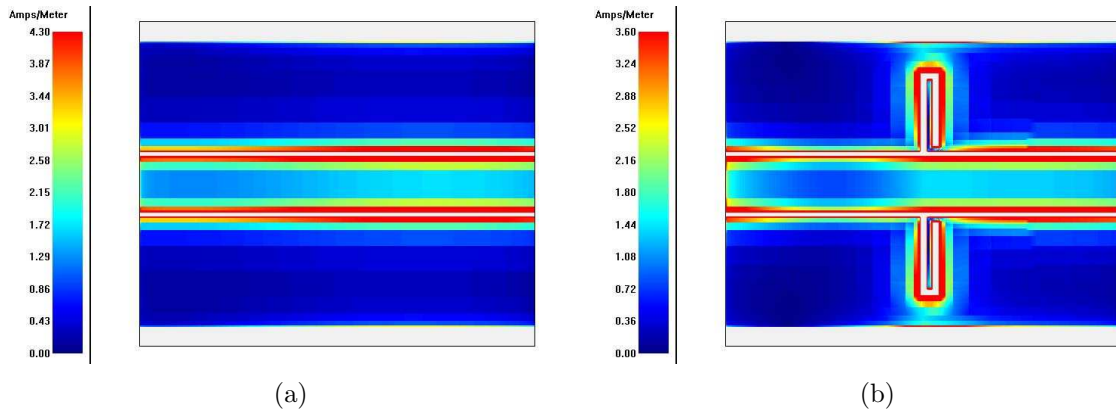


Figure 5.9: Surface current distribution at 4 GHz of (a) Conventional CPW line and (b) SS1S L-shaped defected ground structure

two wideband bandstop filters are designed using cascaded four cells of double-sided two-sections L-shaped DGS. The achieved central frequencies are 6.0 and 3.7 GHz and the band-stop widths are 2.8 and 2.0 GHz with rejection larger than 30 and 25 dB, respectively. All numerical investigations are confirmed experimentally and excellent agreement is achieved.

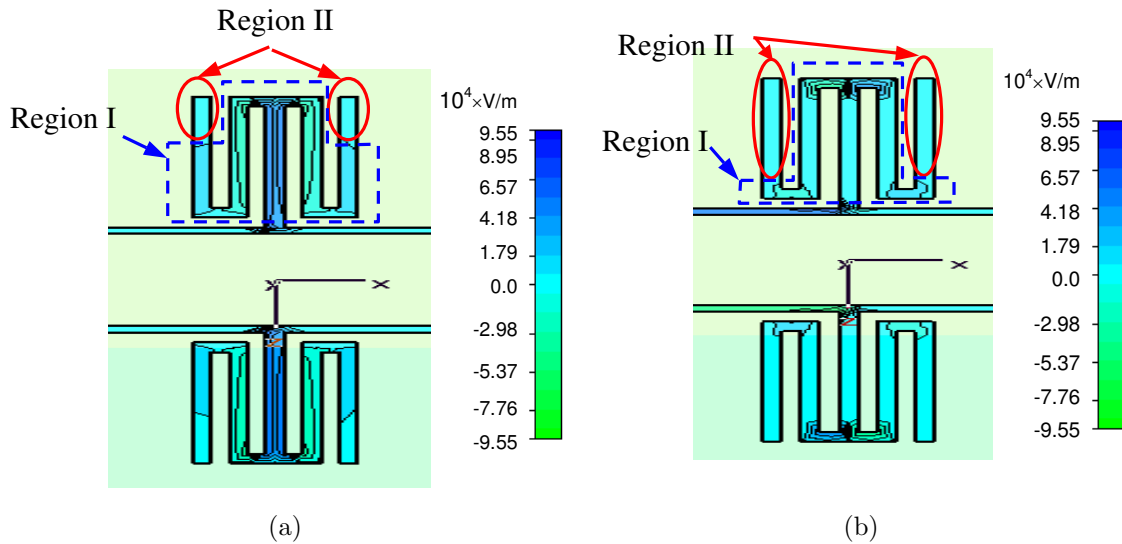


Figure 5.10: Electric field distributions of DS2S DGS at 5.5 GHz (a)  $x$ -component and (b)  $z$ -component

### 5.3.1 Theory and Basic Idea

The electric and magnetic field distributions in an RF multi-conductors structure can be used to determine a proper equivalent circuit. The intensity of these fields

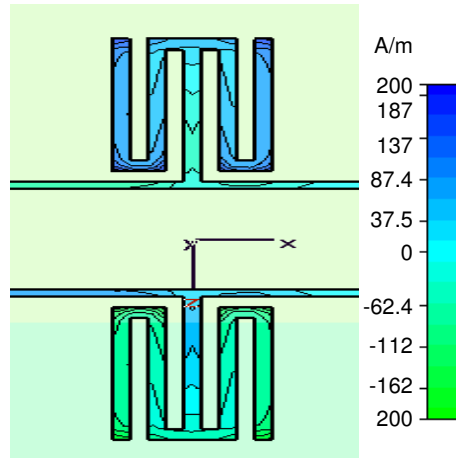


Figure 5.11:  $y$ -Component of the magnetic field distributions for DS2S DGS at 5.5 GHz

determines which parts of the metal contribute to the equivalent circuit. A single-sided one-section (SS1S) L-shaped structure, which defects the ground of the CPW (shown in Fig. 5.7(b)) leads to disturbing the electric and magnetic field distributions and reducing the transmission around a certain frequency  $f_1$  (here  $f_1 = 8.4$  GHz) as shown in Fig. 5.7(c).

The tangential components of the electric field distribution on the metallization plane for the double-sided two-sections (DS2S) L-shaped DGS determined at 5.5 GHz using Microwave Studio version 5.0 are shown in Fig. 5.10 and Fig. 5.11, respectively.

For the sake of illustration, Fig. 5.10 is divided into two regions: region I, where the electric field is highly concentrated in the gap, hence any change in the dimensions of the gap will affect the effective capacitance of the structure. The electric fields reduce toward the end of this region. In region II, the electric field nearly vanishes. This means that the length of the last finger of the last L-section will not affect the effective capacitance of the structure. Fig. 5.11 illustrates the magnetic field distribution on the metallization plane for the DS2S DGS at the same frequency. The current is distributed throughout the whole structure. Therefore any change in the length of the L-section will strongly affect the magnetic field distribution and hence the surface current, which in turn will lead to a change in the effective inductance of the structure.

In conclusion, to control the inductance while keeping the capacitance constant, regions of negligible electric field should be first determined, then changing the current's path length controls the inductance. On the other hand, to have a capacitance-controlled structure the variation of the length of the current pathes should be negligible.

### 5.3.2 Structure Design and Discription

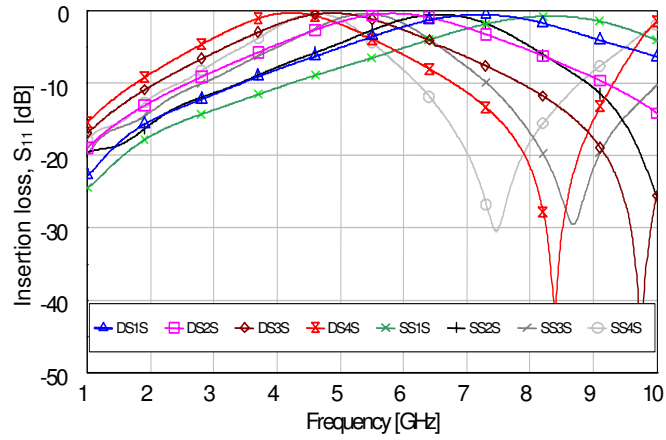
The L-shaped DGSCPW unit cell is shown in Fig. 5.7(b). The height of the defect is  $h$ . The width of the air gap is  $g$ , the strip width is  $t$ , and the distance of the L-shape's edge to the CPW slot is equals to  $d$ . The L-shaped DGS structure looks like an interdigitated capacitor with finger width and spacing being  $b$  and  $t$ , respectively. The L-sections are added in series either at one side or at both sides to keep the symmetry as illustrated in Figs. 5.8(a) and 5.8(b), respectively.

The L-shaped defected ground structure was designed for a coplanar waveguide line with  $50 \Omega$  characteristic impedance ( $G/W/G = 0.2/2.8/0.2$  mm) for good RF impedance matching, where  $W$  is the width of the center conductor and  $G$  is the width of the slot. The substrate height is 0.813 mm, the dielectric constant is 3.38 and the metal thickness is  $35 \mu\text{m}$ . The first step in the design is to optimize the parameters of one L-section at one side to get a stop band response centered at certain frequency (here at 8.38 GHz). The resulting dimensions of the L-shaped, which is etched in both ground planes symmetrically are:  $h = 4$ ,  $s = 0.6$ , and  $g = t = d = 0.3$  mm. The dimensions of the DS2S defect as shown in Fig. 5.14 are  $l = 3.4$ ,  $d = 0.3$ ,  $h = 4$ ,  $b = 0.3$ ,  $t = 0.3$  and  $c$  is 0.0 mm.

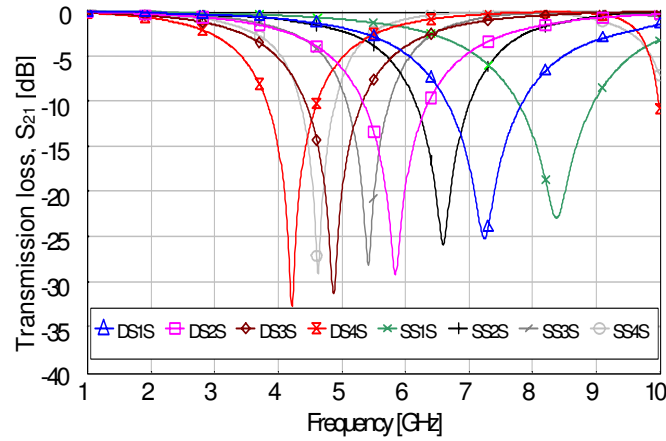
### 5.3.3 EM Simulation and Circuit Modeling

One, two, three, and four L-sections are arranged at one side and at both sides as shown in Figs. 5.8(a) and 5.8(b), respectively. Their performances are investigated using the 3-D EM simulator Microwave Studio version 5.0. The S-parameters of the structures are shown in Fig. 5.12. The transmission loss,  $S_{21}$  depicts a minimum at a frequency determined by the structure geometry and it decreases as the number of L-sections increases. For a single-sided one-section (SS1S), the center frequency is 8.38 GHz, while for the double-sided four-sections (DS4S), it is 4.21 GHz. In all structures, the magnitude of the rejection,  $S_{21}$ , at the resonant frequency is more than 23 dB.

The RF performance of the L-shaped defected ground structures has been modeled using circuit elements as well. The equivalent circuit model is presented in Fig. 5.13(a). It consists of a shunt connected capacitance, inductance, and resistance with two cascaded sections of transmission lines at both sides. The transmission line length is half the physical length of the total structure port to port,  $L/2 = 10$  mm, its characteristic impedance is  $50.4 \Omega$  and the effective dielectric constant is 1.88 as determined by the EM simulator. The S-parameters of the equivalent circuit and the EM simulations for double-sided three-sections (DS3S) DGS are presented in Fig. 5.13(b). Good agreement is achieved. Little difference between the circuit and the EM simulations is observed at high frequencies due to the frequency dependence of the capacitance and inductance. The variation of the equivalent capacitance, inductance, and resistance are almost changed linearly as a function of the number of repeated



(a)



(b)

Figure 5.12: EM simulations for the L-shaped DGS for CPW in terms of the number of repeated L-sections, (a) Return loss  $S_{11}$  and (b) Transmission loss  $S_{21}$ .

L-sections, however the corresponding increasing rates are not  $L_o$ ,  $C_o$ ,  $R_o$ , (the inductance, capacitance and resistance of a unit cell), since the magnitude of the voltage and current along the defect are not constants as predicted in the introduction.

### 5.3.4 Parametric Analysis

Based on numerical experimentations using the 3-D electromagnetic simulator, the L-shaped DGS is analyzed and designed. All its parameters are optimized to obtain specified resonant frequency. A second L-section is added and duplicated at both sides to form a double-sided two-sections (DS2S) DGS as shown in Fig. 5.14 to reduce the resonant frequency from 8.4 to 5.8 GHz. The dimensions of the DS2S are varied to determine which parameter affects the inductance, capacitance, and resistance to

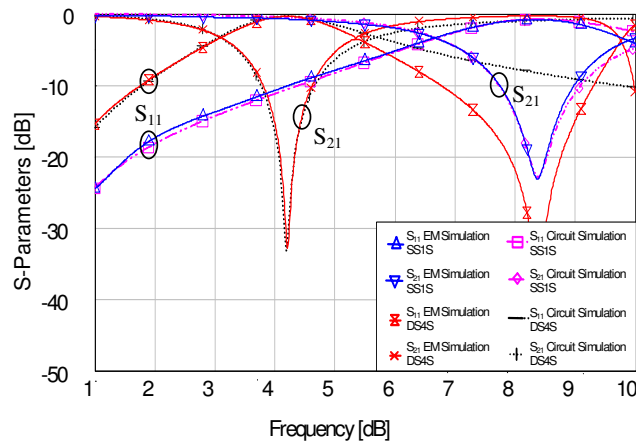
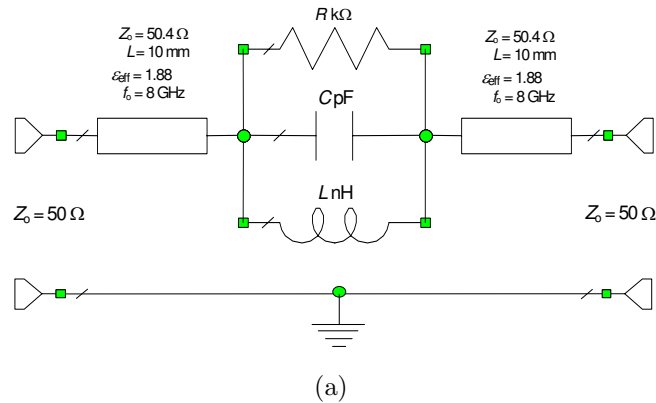


Figure 5.13: L-shaped DGS circuit modeling, (a) Equivalent circuit model, and (b) Equivalent circuit and EM simulations for SS1S and DS4S L-shaped DGS. The circuit parameters  $R$ ,  $L$ , and  $C$  are  $1.3 \text{ k}\Omega$ ,  $0.89 \text{ nH}$ , and  $0.405 \text{ pF}$  for SS1S structure and  $4.5 \text{ k}\Omega$ ,  $2.4 \text{ nH}$ , and  $0.6 \text{ pF}$  for DS4S structure, respectively.

verify the idea presented in Section 5.3.1. Fig. 5.15(a) shows the variations of the DS2S resonant frequency  $f_o$  with all cell dimensions. The width of the central gap ( $g$ ) and the width of the slot ( $t$ ) are multiplied by 10 to be included on the same graph. When the length of the whole defect ( $h$ ) varies, the length of the L-shaped defect ( $l$ ) is kept constant. In this case, the whole defect penetrates the ground. Similarly when the distance between the defect and the slot of the CPW ( $d$ ) varies,  $h$  is kept constant. Thus in the extreme case, the L-shape turns into a T-shape. When  $t$  changes,  $s$  is kept equal to  $0.8 \text{ mm}$ . During simulation, all dimensions are kept constant when one parameter changes. The initial values are those mentioned above. The resonance frequency increases with respect to  $b$ ,  $c$ ,  $l$ , and  $h$  and decreases with respect to  $g$ ,  $t$ , and  $d$ .

For every point shown in Fig. 5.15, the parameters of the equivalent circuit model

are optimized relative to the S-parameters obtained from the EM simulation. The parameters can also be determined using the equations given in [73] knowing the center frequency of the band reject and the 3 dB cutoff frequency taken from the  $S_{21}$  curve. Fig. 5.15(b) shows the variation of the equivalent capacitance as a function of the DS2S dimensions. The capacitance increases as  $l$ ,  $h$  and  $b$  increase and decreases as  $d$ ,  $t$ , and  $g$  increase. Meanwhile it is constant as  $c$  increases. This is consistent with the theoretical predictions. Since the defect acts as an interdigitated capacitor,  $l$ ,  $h$  and  $b$  effectively increase the area and thus increase the total capacitance, while  $g$  and  $t$  increase the separation between the two electrodes and thus reduce the capacitance. As for  $d$ , it decreases the whole area of the capacitor when it decreases and thus the capacitance decreases. On the other hand  $c$  has a different effect, in this region the electric field is weak and hence it does not affect the capacitance. Fig. 5.15(c) illustrates the variation of the equivalent inductance with all sweeping parameters. It increases as all parameters except  $d$  and  $g$  increase. It decreases as  $d$  increases and it remains constant as  $g$  varies. This is also consistent with the theoretical predictions. All parameters except  $d$  and  $g$  increase the length of the current path and this in turn increases the equivalent inductance. On the other hand, when  $d$  increases the length of the defect decreases and consequently the inductance reduces. The central gap width  $g$  does not vary the current path and hence the inductance remains constant.

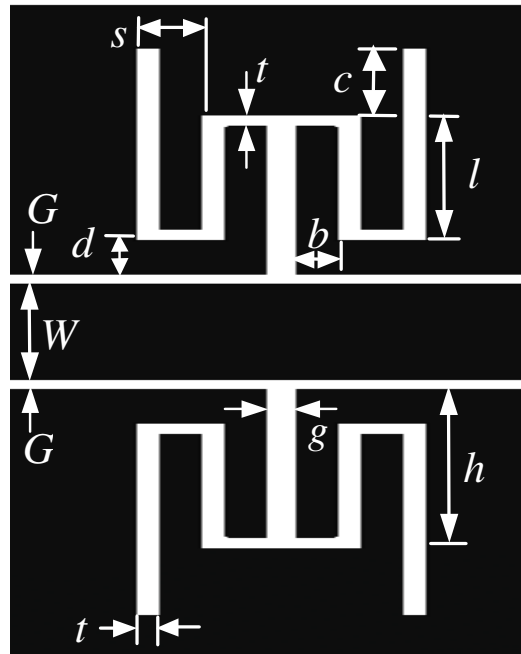


Figure 5.14: Double-sided two-sections (DS2S) L-shaped defected ground structure for CPW line.

The effect of the cell parameters on the equivalent resistance has been studied as

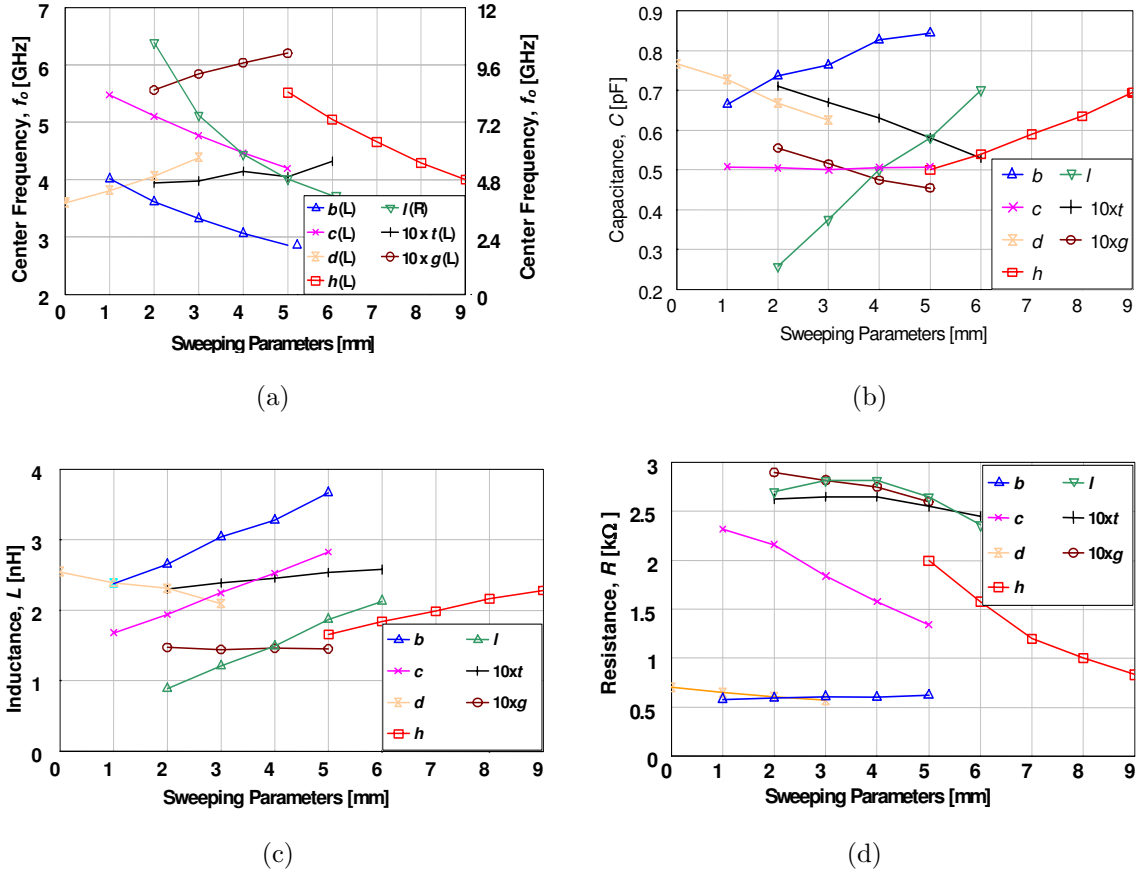


Figure 5.15: Sweeping parameters analysis of the DS2S L-shape DGS, (a) Variation of the center frequency  $f_o$  (GHz), (b) Variation of the equivalent capacitance  $C$  (pF), (c) Variation of the equivalent inductance  $L$  (nH), (d) Variation of the equivalent resistance  $R$  (kΩ) in terms of sweeping parameters. The dimensions are:  $c = 0, h = 4, l = 3.4$ , and  $t = g = d = b = 0.3$ , mm. When  $t$  changes from 0.2 to 0.6, the parameter  $s$  equals to 0.8 mm.

well, as illustrated in Fig. 5.15(d). This resistance corresponds to the radiation, the conductor, and the dielectric losses in the defect as shown in [74]. It is found that the resistance is almost constant as  $b$  and  $d$  change, and minor change occurs when  $l, g$ , and  $t$  change. However, as  $h$  and  $c$  increase, the resistance decreases. This can be explained by the fact that at resonance some of the energy radiates due to the magnetic current induced on the ground plane. The radiated power is roughly related to the DGS size and if its size becomes comparable to the wavelength, it will function as a radiator instead of a resonator. In this structure, the radiation loss is small since the sum of the reflected and transmitted power is very close to unity as depicted in Fig. 5.13(b). Table 5.3.4 summarizes the relation between the sweeping parameters and the equivalent circuit model of the defect.

Table 5.1: DS2S Parameters and their effects on the elements of the equivalent circuit model.

	Ranges (mm)	$f_o$ (GHz)	$C$ (pF)	$L$ (nH)	$R$ (k $\Omega$ )
$b$	1-5	4.02-2.85	↑	↑	–
$h$	5-9	5.52-4.00	↑	↑	↓
$l$	2-6	10.5-4.12	↑	↑	–
$d$	0-3	3.60-4.39	↓	↓	–
$t$	0.2-0.6	3.94-4.31	↓	–	–
$g$	0.2-0.5	5.56-6.20	↓	–	–
$c$	0-4	5.47-4.20	–	↑	↓

↑ increases, ↓ decreases, – constant.

### 5.3.5 Measurements and Applications

Different structures are fabricated on Rogers substrate. All dimensions are as described in the simulations. Pictures of the fabricated single-sided one-section, double-sided two-sections, and double-sided three-sections L-shaped DGS structures for CPW line are shown in Fig. 5.16(a). The fabricated structures are measured using a 8722D vector network analyzer calibrated with standard calibration technique in the frequency band from one to 10 GHz. The measured and the simulated data for the three structures are shown in Figs.5.16(b), 5.16(c),and 5.16(d). Good agreement is achieved.

The unit cell of the L-shaped DGS can also be cascaded periodically to get more flexible characteristics. Fig. 5.17(b) shows the transmission loss  $S_{21}$  for different number of cascaded DS2S L-shaped DGS cells. The separation between the cells is 4 mm and all other dimensions are as described above. The coupling between the cells, which is a function in the separation between the cells and their number, alters the resonance frequency and widens the bandwidth. To obtain a wideband bandstop filters, the double-sided two-sections L-shaped DGS unit-cell is repeated four times as shown in Fig. 5.17(a). The separation between the repeated unit-cells ( $a$ ) is optimized to get the deepest rejection, widest bandwidth, and sharpest edges. The best performance was achieved when  $a = 4$  mm. Two filters having two different central frequencies are fabricated. The first has  $l = 3.4$  mm,  $d = 0.3$  mm, central frequency of 6.0 GHz, bandwidth of 2.8 GHz, and a rejection of larger than 30 dB. The second has  $l = 6.4$  mm,  $d = 2.0$  mm, central frequency of 3.7 GHz, bandwidth of 2.0 GHz, and a rejection of larger than 25 dB. The measured and EM data are illustrated in Fig. 5.17(c) and 5.17(d). The measured and simulated results are in good agreement.

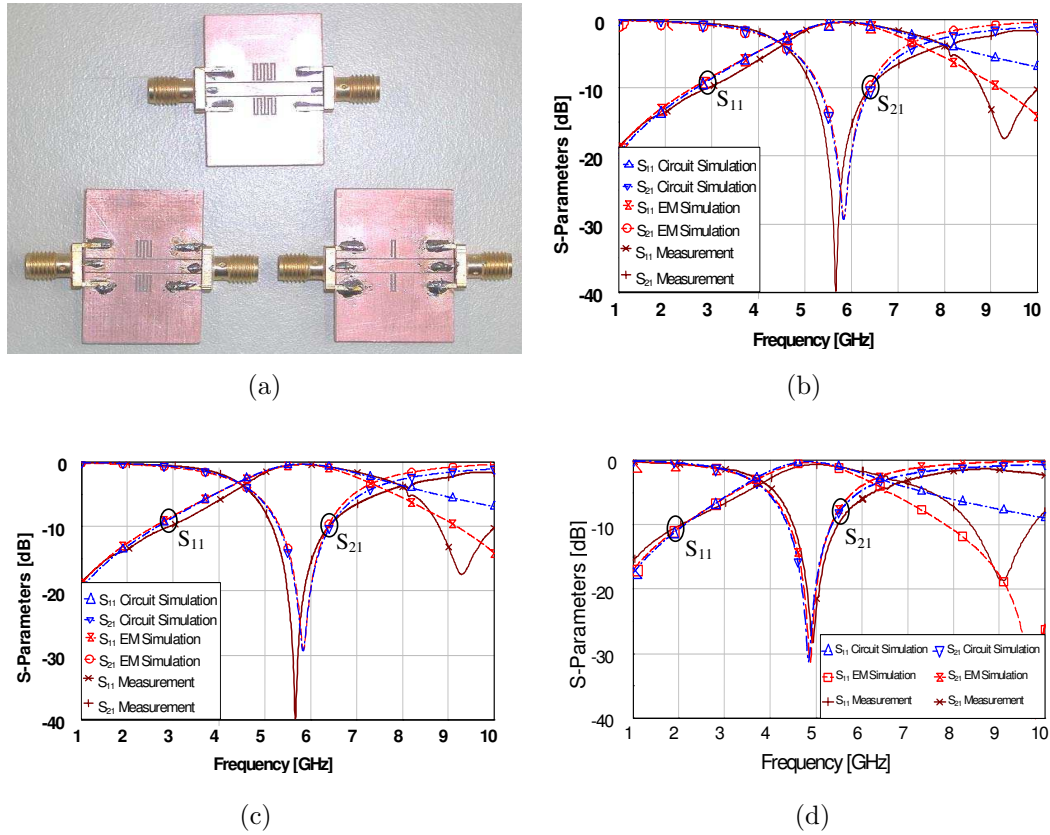


Figure 5.16: (a) Photograph of the fabricated L-shaped DGS structures, (b) S-parameters of single-sided one-section (SS1S), (c) Double-sided two-sections (DS2S), and (d) Double-sided three-sections (DS3S) L-shaped DGS for CPW line.

## 5.4 Conclusion

A two-dimensional periodic defected ground structure (2-D PDGS) for coplanar waveguide line is proposed. The proposed structure is based on the standard dumbbell structure, which is repeated periodically in a simplified and systematic way to control the central resonant frequency. The introduced structure has the advantage of having an almost constant capacitance while the inductance varies linearly as the number of cells increase, which simplifies the design process. The center frequency varies from 7 GHz down to 4 GHz with more than 20 dB rejection in the stopband when the number of cells increase from two to nine cells. Two and four sections of PDGS are cascaded to form wide-bandstop filters with high rejection. Excellent agreement is achieved between the EM and circuit simulations and the experimental results.

An L-shaped defected ground structure for coplanar waveguide line is analyzed and designed. This L-shaped structure consists of L-shaped unit cell that is repeated in single-sided or in double-sided (to keep symmetry) to prolong the current path and

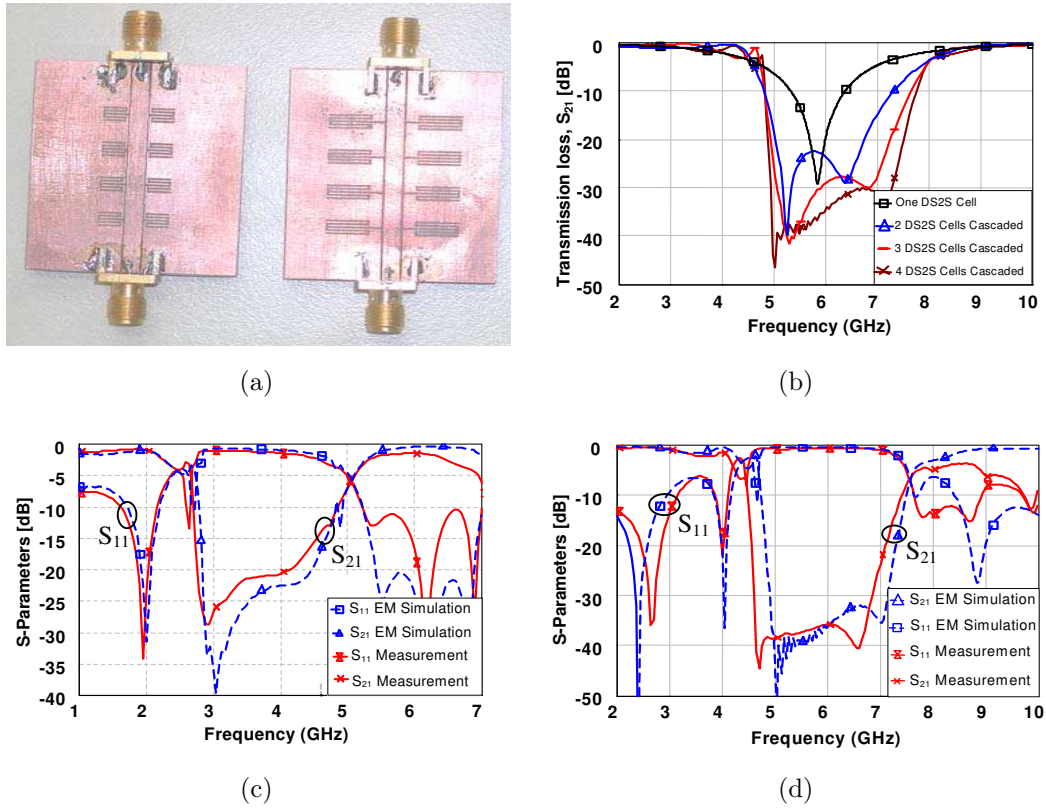


Figure 5.17: Cascaded four-cells DS2S L-shaped DGS for CPW (a) Picture of the fabricated structures, (b) Insertion loss  $S_{21}$  for one, two, three, and four cascaded sections, (c) Measured and EM simulated S-parameters. The separation  $a$  is equal to 4 mm, (c) Parameters are as shown in Fig. 2. (d) Similar to (c) except that  $l = 7$  mm, and  $h = 2$  mm.

hence to increase the effective inductance and the effective capacitance. The center frequency varies from 8.38 GHz for single-sided one L-section (SS1S) down to 4.21 GHz for double-sided four L-sections (DS4S) with more than 23 dB rejection in the stopband. Both electric and magnetic fields within the defect are carefully studied and their impact on the equivalent circuit model was discussed. The structure has a linear variation of the equivalent capacitance and inductance relative to the number of L-sections. It has a very low center frequency with very compact size compared to the standard dumbbell structure with the same area. The variation of the resonant frequency as well as the parameters of the equivalent circuit in terms of the L-shaped design parameters are illustrated. All theoretical predictions are confirmed with the S-parameters measurement. This large number of variable permits the design of resonators that cover a wide range of frequencies (2-12 GHz). Two bandstop filters are designed and experimentally verified using four cascaded cells of double-sided two-sections L-shaped DGS with 4 mm separation. The achieved central frequencies are 6.0 and 3.7 GHz and the stopband widths are 2.8 and 2.0 GHz with rejection larger

---

than 30 and 25 dB, respectively, and low loss ( $< 0.2$  dB) in the pass-band regions. All numerical investigations have been confirmed experimentally and excellent agreement is achieved. It is expected that the L-shaped DGS structure will have potential applications in RF and microwave circuits.

## Chapter 6

# RF MEMS Reconfigurable DGS Resonator

In this chapter, the 2-D PDGS for CPW, which has been introduced in the last chapter, is re-designed on a high-resistivity silicon substrate. The resonant frequency is transferred to be in the K-band for transceivers and automotive applications. The number of the periodic cells controls the resonant frequency as described earlier. Fixed-fixed beam RF MEMS series-resistive switches [12] are constructed on the 2-D PDGS to control the number of the active cells by shorting out the others as shown in Fig. 6.1. Therefore, the resonant frequency is changed according to the number of the un-shortened cells. The 2-D PDGS in the presence of the MEMS switches and the rest of the CPW compose the introduced MEMS reconfigurable DGS resonator, which through this paper will be called loaded resonator. While in absence of the MEMS switches it is called unloaded resonator. The introduced MEMS reconfigurable DGS resonator has approximately a fixed bandwidth of about 8.1 GHz over a wideband frequency range (K-band). The proposed structure can be designed easily for other frequency bands by changing the number of unit-cells of the 2-D PDGS. A cascaded two parallel-resonance circuits model for the MEMS reconfigurable DGS resonator is introduced as well. The equivalent circuit parameters extraction methods have also been derived. Simulations based on the proposed circuit model are in a very good agreement with the electromagnetic (EM) simulations, which suggests that the MEMS reconfigurable DGS resonator is an inductive controlled reconfigured structure. The structure is designed in CPW environment on a high-resistivity silicon substrate. It is therefore suitable for monolithic integration with standard IC process.

The current chapter is organized as follows: section 6.1 describes the design and the optimization of the 2-D PDGS on a high-resistivity silicon substrate to operate at 21.1 GHz. The equivalent circuit model and how the circuit parameters are extracted are described in the same section as well. The RF MEMS series-resistive switch is investigated in section 6.2. Section 6.3 introduces the MEMS reconfigurable DGS resonator and the proposed cascaded two-parallel resonance circuit model and the

method of the circuit-parameters extraction. This is followed by the conclusion.

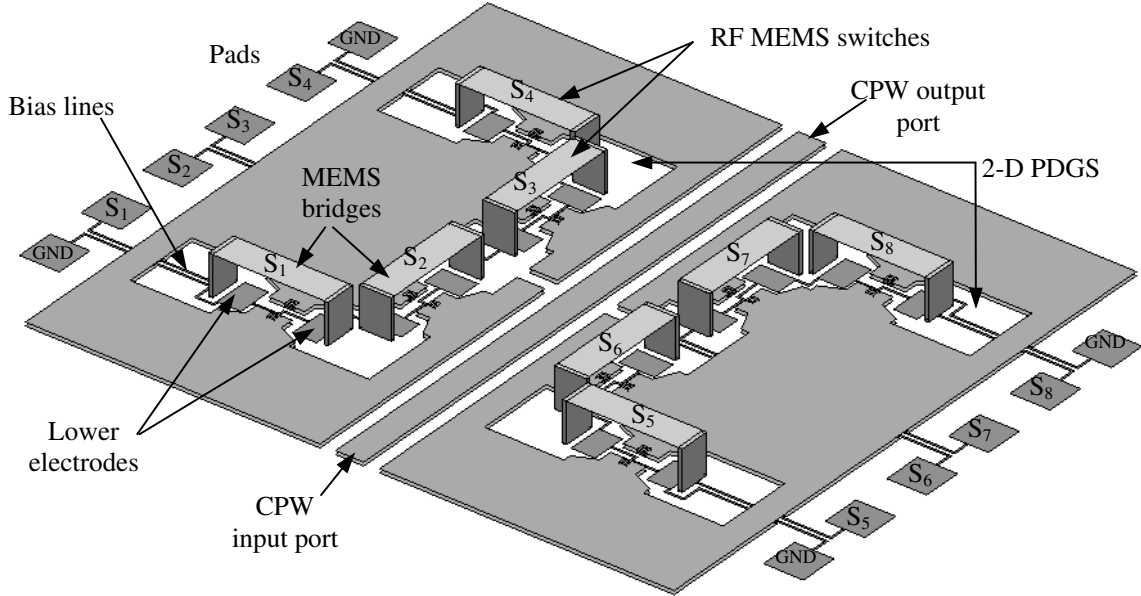
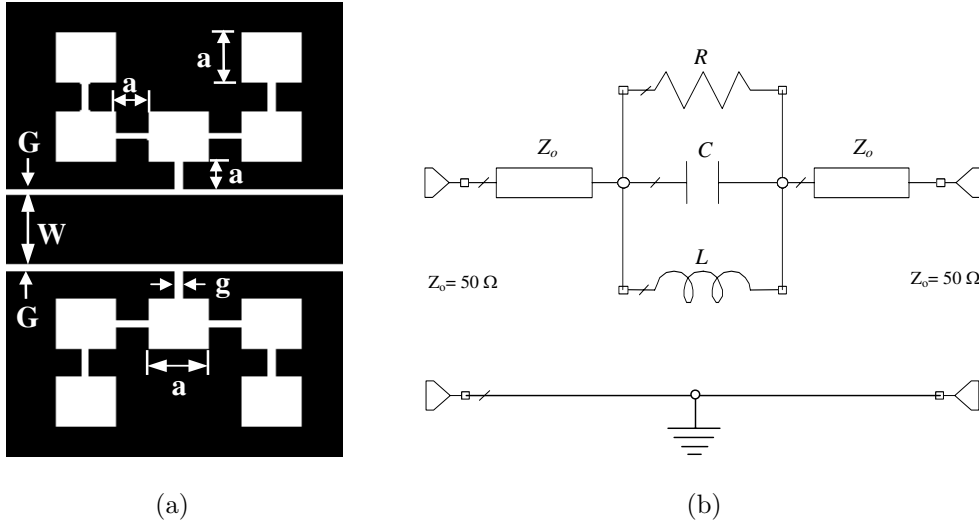


Figure 6.1: Schematic diagram of a MEMS reconfigurable DGS resonator designed using five unit-cells of a 2-D PDGS for CPW line and eight fixed-fixed beam RF MEMS series-resistive switches to get 64 resonance states in the K-band frequency domain.

## 6.1 2-D PDGS for CPW on Si-Substrate

Recently, a 2-D periodic defected ground structure (PDGS) for CPW line has been proposed in [75]. It has been designed for X-band frequency range and fabricated on a Ro4003c substrate using MIC technology. It is based on the repetition of a unit-cell (standard dumbbell) in a simplified and systematic way to control the resonance of the DGS. Here, five cells of the 2-D PDGS are considered as an example for the analysis and the verification of the idea. The structure has been re-designed on a high-resistivity silicon ( $\rho > 4 \text{ k}\Omega\cdot\text{cm}$ ) substrate of  $635 \mu\text{m}$  thickness covered by a  $1.0 \mu\text{m}$   $\text{SiO}_2$  buffer layer. The CPW line has G/W/G equals to  $40/70/40 \mu\text{m}$  corresponding to  $50 \Omega$  characteristic impedance and  $2.5 \mu\text{m}$  thickness of Al metallization. The defect is etched in both sides of the ground planes of the CPW symmetrically. The dimensions of the defected structure, as shown in Fig. 6.2(a), are  $g = 40 \mu\text{m}$  and  $a = 200 \mu\text{m}$ . The designed parameters are optimized to achieve a resonance at a selected frequency (here is  $21.1 \text{ GHz}$ ) with a rejection more than  $34.5 \text{ dB}$  at the resonant frequency and insertion loss of about  $0.1 \text{ dB}$  in the lower passband and with less than  $2.5 \text{ dB}$  in the upper passband as depicted in Fig. 6.2(c).

The 2-D PDGS, shown in Fig. 6.2(a), is analyzed using the full-wave 2.5D planar EM simulator Sonnet version 10.52. The EM simulation provides a frequency response



(a)

(b)

(c)

Figure 6.2: Two-Dimensional periodic DGS for CPW line with five periodic unit-cells, (a) Schematic diagram, (b) Equivalent circuit model, and (c) EM and circuit simulation S-parameters

with one cutoff frequency and one-attenuation pole. This frequency response can be model accurately by a single parallel RLC resonance as shown in Fig. 6.2(b). The resistance  $R$  is always very large and accounts for the different losses in the structure.

To extract the parameters of the equivalent circuit model, the resonant frequency  $\omega_o$  and the 3 dB cutoff frequency  $\omega_c$  are first determined from the EM simulations. The resonant frequency  $\omega_o$  in terms of the parallel resonant circuit elements is given by:

$$\omega_o = 1/\sqrt{LC} \quad (6.1)$$

where  $L$  and  $C$  are the inductance and capacitance of the parallel inductor and capacitor, respectively. The 3 dB cutoff frequency is determined using  $S_{21}$  curve

(assuming that both transmission lines are very short) as follows:

The equivalent impedance of the parallel resonance is given by

$$Z = \frac{1}{1/R + 1/j\omega L + j\omega C} \quad (6.2)$$

and from the circuit theory,

$$S_{21} = \frac{2Z_o}{2Z_o + Z} = \frac{2Z_o}{2Z_o + \frac{1}{1/R + 1/j\omega L + j\omega C}} \quad (6.3)$$

at the 3 dB cutoff frequency point  $\omega_c$

$$|S_{21}| = \frac{2Z_o}{\sqrt{4Z_o^2 + \left(\frac{\omega_c/C}{\omega_o^2 - \omega_c^2}\right)^2}} = \frac{1}{\sqrt{2}}, \text{ assuming } R \gg Z_o \quad (6.4)$$

Rearranging (6.4), the capacitance of the equivalent circuit model is given by:

$$C = \frac{\omega_c}{2Z_o(\omega_o^2 - \omega_c^2)} \quad (6.5)$$

substituting back in (6.1), the inductance value  $L$  can be determined.

The resistance  $R$  in the equivalent circuit model is best fitted around the resonant frequency  $\omega_o$ . In this case, the equivalent impedance is  $Z_s = R$  and the transmission loss  $S_{21}$  is

$$S_{21}|_{\omega=\omega_o} = \left| \frac{2Z_o}{2Z_o + Z_s} \right| = \frac{2Z_o}{2Z_o + R} \Rightarrow R = 2Z_o \frac{1 - S_{21}|_{\omega_o}}{S_{21}|_{\omega_o}} \quad (6.6)$$

To validate the circuit model, the five-cells 2-D PDGS shown in Fig. 6.2(a) with the dimensions given above is simulated using an EM simulator. The extracted  $R$ ,  $L$  and  $C$  are 5.22 k $\Omega$ , 0.546 nH and 0.104 pF, respectively, where  $f_c$  and  $f_o$  are 14.8 and 21.1 GHz, respectively and  $S_{21}|_{\omega_o} = 0.0188$ . The two simulation results are in a very good agreement as illustrated in Fig. 6.2(c).

## 6.2 RF MEMS Series-Resistive Switch

Figure 6.3(a) shows the schematic diagram of a fixed-fixed beam, series-configured, and resistive-contact RF-MEMS switch, which has been introduced in [12]. This switch is implemented in the proposed structure because it operates over a wide frequency band (0-30 GHz). It is based on a fixed-fixed beam, which makes its fabrication process straightforward. Further more, it is compatible with the standard MIC technology and does not require a high DC actuation voltage ( $V_{pi} \approx 20$  Volts). These switches are combined with the 2-D PDGS as shown in Fig. 6.4, such that

when being actuated, some cells will be shorted out and consequently the properties of the DGS structure will change. This will lead to a change in the resonant frequency.

To study the RF performance of the MEMS series-resistive switch whose dimensions are adjusted to fit the slots of the 2-D PDGS, it is re-designed in CPW environment, as shown in Fig. 6.3(a). The substrate is a high-resistivity silicon ( $\rho > 4 \text{ k}\Omega\cdot\text{cm}$ ) coated by a  $1.0 \mu\text{m}$   $\text{SiO}_2$  buffer layer. The bridge of the MEMS switches is made of  $\text{Au}$  to improve the mechanical properties. The corresponding length, width, and thickness of the switch's membrane are  $280$ ,  $80$ , and  $1.0 \mu\text{m}$ , respectively. The initial gap height is  $2.5 \mu\text{m}$ . The lower electrode is made of the high-resistivity metal  $\text{NiCr}$  with a sheet resistance of  $1400 \Omega/\text{square}$  which is coated by a  $0.15 \mu\text{m}$   $\text{Si}_3\text{N}_4$  dielectric layer to prevent DC short circuit. At the OFF-state (no DC biasing voltage is applied) the isolation is caused by a gap in the RF signal line of the CPW underneath the membrane that has a width of  $40 \mu\text{m}$ . At the ON-state (DC biasing voltage is applied) a dimples of  $20 \mu\text{m}^2$  area and  $0.2 \mu\text{m}$  height on the signal line of the CPW underneath the membrane is employed to reduce the contact resistance when it is contacting the bridge. The designed MEMS switch is analyzed using the EM simulator (Sonnet). The RF frequency responses of the single-separated RF MEMS series-resistive switch in both the ON and OFF-states are shown in Fig. 6.3(b). In the ON-state, the insertion loss is about  $0.1 \text{ dB}$  and the return loss is about  $30 \text{ dB}$  up to  $30 \text{ GHz}$ . While in the OFF-state, the isolation is more than  $20 \text{ dB}$  up to  $10 \text{ GHz}$  and more than  $12 \text{ dB}$  up to  $30 \text{ GHz}$ .

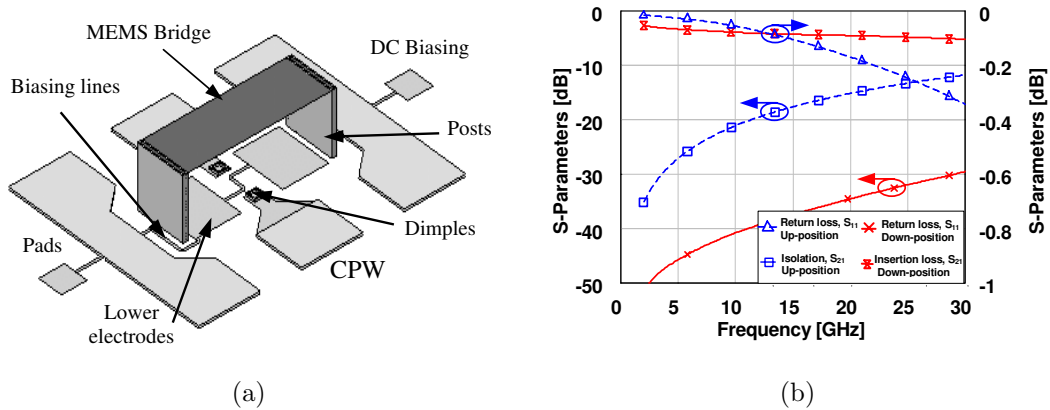


Figure 6.3: Fixed-fixed beam RF MEMS series-resistive switch, (a) Schematic diagram, and (b) RF frequency response of a single-separated switch at the ON and OFF states

### 6.3 RF MEMS Reconfigurable DGS Resonator

Figure 6.1 shows the schematic diagram of the proposed MEMS reconfigurable DGS resonator. While Fig. 6.4 depicts the half-symmetry 2-D plane of the proposed structure illustrated in Fig. 6.1. It consists of five cells of the 2-D PDGS in CPW environment and eight RF MEMS series-resistive switches based on fixed-fixed beam to cover the whole K-band for transceivers and automotive applications. The reconfigured resonator is designed as follows: First the 2-D PDGS in CPW environment is designed as described in section 6.1 to operate at a selected frequency (here is 21.1 GHz) using five unit cells arranged as shown in Fig. 6.2(a). Then eight RF MEMS series-resistive switches that are described in the last section are constructed on both ground planes of the CPW symmetrically around the slots, which join the cells in the 2-D PDGS together. To reduce the parasitic capacitance of the MEMS switches at the up-position (OFF-state of the series switch) and keep the switch isolation quite high, the slots are tapered from  $200\ \mu\text{m}$  down to  $90\ \mu\text{m}$  as illustrated in Fig. 6.4. This taper does not affect the 2-D PDGS response itself and this is checked before constructing the MEMS switches. Another advantage of these tapers is the availability of free space, which allows the increase of the lower-electrodes area. Consequently, the reduction of the pull-down voltage of the MEMS switches.

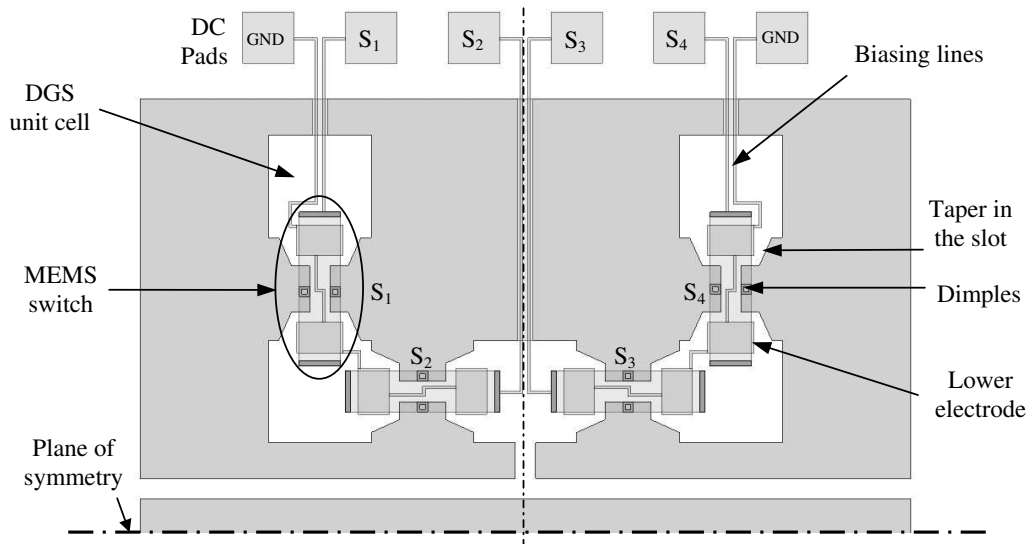


Figure 6.4: Half-symmetrical 2-D view of the RF MEMS reconfigurable DGS resonator, which is depicted in Fig. 6.1.

The introduced MEMS reconfigurable DGS resonator is designed and analyzed using the full-wave 2.5D EM simulator. The RF frequency response of the MEMS reconfigurable DGS resonator in the case of zero applied voltage to all MEMS switches is investigated in Fig. 6.5. The resonant frequency is 19.4 GHz with more than 25 dB rejection. The insertion loss in the lower passband is less than 0.1 dB, while the

bandwidth is about 8.1 GHz. The quality factor (determined from the well-known center-frequency/bandwidth definition  $Q = \omega_o/2\alpha = \omega_o/\Delta\omega_o$ ) is about 2.4, keeping in mind that this value includes the effect of a 500  $\mu\text{m}$  length of the CPW transmission line at both sides and the effects of the RF MEMS switches as well.

Having eight switches, which can be actuated individually,  $2^8$  states can be principally obtained. However, because the structure has a vertical and horizontal symmetries, only  $2^6$  states are available. The highest and the lowest frequency values are determined by “no switches are actuated” and “switches  $S_1, S_2, S_4, S_5, S_6$  and  $S_8$  are actuated”, respectively. Between these two frequencies 64 states are available, which means a fine granularity in discrete frequency steps between the upper and lower limits.

The loaded resonator is analyzed and simulated using the EM simulator at different states of the RF MEMS switches to get the RF frequency response. The lowest resonant frequency (19.4 GHz) has been obtained when no switches are actuated. While the highest resonant frequency (27.1 GHz) is obtained when  $S_1, S_2, S_4, S_5, S_6$  and  $S_8$  are actuated. We should mention here that when all switches are actuated, the defected ground structure would be nearly completely destroyed and the total structure behaves as a simple coplanar transmission line, i.e. there is no filter resonance in this case.

The following cases describe the performance of the loaded resonator at different conditions of the switches:

- Case 1) The MEMS switch  $S_1$  - no symmetry - is actuated. In this case the 2-D PDGS operates with four cells at one side, while the MEMS switch shorts the 5<sup>th</sup> cell. As a result, the resonant frequency increases from 19.4 GHz up to 20.1 GHz.
- Case 2) The two symmetrical switches  $S_1$  and  $S_5$  are actuated. The structure in this case operates with four cells at both sides so that the resonance increases up to 21.1 GHz.
- Case 3) Switches  $S_1$  and  $S_4$  are actuated – no symmetry – to cancel two cells at one side only so that the center frequency shifts further up to 21.9 GHz.
- Case 4) Switches  $S_1$  and  $S_4$  as well as their mirrors images  $S_5$  and  $S_8$  are actuated to change the resonance to 25.3 GHz.
- Case 5) At one side, three switches are actuated (namely,  $S_1, S_2$  and  $S_4$ ) to get the resonance at 22.6 GHz.
- Case 6) The symmetrical switches  $S_1, S_2, S_4$  and  $S_5, S_6, S_8$ , respectively, are biased to get the highest resonant frequency at about 27.1 GHz.

The reflection coefficient  $S_{11}$  and the transmission coefficient  $S_{21}$  in all these cases are illustrated in Fig. 6.5(a) and 6.5(b), respectively.

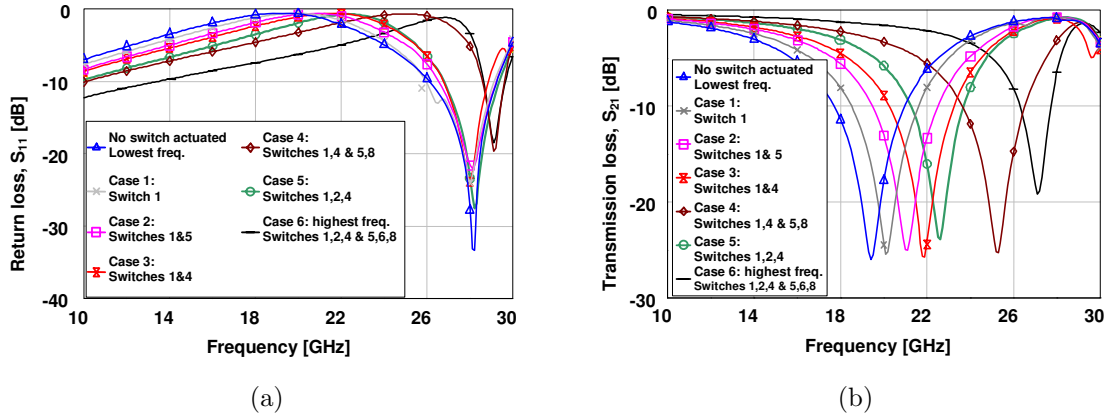


Figure 6.5: RF frequency response of the MEMS reconfigurable DGS resonator in case of no switches are actuated (gives lowest resonant frequency) and in the cases 1, 2, 3, 4, 5, and 6, (case 6 gives the highest resonant frequency). Switches  $S_1$ ,  $S_2$ ,  $S_3$ ,  $S_4$ ,  $S_5$ ,  $S_6$ ,  $S_7$ , and  $S_8$  are depicted in Fig. 6.1 and Fig. 6.4. All dimensions are given in sections 6.1 and 6.2. (a) Reflection coefficient  $S_{11}$ , and (b) Transmission coefficient  $S_{21}$

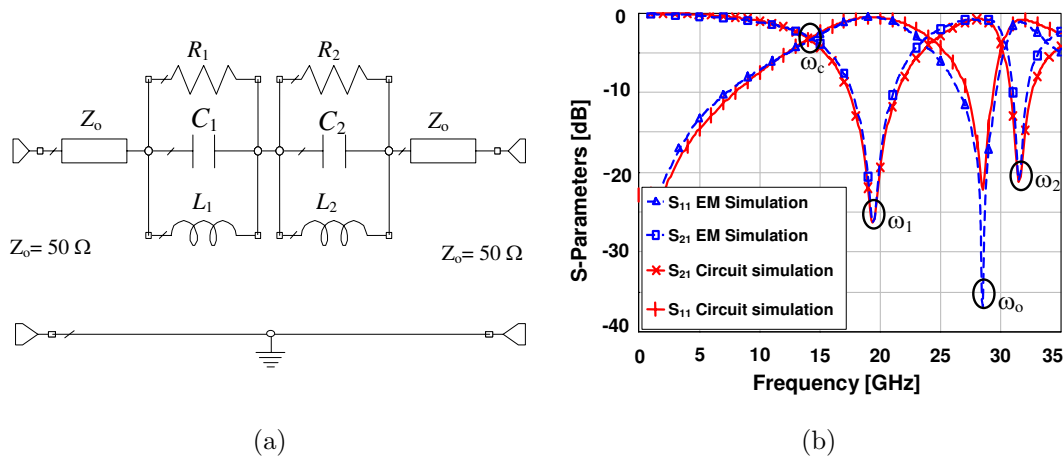


Figure 6.6: MEMS reconfigurable DGS resonator modeling, (a) Equivalent circuit model and (b) RF frequency response in case of all MEMS switches are not actuated (loaded resonator)

### 6.3.1 Circuit Model and Parameters Extraction

The electromagnetic simulation of the loaded resonator shows that it has two attenuation poles and one full-transmission frequency within the range of 0-35 GHz. Hence, two cascaded parallel  $RLC$  circuits in addition to two transmission lines at each end, whose lengths equal to half of the physical length of the total structure (1000  $\mu\text{m}$ ) will model this structure accurately. The equivalent circuit model is depicted in Fig. 6.6(a) and the EM simulations are shown in Fig. 6.6(b). The first and the second stop frequencies,  $\omega_1$  and  $\omega_2$ , can be determined from this frequency response. Moreover, the full-transmission frequency point  $\omega_o$  and the 3 dB cutoff frequency  $\omega_c$  can be determined as well. These frequencies are sufficient to extract all the parameters of the equivalent circuit model as it is shown below.

The equivalent impedance of the cascaded parallel resonance circuits is

$$Z = \frac{1}{1/R_1 + 1/j\omega L_1 + j\omega C_1} + \frac{1}{1/R_2 + 1/j\omega L_2 + j\omega C_2} \quad (6.7)$$

The reflection coefficient  $S_{11}$  is given by

$$S_{11} = \frac{Z}{2Z_o + Z} = \frac{\frac{1}{1/R_1 + 1/j\omega L_1 + j\omega C_1} + \frac{1}{1/R_2 + 1/j\omega L_2 + j\omega C_2}}{2Z_o + \frac{1}{1/R_1 + 1/j\omega L_1 + j\omega C_1} + \frac{1}{1/R_2 + 1/j\omega L_2 + j\omega C_2}}$$

Assuming that  $R \gg Z_o$ ,  $S_{11}$  is reduced to

$$S_{11} = \frac{\frac{j\omega L_1}{1 - \omega^2 L_1 C_1} + \frac{j\omega L_2}{1 - \omega^2 L_2 C_2}}{2Z_o + \frac{j\omega L_1}{1 - \omega^2 L_1 C_1} + \frac{j\omega L_2}{1 - \omega^2 L_2 C_2}} \quad (6.8)$$

The above expression has two poles at

$$\omega_1 = 1/\sqrt{L_1 C_1} \text{ and } \omega_2 = 1/\sqrt{L_2 C_2} \quad (6.9)$$

The transmission coefficient  $S_{21}$  is given by

$$S_{21} = \frac{2Z_o}{2Z_o + Z} = \frac{2Z_o}{2Z_o + \frac{j\omega L_1}{1 - \omega^2 L_1 C_1} + \frac{j\omega L_2}{1 - \omega^2 L_2 C_2}} \quad (6.10)$$

It has full transmission at  $\omega_o$ , which is given by

$$\frac{j\omega_o L_1}{1 - \omega_o^2 L_1 C_1} + \frac{j\omega_o L_2}{1 - \omega_o^2 L_2 C_2} = 0$$

Hence the full transmission frequency  $\omega_o$  is given by:

$$\omega_o = \sqrt{C_1 \omega_1^2 + C_2 \omega_2^2} / \sqrt{C_1 + C_2} \quad (6.11)$$

Similarly the 3 dB cutoff frequency  $\omega_c$  at  $\omega_1$  is determined by  $|S_{21}| = 1/\sqrt{2}$ , which leads to

$$\frac{\omega_c}{2Z_o} \left( \frac{1/C_1}{\omega_1^2 - \omega_c^2} + \frac{1/C_2}{\omega_2^2 - \omega_c^2} \right) = 1 \quad (6.12)$$

From (6.11) and (6.12) the capacitances  $C_1$  and  $C_2$  of the equivalent circuit model are given by:

$$C_1 = \frac{\omega_c}{2Z_o} \left( \frac{(\omega_o^2 - \omega_c^2)(\omega_2^2 - \omega_1^2)}{(\omega_1^2 - \omega_c^2)(\omega_2^2 - \omega_c^2)(\omega_o^2 - \omega_1^2)} \right) \quad (6.13a)$$

$$C_2 = \frac{\omega_c}{2Z_o} \left( \frac{(\omega_o^2 - \omega_c^2)(\omega_2^2 - \omega_1^2)}{(\omega_1^2 - \omega_c^2)(\omega_2^2 - \omega_c^2)(\omega_2^2 - \omega_o^2)} \right) \quad (6.13b)$$

The inductances  $L_1$  and  $L_2$  of the equivalent circuit model can be directly determined from (6.9).

The resistances  $R_1$  and  $R_2$  of the circuit model are best fitted around the resonant frequencies  $\omega_1$  and  $\omega_2$ , respectively. In this case, the impedance around the first resonant frequency  $\omega_1$  is dominated by the first parallel resonance where the equivalent impedance is  $Z_{s1} \approx R_1$  and the transmission loss  $S_{21}$  is given by:

$$S_{21}|_{\omega=\omega_1} = \left| \frac{2Z_o}{2Z_o + Z_{s1}} \right| = \frac{2Z_o}{2Z_o + R_1} \Rightarrow R_1 = 2Z_o \frac{1 - S_{21}|_{\omega_1}}{S_{21}|_{\omega_1}} \quad (6.14a)$$

The impedance around the second resonant frequency  $\omega_2$  is dominantly by the second parallel resonance where the equivalent impedance is  $Z_{s2} \approx R_2$  and the transmission loss  $S_{21}$  is given by:

$$S_{21}|_{\omega=\omega_2} = \left| \frac{2Z_o}{2Z_o + Z_{s2}} \right| = \frac{2Z_o}{2Z_o + R_2} \Rightarrow R_2 = 2Z_o \frac{1 - S_{21}|_{\omega_2}}{S_{21}|_{\omega_2}} \quad (6.14b)$$

To validate the circuit model, the reconfigured resonator is simulated with the dimensions of the five-cells 2-D PDGS being that given in section 6.1. The dimensions of the RF-MEMS switches are given in section 6.2 with all MEMS switches being identical. The extracted  $R_1, R_2, L_1, L_2, C_1$  and  $C_2$  are 1.95, 1.02 k $\Omega$ , 0.4928, 0.0772 nH and 0.1366, 0.3307 pF, respectively. These values correspond to  $f_1, f_2, f_c$  and  $f_o$  of 19.4, 31.5, 14.05, and 28.5 GHz, respectively, while  $|S_{21}| = 0.04887$  and 0.08922 at  $f_1$  and  $f_2$ , respectively. The results of the proposed equivalent-circuit-model simulation are in a very good agreement with the EM simulation results as illustrated in Fig. 6.6(b).

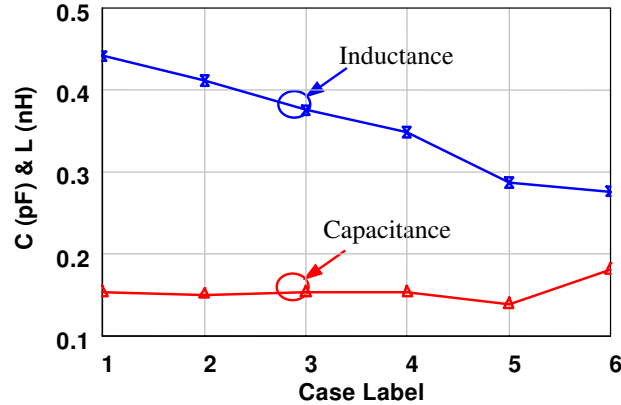


Figure 6.7: Equivalent circuit model capacitance and inductance of the first parallel resonator of Fig. 6.6(a) as a function of the different cases discussed above in terms of switches states.

The introduced MEMS reconfigurable DGS resonator operates as an inductive controlled structure. Fig. 6.7 shows how the equivalent circuit capacitance and inductance of the first parallel resonance change when the different switches change their states from the ON to OFF as discussed in the cases mentioned above. The equivalent capacitance and inductance of the second parallel resonance are almost constant because they don't play any role with the first attenuation pole. As shown in Fig. 6.7, the capacitance is almost constant while the inductance changes linearly as a function of the number of the downstate switches or, in the same meaning, as a function of the active unit cells of the 2-D PDGS. This agrees well with the investigation presented in [75] for the 2-D PDGS. The structure is therefore an inductive controlled one in terms of the number of the periodic cells. Even with the presence of the MEMS switches the 2-D PDGS is still an inductive controlled structure because the MEMS series switches control the number of cells in the 2-D PDGS only.

## 6.4 Conclusion

In this chapter, an RF MEMS reconfigurable DGS resonator using two-dimensional periodic defected ground structures in CPW environment and fixed-fixed beam RF MEMS series-resistive switches that covers the whole K-band for transceivers and/or automotive applications has been presented. The MEMS reconfigurable DGS resonator has been designed on a high-resistivity silicon substrate in CPW environment that is suitable for monolithic integration in the context of a standard planar microwave process. The proposed reconfigured resonator has a bandwidth of 8.1 GHz with more than 20 dB rejection over the whole K-band frequency range. A cascaded double-parallel-resonance circuit model for the reconfigured resonator has been proposed. Methods to extract the parameters of the equivalent circuit from the EM

---

simulations for the 2-D PDGS and the MEMS reconfigurable DGS resonator have been derived as well. The EM and the circuit simulation results are in a very good agreement, which validates the proposed circuit model. Simulation shows that the introduced resonator is an inductive controlled reconfigured structure. The proposed structure is very flexible to be designed for different frequency bands since the resonant frequency can be controlled by either the number of unit cells of the 2-D PDGS or the unit cell dimensions or both. The possible combination of the switches provides a fine granularity in discrete steps over a wide frequency range.

# Chapter 7

## Conclusions

The research contained in this dissertation has developed 2-D and 3-D coupled electromechanical models for RF MEMS switches. It has also produced characterizations of several MEMS switches and defected ground structures in CPW technology. As an application for both MEMS switches and DGS structures, a new RF MEMS reconfigurable DGS resonator has been proposed.

This chapter contains a conclusion of the findings of this research by highlighting the most significant observations concerning the 2-D and 3-D coupled models as well as the design and optimization of these switches, DGS structures, and reconfigurable resonator. Several future research ideas are also presented.

### 7.1 Contributions

Computer simulators are powerful tools that can help in the design of electromechanical devices, and aid in the understanding of the device behavior. Two and three-dimensional simulation coupled models were developed in this thesis, with the applications of the models to describe and characterize proposed RF MEMS switches and MEMS reconfigurable DGS resonator.

Chapter 1 gives a full survey on the MEMS technology and the state-of-the-art of RF-MEMS switches and the previous work in the MEMS switch modeling. In addition, a short review on the DGS structures and its potential application for MEMS technology has been demonstrated.

Chapter 2 and 3 presented contributions in developing 2-D and 3-D coupled electrostatic-mechanical models for electrostatically actuated fixed-fixed bridge RF MEMS switches. The electrostatic models compute the potential distribution in the computational domain very accurately. The actual field distribution and hence the electrostatic force density induced on the membrane have been also calculated accurately. The mechanical models determine the bridge's deformation arises from the

induced electrostatic force by solving the beam/plate equation using the finite difference method. The strong interaction between the electrostatic and mechanical models is considered iteratively. The strengths and weaknesses of the 2-D and 3-D simulation models were compared and contrasted.

Well-characterized RF MEMS switches have been designed in Chapter 4. A  $\pi$ -configuration RF-MEMS switch for wideband and high-isolation applications as well as a single-pole three-throw (SP3T) RF MEMS switch have been presented. The  $\pi$ -switch exhibits a minimum isolation of 50 dB in the frequency range from dc to 50 GHz and of 30 dB in the frequency range from 50 to 60 GHz. The insertion loss ranges from 0.2 to 2 dB and a minimum of 25 dB return loss up to 50 GHz. While the SP3T switch yields an insertion loss of about 0.45 dB and a minimum of 22 dB return loss in the frequency range from dc to 25 GHz. A minimum of 20 dB isolation between the different ports has been achieved over the same frequency range. The equivalent circuit models that describe the switches performance quite well, have been also introduced. The demonstrated results were based on numerical experimentations using a 3-D full wave electromagnetic simulators.

New designs of defected ground structures (DGS) in CPW environment has been proposed in Chapter 5. A 2-D periodic DGS based on the repetition of a lattice shape in both horizontal and vertical directions has been investigated. The design has the advantage of having an almost constant capacitance and linear inductance variation as the number of cells increases, which simplify the design process. An L-shaped DGS for CPW line is also presented and the L-section is repeated at one side or at both sides to control the cutoff frequency characteristics. It has the advantage of being either capacitive or inductive controlled structure. The behavior of the electromagnetic field in the L-shaped DGS has been investigated and the parameters affecting the inductance, capacitance, and resistance of the equivalent circuit model are separately determined. Numerical experimentation of the effect of different design parameters have been carried out, which leads to a very wide variation of the band-stop frequency (2.8-10.5 GHz). High performance bandstop filters using cascaded periodic DGS are designed and experimentally successfully verified. Results show that they have the advantage of very small size.

In Chapter 6 an RF MEMS reconfigurable DGS resonator is designed and optimized. It has approximately a fixed bandwidth of about 8.1 GHz over the whole K-band regime. It can be also easily re-designed for other frequency bands by controlling the number of the unit-cells of the 2-D PDGS. A cascaded two parallel-resonance circuit model for the reconfigurable resonator has been proposed as well. The chapter ended with a quantitative description of the equivalent circuit model parameters extraction.

The developed models have been presented in Matlab version 7 and samples from these programs are given in Appendices A and B.

---

Finally, some related publications to this work are given in page 137.

## 7.2 Suggestions for Future Work

The goal is always to progress towards the eventual objective of developing a full three-dimensional model valid over a wide range of dimensions and actuation regimes. Accurate and general electrostatic models in 2-D and 3-D are always desirable due to the high cost of solving electrostatics problems in three dimensions. Accurate models for the tip of a cantilever will allow accurate characterization of electrostatically actuated cantilever beams. After generalizing the models, a complete software package with a simple graphical user interface can be developed and integrated to any computer-aided design tools for the RF MEMS structures.

Producing good MEMS models is the key to efficient and useful simulations. The 3-D model accuracy can be improved by including higher-order effects, such as axial and residual stresses in the plate equations. Development of new models will allow simulation of a wider range of microsystem designs. Experimental verification of models is extremely important and will remain a worthwhile research area for several years.

Additionally, the introduced DGS structures proved its potential to be applied to design high performance lowpass and bandpass filters with miniaturized size. To study the miniaturization technology, DGS may be important in our future research. We are very interested in building a complete library of the equivalent circuit parameters values in terms of the defect physical dimensions to simplify the design process.

Last, fabricating and measuring the proposed MEMS components in this dissertation to verify the obtained theoretical results is a big coming work.

## Appendices

# Appendix A

## Matlab 2-D Coupled Electrostatic-Mechanical Model Scripts

These are the Matlab scripts to simulate the behavior of an electrostatically actuated fixed-fixed beam RF MEMS capacitive switch. They run on Matlab version 7.0. Comments are sprinkled liberally throughout the script. LapVarPar2D.m is the main program, which is read the switch parameters from the file DataIn.m to produce the output during the simulation ResultsLaVarPar2D.m

### A.1 Matlab Code of the 2-D Coupled Model

#### LaVarPar2D.m

```
% *****  
% 2-D Coupled Electrostatic-Mechanical Model for RF MEMS Shunt Capacitive Switches  
% File name: LapVarPar.m, August, 2005  
% By Ehab K. I. Hamad, E-mail:Ehab.Hamad@E-Technik.Uni-Magdeburg.DE  
% This program calculates bridge deformation at certain actuation voltage for a  
% shunt-capacitive MEMS switch  
% *****  
% Program Algorithm:  
% 1. Solve Laplace's equation using FDM. The generated system of equations are  
%    solved using Band Matrix Method to calculate the potential distribution in  
%    the 2-D computation domain. Hence, the electric field distribution is  
%    computed. Then the induced electrostatic force density distribution on the  
%    membrane is determined.  
% 2. Solve the mechanical equation governing the motion of the movable beam to  
%    determine the deformation corresponding to the induced electrostatic force.  
% 3. Repeat 1. using the new geometry after deformation to determine the new  
%    force distribution.  
% 4. Repeat 2. to determine the new beam deformation.  
% 5. Repeat 1. to 4. until getting the steady-state solution between the  
%    Electrostatic model and mechanical domains.
```

```

clear all
Vo = input('Inter biasing voltage, Vo=');           % Voltage applied to the lower
                                                    % electrode, CPW's signal line
DataIn.m                                           % Read the input file which has the switch parameters

tic                                                % to set the starting up time
EI = E*b*t^3/(12*(1-nu*nu));                    % Beam modulus [Pa.m^4=N.m^2]
Tr = Sigma*(1-nu)*b*t;                          % Residual stress

ng =8;          dg = go/ng;          nd =4;          dd = td/nd;
nm =6;          dm = tm/nm;          nox=4;         dox= tox/nox;
no =4;          dW = 2*(go+td+tm+tox);          xno = 2*dW/no;
n2 = round((W/2-dW)/xno);                xno = (W/2+dW)/(n2+no);
n1 = n2;                                     dL = (L-W)/2-dW;
% no = # of nodes at the lower electrode edges
% n2 = # of nodes in the middle region of the center conductor

m = 2*(ng+nd+nm+nox);                    % Total number of points in the y direction
n = 2*(n1+no+n2);                        % Total number of points in the x direction
% # of points in the metal region are (no+2*n2)*nm
% # of unknowns Lm=(n-1)*(m-1)-(no+2*n2)*nm
% matrix size Lm*Lm to be solved using Band Matrix Method [A][X]=[B]
nmx = no+2*n2+1;  Lm = (n-1)*(m-1)-nmx*(nm+1);          % Lm = Number of Unknown

% Mesh Generation
% *****
% Grid size is uniform over the lower electrode + distance equals to dW at
% the left and at the right edges then increases linearly up to the end of
% the bridge with a number of points in this region equals to n1.
for i=1:m+1,
    for j=1:n1,                % Girding in the x direction
        x(i,j)=xno-2*(dL-n1*xno)*(j-n1)/((n1-1)*n1);    x(i,n-j+1)=x(i,j);
    end
    for j=1:no,                x(i,n1+j)=xno;            x(i,n1+no+2*n2+j)=xno;        end;
    for j=1:n2,                x(i,n1+no+j)=xno;            x(i,n1+no+2*n2+1-j)=xno;    end;
end
for i=1:m+1,  xx(i,1)=0;      for j=1:n,    xx(i,j+1)=xx(i,j)+x(i,j);  end;  end;

H=5;  % Computation domain has H times of (go+td+tm+tox) height in the substrate
dy = H*(go+td+tm+tox);
for i=1:m/2+nox+nm+nd,                % Meshing in the y direction
    for j=1:n+1,
        if i < m/2+1,                y(i,j) = dox+(4*dy/m-2*dox)*(m/2-i)/(m/2-1);
        elseif (i > m/2) & (i < m/2+nox+1),    y(i,j) = dox;
        elseif (i > m/2+nox) & (i < m/2+nox+nm+1),    y(i,j) = dm;
        elseif i > m/2+nox+nm,        y(i,j) = dd;
        end
    end
end

% Set Boundary Conditions
% *****
Epsr = ones(m,n);                    % Air fill

```

```

for i=1:m/2,    for j=1:n,    Epsr(i,j)=11.9;    end;    end;    % Si substrate
for i=1:nox,    for j=1:n,    Epsr(m/2+i,j)=3.9;    end;    end;    % SiO2 layer
% Si3N4 Layer
for i=1:nd, for j=1:(no+2*n2),    Epsr(m/2+nox+nm+i,n1+no/2+j)=6.7;    end;    end;
V = zeros(m+1,n+1);    %Initiating al nodes with zero voltage
for i=1:nm+1,    for j=1:(no+2*n2+1), V(m/2+nox+i,n1+no/2+j)=Vo;    end;    end;

% Initiating A, B, and w matrices
% *****
A = zeros(Lm,Lm);    B = zeros(Lm,1);    w = zeros(1,n+1);
wmax = 10;    it = 0;
while abs(max(w)-wmax) > 1E-9,    % Starting iteration to calculate deformation
it = it+1
if max(w) > go,
    sprintf(' Stopped because Wmax > go, i.e. Vo > Vpi')
    break
end
end

% Auto-adapting the grid size according to the deformation of the bridge
% *****
for i = m/2+nox+nm+nd+1:m,    for j=1:n+1,    y(i,j)=(go-w(j))/ng; end;    end;
for j=1:n+1, yy(1,j)=0;    for i=1:m, yy(i+1,j)=yy(i,j)+y(i,j); end;    end;

% Solve Laplace's equation using FDM and apply the matrix inversion method to find
% out the potential distribution in the 2-D computational domain
% *****
% Corner 1 in the matrix A(Lm x Lm)
i=2;    j=2;    k=1;
B(k) =V(i,j-1)/(x(i,j-1)*(x(i,j-1)+x(i,j)))+V(i-1,j)/(y(i-1,j)*(y(i-1,j)+y(i,j)));
A(k,k) = 1/(x(i,j-1)*x(i,j))+1/(y(i-1,j)*y(i,j));
A(k,k+1) = -1/(x(i,j)*(x(i,j-1)+x(i,j)));
A(k,k+n-1) = -1/(y(i,j)*(y(i-1,j)+y(i,j)));
k=k+1;
for j = 3:n-1,
    B(k) = V(i-1,j)/(y(i-1,j)*(y(i-1,j)+y(i,j)));
    A(k,k) = 1/(x(i,j-1)*x(i,j))+1/(y(i-1,j)*y(i,j));
    A(k,k-1) = -1/(x(i,j-1)*(x(i,j-1)+x(i,j)));
    A(k,k+1) = -1/(x(i,j)*(x(i,j-1)+x(i,j)));
    A(k,k+n-1) = -1/(y(i,j)*(y(i-1,j)+y(i,j)));
    k=k+1;
end
% Corner 2,
j=n;
B(k)=V(i,j+1)/(x(i,j)*(x(i,j)+x(i,j-1)))+V(i-1,j)/(y(i-1,j)*(y(i-1,j)+y(i,j)));
A(k,k) = 1/(x(i,j)*x(i,j-1))+1/(y(i-1,j)*y(i,j));
A(k,k-1) = -1/(x(i,j-1)*(x(i,j-1)+x(i,j)));
A(k,k+n-1) = -1/(y(i,j)*(y(i-1,j)+y(i,j)));
k=k+1;

for i=3:(m/2+nox-1),
    for j = 2:n,
        if j == 2
            B(k) = V(i,j-1)/(x(i,j-1)*(x(i,j-1)+x(i,j)));
            A(k,k+1) = -1/(x(i,j)*(x(i,j-1)+x(i,j)));

```

```

elseif j == n
    B(k) = V(i,j+1)/(x(i,j)*(x(i,j-1)+x(i,j)));
    A(k,k-1) = -1/(x(i,j-1)*(x(i,j-1)+x(i,j)));
else
    B(k)=0.0;
    A(k,k-1) = -1/(x(i,j-1)*(x(i,j-1)+x(i,j)));
    A(k,k+1) = -1/(x(i,j)*(x(i,j-1)+x(i,j)));
end
A(k,k) = 1/(x(i,j-1)*x(i,j))+1/(y(i-1,j)*y(i,j));
A(k,k-n+1) = -1/(y(i-1,j)*(y(i-1,j)+y(i,j)));
A(k,k+n-1) = -1/(y(i,j)*(y(i-1,j)+y(i,j)));
k=k+1;
end
end

i=m/2+nox;
for j=2:(n1+no/2),
    if j == 2
        B(k) = V(i,j-1)/(x(i,j-1)*(x(i,j-1)+x(i,j)));
    else
        B(k) = 0.0;
        A(k,k-1) = -1/(x(i,j-1)*(x(i,j-1)+x(i,j)));
    end
    A(k,k) = 1/(x(i,j-1)*x(i,j))+1/(y(i-1,j)*y(i,j));
    A(k,k+1) = -1/(x(i,j)*(x(i,j-1)+x(i,j)));
    A(k,k-n+1) = -1/(y(i-1,j)*(y(i-1,j)+y(i,j)));
    A(k,k+n-1) = -1/(y(i,j)*(y(i-1,j)+y(i,j)));
    k=k+1;
end

% Line in SiO2 below Metal
for j = (n1+no/2+1):(n1+3*no/2+2*n2+1),
    B(k) = V(i+1,j)/(y(i,j)*(y(i-1,j)+y(i,j)));
    A(k,k) = 1/(x(i,j-1)*x(i,j))+1/(y(i-1,j)*y(i,j));
    A(k,k-1) = -1/(x(i,j-1)*(x(i,j-1)+x(i,j)));
    A(k,k+1) = -1/(x(i,j)*(x(i,j-1)+x(i,j)));
    A(k,k-n+1) = -1/(y(i-1,j-1)*(y(i-1,j)+y(i,j)));
    k=k+1;
end

for j = (n1+3*no/2+2*n2+2):n,
    if j == n
        B(k) = V(i,j+1)/(x(i,j)*(x(i,j-1)+x(i,j)));
    else
        B(k)=0.0;
        A(k,k+1) = -1/(x(i,j)*(x(i,j-1)+x(i,j)));
    end
    A(k,k) = 1/(x(i,j-1)*x(i,j))+1/(y(i-1,j)*y(i,j));
    A(k,k-1)=-1/(x(i,j-1)*(x(i,j-1)+x(i,j)));
    A(k,k-n+1)=-1/(y(i-1,j)*(y(i-1,j)+y(i,j)));
    A(k,k+(n-1-nmx))=-1/(y(i,j)*(y(i-1,j)+y(i,j)));
    k=k+1;
end
end
% SiO2-Si, BVP, Interface between two different media

```

```

k=(n-1)*(m/2-1)+1;          i=m/2+1;
for j=2:n,
    if j == 2,
        B(k) =V(i,j-1)*(y(i,j)*Epsr(i,j-1)+y(i-1,j)*Epsr(i-1,j-1))/x(i,j-1);
        A(k,k+1)=- (y(i-1,j)*Epsr(i-1,j)+y(i,j)*Epsr(i,j))/x(i,j);
    elseif j == n,
        B(k) =V(i,j+1)*(y(i-1,j)*Epsr(i-1,j)+y(i,j)*Epsr(i,j))/x(i,j);
        A(k,k-1)=- (y(i-1,j)*Epsr(i-1,j-1)+y(i,j)*Epsr(i,j-1))/x(i,j-1);
    else
        B(k)=0.0;
        A(k,k-1)=- (y(i-1,j)*Epsr(i-1,j-1)+y(i,j)*Epsr(i,j-1))/x(i,j-1);
        A(k,k+1)=- (y(i-1,j)*Epsr(i-1,j)+y(i,j)*Epsr(i,j))/x(i,j);
    end
    A(k,k) =Epsr(i,j)*(x(i,j)/y(i,j)+y(i,j)/x(i,j))...
            +Epsr(i,j-1)*(x(i,j-1)/y(i,j)+y(i,j)/x(i,j-1))...
            +Epsr(i-1,j)*(x(i,j)/y(i-1,j)+y(i-1,j)/x(i,j))...
            +Epsr(i-1,j-1)*(x(i,j-1)/y(i-1,j)+y(i-1,j)/x(i,j-1));
    A(k,k-n+1)=- (x(i,j-1)*Epsr(i-1,j-1)+x(i,j)*Epsr(i-1,j))/y(i-1,j);
    A(k,k+n-1)=- (x(i,j-1)*Epsr(i,j-1)+x(i,j)*Epsr(i,j))/y(i,j);
    k=k+1;
end

% SiO2-Air
k=(n-1)*(m/2+nox-1)+1;
% SiO2-Air
i=m/2+nox+1;
for j=2:(n1+no/2),
    if j == 2,
        B(k) =V(i,j-1)*(y(i-1,j)*Epsr(i-1,j-1)+y(i,j)*Epsr(i,j-1))/x(i,j-1);
        A(k,k+1)=- (y(i-1,j)*Epsr(i-1,j)+y(i,j)*Epsr(i,j))/x(i,j);
    elseif j == (n1+no/2),
        B(k) =V(i,j+1)*(y(i-1,j)*Epsr(i-1,j)+y(i,j)*Epsr(i,j))/x(i,j);
        A(k,k-1)=- (y(i-1,j)*Epsr(i-1,j-1)+y(i,j)*Epsr(i,j-1))/x(i,j-1);
    else
        A(k,k-1)=- (y(i-1,j)*Epsr(i-1,j-1)+y(i,j)*Epsr(i,j-1))/x(i,j-1);
        A(k,k+1)=- (y(i-1,j)*Epsr(i-1,j)+y(i,j)*Epsr(i,j))/x(i,j);
        B(k)=0.0;
    end
    A(k,k) =Epsr(i,j)*(x(i,j)/y(i,j)+y(i,j)/x(i,j))...
            +Epsr(i,j-1)*(x(i,j-1)/y(i,j)+y(i,j)/x(i,j-1))...
            +Epsr(i-1,j)*(x(i,j)/y(i-1,j)+y(i-1,j)/x(i,j))...
            +Epsr(i-1,j-1)*(x(i,j-1)/y(i-1,j)+y(i-1,j)/x(i,j-1));
    A(k,k-n+1)=- (x(i,j-1)*Epsr(i-1,j-1)+x(i,j)*Epsr(i-1,j))/y(i-1,j);
    A(k,k+(n-1-nmx))=- (x(i,j-1)*Epsr(i,j-1)+x(i,j)*Epsr(i,j))/y(i,j);
    k=k+1;
end

for j= (n1+3*no/2+2*n2+2):n,
    if j == (n1+3*no/2+2*n2+2),
        B(k)=V(i,j-1)*(y(i-1,j)*Epsr(i-1,j-1)+y(i,j)*Epsr(i,j-1))/x(i,j-1);
        A(k,k+1)=- (y(i-1,j)*Epsr(i-1,j)+y(i,j)*Epsr(i,j))/x(i,j);
    elseif j == n,
        B(k)=V(i,j+1)*(y(i-1,j)*Epsr(i-1,j)+y(i,j)*Epsr(i,j))/x(i,j);
        A(k,k-1)=- (y(i-1,j)*Epsr(i-1,j-1)+y(i,j)*Epsr(i,j-1))/x(i,j-1);

```

```

else
    B(k)=0.0;
    A(k,k-1)=-(y(i-1,j)*Epsr(i-1,j-1)+y(i,j)*Epsr(i,j-1))/x(i,j-1);
    A(k,k+1)=-(y(i-1,j)*Epsr(i-1,j)+y(i,j)*Epsr(i,j))/x(i,j);
end
A(k,k) =Epsr(i,j)*(x(i,j)/y(i,j)+y(i,j)/x(i,j))...
    +Epsr(i,j-1)*(x(i,j-1)/y(i,j)+y(i,j)/x(i,j-1))...
    +Epsr(i-1,j)*(x(i,j)/y(i-1,j)+y(i-1,j)/x(i,j))...
    +Epsr(i-1,j-1)*(x(i,j-1)/y(i-1,j)+y(i-1,j)/x(i,j-1));
A(k,k-(n-1-nmx))=-(x(i,j-1)*Epsr(i-1,j-1)+x(i,j)*Epsr(i-1,j))/y(i-1,j);
A(k,k+(n-1-nmx))=-(x(i,j-1)*Epsr(i,j-1)+x(i,j)*Epsr(i,j))/y(i,j);
k=k+1;
end
for i=(m/2+nox+2):(m/2+nox+nm),
    for j=2:n1+no/2,
        if j == 2,
            B(k)=V(i,j-1)/(x(i,j-1)*(x(i,j-1)+x(i,j)));
            A(k,k+1)=-1/(x(i,j)*(x(i,j-1)+x(i,j)));
        elseif j == n1+no/2,
            B(k)=V(i,j+1)/(x(i,j)*(x(i,j-1)+x(i,j)));
            A(k,k-1)=-1/(x(i,j-1)*(x(i,j-1)+x(i,j)));
        else
            B(k)=0.0;
            A(k,k-1)=-1/(x(i,j-1)*(x(i,j-1)+x(i,j)));
            A(k,k+1)=-1/(x(i,j)*(x(i,j-1)+x(i,j)));
        end
        A(k,k) =1/(x(i,j-1)*x(i,j))+1/(y(i-1,j)*y(i,j));
        A(k,k-(n-1-nmx))=-1/(y(i-1,j)*(y(i-1,j)+y(i,j)));
        A(k,k+(n-1-nmx))=-1/(y(i,j)*(y(i-1,j)+y(i,j)));
        k=k+1;
    end
end

for j=(n1+3*no/2+2*n2+2):n,
    if j == (n1+3*no/2+2*n2+2),
        B(k)=V(i,j-1)/(x(i,j-1)*(x(i,j-1)+x(i,j)));
        A(k,k+1)=-1/(x(i,j)*(x(i,j-1)+x(i,j)));
    elseif j == n,
        B(k)=V(i,j+1)/(x(i,j)*(x(i,j-1)+x(i,j)));
        A(k,k-1)=-1/(x(i,j-1)*(x(i,j-1)+x(i,j)));
    else
        B(k)=0.0;
        A(k,k-1)=-1/(x(i,j-1)*(x(i,j-1)+x(i,j)));
        A(k,k+1)=-1/(x(i,j)*(x(i,j-1)+x(i,j)));
    end
    A(k,k) =1/(x(i,j-1)*x(i,j))+1/(y(i-1,j)*y(i,j));
    A(k,k-(n-1-nmx))=-1/(y(i-1,j)*(y(i-1,j)+y(i,j)));
    A(k,k+(n-1-nmx))=-1/(y(i,j)*(y(i-1,j)+y(i,j)));
    k=k+1;
end
end
end

i=m/2+nox+nm+1;
for j=2:n1+no/2,
    if j == 2,

```

```

        B(k)=V(i,j-1)/(x(i,j-1)*(x(i,j-1)+x(i,j)));
        A(k,k+1)=-1/(x(i,j)*(x(i,j-1)+x(i,j)));
    elseif j == n1+no/2,
        B(k)=V(i,j+1)/(x(i,j)*(x(i,j-1)+x(i,j)));
        A(k,k-1)=-1/(x(i,j-1)*(x(i,j-1)+x(i,j)));
    else
        B(k)=0.0;
        A(k,k-1)=-1/(x(i,j-1)*(x(i,j-1)+x(i,j)));
        A(k,k+1)=-1/(x(i,j)*(x(i,j-1)+x(i,j)));
    end
    A(k,k) =1/(x(i,j-1)*x(i,j))+1/(y(i-1,j)*y(i,j));
    A(k,k-(n-1-nmx))=-1/(y(i-1,j)*(y(i-1,j)+y(i,j)));
    A(k,k+(n-1-nmx))=-1/(y(i,j)*(y(i-1,j)+y(i,j)));
    k=k+1;
end

for j=(n1+3*no/2+2*n2+2):n,
    if j == (n1+3*no/2+2*n2+2),
        B(k)=V(i,j-1)/(x(i,j-1)*(x(i,j-1)+x(i,j)));
        A(k,k+1)=-1/(x(i,j)*(x(i,j-1)+x(i,j)));
    elseif j == n,
        B(k)=V(i,j+1)/(x(i,j)*(x(i,j-1)+x(i,j)));
        A(k,k-1)=-1/(x(i,j-1)*(x(i,j-1)+x(i,j)));
    else
        B(k)=0.0;
        A(k,k-1)=-1/(x(i,j-1)*(x(i,j-1)+x(i,j)));
        A(k,k+1)=-1/(x(i,j)*(x(i,j-1)+x(i,j)));
    end
    A(k,k) =1/(x(i,j-1)*x(i,j))+1/(y(i-1,j)*y(i,j));
    A(k,k-(n-1-nmx))=-1/(y(i-1,j)*(y(i-1,j)+y(i,j)));
    A(k,k+n-1)=-1/(y(i,j)*(y(i-1,j)+y(i,j)));
    k=k+1;
end

i=m/2+nox+nm+2;
for j=2:(n1+no/2),
    if j == 2,
        B(k)=V(i,j-1)/(x(i,j-1)*(x(i,j-1)+x(i,j)));
    else
        B(k)=0.0;
        A(k,k-1)=-1/(x(i,j-1)*(x(i,j-1)+x(i,j)));
    end
    A(k,k) =1/(x(i,j-1)*x(i,j))+1/(y(i-1,j)*y(i,j));
    A(k,k+1)=-1/(x(i,j)*(x(i,j-1)+x(i,j)));
    A(k,k-(n-1-nmx))=-1/(y(i-1,j)*(y(i-1,j)+y(i,j)));
    A(k,k+n-1)=-1/(y(i,j)*(y(i-1,j)+y(i,j)));
    k=k+1;
end

for j=(n1+no/2+1):(n1+3*no/2+2*n2+1),
    B(k) =V(i-1,j)/(y(i-1,j)*(y(i-1,j)+y(i,j)));
    A(k,k) =1/(x(i,j)*x(i,j-1))+1/(y(i-1,j)*y(i,j));
    A(k,k-1)=-1/(x(i,j-1)*(x(i,j-1)+x(i,j)));
    A(k,k+1)=-1/(x(i,j)*(x(i,j-1)+x(i,j)));

```

```

    A(k,k+n-1)=-1/(y(i,j)*(y(i-1,j)+y(i,j)));
    k=k+1;
end

for j=(n1+3*no/2+2*n2+2):n,
    if j == n,
        B(k)=V(i,j+1)/(x(i,j)*(x(i,j-1)+x(i,j)));
    else
        B(k)=0.0;
        A(k,k+1)=-1/(x(i,j)*(x(i,j-1)+x(i,j)));
    end
    A(k,k)=1/(x(i,j-1)*x(i,j))+1/(y(i-1,j)*y(i,j));
    A(k,k-1)=-1/(x(i,j-1)*(x(i,j-1)+x(i,j)));
    A(k,k-n+1)=-1/(y(i-1,j)*(y(i-1,j)+y(i,j)));
    A(k,k+n-1)=-1/(y(i,j)*(y(i-1,j)+y(i,j)));
    k=k+1;
end

for i=(m/2+nox+nm+3):(m/2+nox+nm+nd);
    for j=2:n,
        if j == 2,
            B(k)=V(i,j-1)/(x(i,j-1)*(x(i,j-1)+x(i,j)));
            A(k,k+1)=-1/(x(i,j)*(x(i,j-1)+x(i,j)));
        elseif j == n
            B(k)=V(i,j+1)/(x(i,j)*(x(i,j-1)+x(i,j)));
            A(k,k-1)=-1/(x(i,j-1)*(x(i,j-1)+x(i,j)));
        else
            B(k)=0.0;
            A(k,k-1)=-1/(x(i,j-1)*(x(i,j-1)+x(i,j)));
            A(k,k+1)=-1/(x(i,j)*(x(i,j-1)+x(i,j)));
        end
        A(k,k) =1/(x(i,j-1)*x(i,j))+1/(y(i-1,j)*y(i,j));
        A(k,k-n+1)=-1/(y(i-1,j)*(y(i-1,j)+y(i,j)));
        A(k,k+n-1)=-1/(y(i,j)*(y(i-1,j)+y(i,j)));
        if (j == n1+no/2+1) | (j == n1+3*no/2+2*n2+1),
            A(k,k) =Epsr(i,j)*(x(i,j)/y(i,j)+y(i,j)/x(i,j))...
                +Epsr(i,j-1)*(x(i,j-1)/y(i,j)+y(i,j)/x(i,j-1))...
                +Epsr(i-1,j)*(x(i,j)/y(i-1,j)+y(i-1,j)/x(i,j))...
                +Epsr(i-1,j-1)*(x(i,j-1)/y(i-1,j)+y(i-1,j)/x(i,j-1));
            A(k,k-1)=-y(i-1,j)*Epsr(i-1,j-1)+y(i,j)*Epsr(i,j-1))/x(i,j-1);
            A(k,k+1)=-y(i-1,j)*Epsr(i-1,j)+y(i,j)*Epsr(i,j))/x(i,j);
            A(k,k-n+1)=-x(i,j-1)*Epsr(i-1,j-1)+x(i,j)*Epsr(i-1,j))/y(i-1,j);
            A(k,k+n-1)=-x(i,j-1)*Epsr(i,j-1)+x(i,j)*Epsr(i,j))/y(i,j);
            B(k)=0.0;
        end
        k=k+1;
    end
end

i=(m/2+nox+nm+nd+1);
for j=2:(n1+no/2),
    if j == 2,
        B(k)=V(i,j-1)/(x(i,j-1)*(x(i,j-1)+x(i,j)));
    else
        B(k)=0.0;

```

```

        A(k,k-1) = -1/(x(i,j-1)*(x(i,j-1)+x(i,j)));
    end
    A(k,k)=1/(x(i,j-1)*x(i,j))+1/(y(i-1,j)*y(i,j));
    A(k,k+1)=-1/(x(i,j)*(x(i,j-1)+x(i,j)));
    A(k,k-n+1)=-1/(y(i-1,j)*(y(i-1,j)+y(i,j)));
    A(k,k+n-1)=-1/(y(i,j)*(y(i-1,j)+y(i,j)));
    k=k+1;
end

for j=(n1+no/2+1):(n1+3*no/2+2*n2+1),
    B(k)=0.0;
    A(k,k) =Epsr(i,j)*(x(i,j)/y(i,j)+y(i,j)/x(i,j))...
        +Epsr(i,j-1)*(x(i,j-1)/y(i,j)+y(i,j)/x(i,j-1))...
        +Epsr(i-1,j)*(x(i,j)/y(i-1,j)+y(i-1,j)/x(i,j))...
        +Epsr(i-1,j-1)*(x(i,j-1)/y(i-1,j)+y(i-1,j)/x(i,j-1));
    A(k,k-1)=-y(i-1,j)*Epsr(i-1,j-1)+y(i,j)*Epsr(i,j-1))/x(i,j-1);
    A(k,k+1)=-y(i-1,j)*Epsr(i-1,j)+y(i,j)*Epsr(i,j))/x(i,j);
    A(k,k-n+1)=-x(i,j-1)*Epsr(i-1,j-1)+x(i,j)*Epsr(i-1,j))/y(i-1,j);
    A(k,k+n-1)=-x(i,j-1)*Epsr(i,j-1)+x(i,j)*Epsr(i,j))/y(i,j);
    k=k+1;
end

for j=(n1+3*no/2+2*n2+2):n,
    if j == n,
        B(k)=V(i,j+1)/(x(i,j)*(x(i,j-1)+x(i,j)));
    else
        B(k)=0.0;
        A(k,k+1)=-1/(x(i,j)*(x(i,j-1)+x(i,j)));
    end
    A(k,k) =1/(x(i,j-1)*x(i,j))+1/(y(i-1,j)*y(i,j));
    A(k,k-1)=-1/(x(i,j-1)*(x(i,j-1)+x(i,j)));
    A(k,k-n+1)=-1/(y(i-1,j)*(y(i-1,j)+y(i,j)));
    A(k,k+n-1)=-1/(y(i,j)*(y(i-1,j)+y(i,j)));
    k=k+1;
end

for i=(m/2+nox+nm+nd+2):(m-1),
    for j=2:n,
        if j == 2,
            B(k)=V(i,j-1)/(x(i,j-1)*(x(i,j-1)+x(i,j)));
            A(k,k+1)=-1/(x(i,j)*(x(i,j-1)+x(i,j)));
        elseif j == n,
            B(k)=V(i,j+1)/(x(i,j)*(x(i,j-1)+x(i,j)));
            A(k,k-1)=-1/(x(i,j-1)*(x(i,j-1)+x(i,j)));
        else
            B(k)=0.0;
            A(k,k-1)=-1/(x(i,j-1)*(x(i,j-1)+x(i,j)));
            A(k,k+1)=-1/(x(i,j)*(x(i,j-1)+x(i,j)));
        end
        A(k,k) =1/(x(i,j-1)*x(i,j))+1/(y(i-1,j)*y(i,j));
        A(k,k-n+1)=-1/(y(i-1,j)*(y(i-1,j)+y(i,j)));
        A(k,k+n-1)=-1/(y(i,j)*(y(i-1,j)+y(i,j)));
        k=k+1;
    end
end

```

```

end
% Corner 3,
j=2; i=m;
B(k)=V(i,j-1)/(x(i,j-1)*(x(i,j-1)+x(i,j)))+V(i+1,j)/(y(i,j)*(y(i-1,j)+y(i,j)));
A(k,k)=1/(x(i,j-1)*x(i,j))+1/(y(i,j)*y(i-1,j));
A(k,k+1)=-1/(x(i,j)*(x(i,j-1)+x(i,j)));
A(k,k-n+1)=-1/(y(i-1,j)*(y(i-1,j)+y(i,j)));
k=k+1;
for j=3:n-1,
    B(k) = V(i+1,j)/(y(i,j)*(y(i-1,j)+y(i,j)));
    A(k,k)=1/(x(i,j-1)*x(i,j))+1/(y(i-1,j)*y(i,j));
    A(k,k-1)=-1/(x(i,j-1)*(x(i,j-1)+x(i,j)));
    A(k,k+1)=-1/(x(i,j)*(x(i,j-1)+x(i,j)));
    A(k,k-n+1)=-1/(y(i-1,j)*(y(i-1,j)+y(i,j)));
    k=k+1;
end
% Corner 4,
j=n; i=m;
B(k)=V(i,j+1)/(x(i,j)*(x(i,j)+x(i,j-1)))+V(i+1,j)/(y(i,j)*(y(i,j)+y(i-1,j)));
A(k,k)=1/(x(i,j)*x(i,j-1))+1/(y(i,j)*y(i-1,j));
A(k,k-1)=-1/(x(i,j-1)*(x(i,j)+x(i,j-1)));
A(k,k-n+1)=-1/(y(i-1,j)*(y(i-1,j)+y(i,j)));

Phi = inv(A)*B;
ko = 1;
for i = 2:m, % Boundary Value Problem
    for j = 2:n,
        if (((i > (m/2+nox)) & (i < (m/2+nox+nm+2))) & ...
            ((j > (n1+no/2)) & (j < (n1+3*no/2+2*n2+2))))),
            V(i,j)=Vo;
        else
            V(i,j) = Phi(ko); ko = ko+1;
        end
    end
end
clear Phi;

% Calculation of the electric field in the computation domain
% *****
U = 0;
for i = 1:m,
    for j = 1:n,
        x(i,j)=0.5*((V(i,j+1)-V(i,j))/x(i,j)+(V(i+1,j+1)-V(i+1,j))/x(i+1,j));
        Ey(i,j)=0.5*((V(i+1,j)-V(i,j))/y(i,j)+(V(i+1,j+1)-V(i,j+1))/y(i,j+1));
        Exy = sqrt(Ex(i,j)*Ex(i,j) + Ey(i,j)*Ey(i,j));
        U = U+0.125*Eps0*Epsr(i,j)*Exy^2*(x(i,j)+x(i+1,j))*(y(i,j)+y(i,j+1));
    end
end

% Determination of the gap capacitance
% C = Q/V, where Q is the total charge accumulated on the lower electrode
% Qenc = Int(D.ds)
% Q per unit square = Int (D.dl) = Int(Eps E.dl) =Eps Int(Eydx+Exdy)
Q1=0; i=m/2; % bottom

```

```

for j=n1:n-1,      Q1=Q1+Eps0*Epsr(i,j)*Ey(i,j)*(x(i,j)+x(i+1,j))/2; end
Q2=0;   i=m-ng;   % top
for j=n1:n-1,      Q2=Q2+Eps0*Epsr(i,j)*Ey(i,j)*(x(i,j)+x(i+1,j))/2; end
Q3=0;   j=n1;     % left
for i=m/2:m-ng,    Q3=Q3+Eps0*Epsr(i,j)*Ex(i,j)*(y(i,j)+y(i,j+1))/2; end
Q4=0;   j=n-1;    % right
for i=m/2:m-ng,    Q4=Q4+Eps0*Epsr(i,j)*Ex(i,j)*(y(i,j)+y(i,j+1))/2; end
Qenc = abs(Q1)+abs(Q2)+abs(Q3)+abs(Q4); % Total charge
wmax = max(w);

% Determination of the induced electrostatic charge and force distributions on the
% membrane.
% *****
for j=1:n,
    Qm(j) = Eps0*(Ex(m,j)*(y(m,j)+y(m,j+1))+Ey(m,j)*(x(m,j)+x(m+1,j)))...
            *b/(x(m,j)+x(m+1,j));
    f(j) = 0.5*Eps0*(Ex(m,j)*Ex(m,j)+Ey(m,j)*Ey(m,j))*b;
end

Qmo = Qm(1);      Qm(1) = 0;      fo = f(1);      f(1) = 0;
for j = 2:n,
    Qmx = Qm(j);      fox = f(j);
    Qm(j) = 0.5*(Qmo+Qmx);      f(j) = 0.5*(fo+fox);
    Qmo = Qmx;      fo = fox;
end
Qm(n+1) = 0;      f(n+1) = 0;

% Mechanical model
% *****
% Solving beam equation (Euler-Bernoulli Beam Equation) using method of variation
% of parameters to solve 4th order non-homogenous differential equation to
% calculate the beam deformation w(x) arises from the induced electrostatic force
% on the bridge f(x) taking into account the residual and axial stresses.

Tr = Sigma*(1-nu)*b*t;      Ta = 10;      Tao = 0.01;      F = f/EI;
while abs(Ta - Tao) >= 1E-10,
    Ta = Tao;      k = sqrt((Tr+Ta)/EI);
    Ak = [1 0 1 1; 0 1 k -k; 1 L exp(k*L) exp(-k*L); 0 1 k*exp(k*L) -k*exp(-k*L)];
    b1 = -1/(k*k)*Int_0_L(xx(m+1,:).*F,xx(m+1,:))+L/(k*k)*Int_0_L(F,xx(m+1,:))...
          - exp(k*L)/(2*k^3)*Int_0_L(exp(-k*xx(m+1,:)).*F,xx(m+1,:))...
          + exp(-k*L)/(2*k^3)*Int_0_L(exp(k*xx(m+1,:)).*F,xx(m+1,:));
    b2 = 1/(k*k)*Int_0_L(F,xx(m+1,:))...
          - exp(k*L)/(2*k*k)*Int_0_L(exp(-k*xx(m+1,:)).*F,xx(m+1,:))...
          - exp(-k*L)/(2*k*k)*Int_0_L(exp(k*xx(m+1,:)).*F,xx(m+1,:));
    Bk = [0; 0; b1; b2];      ak = inv(Ak)*Bk;
    w(1) = 0;
    for j = 2:n,
        w(j)=ak(1)+ak(2)*xx(m+1,j)+ak(3)*exp(k*xx(m+1,j))+ak(4)*exp(-k*xx(m+1,j))...
              + 1/(k*k)*Int_0_x(xx(m+1,:).*F,xx(m+1,:),j)...
              - xx(m+1,j)/(k*k)*Int_0_x(F,xx(m+1,:),j)...
              + exp(k*xx(m+1,j))/(2*k^3)*Int_0_x(exp(-k*xx(m+1,:)).*F,xx(m+1,:),j)...
              - exp(-k*xx(m+1,j))/(2*k^3)*Int_0_x(exp(k*xx(m+1,:)).*F,xx(m+1,:),j);
    end
    w(n+1) = 0;

```

```

[dw2,x1] = First_derivative2(w,xx(m+1,:));           [Tao] = Int_0_L(dw2,x1);
Tao = E*t*b*Tao/(2*L);
end                                                    % End of the Mechanical model
clear F;      clear dw2;                               clear x1;
C_it(it) = 2E15*U*b/Vo^2;                             % total capacitance in fF
w_it(it) = max(w);
end                                                    % End the iteration to calculate deformation
for j = 1:n+1,                                       shape(j) = go-w(j);           end
CPU_time = toc                                       % Elapsed time in seconds

clear A; clear B; clear Epsr; clear w; clear x; clear y; clear Ex; clear Ey;

save Results2D                                       % Save results in a mat file named Results2D.mat

subplot(2,2,1); hold on
for i=1:m+1, plot(xx(i,:).*1E6,yy(i,:).*1E6); end;
for j=1:n+1, plot(xx(:,j).*1E6,yy(:,j).*1E6); end;
axis([0 L*1E6 0 max(yy(:,1))*1E6]); title('Mesh distribution');
xlabel('x [\mum]'); ylabel('y [\mum]'); hold off

subplot(2,2,2); [c, h]=contour(xx(1,:).*1E6,yy(:,1).*1E6,V); grid;
xlabel('x [\mum]'); ylabel('y [\mum]');
title('Potential distribution')

subplot(2,2,3); plot(xx(1,:).*1E6,Qm), grid;
xlabel('x (\mum)'); ylabel('Q [coulombs/m]'); axis([0 L*1E6 1.5*min(Qm) 0]);
title('Charge density distribution induced on the membrane');

subplot(2,2,4); plot(xx(1,:).*1E6,f), grid; axis([0 L*1E6 0 1.5*max(f)]);
xlabel('x (\mum)'); ylabel('Force, f(x) [N/m]');
title('Force density distribution induced on the bridge');

figure; subplot(2,2,1); plot(w_it*1e6,'linewidth',2), grid;
xlabel('Number iterations'); ylabel('Position [\mum]');
axis([0 it 0.95*min(w_it)*1E6 1.05*max(w_it)*1E6]);
title('Position of the bridge-middle-node vs. # of iterations');

subplot(2,2,2); plot(C_it,'linewidth',2), grid;
xlabel('Number of iterations'); ylabel('Capacitance [fF]');
axis([0 it 0.95*min(C_it) 1.05*max(C_it)]); title('Capacitance vs. iterations');

subplot(2,1,2); plot(xx(1,:).*1E6,shape*1E6), grid;
xlabel('x (\mum)'); ylabel('Gap height (\mum)'); axis([0 L*1E6 0 go*1E6]);
title('Shape of the bridge actuation voltage of Vo');

% The END of the program LapVarPar.m

```

# Appendix B

## Matlab 3-D Coupled Electrostatic-Mechanical Model Scripts

These are the Matlab scripts to simulate the behavior of an electrostatically actuated fixed-fixed beam RF MEMS capacitive switch. They run on Matlab version 7.0. MEMS3D.m is the main program, which reads the switch parameters from the file DataIn.m and it requires an additional program SolvePlateEqUsingFDM.m to solve the plate equation to determine the bridge deformation using the FDM. It produces an output file ResultsMEMS3D.m during the simulation, which has the results.

### B.1 Matlab Code of the 3-D Coupled Model

#### MEMSDModel.m

```
% *****  
% 3-D Coupled Electrostatic-Mechanical Model for RF MEMS Shunt Capacitive Switches  
% File name: MEMS3D_Model.m, August, 2005  
% By Ehab K. I. Hamad, E-mail:Ehab.Hamad@E-Technik.Uni-Magdeburg.DE  
% This program calculates the pull down voltage for a shunt-capacitive MEMS switch  
% *****  
% Program Algorithm:  
% 1. The electrostatic model solves the electrostatic problem of the switch  
%    structure to compute the potential distribution in the 3-D computational  
%    domain. The computation of the potential is based on the integral form of  
%    Gauss's law and constructing an updating equation for the potential.  
% 2. The updated equation is solved using an iterative technique assuming an  
%    artificial absorbing boundary conditions, where the coefficients of the  
%    updating equation are calculated outside the iterative loop, which saves much  
%    time. Then the electrostatic field and force distributions are calculated.  
% 3. The mechanical model determines the bridge deformation, which corresponds to  
%    the electrostatic force calculated by the electrostatic model by  
%    solving the plate equation using the FDM.  
% 4. Re-shape the membrane and repeat 1 to 4 till getting steady-state solution.  
%*****
```

```

clear all;
tic % to measure the starting CPU time
% Input parameters and the MEMS switch dimensions:
Maxiter=input(' Inter Maximum # of iterations, niter ='); % Maximum # of iteration
% to find the potential distribution if
% the specified error could not reach.
percent = input(' Inter required percentage error % = ');
Vg = 0; % Voltage applied to the CPW ground planes and the bridge

DataIn.m % Read an input file which has the switch's parameters

% Calculation of the spring constant K and the pull-down voltage from the 1D model
% given by Muldavin and Rebeiz, MTT-T Juni 2000.
K = 32*E*b*t^3/L^3+8*Sigma*(1-nu)*b*t/L; Vpi1D = sqrt(8*K*go^3/(27*Eps0*W*b));
D = E*t^3/(12*(1-nu^2)); % Flexural rigidity of the bridge [Pa.m^3=N.m]

%-----
L=L/2; ax=2*L; n=30; nx=45; dx=L/n; ns=4; ds=ts/ns;
W=W/2; nwx=round(W/dx); dxo=(ax-L-ts)/(nx-n-ns);
b=b/2; ay=5*b; m=20; ny=40; dy=b/m; dyo=(ay-b)/(ny-m);
% ax, ay, and az are the outer box dimensions along x, y, and z, respectively
% nx, ny, and nz are the number of meshes along x, y, and z, respectively

H=t+go+td+tm+tox; Ha=5*H; Hb=10*H; az=Hb+H+Ha;
nt=4; ng=8; nd=4; nm=4; nox=3;
nH=nt+ng+nd+nm+nox; nHb=nH; nHa=round(0.5*nH); nz=nHb+nH+nHa;
dHa=Ha/nHa; dt=t/nt; dg=go/ng; dd=td/nd;
dm=tm/nm; dox=tox/nox; dHb=Hb/nHb;

tgg = tm; ngz = nm; count = 0; got = 0;
if tg <= tgg, got = 1; end;

% To find how many mesh lines are needed in the CPW's ground planes along z-axis;
while got==0,
    for k = 1:nd, count = count+1; tgg = tgg + dd;
        if tgg >= tg, ngz = ngz+count; got = 1; clear tgg;
            break
        end
    end
    if got == 1, break; end;
    for k = 1:ng, count = count+1; tgg = tgg + dg;
        if tgg >= tg, ngz = ngz+count; got = 1; clear tgg;
            break
        end
    end
    if got == 1, break; end;
    for k = 1:nt, count = count+1; tgg = tgg + dt;
        if tgg >= tg, ngz = ngz+count; got = 1; clear tgg;
            break
        end
    end
    if got ~= 1,
        sprintf(' ERROR: Please check the CPW's ground plane thickness')
    end
end

```

```

        break
    end
end

w = zeros(m+1,n+1);           % Bending function of the bridge in two dimensions
Er = ones(ny,nx,nz);         Er(1:m,1:nwx,nHb+nox+nm+1:nHb+nox+nm+nd) = Epsr;
Er(1:ny,1:nx,nHb+1:nHb+nox) = 3.9;           Er(1:ny,1:nx,1:nHb) = 11.9;
Ex =zeros(ny+1,nx+1,nz+1); Ey =zeros(ny+1,nx+1,nz+1); Ez =zeros(ny+1,nx+1,nz+1);

% Constructing the non-uniform 3-D grid. After deformation this grid is getting to
% be non-rectangular, this non-rectangular grid is treated by linear interpolation
% to be a rectangular.
% -----
for i = 1:ny+1,
    for k = 1:nz+1
        x(i,1,k) = 0;
        for j = 2:n+1,           x(i,j,k) = x(i,j-1,k) + dx;           end;
        for j = n+2:n+ns+1,     x(i,j,k) = x(i,j-1,k) + ds;           end;
        for j = 1:nx-n-ns,
            if (ax-L-ts)/(nx-n-ns) > ds,
                dxo = ds + 2*((ax-L-ts)/(nx-n-ns)-ds)*(j-1)/(nx-n-ns-1);           end;
                x(i,n+ns+1+j,k) = x(i,n+ns+j,k) + dxo;
            end
        end
    end
end
for j = 1:nx+1,
    for k = 1:nz+1,
        y(1,j,k) = 0;
        for i = 2:m+1,           y(i,j,k) = y(i-1,j,k) + dy;           end;
        for i = 1:ny-m,
            if (ay-b)/(ny-m) > dy,
                dyo = dy + 2*((ay-b)/(ny-m)-dy)*(i-1)/(ny-m-1);           end;
                y(m+1+i,j,k) = y(m+i,j,k) + dyo;
            end
        end
    end
end
for i = 1:ny+1,
    for j = 1:nx+1,
        z(i,j,1) = 0;
        for k = 2:nHb+1,           z(i,j,k) = z(i,j,k-1)+dHb;           end;
        for k = nHb+2:nHb+nox+1,   z(i,j,k) = z(i,j,k-1)+dox;           end;
        for k = nHb+nox+2:nHb+nox+nm+1,   z(i,j,k) = z(i,j,k-1)+dm;           end;
        for k = nHb+nox+nm+2:nHb+nox+nm+nd+1,   z(i,j,k) = z(i,j,k-1)+dd;           end;
    end
end

% Starting the applied voltage from Vo = 0 till getting the pull down voltage, Vpi
ii = 0;           Vpi=0;           step=5;
while Vpi == 0,           % Starting voltage loop
    ii = ii+1;
    if w(1,1) >= 0.10*go,   step = 2.0;   end
    if w(1,1) >= 0.15*go,   step = 1.0;   end
    if w(1,1) >= 0.20*go,   step = 0.5;   end           % Variable step voltage
    if w(1,1) >= 0.25*go,   step = 0.2;   end
end

```

```

if ii == 1, Vo = 1E-6; elseif ii == 2, Vo = step; else Vo = Vo+step; end;
Ermax = percent*Vo/100;
wmax = 100; it = 0; Vo

% Starting iterations to calculate the steady-state bridge's deformation by forth
% and back between the electrostatic and mechanical models
while abs(w(1,1) - wmax) > 1E-9,
if w(1,1) > (2/3)*go,
    sprintf(' Stopped because Wmax > go, i.e. Vo > Vpi')
    Vpi = Vo
    break
end
if it >= 15,
    break
end
it=it+1 % Count the number of iterations needed to get the steady-state condition

% Electrostatic Model:
V = zeros(ny+1,nx+1,nz+1); % Initialization of all nodes to be zero
Ccond = zeros(ny,nx,nz); Cg = zeros(ny,nx,nz);
CR = zeros(ny,nx,nz); CL = zeros(ny,nx,nz); CT = zeros(ny,nx,nz);
CB = zeros(ny,nx,nz); CF = zeros(ny,nx,nz); CK = zeros(ny,nx,nz);

% Adapting the mesh size and grid shape in the air gap region above and under the
% membrane while it is getting deformed.
for i = 1:ny+1,
    for j = 1:nx+1,
        if j >= n+1,
            for k = nHb+nox+nm+nd+2:nHb+nox+nm+nd+ng+1,
                z(i,j,k) = z(i,j,k-1)+dg; end
            for k = nHb+nox+nm+nd+ng+2:nHb+nH+1, z(i,j,k) = z(i,j,k-1)+dt; end;
            for k = nHb+nH+2:nz+1, z(i,j,k) = z(i,j,k-1)+dHa; end;
        elseif i >= m+1,
            for k = nHb+nox+nm+nd+2:nHb+nox+nm+nd+ng+1,
                z(i,j,k) = z(i,j,k-1)+(go-w(m+1,j))/ng; end;
            for k = nHb+nox+nm+nd+ng+2:nHb+nH+1, z(i,j,k) = z(i,j,k-1)+dt; end;
            for k = nHb+nH+2:nz+1, z(i,j,k) = z(i,j,k-1)+(Ha+w(m+1,j))/nHa; end;
        else
            for k = nHb+nox+nm+nd+2:nHb+nox+nm+nd+ng+1,
                z(i,j,k) = z(i,j,k-1)+(go-w(i,j))/ng; end
            for k = nHb+nox+nm+nd+ng+2:nHb+nH+1, z(i,j,k) = z(i,j,k-1)+dt; end;
            for k = nHb+nH+2:nz+1, z(i,j,k) = z(i,j,k-1)+(Ha+w(i,j))/nHa; end;
        end
    end
end
end

% The computation of the potential distribution in the 2-D computational domain.
% constructing the potential coefficients matrix before starting the iterations.
% -----
for i = 1:ny,
    for j = 1:nx,
        for k = 2:nz
            if k > nHb+nox & k <= nHb+nox+nm+1 & j <= nwx+1,
                Ccond(i,j,k) = Vo; % Voltage applied to the CPW signal line
            end
        end
    end
end

```

```

elseif (k > nHb+nox & k <= nHb+nox+ngz+1 & j >= n+1) | (k > nHb+nox...
    & k <= nHb+nox+nm+nd+ng+1 & j > n & j <= n+ns+1 & i <= m+1)...
    | (k > nHb+nox+nm+nd+ng & k <= nHb+nH+1 & j <= n+ns+1 & i <= m+1),
    Cg(i,j,k)= Vg; % Voltage applied to the CPW ground planes & bridge
elseif i == 1 & j == 1 & k > nHb+nox+nm+nd+1, % Coefficients for nodes
    ZT = 0.25*(2*z(i,j,k+1)+z(i,j+1,k+1)+z(i+1,j,k+1)); % on the z-axis
    ZB = 0.25*(2*z(i,j,k-1)+z(i,j+1,k-1)+z(i+1,j,k-1));
    x2 = x(i,j+1,k)-x(i,j,k); y2 = y(i+1,j,k)-y(i,j,k);
    z1e = z(i,j,k)-z(i,j,k-1); z2e = z(i,j,k+1)-z(i,j,k);
    z1 = z(i,j,k)-ZB; z2 = ZT-z(i,j,k);
    t1 = 0; t2 = Er(i,j,k)*x2*z2/y2 + Er(i,j,k-1)*x2*z1/y2;
    t3 = 0; t4 = Er(i,j,k)*y2*z2/x2 + Er(i,j,k-1)*y2*z1/x2;
    t5 = Er(i,j,k-1)*x2*y2/z1e; t6 = Er(i,j,k)*x2*y2/z2e;
    Co = t1+t2+t3+t4+t5+t6;
    CF(i,j,k) = t1/Co; CK(i,j,k) = t2/Co; CL(i,j,k) = t3/Co;
    CR(i,j,k) = t4/Co; CB(i,j,k) = t5/Co; CT(i,j,k) = t6/Co;
elseif i == 1 & j == 1,
    x2 = x(i,j+1,k)-x(i,j,k); y2 = y(i+1,j,k)-y(i,j,k);
    z1 = z(i,j,k)-z(i,j,k-1); z2 = z(i,j,k+1)-z(i,j,k);
    t1 = 0; t2 = Er(i,j,k)*x2*z2/y2 + Er(i,j,k-1)*x2*z1/y2;
    t3 = 0; t4 = Er(i,j,k)*y2*z2/x2 + Er(i,j,k-1)*y2*z1/x2;
    t5 = Er(i,j,k-1)*x2*y2/z1; t6 = Er(i,j,k)*x2*y2/z2;
    Co = t1+t2+t3+t4+t5+t6;
    CF(i,j,k) = t1/Co; CK(i,j,k) = t2/Co; CL(i,j,k) = t3/Co;
    CR(i,j,k) = t4/Co; CB(i,j,k) = t5/Co; CT(i,j,k) = t6/Co;
elseif i <= m+1 & j == 1 & k > nHb+nox+nm+nd+1, % Symmetry along x-axis
    ZT = 0.125*(4*z(i,j,k+1)+2*z(i,j+1,k+1)+z(i+1,j,k+1)+z(i-1,j,k+1));
    ZB = 0.125*(4*z(i,j,k-1)+2*z(i,j+1,k-1)+z(i+1,j,k-1)+z(i-1,j,k-1));
    x2 = x(i,j+1,k)-x(i,j,k); z1 = z(i,j,k)-ZB; z2 = ZT-z(i,j,k);
    y1 = y(i,j,k)-y(i-1,j,k); y2 = y(i+1,j,k)-y(i,j,k);
    z1e = z(i,j,k)-z(i,j,k-1); z2e = z(i,j,k+1)-z(i,j,k);
    t1 = Er(i-1,j,k)*x2*z2/y1 + Er(i-1,j,k-1)*x1*z1/y1;
    t2 = Er(i,j,k)*x2*z2/y2 + Er(i,j,k-1)*x2*z1/y2;
    t3 = 0;
    t4 = Er(i,j,k)*y2*z2/x2 + Er(i-1,j,k)*y1*z2/x2...
        + Er(i,j,k-1)*y2*z1/x2 + Er(i-1,j,k-1)*y1*z1/x2;
    t5 = Er(i,j,k-1)*x2*y2/z1e + Er(i-1,j,k-1)*x2*y1/z1e;
    t6 = Er(i,j,k)*x2*y2/z2e + Er(i-1,j,k)*x2*y1/z2e ;
    Co = t1+t2+t3+t4+t5+t6;
    CF(i,j,k) = t1/Co; CK(i,j,k) = t2/Co; CL(i,j,k) = t3/Co;
    CR(i,j,k) = t4/Co; CB(i,j,k) = t5/Co; CT(i,j,k) = t6/Co;
elseif j == 1, % Symmetry along x-axis, yz-plane
    x2 = x(i,j+1,k)-x(i,j,k);
    y1 = y(i,j,k)-y(i-1,j,k); y2 = y(i+1,j,k)-y(i,j,k);
    z1 = z(i,j,k)-z(i,j,k-1); z2 = z(i,j,k+1)-z(i,j,k);
    t1 = Er(i-1,j,k)*x2*z2/y1 + Er(i-1,j,k-1)*x1*z1/y1;
    t2 = Er(i,j,k)*x2*z2/y2 + Er(i,j,k-1)*x2*z1/y2;
    t3 = 0;
    t4 = Er(i,j,k)*y2*z2/x2 + Er(i-1,j,k)*y1*z2/x2...
        + Er(i,j,k-1)*y2*z1/x2 + Er(i-1,j,k-1)*y1*z1/x2;
    t5 = Er(i,j,k-1)*x2*y2/z1 + Er(i-1,j,k-1)*x2*y1/z1;
    t6 = Er(i,j,k)*x2*y2/z2 + Er(i-1,j,k)*x2*y1/z2 ;
    Co = t1+t2+t3+t4+t5+t6;
    CF(i,j,k) = t1/Co; CK(i,j,k) = t2/Co; CL(i,j,k) = t3/Co;

```

```

CR(i,j,k) = t4/Co;          CB(i,j,k) = t5/Co;          CT(i,j,k) = t6/Co;
elseif i == 1 & j < n+1 & k > nHb+nox+nm+nd+1, % Symmetry along y-axis
ZT = 0.125*(4*z(i,j,k+1)+z(i,j+1,k+1)+z(i,j-1,k+1)+2*z(i+1,j,k+1));
ZB = 0.125*(4*z(i,j,k-1)+z(i,j+1,k-1)+z(i,j-1,k-1)+2*z(i+1,j,k-1));
x1 = x(i,j,k)-x(i,j-1,k);          x2 = x(i,j+1,k)-x(i,j,k);
y2 = y(i+1,j,k)-y(i,j,k);          z1 = z(i,j,k)-ZB;          z2 = ZT-z(i,j,k);
z1e = z(i,j,k)-z(i,j,k-1);          z2e = z(i,j,k+1)-z(i,j,k);
t1 = 0;
t2 = Er(i,j,k)*x2*z2/y2          + Er(i,j-1,k)*x1*z2/y2...
    + Er(i,j,k-1)*x2*z1/y2          + Er(i,j-1,k-1)*x1*z1/y2;
t3 = Er(i,j-1,k)*y2*z2/x1          + Er(i,j-1,k-1)*y2*z1/x1;
t4 = Er(i,j,k)*y2*z2/x2          + Er(i,j,k-1)*y2*z1/x2;
t5 = Er(i,j,k-1)*x2*y2/z1e          + Er(i,j-1,k-1)*x1*y2/z1e;
t6 = Er(i,j,k)*x2*y2/z2e          + Er(i,j-1,k)*x1*y2/z2e;
Co = t1+t2+t3+t4+t5+t6;
CF(i,j,k) = t1/Co;          CK(i,j,k) = t2/Co;          CL(i,j,k) = t3/Co;
CR(i,j,k) = t4/Co;          CB(i,j,k) = t5/Co;          CT(i,j,k) = t6/Co;
elseif i == 1, % Symmetry along y-axis, xz-plane
x1 = x(i,j,k)-x(i,j-1,k);          x2 = x(i,j+1,k)-x(i,j,k);
y2 = y(i+1,j,k)-y(i,j,k);
z1 = z(i,j,k)-z(i,j,k-1);          z2 = z(i,j,k+1)-z(i,j,k);
t1 = 0;
t2 = Er(i,j,k)*x2*z2/y2          + Er(i,j-1,k)*x1*z2/y2...
    + Er(i,j,k-1)*x2*z1/y2          + Er(i,j-1,k-1)*x1*z1/y2;
t3 = Er(i,j-1,k)*y2*z2/x1          + Er(i,j-1,k-1)*y2*z1/x1;
t4 = Er(i,j,k)*y2*z2/x2          + Er(i,j,k-1)*y2*z1/x2;
t5 = Er(i,j,k-1)*x2*y2/z1          + Er(i,j-1,k-1)*x1*y2/z1;
t6 = Er(i,j,k)*x2*y2/z2          + Er(i,j-1,k)*x1*y2/z2;
Co = t1+t2+t3+t4+t5+t6;
CF(i,j,k) = t1/Co;          CK(i,j,k) = t2/Co;          CL(i,j,k) = t3/Co;
CR(i,j,k) = t4/Co;          CB(i,j,k) = t5/Co;          CT(i,j,k) = t6/Co;
elseif i <= m+1 & j < n+1 & k > nHb+nox+nm+nd+1, % Non-rectangular region
ZT = 0.125*(4*z(i,j,k+1)+z(i,j+1,k+1)+z(i,j-1,k+1)+z(i+1,j,k+1)...
    +z(i-1,j,k+1));
ZB = 0.125*(4*z(i,j,k-1)+z(i,j+1,k-1)+z(i,j-1,k-1)+z(i+1,j,k-1)...
    +z(i-1,j,k-1));
x1 = x(i,j,k)-x(i,j-1,k);          x2 = x(i,j+1,k)-x(i,j,k);
y1 = y(i,j,k)-y(i-1,j,k);          y2 = y(i+1,j,k)-y(i,j,k);
z1 = z(i,j,k)-ZB;          z2 = ZT-z(i,j,k);
z1e = z(i,j,k)-z(i,j,k-1);          z2e = z(i,j,k+1)-z(i,j,k);
t1 = Er(i-1,j,k)*x2*z2/y1          + Er(i-1,j-1,k)*x1*z2/y1...
    + Er(i-1,j,k-1)*x2*z1/y1          + Er(i-1,j-1,k-1)*x1*z1/y1;
t2 = Er(i,j,k)*x2*z2/y2          + Er(i,j-1,k)*x1*z2/y2...
    + Er(i,j,k-1)*x2*z1/y2          + Er(i,j-1,k-1)*x1*z1/y2;
t3 = Er(i-1,j-1,k)*y1*z2/x1          + Er(i,j-1,k)*y2*z2/x1...
    + Er(i-1,j-1,k-1)*y1*z1/x1          + Er(i,j-1,k-1)*y2*z1/x1;
t4 = Er(i,j,k)*y2*z2/x2          + Er(i-1,j,k)*y1*z2/x2...
    + Er(i,j,k-1)*y2*z1/x2          + Er(i-1,j,k-1)*y1*z1/x2;
t5 = Er(i,j,k-1)*x2*y2/z1e          + Er(i-1,j,k-1)*x2*y1/z1e...
    + Er(i-1,j-1,k-1)*x1*y1/z1e          + Er(i,j-1,k-1)*x1*y2/z1e;
t6 = Er(i,j,k)*x2*y2/z2e          + Er(i-1,j,k)*x2*y1/z2e...
    + Er(i-1,j-1,k)*x1*y1/z2e          + Er(i,j-1,k)*x1*y2/z2e;
Co = t1+t2+t3+t4+t5+t6;
CF(i,j,k) = t1/Co;          CK(i,j,k) = t2/Co;          CL(i,j,k) = t3/Co;

```

```

        CR(i,j,k) = t4/Co;          CB(i,j,k) = t5/Co;          CT(i,j,k) = t6/Co;
    else
        % Coefficients for general node
        x1 = x(i,j,k)-x(i,j-1,k);          x2 = x(i,j+1,k)-x(i,j,k);
        y1 = y(i,j,k)-y(i-1,j,k);          y2 = y(i+1,j,k)-y(i,j,k);
        z1 = z(i,j,k)-z(i,j,k-1);          z2 = z(i,j,k+1)-z(i,j,k);
        t1 = Er(i-1,j,k)*x2*z2/y1          + Er(i-1,j-1,k)*x1*z2/y1...
            + Er(i-1,j,k-1)*x2*z1/y1      + Er(i-1,j-1,k-1)*x1*z1/y1;
        t2 = Er(i,j,k)*x2*z2/y2            + Er(i,j-1,k)*x1*z2/y2...
            + Er(i,j,k-1)*x2*z1/y2        + Er(i,j-1,k-1)*x1*z1/y2;
        t3 = Er(i-1,j-1,k)*y1*z2/x1        + Er(i,j-1,k)*y2*z2/x1...
            + Er(i-1,j-1,k-1)*y1*z1/x1    + Er(i,j-1,k-1)*y2*z1/x1;
        t4 = Er(i,j,k)*y2*z2/x2            + Er(i-1,j,k)*y1*z2/x2...
            + Er(i,j,k-1)*y2*z1/x2        + Er(i-1,j,k-1)*y1*z1/x2;
        t5 = Er(i,j,k-1)*x2*y2/z1          + Er(i-1,j,k-1)*x2*y1/z1...
            + Er(i-1,j-1,k-1)*x1*y1/z1    + Er(i,j-1,k-1)*x1*y2/z1;
        t6 = Er(i,j,k)*x2*y2/z2            + Er(i-1,j,k)*x2*y1/z2...
            + Er(i-1,j-1,k)*x1*y1/z2      + Er(i,j-1,k)*x1*y2/z2;
        Co = t1+t2+t3+t4+t5+t6;
        CF(i,j,k) = t1/Co;          CK(i,j,k) = t2/Co;          CL(i,j,k) = t3/Co;
        CR(i,j,k) = t4/Co;          CB(i,j,k) = t5/Co;          CT(i,j,k) = t6/Co;
    end
end
end
end

% Iterations to calculate the potential distribution in the computational domain
% using the updating potential's equation with applying two symmetries along x
% and y axes. In the non-rectangular region (curved grid) a linear interpolation
% technique is employed to get the potential at nodes on virtual rectangular grid.
% -----
for ko = 1:Maxiter,
    residual = 0;          % initialize the residual
    for i = 1:ny,
        for j = 1:nx,
            for k = 2:nz
                if i == 1 & j == 1 & k > nHb+nox+nm+nd+1, % Nodes on the z-axis
                    VR = V(i,j+1,k-1)+(V(i,j+1,k)-V(i,j+1,k-1))*(z(i,j,k)...
                        -z(i,j+1,k-1))/(z(i,j+1,k)-z(i,j+1,k-1));
                    VK = V(i+1,j,k)+(V(i+1,j,k+1)-V(i+1,j,k))*(z(i,j,k)...
                        -z(i+1,j,k))/(z(i+1,j,k+1)-z(i+1,j,k));
                    Vnew = CK(i,j,k)*VK + CR(i,j,k)*VR + CB(i,j,k)*V(i,j,k-1)...
                        + CT(i,j,k)*V(i,j,k+1) + Ccond(i,j,k) + Cg(i,j,k);
                elseif i == 1 & j == 1,
                    Vnew = CK(i,j,k)*V(i+1,j,k) + CR(i,j,k)*V(i,j+1,k)...
                        + CB(i,j,k)*V(i,j,k-1) + CT(i,j,k)*V(i,j,k+1)...
                        + Ccond(i,j,k) + Cg(i,j,k);
                elseif i==1 & j<n+1 & k > nHb+nox+nm+nd+1, % Symmetry along y-axis
                    VL = V(i,j-1,k)+(V(i,j-1,k+1)-V(i,j-1,k))*(z(i,j,k)...
                        -z(i,j-1,k))/(z(i,j-1,k+1)-z(i,j-1,k));
                    VR = V(i,j+1,k-1)+(V(i,j+1,k)-V(i,j+1,k-1))*(z(i,j,k)...
                        -z(i,j+1,k-1))/(z(i,j+1,k)-z(i,j+1,k-1));
                    VK = V(i+1,j,k) + (V(i+1,j,k+1)-V(i+1,j,k))*(z(i,j,k)...
                        -z(i+1,j,k))/(z(i+1,j,k+1)-z(i+1,j,k));
                    Vnew = CK(i,j,k)*VK + CL(i,j,k)*VL...

```

```

        + CR(i,j,k)*VR + CB(i,j,k)*V(i,j,k-1)...
        + CT(i,j,k)*V(i,j,k+1) + Ccond(i,j,k) + Cg(i,j,k);
elseif i == 1, % Symmetry along y-axis, xz-plane
    Vnew = CK(i,j,k)*V(i+1,j,k) + CL(i,j,k)*V(i,j-1,k)...
        + CR(i,j,k)*V(i,j+1,k) + CB(i,j,k)*V(i,j,k-1)...
        + CT(i,j,k)*V(i,j,k+1) + Ccond(i,j,k) + Cg(i,j,k);
elseif i<=m+1 & j==1 & k>nHb+nox+nm+nd+1, % Symmetry along x-axis
    VR = V(i,j+1,k-1)+(V(i,j+1,k)-V(i,j+1,k-1))*(z(i,j,k)...
        -z(i,j+1,k-1))/(z(i,j+1,k)-z(i,j+1,k-1));
    VK = V(i+1,j,k)+(V(i+1,j,k+1)-V(i+1,j,k))*(z(i,j,k)...
        -z(i+1,j,k))/(z(i+1,j,k+1)-z(i+1,j,k));
    VF = V(i-1,j,k-1)+(V(i-1,j,k)-V(i-1,j,k-1))*(z(i,j,k)...
        -z(i-1,j,k-1))/(z(i-1,j,k)-z(i-1,j,k-1));
    Vnew = CF(i,j,k)*VF + CK(i,j,k)*VK...
        + CR(i,j,k)*VR + CB(i,j,k)*V(i,j,k-1)...
        + CT(i,j,k)*V(i,j,k+1) + Ccond(i,j,k) + Cg(i,j,k);
elseif j == 1, % Symmetry along x-axis, yz-plane
    Vnew = CF(i,j,k)*V(i-1,j,k) + CK(i,j,k)*V(i+1,j,k)...
        + CR(i,j,k)*V(i,j+1,k) + CB(i,j,k)*V(i,j,k-1)...
        + CT(i,j,k)*V(i,j,k+1) + Ccond(i,j,k) + Cg(i,j,k);
elseif i<=m+1 & j<n+1 & k>nHb+nox+nm+nd+1 % Non-rectangular region
    VL = V(i,j-1,k)+(V(i,j-1,k+1)-V(i,j-1,k))*(z(i,j,k)...
        -z(i,j-1,k))/(z(i,j-1,k+1)-z(i,j-1,k));
    VR = V(i,j+1,k-1)+(V(i,j+1,k)-V(i,j+1,k-1))*(z(i,j,k)...
        -z(i,j+1,k-1))/(z(i,j+1,k)-z(i,j+1,k-1));
    VK = V(i+1,j,k)+(V(i+1,j,k+1)-V(i+1,j,k))*(z(i,j,k)...
        -z(i+1,j,k))/(z(i+1,j,k+1)-z(i+1,j,k));
    VF = V(i-1,j,k-1)+(V(i-1,j,k)-V(i-1,j,k-1))*(z(i,j,k)...
        -z(i-1,j,k-1))/(z(i-1,j,k)-z(i-1,j,k-1));
    Vnew = CF(i,j,k)*VF+CK(i,j,k)*VK+CL(i,j,k)*VL+CR(i,j,k)*VR...
        + CB(i,j,k)*V(i,j,k-1) + CT(i,j,k)*V(i,j,k+1)...
        + Ccond(i,j,k) + Cg(i,j,k);
else % General node in the computational domain
    Vnew = CF(i,j,k)*V(i-1,j,k) + CK(i,j,k)*V(i+1,j,k)...
        + CL(i,j,k)*V(i,j-1,k) + CR(i,j,k)*V(i,j+1,k)...
        + CB(i,j,k)*V(i,j,k-1) + CT(i,j,k)*V(i,j,k+1)...
        + Ccond(i,j,k) + Cg(i,j,k);
end
r = abs(Vnew - V(i,j,k)); % check accuracy
if r > residual, residual = r; end
V(i,j,k) = Vnew;
end
end
end
iter(ko) = ko; % set the residual and iteration number in arrys
resid(ko) = residual; niter = ko;
if residual <= Ermax,
    break
end
end
clear CF; clear CK; clear CL; clear CR; clear CB; clear CT;
clear Ccond; clear Cg; clear Co; clear t1; clear t2; clear t3;
clear t4; clear t5; clear t6;

```

```

% The electric field calculation in the 2-D computation domain, E(x,y,z)=Ex+Ey+Ez
% -----
for i = 1:ny,
    for j = 1:nx+1,
        for k = 2:nz,
            if (k > nHb+nox & k <= nHb+nox+nm+1 & j < nwx+1) | (k > nHb+nox ...
                & k <= nHb+nox+ngz+1 & j > n+1) | (k > nHb+nox ...
                & k <= nHb+nox+nm+nd+ng+1 & j > n+1 & j < n+ns+1 & i <= m+1)...
                | (k >= nHb+nox+nm+nd+ng+1 & k <= nHb+nH+1 & j < n+ns+1 & i <= m+1),
                Ex(i,j,k) = 0;
            elseif i <= m+1 & j == 1 & k > nHb+nox+nm+nd+1,
                VR = V(i,2,k-1)+(V(i,2,k)-V(i,2,k-1))*(z(i,1,k)-z(i,2,k-1))...
                    /(z(i,2,k)-z(i,2,k-1));
                VRR = V(i,3,k-1)+(V(i,3,k)-V(i,3,k-1))*(z(i,1,k)-z(i,3,k-1))...
                    /(z(i,3,k)-z(i,3,k-1));
                Ex(i,1,k) = (x(i,2,k)+x(i,3,k))*V(i,1,k)/(x(i,2,k)*x(i,3,k))...
                    +(x(i,2,k)*VRR/x(i,3,k)-x(i,3,k)*VR/x(i,2,k))...
                    /(x(i,3,k)-x(i,2,k));
            elseif i <= m+1 & j <= n+1 & k > nHb+nox+nm+nd+1, % Non-rectangular grid
                VL = V(i,j-1,k)+(V(i,j-1,k+1)-V(i,j-1,k))*(z(i,j,k)-z(i,j-1,k))...
                    /(z(i,j-1,k+1)-z(i,j-1,k));
                VR=V(i,j+1,k-1)+(V(i,j+1,k)-V(i,j+1,k-1))*(z(i,j,k)-z(i,j+1,k-1))...
                    /(z(i,j+1,k)-z(i,j+1,k-1));
                Ex(i,j,k) = -(x(i,j,k)-x(i,j+1,k))*VL/((x(i,j-1,k)-x(i,j,k))...
                    *(x(i,j-1,k)-x(i,j+1,k)))-(2*x(i,j,k)-x(i,j-1,k)-x(i,j+1,k))...
                    *V(i,j,k)/((x(i,j,k)-x(i,j-1,k))*(x(i,j,k)-x(i,j+1,k))...
                    -(x(i,j,k)-x(i,j-1,k))*VR/((x(i,j+1,k)-x(i,j-1,k))...
                    *(x(i,j+1,k)-x(i,j,k)));
            elseif j == 1,
                Ex(i,1,k) = (x(i,2,k)+x(i,3,k))*V(i,1,k)/(x(i,2,k)*x(i,3,k))...
                    +(x(i,2,k)*V(i,3,k)/x(i,3,k)-x(i,3,k)*V(i,2,k)/x(i,2,k))...
                    /(x(i,3,k)-x(i,2,k));
            elseif j == nx+1,
                Ex(i,j,k) = -(x(i,j,k)-x(i,j-1,k))*V(i,j-2,k)/((x(i,j-2,k)...
                    -x(i,j-1,k))*(x(i,j-2,k)-x(i,j,k)))-(x(i,j,k)-x(i,j-2,k))...
                    *V(i,j-1,k)/((x(i,j-1,k)-x(i,j-2,k))*(x(i,j-1,k)-x(i,j,k)));
            else
                Ex(i,j,k)=-x(i,j,k)-x(i,j+1,k))*V(i,j-1,k)/((x(i,j-1,k)-x(i,j,k))...
                    *(x(i,j-1,k)-x(i,j+1,k)))-(2*x(i,j,k)-x(i,j-1,k)-x(i,j+1,k))...
                    *V(i,j,k)/((x(i,j,k)-x(i,j-1,k))*(x(i,j,k)-x(i,j+1,k))...
                    -(x(i,j,k)-x(i,j-1,k))*V(i,j+1,k)/((x(i,j+1,k)-x(i,j-1,k))...
                    *(x(i,j+1,k)-x(i,j,k)));
            end
        end
    end
end

for i = 1:ny+1,
    for j = 1:nx,
        for k = 2:nz,
            if (k > nHb+nox & k <= nHb+nox+nm+1 & j <= nwx+1) | (k > nHb+nox ...
                & k <= nHb+nox+ngz+1 & j >= n+1) | (k > nHb+nox ...
                & k <= nHb+nox+nm+nd+ng+1 & j >= n+1 & j <= n+ns+1 & i < m+1)...
                | (k >= nHb+nox+nm+nd+ng+1 & k <= nHb+nH+1 & j <= n+ns+1 & i < m+1),

```

```

    Ey(i,j,k) = 0;
elseif i == 1 & j < n+1 & k > nHb+nox+nm+nd+1,
    VK = V(2,j,k-1)+(V(2,j,k)-V(2,j,k-1))*(z(1,j,k)-z(2,j,k-1))...
        /(z(2,j,k)-z(2,j,k-1));
    VKK = V(3,j,k-1)+(V(3,j,k)-V(3,j,k-1))*(z(1,j,k)-z(3,j,k-1))...
        /(z(3,j,k)-z(3,j,k-1));
    Ey(1,j,k) = (y(2,j,k)+y(3,j,k))*V(1,j,k)/(y(2,j,k)*y(3,j,k))...
        +(y(2,j,k)*VKK/y(3,j,k)-y(3,j,k)*VK/y(2,j,k))...
        /(y(3,j,k)-y(2,j,k));
elseif i<=m+1 & j < n+1 & k > nHb+nox+nm+nd+1, % Non-rectangular grid
    VF = V(i-1,j,k)+(V(i-1,j,k+1)-V(i-1,j,k))*(z(i,j,k)-z(i,j,k-1))...
        /(z(i-1,j,k+1)-z(i-1,j,k));
    VK=V(i+1,j,k-1)+(V(i+1,j,k)-V(i+1,j,k-1))*(z(i,j,k)-z(i+1,j,k-1))...
        /(z(i+1,j,k)-z(i+1,j,k-1));
    Ey(i,j,k) = -(y(i,j,k)-y(i+1,j,k))*VF/((y(i-1,j,k)-y(i,j,k))...
        *(y(i-1,j,k)-y(i+1,j,k)))-(2*y(i,j,k)-y(i-1,j,k)-y(i+1,j,k))...
        *V(i,j,k)/((y(i,j,k)-y(i-1,j,k))*(y(i,j,k)-y(i+1,j,k)))...
        -(y(i,j,k)-y(i-1,j,k))*VK/((y(i+1,j,k)-y(i-1,j,k))...
        *(y(i+1,j,k)-y(i,j,k)));
elseif i == 1,
    Ey(1,j,k) = (y(2,j,k)+y(3,j,k))*V(1,j,k)/(y(2,j,k)*y(3,j,k))...
        +(y(2,j,k)*V(3,j,k)/y(3,j,k)-y(3,j,k)*V(2,j,k)/y(2,j,k))...
        /(y(3,j,k)-y(2,j,k));
elseif i == ny+1,
    Ey(i,j,k) = -(y(i,j,k)-y(i-1,j,k))*V(i-2,j,k)/((y(i-2,j,k)...
        -y(i-1,j,k))*(y(i-2,j,k)-y(i,j,k)))-(y(i,j,k)-y(i-2,j,k))...
        *V(i-1,j,k)/((y(i-1,j,k)-y(i-2,j,k))*(y(i-1,j,k)-y(i,j,k)));
else
    Ey(i,j,k)=- (y(i,j,k)-y(i+1,j,k))*V(i-1,j,k)/((y(i-1,j,k)-y(i,j,k))...
        *(y(i-1,j,k)-y(i+1,j,k)))-(2*y(i,j,k)-y(i-1,j,k)-y(i+1,j,k))...
        *V(i,j,k)/((y(i,j,k)-y(i-1,j,k))*(y(i,j,k)-y(i+1,j,k)))...
        -(y(i,j,k)-y(i-1,j,k))*V(i+1,j,k)/((y(i+1,j,k)-y(i-1,j,k))...
        *(y(i+1,j,k)-y(i,j,k)));
end
end
end
end

for i = 1:ny,
    for j = 1:nx,
        for k = 1:nz+1
            if (k > nHb+nox+1 & k <= nHb+nox+nm & j <= nwx+1) | (k > nHb+nox+1 ...
                & k <= nHb+nox+ngz & j >= n+1) | (k > nHb+nox+1 ...
                & k <= nHb+nox+nm+nd+ng+1 & j >= n+1 & j <= n+ns+1 & i <= m+1)...
                | (k > nHb+nox+nm+nd+ng+1 & k <= nHb+nH & j <= n+ns+1 & i <= m+1),
                Ez(i,j,k) = 0;
            elseif k == 1,
                Ez(i,j,k)=(z(i,j,k+1)*V(i,j,k+2)/z(i,j,k+2)-z(i,j,k+2)*V(i,j,k+1)...
                    /z(i,j,k+1))/z(i,j,k+2)-z(i,j,k+1));
            elseif k == nz+1,
                Ez(i,j,k) = -(z(i,j,k)-z(i,j,k-1))*V(i,j,k-2)/((z(i,j,k-2) ...
                    -z(i,j,k-1))*(z(i,j,k-2)-z(i,j,k)))-(z(i,j,k)...
                    -z(i,j,k-2))*V(i,j,k-1)/((z(i,j,k-1)-z(i,j,k-2))...
                    *(z(i,j,k-1)-z(i,j,k)));
            end
        end
    end
end

```

```

else
    Ez(i,j,k) = -(z(i,j,k)-z(i,j,k+1))*V(i,j,k-1)/((z(i,j,k-1)...
        -z(i,j,k))*(z(i,j,k-1)-z(i,j,k+1)))-(2*z(i,j,k)...
        -z(i,j,k-1)-z(i,j,k+1))*V(i,j,k)/((z(i,j,k)...
        -z(i,j,k-1))*(z(i,j,k)-z(i,j,k+1)))-(z(i,j,k)...
        -z(i,j,k-1))*V(i,j,k+1)/((z(i,j,k+1)-z(i,j,k-1))...
        *(z(i,j,k+1)-z(i,j,k)));
end
end
end
clear V;

% Calculation of the total charge accumulated on the CPW signal line to
% determine
% the switch capacitance by applying Gauss's law: Qenc= Int(D.ds) around the
% center conductor of the CPW (lower electrode).
% -----
k_B = floor(nHb/2); % selected bottom surface location
j_R = floor((n+nwx)/2); % selected right surface location
k_T = nHb+nox+nm+nd; % selected top surface location
k = k_B; Qinc = 0; % bottom surface
for i = 2:ny,
    x2 = x(i,2,k)-x(i,1,k); y1 = y(i,1,k)-y(i-1,1,k); y2 = y(i+1,1,k)-y(i,1,k);
    Qinc = Qinc + 0.5*Ez(i,1,k)*(Er(i,1,k-1)*x2*y2+Er(i-1,1,k-1)*x2*y1);
    for j = 2:j_R,
        x1 = x(i,j,k)-x(i,j-1,k); x2 = x(i,j+1,k)-x(i,j,k);
        y1 = y(i,j,k)-y(i-1,j,k); y2 = y(i+1,j,k)-y(i,j,k);
        Qinc = Qinc + 0.25*Ez(i,j,k)*(Er(i,j,k-1)*x2*y2+Er(i-1,j,k-1)*x2*y1...
            + Er(i-1,j-1,k-1)*x1*y1 + Er(i,j-1,k-1)*x1*y2);
    end
end
j = j_R; % Right surface
for i = 2:ny,
    for k = k_B:k_T,
        y1 = y(i,j,k)-y(i-1,j,k); y2 = y(i+1,j,k)-y(i,j,k);
        z1 = z(i,j,k)-z(i,j,k-1); z2 = z(i,j,k+1)-z(i,j,k);
        Qinc = Qinc - 0.25*Ex(i,j,k)*(Er(i,j,k)*y2*z2+Er(i-1,j,k)*y1*z2...
            + Er(i,j,k-1)*y2*z1 + Er(i-1,j,k-1)*y1*z1);
    end
end
k = k_T; % Top surface
for i = 2:ny,
    x2 = x(i,2,k)-x(i,1,k); y1 = y(i,1,k)-y(i-1,1,k); y2 = y(i+1,1,k)-y(i,1,k);
    Qinc = Qinc - 0.5*Ez(i,1,k)*(Er(i,1,k)*x2*y2 + Er(i-1,1,k)*x2*y1);
    for j = 2:j_R,
        x1 = x(i,j,k)-x(i,j-1,k); x2 = x(i,j+1,k)-x(i,j,k);
        y1 = y(i,j,k)-y(i-1,j,k); y2 = y(i+1,j,k)-y(i,j,k);
        Qinc = Qinc - 0.25*Ez(i,j,k)*(Er(i,j,k)*x2*y2+Er(i-1,j,k)*x2*y1...
            + Er(i-1,j-1,k)*x1*y1 + Er(i,j-1,k)*x1*y2);
    end
end
Qinc = Qinc*4*Eps0; % Multiplied by 4 due to two the symmetries
Cap = 1E15*abs(Qinc)/Vo; % Total switch capacitance in fF

```

```

% Calculation of the electrostatic force induced on the membrane.
% -----
k = nHb+nox+nm+nd+ng+1;
for i = 1:m+1,
    for j = 1:n+1,
        if i == 1 & j == 1,
            f(i,j) = -0.5*Eps0*Ez(i,j,k)*Ez(i,j,k);
        elseif i == 1,
            f(i,j) = -0.5*Eps0*(Ex(i,j,k)*Ex(i,j,k)+Ez(i,j,k)*Ez(i,j,k));
        elseif j == 1,
            f(i,j) = -0.5*Eps0*(Ey(i,j,k)*Ey(i,j,k)+Ez(i,j,k)*Ez(i,j,k));
        else
            f(i,j) = -0.5*Eps0*(Ex(i,j,k)^2+Ey(i,j,k)^2+Ez(i,j,k)^2);
        end
    end
end

% Calling the mechanical model to determine the bridge deformation caused when
% applying the DC biasing voltage Vo.
% The mechanical model solves the plate equation using the FDM and matrix
% inversion method to calculate the bending function w(x,y) due to the
% electrostatic force induced on the membrane P(x,y), when applying Vo.
P = [flipud(f); f(2:m+1,:)]/D;          P = [fliplr(P) P(:,2:n+1)]; clear f;

[Wm] = SolvePlateEqUsingFDM(2*m,2*n,dx,dy,t,nu,P);

wmax = w(1,1);          w(1:m+1,1:n+1) = abs(Wm(m+1:2*m+1,n+1:2*n+1));
end                      % End the iteration, which calculates the deformation

g(ii) = go - w(1,1);    fv(ii) = D*abs(P(m+1,n+1));    C(ii) = Cap;    Vi(ii) = Vo;
shape(1:2*m+1,1:2*n+1,ii) = go - abs(Wm(1:2*m+1,1:2*n+1));    clear Wm;
end                      % End Vo loop
X = x(1,:,1);          X = X';          Y = y(:,1,1);          P = abs(P);
Xb(1:n+1)=X(1:n+1);    Xb=[Xb L+Xb(1:n)];    Yb(1:m+1)=Y(1:m+1);    Yb=[Yb b+Yb(1:m)];
Xb=Xb*1e6;            Yb=Yb*1e6;            L=L*2e6;                b=b*2e6;
CPU_Time = toc          % to measure the CPU elapsed time

clear Ex; clear Er; clear z1e; clear z2e; clear wmax; clear count;
clear Ey; clear x1; clear x2; clear y1; clear y2; clear z1; clear z2;
clear Ez; clear ZT; clear ZB; clear VL; clear VR; clear VF; clear VK;
clear i; clear j; clear k; clear k_B; clear k_T; clear j_R;

save Results_MEMS3D          % save results in a mat file

figure;          % surf
mesh(Xb,Yb,P*D);          axis([0 L 0 b 0 1.2*D*max(max(P))]);
xlabel('x [\num]');          ylabel('y [\num]');          zlabel('Force density [N/m^2]');
title('Electrostatic force density distribution at pull down');

figure;          mesh(Xb,Yb,shape(:,:,ii)*1E6);          axis([0 L 0 b -go*1e6 go*1E6]);
xlabel('x [\num]');          ylabel('y [\num]');          zlabel('Gap height [\num]');
title('Shape of the deformed membrane at actuation voltage \geq V_{\pi}');

```

```
figure; subplot(1,3,1); plot(Vi,g*1e6), grid;
xlabel('Voltage [Volts]'); ylabel('Position [\mum]');
axis([0 10*(floor(Vo/10)+1) 0 go*1E6]);
title('Bridge center position vs. applied voltage');

subplot(1,3,2); plot(Vi,C), grid;
xlabel('Voltage [Volts]'); ylabel('Capacitance [fF]');
axis([0 10*(floor(Vo/10)+1) 0.99*min(C) 1.01*max(C)]);
title('Capacitance vs. applied voltage');

subplot(1,3,3); plot(Vi,fv/1000), grid;
xlabel('Voltage [Volts]'); ylabel('Force density [kN/m^2]');
axis([0 10*(floor(Vo/10)+1) 0.95*min(abs(fv/1000)) 1.05*max(abs(fv/1000))]);
title('Force density induced on the bridge center node vs. applied voltage');

figure; plot(iter,resid), grid;
title(' Error = %');
xlabel('Number of iterations'); ylabel('Residual');

% The END of the main program MEMS3DModel.m
```

# Bibliography

- [1] J. J. Yao, “Topical Review: RF MEMS From a Device Perspective,” *J. Micromech. Microeng.*, vol. 10, no. 4, pp. R9–R38, December 2000.
- [2] S. Lucyszyn, “Review of Radio Frequency Microelectromechanical Systems Technology,” *IEE Proceedings - Science, Measurement and Technology*, vol. 151, no. 2, pp. 93–103, March 2004.
- [3] G. M. Rebeiz and J. B. Muldavin, “RF MEMS Switches and Switch Circuits,” *IEEE Microwave magazine*, pp. 59–71, December 2001.
- [4] E. R. Brown, “RF-MEMS Switches for Reconfigurable Integrated Circuits,” *IEEE Trans. Microwave Theory Tech.*, vol. 46, no. 11, pp. 1868–80, November 1998.
- [5] H. A. C. Tilmans, W. D. Raedt, and E. Beyne, “MEMS for Wireless Communications: from RF-MEMS Components to RF-MEMS-SiP,” *J. Micromech. Microeng.*, vol. 13, no. 4, pp. S139–S163, July 2003.
- [6] H. J. D. L. Santos and R. J. Richards, “MEMS for RF/Microwave Wireless Applications: The Next Wave Part I,” *Microwave Journal*, March 2001.
- [7] L. P. B. Katehi, E. Harvey, and E. Brown, “MEMS and Si Micromachined Circuits for High-Frequency Applications,” *IEEE Trans. Microwave Theory Tech.*, vol. 50, no. 3, pp. 858–866, March 2002.
- [8] B. Sulouff, “Surface Micromachining and Inertial Sensors,” Tutorial 2A, *Pan-American Advanced Studies Institutes on MEMS*, San Carlos de Bariloche, Argentina, June 2004.
- [9] H. J. D. L. Santos, *Introduction to Microelectromechanical Microwave Systems*, 2nd ed. Boston, London: Artch House, Inc., September 2004.
- [10] S. P. Pacheco, L. P. B. Katehi, and C. T.-C. Nguyen, “Design of Low Actuation Voltage RF MEMS Switch,” *2000 IEEE MTT-S Int. Microwave Symp. Dig.*, Boston, vol. 1, pp. 165–168, June 2000.
- [11] D. Balaraman, S. K. Bhattacharya, F. Ayazi, and J. Papapolymerou, “Low-Cost Low Actuation Voltage Copper RF MEMS Switches,” *2002 IEEE MTT-S Int. Microwave Symp. Dig.*, Seattle, Washington, vol. 2, pp. 1225–28, June 2002.

- 
- [12] J. B. Muldavin and G. M. Rebeiz, "All-Metal High-Isolation Series and Series/Shunt MEMS switches," *IEEE Microwave Wireless Comp. Lett.*, vol. 11, pp. 373–375, September 2001.
- [13] R. E. Mihailovich, M. Kim, J. B. Hacker, E. A. Sovero, J. Studer, J. A. Higgins, and J. F. DeNatale, "MEM Relay for Reconfigurable RF Circuits," *IEEE Microwave Wireless Comp. Lett.*, vol. 11, no. 2, pp. 53–55, February 2001.
- [14] V. K. Varadan, K. J. Vinoy, and K. A. Jose, *RF MEMS and Their Applications*, 1st ed. Pennsylvania State University, USA: John Wiley & Sons, Inc., December 2002.
- [15] C. L. Goldsmith and S. Eshelman, "Performance of Low-Loss RF MEMS Capacitive Switches," *IEEE Microwave and Guided Wave Letters*, vol. 8, no. 8, pp. 269–271, August 1998.
- [16] S. Duffy, C. Bozler, S. Rabe, J. Knecht, L. Travis, P. Wyatt, C. Keast, and M. Gouker, "MEMS for Microswitches Reconfigurable Microwave Circuitry," *IEEE Microwave Wireless Comp. Lett.*, vol. 11, no. 3, pp. 106–108, March 2001.
- [17] S. Majumder, J. Lampen, R. Morrison, and J. Maciel, "A Packaged, High-Lifetime Ohmic MEMS RF Switch," *IEEE MTT-S Int. Microwave Symp. Dig.*, Philadelphia, Pennsylvania, USA, pp. 1935–39, June 2003.
- [18] J. B. Muldavin and G. M. Rebeiz, "Novel Series and Shunt MEMS Switch Geometries for X-Band Applications," *European Microwave Conference*, Paris, France, pp. 261–264, October 2000.
- [19] D. Hyman, J. Lam, B. Warneke, A. Schmitz, T. Hsu, J. Brown, J. Schaffner, A. Walston, R. Loo, M. Mehregany, and J. Lee, "Surface-Micromachined RF MEMS Switches on GaAs Substrates," *RFMiCAE*, vol. 9, no. 4, pp. 348–361, July 1999.
- [20] Z. J. Yao, S. Chen, S. Eshelman, , and C. Goldsmith, "Micromachend Low-Loss Microwave Switches," *IEEE/ASME J. Microelectromech. Sys.*, vol. 8, no. 2, pp. 129–134, June 1999.
- [21] D. Peroulis, S. Pacheco, K. Sarabandi, and L. P. Katehi, "MEMS Devices for High Isolation Switching and Tunable Filtering," *2000 IEEE MTT-S Int. Microwave Symp. Dig.*, Boston, MA, USA, vol. 2, pp. 1217–20, June 2000.
- [22] Y. Zhu and H. D. Espinosa, "Reliability of Capacitive RF MEMS Switches at High and Low Temperatures," *Int. J. RF and Microwave CAE*, vol. 14, pp. 317–328, 2004.
- [23] J. B. Muldavin and G. M. Rebeiz, "High-Isolation CPW MEMS Shunt Switches-Part 1: Modeling," *IEEE Trans. Microwave Theory Tech.*, vol. 48, no. 6, pp. 1045–52, June 2000.

- [24] P. Osterberg, H. Yie, X. Cai, J. White, and S. Senturia, "Self-Consistent Simulation and Modeling of Electrostatically Deformed Diaphragms," *17th IEEE Int. Conference on Microelectromechanical Systems, MEMS'94*, Oiso, Japan, pp. 28–32, January 1994.
- [25] P. M. Osterberg, "Electrostatically Actuated Microelectromechanical Test Structures for Material Property Measurement," Ph.D. dissertation, Massachusetts Inst. of Tech., Cambridge, MA, USA, September 1995.
- [26] R. V. Sabariego, J. Gyselinck, P. Dular, J. D. Coster, F. Henrotte, and K. Hameyer, "Coupled Mechanical-Electrostatic FE-BE Analysis With FMM Acceleration: Application to a Shunt Capacitive MEMS Switch," *The International Journal for Computation and Mathematics in Electrical and Electronic Engineering (COMPEL)*, vol. 23, no. 4, pp. 876–884, December 2004.
- [27] J.-M. Huang, K. Liew, C. Wong, S. Rajendran, M. Tan, and A. Liu, "Mechanical Design and Optimization of Capacitive Micromachined Switch," *Journal of Sensors and Actuators A: Physical*, vol. 93, no. 3, pp. 273–285, October 2001.
- [28] B. Choi and E. G. Lovell, "Improved Analysis of Microbeams Under Mechanical and Electrostatic Loads," *J. Micromech. Microeng.*, vol. 7, no. 1, pp. 24–29, March 1997.
- [29] E. K. Chan, K. Garikipati, and R. W. Dutton, "Characterization of Contact Electromechanics Through Capacitance-Voltage Measurements and Simulations," *IEEE/ASME J. Microelectromech. Syst.*, vol. 8, no. 2, pp. 208–217, June 1999.
- [30] L. Zhang, T. Yu, and Y. Zhao, "Numerical Analysis of Theoretical Model of the RF MEMS Switches," *Acta Mechanica Sinica*, vol. 20, no. 2, pp. 178–184, April 2004.
- [31] Q. Meng, M. Mehregany, and R. L. Mullen, "Theoretical Modeling of Microfabricated Beams With Elastically Restrained Supports," *IEEE/ASME J. Microelectromech. Syst.*, vol. 2, no. 3, pp. 128–137, September 1993.
- [32] Y. Zhu and H. D. Espinosa, "Design of Radio Frequency (RF) MEMS Switches: Modeling," *Proc. of ASME Int. Mechanical Engineering Congress & Exposition (IMECE'03)*, Washington, D.C., pp. 16–21, November 2003.
- [33] H. D. Espinosa, M. Fischer, Y. Zhu, and S. Lee, "3-D Computational Modeling of RF MEMS Switches," *Technical Proceedings of the 4<sup>th</sup> Int. Conf. on Modeling and Simulation of Microsystems*, South California, USA, vol. 4, pp. 402–405, March 2001.
- [34] J. R. Gilbert, R. Legtenberg, and S. D. Senturia, "3D Coupled Electro-Mechanics for MEMS: Application of CoSolve-EM," *Proc. of the 8th IEEE Micro Electro Mechanical Systems Conference*, Amsterdam, Netherlands, January 1995.
- [35] CoventorWare, Coventor, Inc., <http://www.coventor.com>.

- [36] Abaqus, ABAQUS, Inc., <http://www.hks.com>.
- [37] IntelliSuite, IntelliSense Software Corp, <http://www.intellisensesoftware.com>.
- [38] Ansys, ANSYS, Inc., <http://www.ansys.com>.
- [39] D. Ahn, J. S. Park, C. S. Kim, Y. Qian, and T. Itoh, "A Design of the Lowpass Filter Using the Novel Microstrip Defected Ground Structure," *IEEE Trans. Microwave Theory Tech.*, vol. 49, no. 1, pp. 86–93, January 2001.
- [40] H.-M. Kim and B. Lee, "Analysis and Synthesis of Defected Ground Structures (DGS) Using Transmission Line Theory," *2005 European Microwave Conference*, Paris, France, vol. 1, pp. 397–400, October 2005.
- [41] J.-S. Lim, C.-S. Kim, Y.-T. Lee, D. Ahn, and S. Nam, "A Spiral-Shaped Defected Ground Structure for Coplanar Waveguide," *IEEE Microwave Wireless Comp. Lett.*, vol. 12, no. 9, pp. 330–332, September 2002.
- [42] A. Abdel-Rahman, A. K. Verma, A. Boutejdar, and A. S. Omar, "Control of Bandstop Response of Hi-Lo Microstrip Lowpass Filter Using Slot in Ground Plane," *IEEE Trans. Microwave Theory Tech.*, vol. 52, no. 3, pp. 1008–13, March 2004.
- [43] J.-S. Lim, Y.-T. Lee, C.-S. Kim, D. Ahn, and S. Nam, "A Vertically Periodic Defected Ground Structure and Its Application in Reducing the Size of Microwave Circuits," *IEEE Microwave Wireless Comp. Lett.*, vol. 12, no. 12, pp. 479–481, December 2002.
- [44] V. Radisic, Y. Qian, R. Coccioli, and T. Itoh, "Novel 2-D Photonic Bandgap Structure for Microstrip Lines," *IEEE Microwave and Guided Wave Letters*, vol. 8, pp. 69–71, February 1998.
- [45] J.-S. Lim, C.-S. Kim, Y.-T. Lee, and et al, "A New Type of Low Pass Filter With Defected Ground Structure," *European Microwave Week 2002*, Milan, Italy, pp. 24–26, September 2002.
- [46] M.-L. Her, C.-M. Chang, Y.-Z. Wang, F.-H. Kung, and Y.-C. Chiou, "Improved Coplanar Waveguide (CPW) Bandstop Filter with Photonic Bandgap (PBG) Structure," *Microwave and Optical Technology Letters*, vol. 38, no. 4, pp. 274–277, August 2003.
- [47] J.-S. Yoon, J.-G. Kim, J.-S. Park, C.-S. Park, J.-B. Lim, H.-G. Cho, and K.-Y. Kang, "A New DGS Resonator and Its Application to Bandpass Filter Design," *2004 IEEE MTT-S Int. Microwave Symp. Dig.*, Texas, pp. 1605–08, June 2004.
- [48] K. T. Chan, A. Chin, M.-F. Li, D.-L. Kwong, S. P. Mcalister, D. S. Duh, W. J. Lin, , and C. Y. Chang, "High-Performance Microwave Coplanar Bandpass and Bandstop Filters on Si Substrates," *IEEE Trans. Microwave Theory Tech.*, vol. 51, no. 9, pp. 2036–40, September 2003.

- [49] J.-S. Lim, J.-S. Park, Y.-T. Lee, D. Ahn, and S. Nam, "Application of Defected Ground Structure in Reducing the Size of Amplifiers," *IEEE Microwave Wireless Comp. Lett.*, vol. 12, no. 7, p. 261, July 2002.
- [50] Y. Chung, S.-S. Jeon, D. Ahn, J.-J. Choi, and T. Itoh, "High Isolation Dual-Polarized Patch Antenna Using Integrated Defected Ground Structure," *IEEE Microwave Wireless Comp. Lett.*, vol. 14, no. 1, pp. 4–6, January 2004.
- [51] H. Liu, X. Sun, and Z. Li, "Novel Two-Dimensional (2-D) Defected Ground Array for Planar Circuits," *Active and Passive Electronic Components*, vol. 27, no. 3, pp. 161–167, September 2004.
- [52] Y.-Q. Fu, N.-C. Yuan, and G.-H. Zhang, "A Novel Fractal Microstrip PBG structure," *Microwave and Optical Technology Letters*, vol. 32, no. 2, pp. 136–138, December 2001.
- [53] T.-Y. Yun and K. Chang, "Uniplanar One-Dimensional Photonic-Bandgap Structures and Resonators," *IEEE Trans. Microwave Theory Tech.*, vol. 49, no. 3, pp. 86–93, March 2001.
- [54] C. T.-C. Nguyen, L. P. B. Katehi, and G. M. Rebeiz, "Micromachined Devices for Wireless Communications (invited)," *Proc. IEEE*, vol. 86, no. 8, pp. 1756–68, August 1998.
- [55] K. M. Strohm, F. J. Schmckle, and B. Schauwecker, "Silicon Micromachined RF MEMS Resonators," *2002 IEEE MTT-S Int. Microwave Symp. Dig.*, Seattle, Washington, pp. 1209–12, June 2002.
- [56] X. J. Zhang, A. Q. Liu, M. F. Karim, A. B. Yu, and Z. X. Shen, "MEMS-Based Photonic Bandgap (PBG) Band-Stop Filter," *2004 IEEE MTT-S Int. Microwave Symp. Dig.*, Texas, USA, pp. 1463–66, June 2004.
- [57] W. Pan, P. Fiorini, O. D. Monaco, K. Baert, B. Nauwelaers, and R. Mertens, "Micromachined Tunable Dielectric Resonators," *Workshop on Semiconductor Sensor and Actuator Technology (3rd SeSens)*, Veldhoven, The Netherlands, pp. 653–656, November 2002.
- [58] C.-L. Dai and W.-C. Yu, "A Micromachined Tunable Resonator Fabricated by the CMOS Post-process of Etching Silicon Dioxide," *Microsystem Technologies*, vol. 12, no. 8, pp. 766–772, July 2004.
- [59] L. X. Zhang and Y.-P. Zhao, "Electromechanical Model of RF MEMS Switches," *Microsystem Technologies*, vol. 9, no. 6-7, pp. 420–426, September 2003.
- [60] A. Z. Elsherbeni, "The Finite Difference Technique for Electromagnetic Applications," Course notes: *Electrical Eng. Dept., The University of Mississippi, University, MS 38677, USA*, May 2005.
- [61] S. P. Timoshenko and J. M. Gere, *Theory of Elastic Stability*, 2nd ed. New York: McGraw-Hill Inc., 1961.

- [62] W. E. Boyce and R. C. DiPrima, *Elementary Differential Equations and Boundary Value Problems*, 6th ed. New York: John Wiley & Sons, Inc., 1997.
- [63] G. M. Rebeiz, *RF MEMS Theory, Design, and Technology*, 1st ed. Hoboken, New Jersey: John Wiley & Sons, Inc., June 2003.
- [64] J. M. Gere and S. P. Timoshenko, *Mechanics of Materials*, 4th ed. UK: Stanley Thornes (Publishers) Ltd, 1999.
- [65] E. Ventsel and T. Krauthammer, *Thin Plates and Shells: Theory, Analysis, & Applications*, 1st ed. New York: Marcel Dekker, Inc., 2001.
- [66] E. K. I. Hamad, A. Z. Elsherbeni, A. M. E. Safwat, and A. S. Omar, "Two-Dimensional Coupled Electrostatic-Mechanical Model for RF MEMS Switches," *Applied Computational Electromagnetic Society Journal*, vol. 21, no. 1, pp. 26–36, March 2006.
- [67] J. B. Muldavin and G. M. Rebeiz, "Novel DC-Contact MEMS Shunt Switches and High-Isolation Series/Shunt Designs," *European Microwave Conference*, Excel, London, U.K., pp. 275–277, September 2001.
- [68] Sonnet 10.52, Sonnet Software, Inc., <http://www.sonnetusa.com/>.
- [69] Microwave Office 5.53, Applied Wave Research, Inc., [http://web.appwave.com/Products/Microwave\\_Office/Overview.php](http://web.appwave.com/Products/Microwave_Office/Overview.php).
- [70] S. P. Pacheco, D. Peroulis, and L. P. B. Katehi, "MEMS Single-Pole Double-Throw (SPDT) X and K-Band Switching Circuits," *2001 IEEE MTT-S Int. Microwave Symp., Dig.*, Phoenix, AZ, pp. 321–324, June 2001.
- [71] M. Daneshmand and R. R. Mansour, "Fabrication and Modeling of an SP3T RF MEMS Switch," *IEEE AP-Symposium and North American Radio Science Meeting*, Columbus, Ohio, USA, June 2003.
- [72] Q. Xue, K. M. Shum, and C. H. Chan, "Novel 1-D Microstrip PBG cells," *IEEE Microwave and Guided Wave Letters*, vol. 10, pp. 403–405, October 2000.
- [73] I. Chang and B. Lee, "Design of Defected Ground Structures for Harmonic Control of Active Microstrip Antenna," *2002 IEEE Antennas and Propagation Society Int. Symp.*, San Antonio, USA, vol. 2, pp. 852–855, June 2002.
- [74] Y.-T. Lee, J.-S. Lim, S. Kim, J. Lee, S. N., K.-S. Seo, and D. Ahn, "Application of CPW Based Spiral-Shaped Defected Ground Structure to The Reduction of Phase Noise in V-band MMIC Oscillator," *2003 IEEE MTT-S Int. Microwave Symp. Dig.*, Pennsylvania, USA, pp. 2253–56, June 2003.
- [75] E. K. I. Hamad, A. M. E. Safwat, and A. S. Omar, "2-D Periodic Defected Ground Structure for Coplanar Waveguide," *Proc. of German Microwave Conference (GeMiC 2005)*, Ulm, Germany, pp. 25–28, April 2005.

# Curriculum Vitae

Name: Ehab K. I. Hamad  
Date of Birth: November 8, 1970 in Assiut, Egypt  
Nationality: Egyptian  
Status: Married, 3 Children  
Address: Ernst-Lehmann-Str. 1/ App. 12,  
D-39106 Magdeburg, Germany  
E-mail: e.hamad@ieee.org / ehamad@iee.org

## Education

10.2001-9.2006 Works towards Ph.D. degree at the Institute for Electronics, Signal Processing, and Comm., University of Magdeburg, Magdeburg, Germany.  
10.1999 M.Sc. in Electronics and Comm. from Assiut University, Assiut, Egypt.  
07.1994 B.Sc. in Electrical Engineering from Assiut University, Assiut, Egypt.  
07.1989 Secondary School Certificate, Assiut, Egypt.

## Work Experience

1996 - 2000 Teaching/Research Assistant in Electrical Engineering Dept., Aswan Faculty of Engineering, South Valley University, Aswan, Egypt.  
01.2002 till now Research Assistant for a MEMS research group, Chair of Microwave and Communication Engineering, Otto-von-Guericke University of Magdeburg, Magdeburg, Germany.

Magdeburg, 25.09.2006

*Ehab K. I. Hamad*

# Related Publications

The presented thesis is based on the following international reviewed journal and conference papers:

## Journal Papers:

1. Ehab K. I. Hamad, Atef Z. Elsherbeni, Veysel Demir, and Abbas S. Omar, "**Three-Dimensional Coupled Electrostatic-Mechanical Model for RF MEMS Switches**", Submitted to an international journal.
2. Ehab K. I. Hamad, Amr M. E. Safwat, and Abbas S. Omar, "**A MEMS Reconfigurable DGS Resonator for K-band Applications**", *IEEE/ASME Journal of Microelectromechanical Systems*, Vol. 15, No. 4, August 2006.
3. Ehab Hamad and Abbas Omar, "**An Improved Two-Dimensional Coupled Electrostatic-Mechanical Model for RF MEMS Switches**", *Journal of Micromechanics and Microengineering*, Vol. 16, No. 7, pp. 1424-29, July 2006.
4. Ehab K. I. Hamad, Atef Z. Elsherbeni, Amr M. E. Safwat, and Abbas S. Omar, "**Two-Dimensional Coupled Electrostatic-Mechanical Model for RF MEMS Switches**", *Applied Computational Electromagnetic Society (ACES) Journal*, Vol. 21, No. 1, pp. 26-36, March 2006.
5. Ehab K. I. Hamad, Amr M. E. Safwat, and Abbas S. Omar, "**Controlled Capacitance and Inductance Behavior of L-Shaped Defected Ground Structure for Coplanar Waveguide**", *IEE Proc. - Microwaves, Antennas and Propagation*, Vol. 152, No. 5, pp. 299-304, October 2005.

## Conference Papers:

6. Anatoliy Batmanov, Ehab K. I. Hamad, Edmund P. Burte, and Abbas S. Omar, "**Design of H-Shaped Low Actuation-Voltage RF-MEMS Relays**", *2006 Asia-Pacific Microwave Conference (APMC 2006)*, Yokohama, Japan, December 2006.

7. Atallah Balalem, Ehab K. I. Hamad, Jan Machac, and Abbas S. Omar, "**Band-pass Filters on a Modified Multilayer Coplanar Line**", *2006 IEEE MTT-S Int. Microwave Symp. Dig.*, San Francisco, CA, pp. 531-534, June 2006.
8. Ehab K. I. Hamad, Abbas S. Omar, and Atef Z. Elsherbeni, "**Three-Dimensional Electromechanical Coupled Analysis for Capacitive RF MEMS Switches**", *The 22nd Int. Review of Progress in Applied Computational Electromagnetics (ACES 2006)*, Miami, FL, USA, pp. 574-580, March 2006.
9. Ehab K. I. Hamad, Amr M. E. Safwat, and Abbas S. Omar, "**L-Shaped Defected Ground Structure for Coplanar Waveguide**", *2005 IEEE Antennas and Propagation Society Int. Symp.*, Vol. 2B, Washington DC, USA, pp. 663-666, July 2005.
10. Ehab K. I. Hamad, Amr M. E. Safwat, and Abbas S. Omar, "**2D Periodic Defected Ground Structure for Coplanar Waveguide**", In Proc. Conf., *German Microwave Conference (GeMiC 2005)*, Ulm, Germany, pp. 25-28, April 2005.
11. Ehab K. I. Hamad, Amr M. E. Safwat, and Abbas S. Omar, "**2D Coupled Electrostatic-Mechanical Model for Shunt-Capacitive MEMS Switch Based on Matlab Program**", *IEEE/ACES Int. Conf. on Wireless Communications and Applied Computational Electromagnetics (ACES 2005)*, Honolulu, Hawaii, USA, pp. 754-758, April 2005.
12. Ehab K. I. Hamad, Galal E. Nadim, and Abbas S. Omar, "**A Proposed SP3T Wideband RF MEMS Switch**", *2004 IEEE Antennas and Propagation Society Int. Symp.*, Vol. 3, Monterey, CA, USA, pp. 2839-42, June 2004.
13. Ehab K. I. Hamad, Galal E. Nadim, and Abbas S. Omar, "**A Proposed  $\pi$ -Structure RF MEMS Switch for Wide Bandwidth and High Isolation Applications**", in Proc. Conf., *The Applied Computational Electromagnetics Society (ACES 2004)*, Syracuse, NY, USA, April 2004.